Multiple Timescale Spectral Analysis of Aeroelastic Systems

by

Julien Heremans

A thesis submitted in partial fulfillment of the requirements for the degree of Doctor of Philosophy in Engineering Sciences

July 2025

Members of the Jury

President — Prof. T. Andrianne
University of Liège

Advisor — Prof. V. Denoël
University of Liège

Prof. G. Dimitriadis
University of Liège

Hon. Prof. V. de Ville de Goyet
University of Liège

Prof. L. Caracoglia
Northeastern University

Prof X. Amandolese
Conservatoire National des Arts & Métiers

À celles et ceux qui m'ont façonné.

Abstract

This Thesis presents the development of a computationally efficient methodology for evaluating the aeroelastic response of large multi-degree-of-freedom (MDOF) structures subjected to turbulent wind excitation. In the context of civil engineering, and particularly the design of long-span bridges, the design process involves numerous iterations, with frequent updates to structural properties and loading conditions. Traditional buffeting analysis methods, while accurate, are often computationally intensive and thus unsuitable for early-stage design or extensive parametric studies. The methodology developed herein provides a practical alternative, significantly reducing computational costs while maintaining sufficient accuracy for preliminary assessments.

The proposed approach builds upon the Multiple Timescale Spectral Analysis (MTSA) framework and extends the classical background/resonant decomposition introduced by Davenport to aeroelastic systems. The method operates in the frequency domain and aims to estimate the response variances across the entire wind speed envelope. This is achieved through an analytical approximation of the system's response Power Spectral Density (PSD), decomposed into background and resonant components. The resulting semi-analytical expressions allow the response variances to be analytically integrated with high efficiency, providing significant savings in computational time for high-dimensional structural systems.

The methodology was first validated on single-degree-of-freedom (SDOF) and two-degree-of-freedom (2DOF) models, demonstrating high accuracy and consistency with reference solutions. The MTSA approach was then generalized to MDOF systems, addressing key challenges such as modal coupling, frequency-dependent aeroelastic effects, and the use of complex modal bases. A detailed investigation was conducted on the influence of the modal basis and the formulation of the impedance matrix. The use of wind-on modal bases including left and right eigenvectors, combined with a linear gradient-based impedance formulation, was shown to yield optimal accuracy and robustness.

Two numerical tools were developed to support the implementation of the method. The first is a robust continuation algorithm designed to precompute wind-dependent modal properties, including complex mode shapes, across the design envelope. The second is a bisection-based algorithm for determining critical flutter velocities, formulated through the separation of the real and imaginary parts of the flutter condition, providing improved convergence and mode-tracking capabilities.

Overall, this Thesis contributes a complete, systematic, and computationally efficient framework for aeroelastic analysis at the early design stage. It facilitates rapid response predictions over a wide parameter space and offers significant potential for integration into modern iterative design processes, supporting both robustness and flexibility in the preliminary stages of long-span bridge design.

Ackowledgements

Voici plus de 5 ans que les tortueux chemins de la vie m'ont mené à emprunter la voie d'une thèse de doctorat. Cette destination n'était certainement pas dans la direction que j'imaginais suivre à l'issue de mes études. Le jour où je me suis d'ailleurs décidé à monter dans le train conduit par mon promoteur, Vincent Denoël, j'avais paradoxalement prévu de le rencontrer pour décliner sa proposition. Mais comme parfois dans la vie, et comme souvent avec Vincent, quelque chose de magique a opéré: il n'en fallut pas plus pour changer le cap.

C'est ainsi que j'ai embarqué avec Vincent et son équipe, initialement en tant qu'ingénieur de recherche, puis en tant que doctorant. Un regard jeté par-dessus l'épaule suffit à mesurer à quel point ces années ont filé à vive allure — et combien de kilomètres ont été parcourus au fil de ces quelques années riches en rebondissements.

Arrivé presque à destination, je voudrais particulièrement remercier Vincent, pour son implication indéfectible dans nos projets, depuis leur montage, jusqu'à leur aboutissement. Sans parler de ses inépuisables compétences techniques et scientifiques, j'ai spécialement apprécié ses qualités humaines, son enthousiasme, sa pédagogie, sa patience et sa soif de partage qui firent que les obstacles rencontrés en route semblèrent souvent moins impressionnants. Je pense que les plus belles leçons que je tirerai de cette rencontre ne sont incroyablement ni techniques, ni scientifiques.

Merci à tous ceux qui ont contribué à ce voyage, notamment par le financement de cette recherche: la Région Wallonne et le bureau d'étude Greisch via le projet Finelg2020, le FNRS pour le soutien à travers une bourse FRIA, la Faculté de Sciences Appliquées de l'ULiège pour la bourse fin de thèse, ainsi que le secteur SE pour les derniers mois. Merci aussi aux membres du jury pour avoir accepté d'évaluer ce travail et pour le temps qu'ils y consacreront.

J'ai eu la chance de faire la route avec de formidables collègues, Anass, Margaux, Michele, Kevin, François, Florence et Loris sans qui la route aurait parfois pu sembler très longue. La liste est bien entendu plus longue... Je les remercie pour tous ces bons moments passés ensemble et pour tous ces mémorables souvenirs que j'emporte précieusement avec moi dans mes valises.

Merci aussi à toutes ces personnes que j'ai rencontrées pendant ce voyage, que ce soit autour d'un repas à la cafète, au Dino, d'un wok à Boncelles, d'une raclette au B52, d'un café à Montef ou d'une bière à un afterwork ou aux Trottis. Merci aussi à toutes ces rencontres enrichissantes, aussi dans de circonstances plus sérieuses. Je pense à celles impliquées dans le projet Finelg qui m'ont conforté dans ma passion des développements numériques, Vincent, Marco, Julian et tant d'autres, aussi à celles impliquées dans le concours Faites le Pont. Dans un registre encore plus sérieux, tous les vélotaffeurs notamment Patrick, Romain, Cédric et Philippe. J'ai eu beaucoup de plaisir à rouler et courir ces 18.000 km à vos côtés au cours de ces années.

A l'heure de débarquer de ce train, je voudrais remercier toutes celles et ceux qui m'ont soutenu dans certains moments difficiles. Je remercie particulièrement ma famille, mes supporters de toujours, qui y ont cru parfois plus que moi. Leurs encouragements ont été essentiels, notamment dans la dernière ligne droite.

Je voudrais enfin particulièrement remercier ma compagne, Florence, ma fidèle équipière depuis maintenant plus de 12 ans, qui me suit, me porte et m'encourage jour après jour dans mes projets les plus fous. Son inconditionnel support émotionnel, affectif et logistique a été inestimable. Je lui dois une part précieuse de cette réussite.

Contents

Chapter 1

Introduction

The design and construction of bridge decks have long represented a pinnacle of engineering innovation, showcasing the balance between form and function, aesthetics, and structural integrity. Over the years, engineers have consistently pushed the boundaries of what is possible, driven by a relentless desire to create structures that are not only strong and durable but also elegant and efficient. As engineering capabilities have advanced, so too have the ambitions for bridge designers, leading to the construction of spans that cover ever-greater distances. These longer span bridge designs come with new challenges, particularly the need to design more slender structures, while still ensuring both safety and comfort of the users. Figure 1.1 illustrates the remarkable growth in demand for large-span bridges over recent decades, with more than 30 projects featuring main spans exceeding 1000 meters either completed or under construction in the past 25 years.

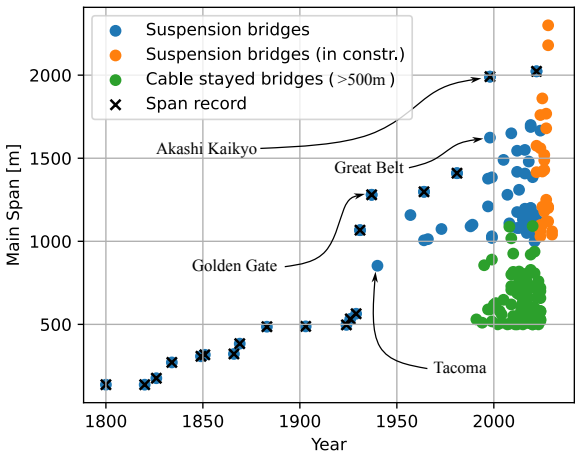

Figure 1.1: Historical evolution of the main spans over years from 1800 to 2024, for 79 suspension bridges, and 94 cable supported bridges.

In parallel with this race to achieve larger spans, the early 21st century has also seen the emergence of a new and fundamental concern concerning resource utilization. Indeed, minimizing material usage has today become not just an engineering goal but a critical challenge, driven by the urgent need to reduce CO2 emissions and conserve primary resources. The environmental impact of construction is now a central consideration in every project, with sustainability and resource efficiency integrated into the core of design analysis. This shift has elevated the importance of creating structures that use fewer materials without compromising on safety or performance. Engineers are today tasked with balancing these competing demands–creating bridges that are both environmentally responsible and economically viable, all while maintaining the highest standards of structural integrity and aesthetic appeal. Although this observation

applies broadly to civil engineering, it is increasingly relevant in fields such as aeronautics, automotive, material sciences, and transport, where resource and energy efficiency are key drivers of innovation. To meet these challenges, engineers, and more particularly civil engineers must delve deeper into design details, continually adopting newer techniques and innovative methods. The method presented in this Thesis does not redefine flutter and buffeting analysis, but aims at reducing the associated computational costs, allowing to speed up the parametric design of complex structure.

The modern vision of architecture also tends to lead to the erection of refined and lightweight structures, driven by both aesthetic and environmental considerations. Number of recent designs prioritize these qualities over some important design requirements because they are destined to be not only visually striking but are also viewed as artistic masterpieces, enhancing the city's visual appeal. Additionally, slender structures are seen as more harmonious with their environment, blending seamlessly with natural landscapes and urban settings. This integration not only reduces visual impact but also reflects a broader trend towards creating sustainable and aesthetically pleasing infrastructure that respects and complements its environmental context.

This design with increased slenderness, while aesthetically pleasing and material-efficient, results in structures with lower natural frequencies, making them more susceptible to dynamic effects and low-frequency loading in general. Additional architectural choices may also sometimes lead structures to deal with disabling characteristics such as very low structural damping or a highly aeroelastically susceptible deck profile. Hence, this emphasis on architectural considerations, material efficiency, environmental stewardship has brought new challenges to the forefront of bridge engineering. This Thesis is provides an innovative solution to investigate the design of civil engineering structures subjected to aeroelastic loads.

As with any scientific discipline, today's knowledge is constrained by the current scope of research within the scientific community, leaving substantial room for further exploration, especially in emerging fields. Aeroelasticity and wind engineering in general, particularly in the context of civil engineering applications, are indisputably one of these fields with vast potential for advancement. This project focuses specifically on one particular phenomenon: flutter. Flutter is an aeroelastic instability, characterized by self-excited vibration that occurs in various types of structures such as aircraft and bridges. It can result in dangerous oscillations, or even total loss of the structure, which makes it a serious concern for design engineers. As bridge designs become increasingly ambitious in their pursuit of material efficiency and longer spans, the need to thoroughly understand and control the structural response of aeroelastically loaded structures is more critical than ever. This understanding is fundamental to reduce the safety margins to an optimal and safe operational level. This Thesis however, does not investigate the mechanism of flutter in itself, but presents rather a solution to carry out a complete and computationally efficient buffeting analysis with unsteady effects.

As will be discussed in detail later, the method presented in this Thesis is an approximation technique. While it does not achieve the level of accuracy offered by the advanced flutter analysis methods available today, it allows for a significantly faster analysis—reducing computation time by an order of magnitude [1]. This method is particularly suited for early design stages or parametric studies, where section properties and loads are expected to vary frequently, rather than for the final design where classical buffeting analysis method remain indispensable to meet the accuracy standards. The iterative nature of the design process means that a combination of checks is repeated numerous times for all load combinations, construction stages, and section shapes for instance. Ideally, with each iteration, all analyses must be performed as the dataset changes, which can be quite time-consuming, especially for buffeting analysis when a complex aeroelastic model is involved. Hence, at early design phases, and particularly if the number of parameters considered in the design is large, the use of a fast approximation method enables design engineers to quickly assess the structural behaviour without waiting for lengthy recalculations each time design data is updated.

In this first chapter, we will explore aerodynamic excitations, introduce the concepts of buffeting, and develop a physical understanding of self-excited forces. The phenomenon of flutter will be examined in detail, alongside a review of existing methods for buffeting analysis, with particular focus on the spectral method, which serves as the foundation for the approximation method developed in subsequent chapters. Finally, we will introduce the key concept underlying the novel method, the multiple timescale spectral analysis, and provide a glimpse of its capabilities, outlining the motivations having driven this project.

1.1 Wind and turbulence

Wind is the natural movement of air across the Earth's surface, driven primarily by differences in atmospheric pressure caused by uneven heating of the planet. At altitudes of approximately 1000 meters above the ground, wind speeds are almost not influenced by the boundary layer effects near the Earth's surface. At these heights, wind speed results from a balance between the forces resulting from the atmospheric pressure gradients, driving air from high to low-pressure regions, and the Coriolis force, which arises from the Earth's rotation [2]. Closer to the ground, the roughness of the surface due to topography, vegetation, and urbanisation of the surface reduces the speed of the wind, at least on average. It also generates turbulence, characterized by spatial and time variation of the wind velocity. This region of the atmosphere where friction effects are dominant is called the atmospheric boundary layer.

At a macro-scale, the wind in the atmospheric boundary layer may be seen as a set of vortices of different sizes —small, medium or large— from several dozens of meters to two hundreds of meters length, convected by a mean wind flow. Each vortex shed at a frequency f causes in a point of the space a periodic fluctuation in speed with circular frequency $\omega = 2\pi f$ in the three considered directions. These vortices are the cause of the spatial coherence of the wind, while the density of the vortices in the macroscopic medium and their convection speed translates the time correlation of the wind. Mathematically, this is modelled by two very different timescales affecting the wind speeds, as depicted in Figure 1.2 illustrating the power spectrum of the horizontal wind speed in the atmospheric boundary layer for different scales ranging from 1 year to 1 second. The first timescale is associated with the slow variations of the order of several hours to days and is due to the passage of synoptic storm systems induced by differences in atmospheric pressure at a cyclonic scale [3]. The second variation relates to the rapid variation, with representing period of one minute or one second and is due to the turbulence induced by the surface roughness. For this reason, the wind velocity in any point $P(x, y, z)$ is mathematically characterized by an average velocity, and a fluctuating vector

$$\mathbf{u}(t, x, y, z) = \begin{bmatrix} U(x, y, z) \\ 0 \\ 0 \end{bmatrix} + \begin{bmatrix} u(t, x, y, z) \\ v(t, x, y, z) \\ w(t, x, y, z) \end{bmatrix}, \tag{1.1}$$

where U is the 10-minute averaged wind speed, and u, v and w are the fluctuating time-dependent components in the along-wind —parallel to U—, lateral and vertical directions. An example of synthetic 10-minute time histories of horizontal wind speeds is shown in Figure 1.3 for two 30m distant nodes of a bridge deck. This coherent time series were generated according to [4].

The average wind speed is characterized by a reference wind speed U_{ref}, equal to the average wind speed at sufficiently large height above the ground where turbulence has no effect any more. For design stages, this value is considered as a constant since the typical duration of the design events —usually 10 minutes— is always much smaller than the period of the slow timescale of the wind properties variation. This constant reference value is chosen according to the standards, depending of the return period of the event, the season and the orientation of the main wind.

Inside the atmospheric boundary layer, the wind profile is not uniform over the elevation due to friction effect. The actual average wind speed is evaluated at a given height z using

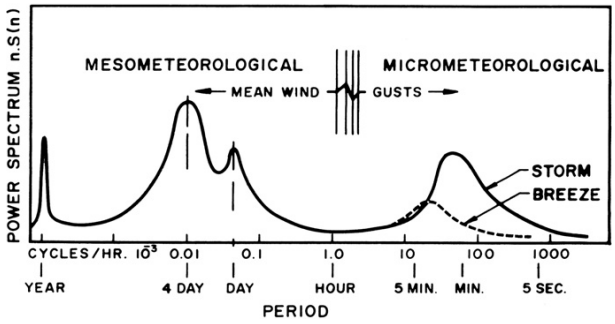

Figure 1.2: Spectrum of the horizontal wind speed variation in the atmospheric boundary layer. Figure taken from [5].

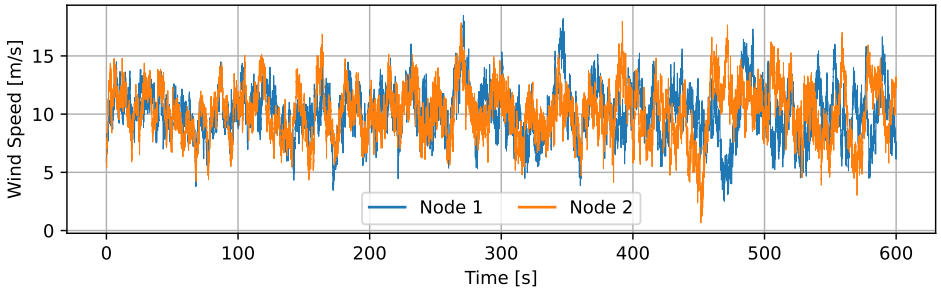

Figure 1.3: Example of spatially coherent wind speed time histories generated at two 30 m distant nodes, on a deck level. The reference average speed is 10 m/s.

semi-empirical models such as the power law or, more frequently, the logarithmic law

$$U(z) = U_{\text{ref}}\, k_r(z_0) \log\left(\frac{z}{z_0}\right), \tag{1.2}$$

where the rugosity factor k_r and the height of a characteristic rugosity z_0 accounts both for the rugosity of the terrain and are generally provided by design codes [6].

From a practical point of view, the turbulence is mathematically formalized in the frequency domain by a power spectral density (PSD). The power spectral density of the wind speed quantifies how the power of wind speed fluctuations is distributed across different frequency components. It provides a statistical representation of the energy content in wind speed variations as a function of frequency. The formulation of a spectrum has been the object of intensive research [7, 8, 9, 10, 11], where some are now considered as universal reference. This is for instance the case of the Von Karman spectrum [12], that expresses the power spectral density of the longitudinal fluctuating wind speed at a point $P_i(x_i, y_i, z_i)$ as

$$S_{ii}(z_i, \omega) = \frac{2L_x^u/\pi}{U\left[70.7\left(\dfrac{\omega L_x^u}{2\pi U}\right)^2 + 1\right]^{5/6}}\, \sigma_u^2(z) \tag{1.3}$$

where L_x^u is the turbulence length scale, representing the characteristic length of turbulent vortices in the main wind direction —typically ranging from a decade to a hundred meters—, and σ_u the standard deviation of the turbulent longitudinal component u. This standard deviation may be evaluating according to $\sigma_u = k_r U_{\text{ref}}$ or can be directly computed from statistical processing of on-site measurements.

Numerous spectra have been proposed by various authors to model turbulence. These models may account for the turbulence scale, the altitude, or specific applications contexts for instance to

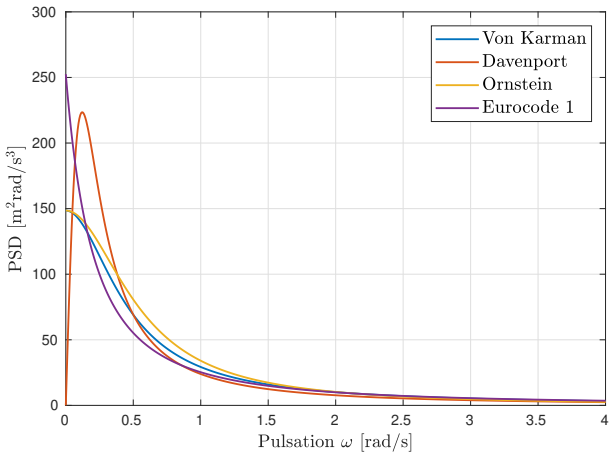

Figure 1.4: Comparison between four commonly used power spectral densities of longitudinal fluctuating wind speeds used in wind engineering.

accommodate orographic constraints. Figure 1.4 illustrates some commonly used PSD formulations for the longitudinal fluctuating wind speed u. All these models share important similarities as they are tailored to atmospheric turbulence. These spectra as well as the associated forces are often referred to as *buffeting* spectra or forces. It may be interesting to mention that beyond this particular application, many other turbulence models have been developed for wider frameworks, for instance by Heisenberg [13] and Kolmogorov [14], but are not very useful in wind engineering.

The PSD that we use is such that we recover the variance when integrated over all circular frequencies, including both negative and positive sides ($\omega \in]-\infty, \infty[$). This corresponds to a two-sided PSD defined in angular frequency (rad/s). It is not a one-sided PSD (defined only for $\omega > 0$), nor is it expressed in Hertz (Hz). Different scaling conventions are used in the literature, so that formulations may differ by a factor of 2, 2π, or even 4π, depending on the domain (frequency vs angular frequency) and whether a one- or two-sided spectrum is used. The convention adopted here will be kept consistently throughout the manuscript.

As introduced above, the translation of the eddies responsible for turbulence is the cause of the fluctuating components of velocity to exhibit spatial coherence. This means that wind speed fluctuations at two points in space, separated by several dozen meters, are neither identical nor statistically independent either. This spatial coherence is modelled by means of a coherence function $\Gamma_{ij}(\omega)$ which establishes a relationship between the power spectral densities of wind speeds evaluated at two distinct points of the space P_i and P_j

$$\Gamma_{ij}(P_i, P_j, \omega) = \frac{S_{ij}(\omega)}{\sqrt{S_{ii}(\omega) S_{jj}(\omega)}}. \tag{1.4}$$

This function is generally modelled as an exponential function decaying with the frequency and the internodal distance [9]

$$\Gamma_{ij}(P_i, P_j, \omega) = \exp\left(-\frac{\omega\sqrt{C_x^2\Delta x^2 + C_y^2\Delta y^2 + C_z^2\Delta z^2}}{\pi(U_i + U_j)}\right). \tag{1.5}$$

where C_x, C_y and C_z are the coherence coefficients in the x, y and z directions, and Δ_x, Δ_y and Δ_z are the corresponding internodal distances.

Equations (1.3), together with (1.4) and (1.5), provide all the necessary material to construct the PSD matrix of the wind speeds, written $S_{\mathbf{uu}}(\omega)$ or $S_{\mathbf{ww}}(\omega)$ respectively for the u and w fluctuating components, which will subsequently be used to compute the aerodynamic forces

and assess the structural response. When constructing the global wind speed PSD matrix $S_{\mathbf{uu}}$, it is important to note that, although the wind speed components u, v, and w are spatially correlated when considered separately, little coherence will be assumed between these components as proposed by [15]. This is mathematically expressed as $\Gamma_{uv} = \Gamma_{uw} = \Gamma_{vw} = 0$.

1.2 Introduction to the aerodynamic excitations

The interaction between a structure and its surrounding fluid has always been a great concern for civil engineers. Until the 20th century, this interaction was largely overlooked [16], which led to several disastrous events in the 19th century [17], during the early stages of long-span bridge engineering. As spans grew longer and structures became more flexible, these failures highlighted the need for a deeper understanding of aerodynamic phenomena. The collapse of the Tacoma Narrows Bridge in 1940 [18] marked a turning point, emphasizing the necessity of integrating aerodynamic concepts into bridge design. To address this growing complexity, the subsequent sections of this Thesis will provide a concise overview of key aerodynamic principles, forming the foundation for the analyses presented later in this document.

1.2.1 Aerodynamic loads in uniform flows

Aerodynamics is a broad field encompassing various disciplines related to the study of airflows and their effects on solids immersed in the flow. In civil engineering, the focus is exclusively on wind-induced flows, which inherently involve low Mach and high Reynolds numbers. The Mach number quantifies the flow speed relative to the speed of sound. The low Mach numbers encountered in wind engineering, typically $\mathrm{Ma} \ll 0.3$, justify the assumption of incompressible flow [19, 20].

The Reynolds number expresses the relative importance of inertial forces over viscous forces in the flow

$$\mathrm{Re} = \frac{\rho |\mathbf{v}| D}{\nu}, \tag{1.6}$$

where ρ is the air density, $\mathbf{v}$ is the fluid velocity and D is a characteristic length of the solid (such as diameter for a cylinder, the width of a foil or bridge deck) and ν the kinematic viscosity. Consequently, this number is a dimensionless measure of the turbulence of a fluid flow. Because of the relative importance of the turbulent effects in the boundary layer, bridge engineering applications typically involve high Reynolds numbers ranging from 10^4 to 10^6.

The behaviour of fluids at the macroscopic scale is governed by the Navier-Stokes equations. Solving these equations directly is often impractical due to the turbulent nature of the flow, and due to the complexity of the structures and flow scenarios encountered in civil engineering. Certain old and well established aeroelastic models such as the flat plate model are however based on Bernoulli's equation, an integral form of the Navier-Stokes equation degenerated to irrotational flows. This equation is very important in wind engineering and is used almost all of the actual models whether these are numerical or experimental—even though not sufficient for modelling all the particular aspects related to the boundary layers such as flow separation, friction drag, etc. This equation reads

$$\rho \frac{\partial \phi}{\partial t} + \frac{1}{2} \rho |\boldsymbol{\nabla} \phi|^2 + p = \text{Constant}. \tag{1.7}$$

where $\mathbf{v} = \boldsymbol{\nabla} \phi$ is the vector containing the fluid velocity in the coordinates system, ϕ is the potential of the velocity, p the pressure. When particularized to stationary flows, it allows to link directly the static and dynamic pressure to a constant total pressure p_0

$$\frac{1}{2} \rho |\mathbf{v}|^2 + p = p_0, \tag{1.8}$$

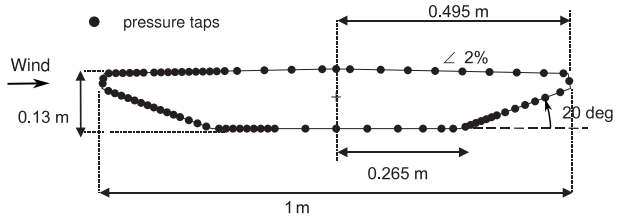

Figure 1.5: Description of a reduced model of the the Sunshine Skyway Bridge deck section, and location of the pressure measurement tabs. Figure adapted from [26].

which is a good starting point when it comes to formulate the aerodynamic loads applied on a solid. It represents the normal force acting on a infinitesimal element of surface of a solid immersed in a flow, if all viscous effects were negligible. Practice shows however that this assumption is not always valid for streamlined sections. This static pressure is therefore complemented by a friction drag and lift originating from the formation of a boundary layer developed by the viscous flow around the solid. The shear stress in the boundary layer results from the gradient of the fluid particle velocity existing inside the boundary layer. This shear is usually low for bluff bodies but is significant for streamlined bodies such as airfoils or some bridge decks.

More generally, the dynamic pressure can be characterized using a dimensionless pressure called pressure coefficient

$$C_p = \frac{p - p_0}{\frac{1}{2}\rho|\mathbf{v}|^2}. \tag{1.9}$$

This coefficient involves the effects of the static pressure, the dynamic pressure and the shear stress. It plays an important role in the characterization of the load acting on the body. It may be measured in wind-tunnels using pressure taps [21, 22, 23] or alternatively numerically calculated using computational fluid dynamics (CFD) methods [19, 20, 24, 25]. An example of pressure coefficient distribution over a bridge deck section is shown in Figure 1.5 for several angles of attack α. The prototype tested is a reduced model of the Sunshine Skyway Bridge deck and is described in Figure 1.5.

The aerodynamic forces are the result of the superposition of all pressure distributions acting on the outer surface of the body. For two-dimensional bodies, the resultant load is typically decomposed and expressed in the deck coordinate system as a set of two forces and one torque. The force aligned with the flow direction is referred to as the drag force F_D, while the force perpendicular to the flow is the lift force F_L. The torsional moment F_M arises from the cumulated effect of elementary torques resulting from the pressure distribution on the body and their lever arm with respect to a chosen reference point. Examples of lift, drag and moment are represented in Figure 1.7.

In structural dynamics, it is often practical to reference forces to the centre of torsion, which is the point where a pure rotational motion does not induce horizontal or vertical displacement. This choice aligns the aerodynamic loading with the modal properties of the bridge.

It is common to represent the aerodynamic forces by dimensionless coefficients C_D, C_L and C_M, so that they can be consistently transposed from a reduced to a real model. These coefficients are expressed as follows

$$C_D(\alpha, \mathbf{v}) = \frac{F_D}{\frac{1}{2}\rho|\mathbf{v}|^2 B}, \qquad C_L(\alpha, \mathbf{v}) = \frac{F_L}{\frac{1}{2}\rho|\mathbf{v}|^2 B}, \qquad C_M(\alpha, \mathbf{v}) = \frac{F_M}{\frac{1}{2}\rho|\mathbf{v}|^2 B^2}. \tag{1.10}$$

where B represents the width of the section.

Like pressure coefficients C_p, aerodynamic loads and their associated coefficients depend on the angle of attack α, defined by the orientation of the mean wind flow $\mathbf{v}$ relative to the angular position of the bridge. These coefficients are typically obtained through wind-tunnel testing using force sensors or trough integration of the pressure all over the surface of the body

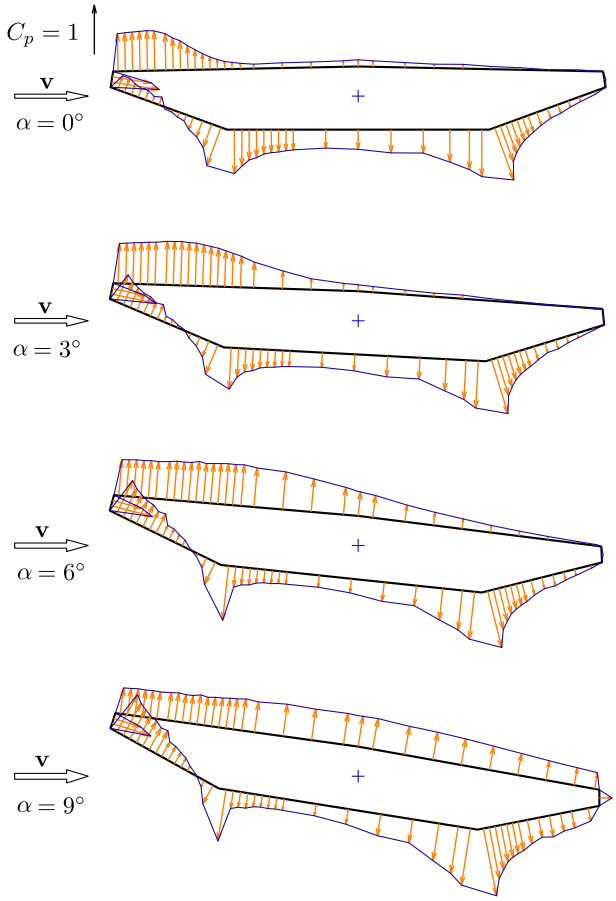

Figure 1.6: Average pressure coefficient distribution over the Sunshine Skyway Bridge deck section. Figure adapted from [26].

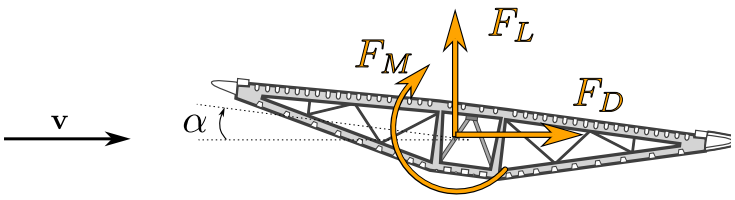

Figure 1.7: Aerodynamic forces of drag and lift and aerodynamic torque, acting on a bridge deck subjected to a wind with angle of attack α.

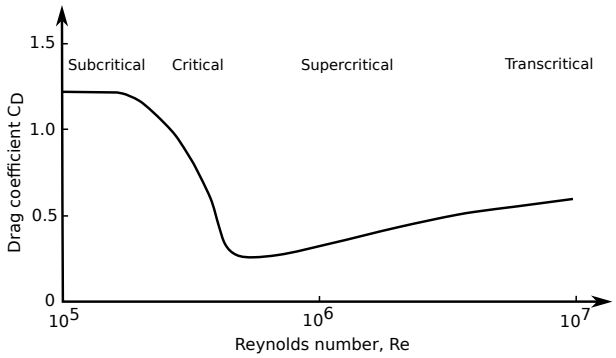

Figure 1.8: Evolution of the average drag coefficient with Reynolds number for a circular cylinder. Adapted from [28].

after computing the pressure distribution using CFD methods. For a fixed wind speed, these coefficients are generally measured or computed for various incidences. Figure 1.9 illustrates the variation of the lift, drag and moment coefficients with respect to α obtained from wind-tunnel testing either from the integration of the pressure distributions or directly from the force measurement.

The coefficients given in Figure 1.9 are averaged values. In reality, these coefficients fluctuate over time due to the turbulence in the boundary layer at the solid/fluid interface. In particular, this turbulence influences the flow in the boundary layer, the location of the turbulent/laminar transition points and the location of the flow separation and reattachment points, which can greatly modify the downstream flow mechanism and consequently the pressure distribution. The importance of this intrinsic turbulence is translated by the strong dependence of the pressure distribution (or force coefficients) on the Reynolds number. Such dependence can be observed in Figure 1.8, which illustrates the evolution of the average drag coefficient with Reynolds number through different flow regimes around an infinite length circular cylinder [27].

However, most of these changes in the flow mechanism do not occur in the Reynolds range considered for bridge aerodynamics. More importantly, bridge deck sections generally involve sharp edges where flow separation systematically occurs at geometrically fixed points, regardless of the Reynolds number. The flow pattern is then primarily dictated by the geometry of the section rather than by the characteristics of the incoming flow. As a result, the mean pressure distribution—and hence the force coefficients—becomes relatively insensitive to the exact value of the Reynolds number within the typical operating range. Consequently, bridge deck sections are usually considered to be insensitive to moderate variations in upwind turbulence or incoming wind speed.

It is important to emphasize that the force coefficients are defined under the assumptions of a fixed body in a uniform flow. This implies, first, that the prototype must not move or deform under the applied aerodynamic force and, on the other hand, that all fluid particles in the upstream flow have the same (average) velocity. In fact, these assumptions are very restrictive for civil engineering applications because structures vibrate and usually deform under aerodynamic action, and also because the incoming flow is always turbulent. In the next sections, the evaluation of the aerodynamic loads in civil engineering will be discussed in detail, and see how the previously introduced theory can be used for this matter.

1.2.2 Aerodynamic loads in turbulent flows

When the upstream flow is turbulent such as in the atmospheric boundary layer, the uniformity of the incoming flow is not observed anymore and the forces and moment calculated according to (1.10) are no more valid. A correction must therefore be made to the previous theory to account for the turbulence of the incoming flow.

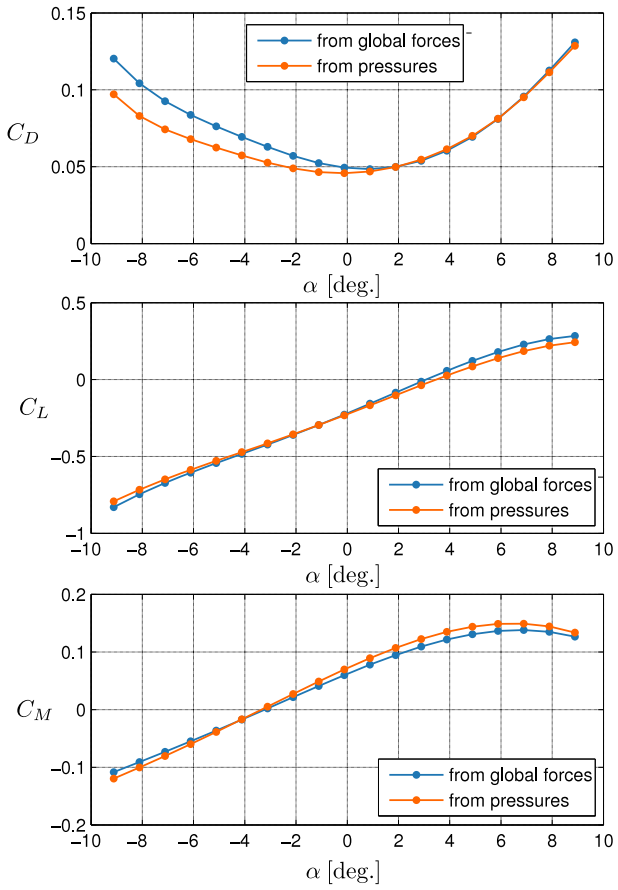

Figure 1.9: Average drag, lift and moment coefficients for the Sunshine Skyway Bridge deck section, obtained from direct measurement of the force or from the integration of the pressure distribution. Figure adapted from [26].

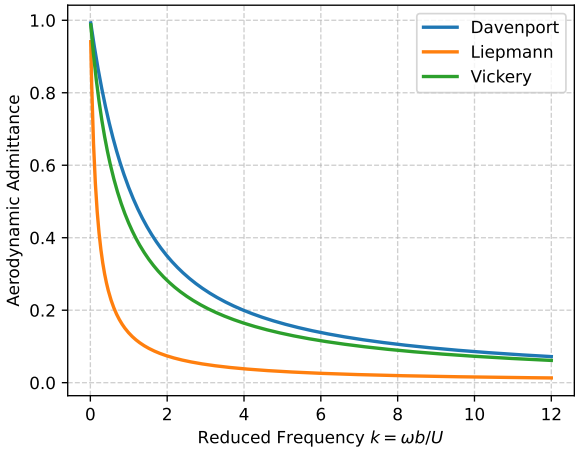

Figure 1.10: Example of aerodynamic admittance functions used to evaluate the effect of incoming turbulence on the aerodynamic forces.

The first research carried out on the impact of incoming turbulence are rooted by Küssner. Küssner's function describes how the transient lift develops due to a transverse gust, introducing the idea of spatial filtering. This work was initiated in time domain, and its equivalent in frequency domain has led to the formulation of the aerodynamic admittance $|\Theta(\omega)|^2$. Admittance extends Küssner's functions to quantify the attenuation of static aerodynamic forces caused by turbulence as it varies across the bridge deck, incorporating both spatial coherence and frequency-dependent effects. In general, this admittance is tailored to lift, drag or moment and to u, v or w and they must be experimentally derived. Some author such as Sears [29] and Liepmann [30] have however proposed formulations for simple cases, while some others have proposed semi-empirical formulations. Several admittance functions are presented in Figure 1.10.

At cross section level, the unsteady force resulting from the turbulence of the incoming flow is then calculated by applying an aerodynamic admittance module directly to the aerodynamic force that would be measured in a uniform flow.

1.2.3 Classification of fluid excitations

The previous section introduced the drag, lift, and moment coefficients, which are used to evaluate the aerodynamic loads acting on fixed sections in uniform flows. The assumption of uniform flow is quite restrictive, and not compatible with civil engineering applications. In practice, different forces may be categorized depending on the particular flow conditions.

The first force arising from a uniform free-stream flow over fixed body is the *static aerodynamic force*. It is determined based on the average wind speed in the upwind flow. Under this static force, the bridge undergoes a deformation that may affect the angle of attack and consequently the force coefficients. Aside from inducing this static deformation, the static aerodynamic force has no direct impact on the bridge's dynamic response and is therefore often treated separately in the analysis.

When the upstream flow is turbulent, fluctuations in wind speed induce vibrations of the structure, known as buffeting. This random excitation is typically modelled using stochastic approaches, where the wind fluctuations are described by their power spectral density.

Large-span bridge decks are generally flexible, deforming, tilting, and moving under fluctuating aerodynamic loads. When the convective frequency of the turbulent incoming flow is much larger than the natural vibration frequencies of the deck, the flow is considered to adapt almost instantaneously to the structural motion, as if it cannot capture the rapid motion of the obstacle. This forms the basis of the quasi-steady approach that will be discussed more in detail in later

Section 1.3.1. Essentially, this method assumes a one-way interaction where the slow motion of the structure influences the flow, but the reciprocal fluid-structure interaction is neglected. Under this framework, the instantaneous aerodynamic forces acting on an obstacle are treated as if the flow was steady. These forces are calculated using the same lift, drag, and moment coefficients as in uniform flows, applied to the effective instantaneous wind speed and angle of attack.

When the vibration frequency is high compared to the convective frequency, the induced flow is expected to vary significantly within one oscillation cycle to adapt to the motion of the section. The relatively rapid motion of the deck changes the flow conditions and the aerodynamic load can not be expressed as in the quasi-steady model any longer. This fluid/structure interaction is called *unsteady aerodynamics*, and the associated loads are referred to as *aeroelastic loads* or *unsteady loads*. The fact that these forces are dependent on the movement of the structure also sometimes earns them the name of *self-exciting* forces. Their motion-dependent nature means they are susceptible to affect the system's dynamic properties, such as natural frequencies and damping ratios.

Another aerodynamic excitation mechanism is vortex shedding, which can lead to vortex-induced vibrations (VIV). Flows over bluff bodies, such as bridge decks, are inherently characterized by the shedding of vortices. This phenomenon arises from the detachment of flow around the body and is influenced by its geometric features, such as smooth curves or sharp edges [31, 32]. Vortices are shed at a dimensionless frequency determined by the Strouhal number (St), which relates the vortex-shedding frequency to the characteristic length of the section and the average wind speed,

$$St = \frac{fD}{U}, \tag{1.11}$$

where D is a characteristic length of the section perpendicular to the flow. Because of the complexity of the flow mechanism, the Strouhal number is usually derived from experimental wind-tunnel measurements [33]. Vortex shedding results in a periodic excitation force, whose period is characterized by the vortex shedding frequency. The critical concern with vortex shedding lies in its potential to excite resonant frequencies of the structure, leading to VIV. This resonance can result in significant oscillations, posing risks to structural integrity or causing fatigue related issues. VIV is further complicated by the mechanism of lock-in, where the shedding frequency locks onto the structural natural frequency, maintaining resonance even as wind speed varies slightly.

The main four different aerodynamic excitations have been presented in this section, namely the mean wind forces, the buffeting forces, the aeroelastic forces and the VIV. The mean force is usually left aside and treated in a static analysis. The dynamic analysis then focuses on the last three remaining forces, the effects of which are illustrated in Figure 1.11, which shows a schematic of a classical structural response of a structure, simultaneously subjected to the three aerodynamic actions, and shows in which wind speed range each of these actions is likely to affect the dynamic response. Buffeting effects occur within the frequency ranges defined by the natural vibration frequencies of the structure. The eigenfrequency can change due to aeroelastic effects, and may therefore not align with the wind-off eigenfrequencies, as illustrated by the frequency shift in Figure 1.11. The VIV also occurs within these frequency ranges, although the responding modes are not necessarily identical. While buffeting is a forcing action proportional to the square of the mean wind speed, and VIV is a self-limited phenomenon, the effect of self-excited forces is significantly different as they can result in a critical stability. For wind speeds larger than the critical limit U_{cr}, the system passes from a stable state to an unstable state, virtually experiencing unbounded oscillation amplitudes in a linear model. This phenomenon is called aeroelastic instability and is analysed by means of a critical analysis. This is the major difference with respect to buffeting and VIV, which both result in bounded amplitudes.

Although these three primary excitation mechanisms are typically presented separately (see Figure 1.11), they sometimes do not act independently. Instead, their interactions can lead

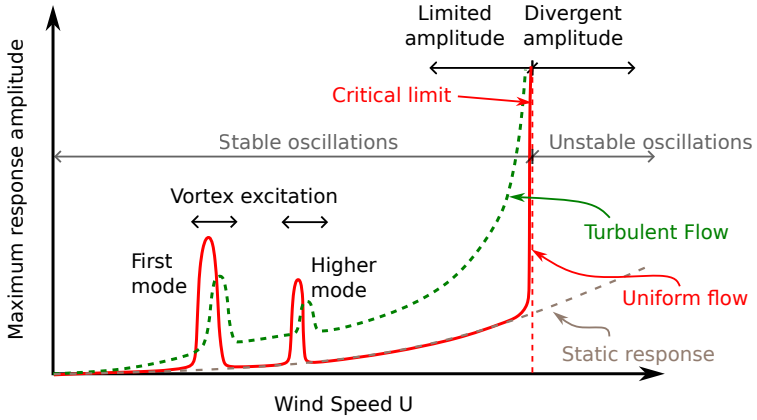

Figure 1.11: Schematic response of a civil engineering structure subjected to the four concomitant aerodynamic excitations in uniform and non-uniform flows. Figure adapted from [34].

to complex responses, and their combined effects are often non-additive [35, 36]. In practice, aeroelastic and buffeting effects are frequently considered together, as this approach allows for the incorporation of fluid-structure interaction phenomena [37]. The consideration of this fluid-structure interaction is very important to predict the buffeting response as aeroelastic force may inject additional energy into the oscillating system, and increase the amplitude of vibrations [38, 39].

By contrast, VIV effects are commonly treated separately from aeroelastic effects, even though this decoupling can be questioned in certain scenarios [36, 40]. This simplification is generally deemed acceptable for low-amplitude vibrations where no lock-in phenomenon is expected to occur in the considered wind speed range. In essence, VIV analysis is conducted independently, assuming no significant interaction with aeroelastic forces, provided the wind speed is sufficiently distant from the critical VIV onset speed and the vibration amplitudes of the bridge deck remain small.

In this Thesis, we adopt this decoupled approach. Specifically, we focus on the simultaneous action of buffeting and aeroelastic forces, excluding the consideration of VIV, which could therefore be treated in a separate analysis [41, **?**]. We are therefore left with two effects: turbulence, and self-excited forces. Although there is no evidence that these can be rigorously expressed a sum of two forcing terms, there is the current modelling option used in the literature [35, 42]. As a consequence, two forcing terms will be considered in an additive manner in the equations of motion

$$\mathbf{M}_s\ddot{\mathbf{x}}(t) + \mathbf{C}_s\dot{\mathbf{x}}(t) + \mathbf{K}_s\mathbf{x}(t) = \mathbf{f}_{\mathrm{se}}(t) + \mathbf{f}_{\mathrm{bu}}(t), \tag{1.12}$$

where $\mathbf{M}_s$, $\mathbf{C}_s$, $\mathbf{K}_s$ are the nodal structural matrices of mass, damping and stiffness, respectively expressed in kg, $\mathrm{N\,s\,m^{-1}}$ and $\mathrm{N\,m^{-1}}$, $\mathbf{x}(t)$ is the nodal displacement vector, $\dot{\mathbf{x}}(t)$ its time derivative, and where $\mathbf{f}_{\mathrm{se}}(t)$ and $\mathbf{f}_{\mathrm{bu}}(t)$ stand respectively for the self-excited, and the buffeting nodal forces in N. When turbulence and aeroelastic effects are considered together, the bifurcation from stable to unstable behaviour is much more gradual, as observed by the green curve in Figure 1.11. Turbulence is also known to have a retarding effect on the onset of instability [35].

In a frequency domain approach, spectral formulation is obtained by taking the Fourier transform of (1.12),

$$\left(-\omega^2\mathbf{M}_s + \mathrm{i}\omega\mathbf{C}_s + \mathbf{K}_s\right)\mathbf{X}(\omega) = \mathbf{F}_{\mathrm{se}}(\omega) + \mathbf{F}_{\mathrm{bu}}(\omega), \tag{1.13}$$

where $\mathbf{X}(\omega)$, $\mathbf{F}_{\mathrm{se}}(\omega)$ and $\mathbf{F}_{\mathrm{bu}}(\omega)$ respectively stand for the spectral representation of the nodal displacement $\mathbf{x}(t)$, the self-excited forces $\mathbf{f}_{\mathrm{se}}(t)$, and the buffeting force $\mathbf{f}_{\mathrm{bu}}(t)$.

Despite of the simplicity of this canonical equation, the formulation of these forces is not straightforward. Depending on the solution scheme, several formulations are even possible. The

following sections are dedicated to presenting these aerodynamic forces, describing the analysis of buffeting and aeroelastic effects, and detailing their integration into structural response evaluation.

1.3 The quasi-steady model

1.3.1 The model

In section 1.2.3, we have already discussed how the motion of a body immersed in a fluid may interacts with the flow, perturbing the flow pattern. The quasi-steady regime was introduced to describe wind loads when the structural oscillations are slower than the time required for the flow to react to the structural motion. Physically, if the time needed for a convected eddy to travel the width of the deck is much lower than the characteristic timescale of the structure's motion given by the period T of one oscillation, it is legitimate to assume that the flow of fluid particles around the bridge deck is insensitive to the slow bridge deck motion. The fluid-structure interaction occurs then as if the flow keep up as being unable to see the structural motion, and remains therefore identical to what it would be if the structure was exactly fixed. In other words, the flow may be supposed as quasi-steady. This framework is known as the quasi-steady assumption.

It ensues that equations (1.10) remain valid when the conditions of the quasi-steady assumption are observed: as if the obstacle was fixed and the flow was uniform. These expressions are very general, but in fact too complicated to be used in practice. In this section, we will derive simple expressions for the aerodynamic forces, assuming the quasi-steady theory.

In the quasi-steady model, considering the motion of the bridge section in the flow, and the fluctuation of the flow itself due to the upstream turbulence, the wind speed vector $\mathbf{u}$ used in (1.10) is replaced by an effective incident wind speed vector $\mathbf{u}_{\text{app}}(t)$, representing the relative instantaneous wind flow as a function of time

$$F_L(t) = \frac{1}{2}\rho C_L(\alpha_{\text{eff}})B|\mathbf{u}_{\text{app}}(t)|^2, \tag{1.14a}$$

$$F_D(t) = \frac{1}{2}\rho C_D(\alpha_{\text{eff}})B|\mathbf{u}_{\text{app}}(t)|^2, \tag{1.14b}$$

$$F_M(t) = \frac{1}{2}\rho C_M(\alpha_{\text{eff}})B^2|\mathbf{u}_{\text{app}}(t)|^2. \tag{1.14c}$$

These forces are expressed in the mean wind axis, tilt by an angle α_0 with respect to the horizontal axis. Considering the structure's motion, the incident wind vector is decomposed according to Figure 1.12 and expressed as

$$\mathbf{u}_{\text{app}}(t) = \begin{bmatrix} U + u(t) \\ w(t) \end{bmatrix} - \begin{bmatrix} \dot{p}(t) \\ \dot{h}(t) + rB\dot{\alpha}(t) \end{bmatrix} \tag{1.15}$$

where r is a coefficient dependent on the shape of the cross section, relating the dimensionless distance from the centre of stiffness with respect to the aerodynamic centre, equal to $\frac{1}{4}$ for the flat plate sections. The mean wind speed direction is orthogonal to the deck. The squared norm of this vector is expanded as

$$|\mathbf{u}_{\text{app}}(t)|^2 = U^2 + 2Uu - 2U\dot{p} + u^2 + \dot{p}^2 - 2u\dot{p} + w^2 + \dot{h}^2 - 2w\dot{h} + 2rB\dot{\alpha}\left(\frac{rB\dot{\alpha}}{2} - w + \dot{h}\right). \tag{1.16}$$

Assuming that the turbulent components u, v and w are small with respect to the average wind speed U, the three first terms are one order of magnitude higher than the remaining ones. The quadratic norm may then be linearized by neglecting the higher order terms

$$|\mathbf{u}_{\text{app}}(t)|^2 = U^2 + 2Uu(t) - 2U\dot{p}(t). \tag{1.17}$$

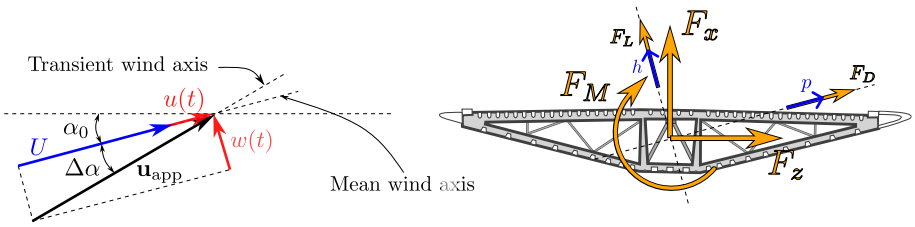

Figure 1.12: Conventional orientation of the aerodynamic forces of drag and lift and aerodynamic torque, acting on a bridge deck section, and decomposition of the incident wind vector.

This assumption may be discussed in the case of areas where the turbulence is important such as in urban areas where the turbulence intensity may reach 20% or more. Assuming a peak factor of 3, it is not impossible in some gusts to get fluctuating wind speed of about 50% of the average velocity [43]. In this case, this assumption is not valid, and this equation cannot be linearized in u and $\dot{p}$.

The effective angle of attack is expressed as the sum of one mean contribution resulting from the static part of the loading, and two fluctuating contributions: the first is related to the apparent rotation angle α of the deck section, and the second is the equivalent contribution related to the incidence of the turbulent wind

$$\alpha_{\text{eff}}(t) = \alpha_0 + \Delta\alpha(t) + \alpha(t) \tag{1.18}$$

Considering the structural velocities and the fluctuating turbulent velocities, the fluctuating contribution $\Delta\alpha(t)$ is equal to

$$\Delta\alpha(t) = \arctan\left[\frac{w - \dot{h} - rB\dot{\alpha}}{U + u - \dot{p}}\right]. \tag{1.19}$$

Assuming again that the wind speed fluctuations are small with respect to the average wind speed, and that $\arctan(\varepsilon) = \varepsilon + \mathcal{O}(\varepsilon^2)$ for small ε, the effective angle of attack is linearized as

$$\Delta\alpha(t) = \frac{w(t) - \dot{h}(t) - rB\dot{\alpha}(t)}{U}. \tag{1.20}$$

In a very general manner, the drag, lift and moment coefficients are measured in wind tunnel, and provided for a set of discrete angles. This data is post-processed in order to obtain continuous functions of the angle of attack. For small angles of attack, it is convenient to linearize these coefficients around the static angle

$$C_i(\alpha_{\text{eff}}) = C_i(\alpha_0) + C_i'(\alpha_0)\left[\alpha_{\text{eff}}(t) - \alpha_0\right] = C_i(\alpha_0) + C_i'(\alpha_0)\left[\Delta\alpha(t) + \alpha(t)\right] \tag{1.21}$$

where the subscript i refers to any force in $\{L, M, D\}$, and where $C_i'(\alpha_0) = \left.\frac{dC_i}{d\alpha}\right|_{\alpha_0}$. In practice, [43] has shown that the variance of the angle of attack is of the order of the turbulence intensity. It is then not rare to observe fluctuating incidence angles higher than 10°. For such angles of attack, it is clear that a linear expansion of the force coefficient is questionable (see for instance Figure 1.9a), but is still a standard approach today, even though some more advanced formulations exist. Injecting (1.20) in (1.21) conducts to

$$C_i(\alpha_{\text{eff}}) = C_i(\alpha_0) + C_i'(\alpha_0)\left(\frac{w(t) - \dot{h}(t) - rB\dot{\alpha}(t)}{U} + \alpha(t)\right) \tag{1.22}$$

This latter equation, together with the linear formulation of the norm of the speed (1.17) may be used in (1.14a), (1.14b) and (1.14c) to yield

$$F_L = \frac{1}{2}\rho U^2 B\left[C_L(\alpha_0) + C'_L(\alpha_0)\left(\frac{w(t) - \dot{h}(t) - rB\dot{\alpha}(t)}{U}\right) + \alpha(t)\right]\left[1 + 2\frac{u(t)}{U} - \frac{2\dot{p}(t)}{U}\right] \tag{1.23a}$$

$$F_D = \frac{1}{2}\rho U^2 B\left[C_D(\alpha_0) + C'_D(\alpha_0)\left(\frac{w(t) - \dot{h}(t) - rB\dot{\alpha}(t)}{U} + \alpha(t)\right)\right]\left[1 + 2\frac{u(t)}{U} - \frac{2\dot{p}(t)}{U}\right] \tag{1.23b}$$

$$F_M = \frac{1}{2}\rho U^2 B^2\left[C_M(\alpha_0) + C'_M(\alpha_0)\left(\frac{w(t) - \dot{h}(t) - rB\dot{\alpha}(t)}{U} + \alpha(t)\right)\right]\left[1 + 2\frac{u(t)}{U} - \frac{2\dot{p}(t)}{U}\right]. \tag{1.23c}$$

We assume one last time that the average wind speed is of one order superior to the fluctuating wind speed and the structural velocity, to get

$$F_L = \frac{1}{2}\rho U^2 B\left[C_L(\alpha_0)\left(1 + 2\frac{u(t)}{U} - \frac{2\dot{p}(t)}{U}\right) + C'_L(\alpha_0)\left(\frac{w(t) - \dot{h}(t) - rB\dot{\alpha}(t)}{U} + \alpha(t)\right)\right] \tag{1.24a}$$

$$F_D = \frac{1}{2}\rho U^2 B\left[C_D(\alpha_0)\left(1 + 2\frac{u(t)}{U} - \frac{2\dot{p}(t)}{U}\right) + C'_D(\alpha_0)\left(\frac{w(t) - \dot{h}(t) - rB\dot{\alpha}(t)}{U} + \alpha(t)\right)\right] \tag{1.24b}$$

$$F_M = \frac{1}{2}\rho U^2 B^2\left[C_M(\alpha_0)\left(1 + 2\frac{u(t)}{U} - \frac{2\dot{p}(t)}{U}\right) + C'_M(\alpha_0)\left(\frac{w(t) - \dot{h}(t) - rB\dot{\alpha}(t)}{U} + \alpha(t)\right)\right]. \tag{1.24c}$$

These forces, expressed in a tilted coordinate system are projected onto the bridge deck coordinate system, where all forces of the system are applied. This projection is carried out as follows, introducing a rotation matrix $\mathbf{R}$

$$\begin{pmatrix} F_x \\ F_z \\ F_M \end{pmatrix} = \begin{pmatrix} \cos\alpha_0 & -\sin\alpha_0 & 0 \\ \sin\alpha_0 & \cos\alpha_0 & 0 \\ 0 & 0 & 1 \end{pmatrix}\begin{pmatrix} F_L \\ F_D \\ F_M \end{pmatrix} = \mathbf{R}\begin{pmatrix} F_L \\ F_D \\ F_M \end{pmatrix}. \tag{1.25}$$

In the right hand side of the previous equation, the aerodynamic forces F_D, F_L, F_M are expressed as a function of (i) the component of the wind turbulent in the local coordinate system related to the wind, (ii) the angular position of the deck α and (iii) the displacement and velocities h, p, $\dot{h}$ and $\dot{p}$ of the deck in the same coordinate system. These latter quantities can be expressed in the coordinate system of the deck by means of a rotation matrix. The aerodynamic loads F_x, F_z and F_M can be expressed as function of u, v and w and the global deck displacement and velocities,

$$\mathbf{F} = \mathbf{A}_u u(t) + \mathbf{A}_w w(t) + \mathbf{A}_{\dot{\mathbf{x}}}\dot{\mathbf{x}}(t) + \mathbf{A}_{\mathbf{x}}\mathbf{x}(t) + \mathbf{b}. \tag{1.26}$$

where $\dot{\mathbf{x}}$ denotes to the time derivative of the nodal displacement vector $\mathbf{x} = \mathbf{R}\begin{bmatrix} p & h & \alpha \end{bmatrix}^{\mathsf{T}}$. The matrices $\mathbf{A}_u$, $\mathbf{A}_w$, $\mathbf{A}_{\dot{\mathbf{x}}}$ and $\mathbf{A}_{\mathbf{x}}$ are the force coefficient matrices expressed as

$$\mathbf{A}_u = \frac{1}{2}\rho UB\begin{bmatrix} 2\bar{C}_z \\ 2\bar{C}_x \\ 2B\bar{C}_M \end{bmatrix}, \quad \mathbf{A}_w = \frac{1}{2}\rho UB\begin{bmatrix} C'_z + C_x \\ C'_x - C_z \\ BC'_M \end{bmatrix}, \tag{1.27}$$

$$\mathbf{A}_{\dot{\mathbf{x}}} = -\frac{1}{2}\rho UB\begin{bmatrix} \bar{C}'_z + \bar{C}_x & 2\bar{C}_z & (\bar{C}'_z + \bar{C}_x)rB \\ \bar{C}'_x - \bar{C}_z & 2\bar{C}_x & (\bar{C}'_x - \bar{C}_z)rB \\ BC'_M & 2BC_M & C'_M rB^2 \end{bmatrix}, \qquad \mathbf{A}_{\mathbf{x}} = \frac{1}{2}\rho U^2 B\begin{bmatrix} 0 & 0 & \bar{C}'_z \\ 0 & 0 & \bar{C}'_x \\ 0 & 0 & \bar{C}'_M \end{bmatrix} \tag{1.28}$$

and $\mathbf{b}$ is the static contribution to the buffeting forces

$$\mathbf{b} = \begin{bmatrix} \bar{C}_z \\ \bar{C}_x \\ \bar{C}_M \end{bmatrix}. \tag{1.29}$$

In these expressions, the coefficients C_x and C_z have been defined by

$$\begin{pmatrix} C_x \\ C_z \\ C_M \end{pmatrix} = \begin{pmatrix} \cos\alpha_0 & -\sin\alpha_0 & 0 \\ \sin\alpha_0 & \cos\alpha_0 & 0 \\ 0 & 0 & 1 \end{pmatrix} \begin{pmatrix} C_L \\ C_D \\ C_M \end{pmatrix} = \mathbf{R} \begin{pmatrix} C_L \\ C_D \\ C_M \end{pmatrix}. \tag{1.30}$$

This transformation is valid for the coefficients as well as their derivative (indicated by a prime $'$) and their averaged valued, indicated by a overhead bar $\bar{\cdot}$.

Equation (1.26) holds at every cross section of the deck in conjunction with the deck motions and the components of wind turbulence at the same cross section. By repeating this for the entire structure, the linearized version of the quasi-steady model is obtained.

It is the simplest formulation for aerodynamic forces acting on a structure in turbulent wind conditions. This model is widely used for the following reason: the equations are linear in the random processes, in the fluctuating components, as well as in the structural velocities. Since u and w are modelled as Gaussian processes when the forces are expressed in this linear form, the structural response remains Gaussian, allowing then straightforward characterization using the first two statistical moments. While higher-order formulations of aerodynamic forces are possible, they become significantly more complex, both in terms of expressions and solution techniques [44, 45]. In this Thesis, only linear aerodynamic forces will be considered.

1.3.2 The implications of the model

This model forms the basis of an aeroelastic model. Each of the equations of (1.26) involves 3 terms

- **The constant term b:** representing the average wind speed force, responsible for the static response;
- **The buffeting terms $\mathbf{A}_u u(t)$ and $\mathbf{A}_w w(t)$:** two terms proportional to turbulent velocities. These terms are the buffeting contributions to the lift, drag and moment. They fluctuate over time around the mean value;
- **The self-excited terms $\mathbf{A}_{\dot{\mathbf{x}}}\dot{\mathbf{x}}(t)$ and $\mathbf{A}_{\mathbf{x}}\mathbf{x}(t)$:** two terms proportional to the structural velocity or rotation; these are motion dependent terms modelling the interaction between wind and structure. They originate from the fact the wind induced force depends on the structural velocity and the apparent incidence. The wind force then adds a contribution to the structural damping of the structure. The aerodynamic loading also adds an aerodynamic stiffness due to the deck rotation α, even though this contribution is often neglected when imposing the small rotation assumption.

The aeroelastic stiffness and damping arise from the fluid-structure interaction. However, the quasi-steady assumption simplifies this interaction, as it assumes that the structural dynamic timescales are much larger than the eddy convection timescale in the turbulent wind field. Releasing this assumption allows then for a more general consideration of fluid-structure interaction. This is precisely the scope of the unsteady model.

1.4 The unsteady model

In the previous section on the quasi-steady approach, an expression of the self-excited forces was explicitly derived. For instance, the instantaneous lift was expressed using an effective angle of attack, which incorporates the time derivatives $\dot{h}$, $\dot{\alpha}$ and $\dot{p}$ thereby reflecting a memory effect of the structure. This modelling approach captures the essence of fluid-structure interaction in a simplified form.

Beyond the quasi-steady representation, two widely established approaches exist for modelling self-excited forces: the frequency domain representations and the time domain representation. These two representation methods will both be illustrated first on a simple cross section idealized as a flat plate, and then on a general bridge section.

Historically, the flat plate model was the root theory to represent highly profiled bodies, such as foils, including cambered ones. While these models may still find applications in aeronautics today, they are obviously incompatible with bluff bodies like bridge decks. Nevertheless, this well-established theory remains relevant even in bridge engineering [46], serving as a pedagogical example or a fundamental benchmark for aeroelastic applications.

1.4.1 The time domain representations

1.4.1.A Instigative works on the flat plate model

The first works in unsteady aerodynamics were pioneered by Wagner [47], who analytically studied the unsteady lift resulting from a sudden change in the angle of attack of a flat plate subjected to steady laminar flow.

The model he considered is a 2D representation of a flat plate with infinite span and of chord c. The rotation axis is located at a distance x_c from the trailing edge. This configuration, illustrated in Figure 1.13, represents the initial setup at $t = 0$, immediately after the change in angle of attack $\mathrm{d}\alpha$ is applied.

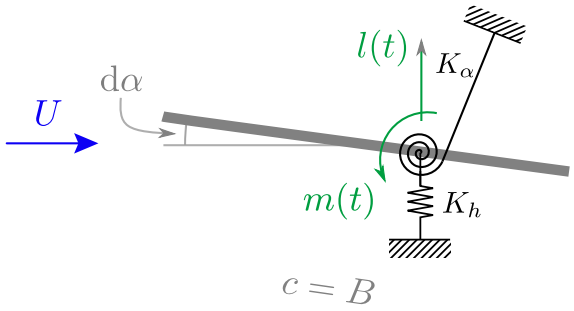

Figure 1.13: Schematic representation of a pitch-plunge model of a flat plate.

Wagner proposed that the evolution of lift was governed by the gradual formation and shedding of vortices at the trailing edge, which in turn alters the circulation around the airfoil over time. Assuming an infinitesimal and sudden change in the angle of attack $\mathrm{d}\alpha$, the incremental unsteady lift is expressed using the Wagner function $\Phi(t)$ as:

$$\mathrm{d}l(t) = \mathrm{d}l_{\text{steady}}\Phi(t) = \frac{1}{2}\rho U^2(2\pi c)\mathrm{d}\alpha\Phi(t), \qquad t > 0 \tag{1.31}$$

If the impulse change in the angle of attack occurs at $t = \tau$, the unsteady lift becomes:

$$\mathrm{d}l(t) = \frac{1}{2}\rho U^2(2\pi c)H(\tau)\Phi(t-\tau)\mathrm{d}\alpha \tag{1.32}$$

where $H(t)$ is the Heaviside step function. For an arbitrary time-dependent angle of attack $\alpha(t)$, the incremental changes are obtained from its time derivative, $\mathrm{d}\alpha = \dot{\alpha}\,\mathrm{d}t$. Superimposing all the elementary lift contributions for successive changes in the angle of attack from $\tau \in]-\infty, t]$ leads to the unsteady lift being represented as a convolution integral

$$l(t) = \int_{-\infty}^{t} \mathrm{d}l(t) = \frac{1}{2}\rho U^2(2\pi c)\int_{-\infty}^{t} H(\tau)\Phi(t-\tau)\dot{\alpha}\,\mathrm{d}\tau \tag{1.33}$$

where a zero lift is assumed as $t \to -\infty$.

This result forms a cornerstone of unsteady aerodynamic theory and has inspired numerous developments in aeroelasticity. However, its application remains limited in bridge engineering, where the behaviour of bluff bodies significantly differs from the basic flat plate.

1.4.1.B Bluff-body models

In the case of bluff bodies, the self-excited forces may not be described using the circulatory theory, as was previously done with a flat plate. This is mainly because, for flow over bluff-bodies, anarchic separation and reattachment of the flow occur at the body boundary, which is incompatible with the assumption of a single point source of all shed vortexes [34]. Furthermore, these analytical studies are restricted to laminar and streamlined flows, which inherently differs from flow patterns associated with bluff-bodies.

Some authors, inspired by Wagner's work formulated a more general framework to evaluate the three aeroelastic unsteady forces using the three-dimensional degree-of-freedom model accounting for the bridge engineering specificities. A very general model was formalized by [11]

$$F_L = \frac{1}{2}\rho U^2 C'_L \int_{-\infty}^{t} \Phi_{L\alpha}(t-\tau)B\dot{\alpha}(\tau) + \Phi_{Lh}(t-\tau)2\ddot{h}(\tau) + \Phi_{Lp}(t-\tau)2\ddot{p}(\tau)\,\mathrm{d}\tau, \tag{1.34}$$

$$F_D = \frac{1}{2}\rho U^2 C'_D \int_{-\infty}^{t} \Phi_{D\alpha}(t-\tau)B\dot{\alpha}(\tau) + \Phi_{Dh}(t-\tau)2\ddot{h}(\tau) + \Phi_{Dp}(t-\tau)2\ddot{p}(\tau)\,\mathrm{d}\tau, \tag{1.35}$$

$$F_M = \frac{1}{2}\rho U^2 B C'_M \int_{-\infty}^{t} \Phi_{M\alpha}(t-\tau)B\dot{\alpha}(\tau) + \Phi_{Mh}(t-\tau)2\ddot{h}(\tau) + \Phi_{Mp}(t-\tau)2\ddot{p}(\tau)\,\mathrm{d}\tau \tag{1.36}$$

where $\Phi_{L,x}(t)$, $\Phi_{M,x}(t)$ and $\Phi_{D,x}(t)$ with x in $\{\alpha, h, p\}$ referring to the indicial response functions respectively describing the lift, moment and drag force corresponding to a unit change of α, h and p.

In the same spirit, some authors have considered impulse response functions rather than step functions, to produce a very similar way for evaluating the unsteady forces

$$F_L = \frac{1}{2}\rho U^2 \int_{-\infty}^{t} I_{L\alpha}(t-\tau)B\alpha(\tau) + I_{Lh}(t-\tau)h(\tau) + I_{Lp}(t-\tau)p(\tau)\,\mathrm{d}\tau, \tag{1.37}$$

$$F_D = \frac{1}{2}\rho U^2 \int_{-\infty}^{t} I_{D\alpha}(t-\tau)B\alpha(\tau) + I_{Dh}(t-\tau)h(\tau) + I_{Dp}(t-\tau)p(\tau)\,\mathrm{d}\tau, \tag{1.38}$$

$$F_M = \frac{1}{2}\rho U^2 \int_{-\infty}^{t} I_{M\alpha}(t-\tau)B\alpha(\tau) + I_{Mh}(t-\tau)h(\tau) + I_{Mp}(t-\tau)p(\tau)\,\mathrm{d}\tau \tag{1.39}$$

where $I_{L,x}(t)$, $I_{M,x}(t)$ and $I_{D,x}(t)$ with x in $\{\alpha, h, p\}$ referring to the impulse response function respectively describing the lift, moment and drag force corresponding to an impulse in α, h and p.

The unit response functions are characterized experimentally or numerically with CFD. These functions can be approximated by rational function approximations. The first methods were formalized in aeronautics by [48, 49] and in civil engineering by [50, 51] based on a non-linear least square fitting. Some authors proposed a direct extraction from wind tunnel experiments [52, 53].

1.4.2 Frequency domain formulations

In practice, most flutter analysis methodologies result in aeroelastic equations of motion formulated as a second order differential equation such as (1.12) with frequency-dependent coefficients to model the aerodynamic loads. In this very general manner, self-excited forces may be expressed under the following canonical form

$$\mathbf{f}_{\mathrm{se}}(t) = \mathbf{f}(\mathbf{x}(t), \dot{\mathbf{x}}(t), \ddot{\mathbf{x}}(t)) \tag{1.40}$$

where $\mathbf{f}$ is a vector valued function which differs depending on the application.

In bridge engineering, this function typically takes the form of a first order differential operator of the displacement $\mathbf{x}$, with speed and time-dependent coefficients. In aeronautic applications

the load vector is usually expressed in a single term introducing $\mathbf{Q}(k)$ the complex aerodynamic force matrix [54, 55], so that the aeroelastic forces read

$$\mathbf{F}_{\text{se}}(\omega) = \frac{1}{2}\rho U^2 \mathbf{Q}\left(\frac{\omega b}{U}\right)\mathbf{X}(\omega) \tag{1.41}$$

where $\mathbf{F}_{\text{se}}(\omega)$ and $\mathbf{X}(\omega)$ are respectively the Fourier transform of $\mathbf{f}_{\text{se}}(t)$ and $\mathbf{x}(t)$, and where $k = \omega b/U$ is the reduced frequency, $b = B/2$ is a characteristic length. Therefore, this aerodynamic model corresponds equivalently to a differential system with speed and frequency-dependent properties.

Because the aeroelastic forces are most often derived in frequency domain, the following notation is sometimes used in the literature [55, 56], expressing the self-excited force with a time-frequency domain equation:

$$\mathbf{F}_{\text{se}}(t) = \frac{1}{2}\rho U^2 \mathbf{Q}\,(k)\,\mathbf{x}(t). \tag{1.42}$$

This equation involves the product of a time and frequency-dependent variables $\mathbf{Q}(k)$ and $\mathbf{x}(t)$, which is formally wrong from a mathematical standpoint since the problem should be formulated in the time or frequency domain, but not in both a the same time. It needs to be interpreted as a convolution in the time domain, or as a product in the frequency domain such as in (1.41), but not as a product of two functions of k and t.

There are three families of methods used to determine aeroelastic forces in frequency domain. The first comprises analytical methods, which are based on the study of potential flow over infinite wings [57]. The second includes semi-empirical models, such as those described in [58, 59], while the third consists of numerical methods like the Doublet Lattice Method [60] or the Source and Doublet Panel Method [56]. Despite analytical methods were rooted in the earliest studies of aeroelasticity, they remain today valuable for developing physical insight although numerical methods are predominantly utilized in the aerospace industry (see for instance ZAERO [61]). In civil engineering and particularly bridge engineering, semi-empirical models are almost exclusively applied. This section will present two models: the analytical flat plate model and the semi-empirical Scanlan model.

1.4.2.A The flat plate model

Wagner's function presented earlier has in fact its exact equivalent in the frequency domain: Theodorsen's function [62]. Theodorsen [57] focused on a flat plate oscillating harmonically at a constant pulsation and introduced a frequency domain representation of the Wagner function, known as the complex Theodorsen's function. This formulation, captures equivalently the circulatory effects in unsteady flow, and will be developed further in this section.

The model considered by Theodorsen is the same as the one depicted in Figure 1.13, except the flat plate is oscillating at a constant pulsation. This Figure represents then a snapshot of the configuration, when the flat plate forms an angle of attack $\mathrm{d}\alpha$ with the incoming wind direction.

The aerodynamic lift and moment acting on the plate at the rotation centre are given by [55]

$$l(t) = \left[\rho\pi b^2 U \mathrm{i}\omega\alpha + \pi\rho U c C(k)\left(U\alpha + \mathrm{i}\omega h + \left(\frac{3}{4}c - x_f\right)\mathrm{i}\omega\alpha\right) + \rho\pi b^2\left(-\omega^2 h + \left(x_f - \frac{c}{2}\right)\omega^2\alpha_0\right)\right] e^{\mathrm{i}\omega t} \tag{1.43}$$

and

$$m(t) = \left[\frac{\rho\pi b^4}{8}\omega^2\alpha + \pi\rho U e c^2 C(k)\left(U\alpha + \mathrm{i}\omega h + \left(\frac{3}{4}c - x_f\right)\mathrm{i}\omega\alpha\right) - \left(\frac{3}{4}c - x_f\right)\rho\pi b^2 U\mathrm{i}\omega\alpha + \left(x_f - \frac{c}{2}\right)\rho\pi b^2\left(-\omega^2 h + \left(x_f - \frac{c}{2}\right)\omega^2\alpha\right)\right] e^{\mathrm{i}\omega t}. \tag{1.44}$$

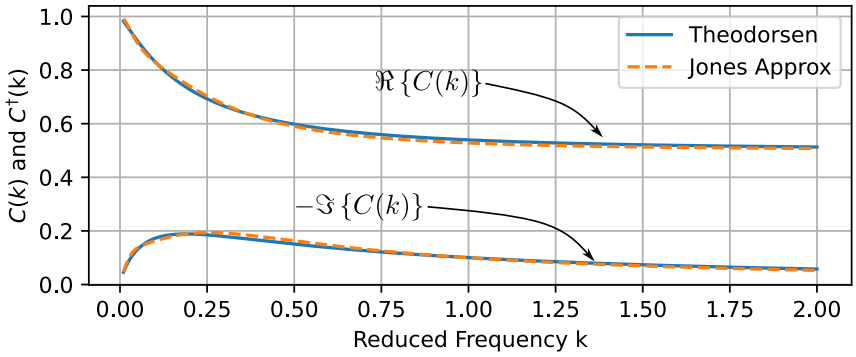

Figure 1.14: Comparison of Theodorsen's and Jones' function.

where $C(k)$ refers to the complex Theodorsen function

$$C(k) = F + \mathrm{i}G = \frac{-J_1(k) + \mathrm{i}Y_1(k)}{-(J_1(k) + Y_0(k)) + \mathrm{i}(Y_1(k) - J_0(k))}. \tag{1.45}$$

with $J_0(k)$, $J_1(k)$ respectively the Bessel functions of the first kind and $Y_0(k)$, $Y_1(k)$ the Bessel functions of the second kind. Jones [63] has proposed a rational fraction approximation for this function, that takes a quite simple expression

$$C^\dagger(k) = 1 - \frac{0.165}{1 - \frac{0.0455}{k}\mathrm{i}} - \frac{0.335}{1 - \frac{0.3}{k}\mathrm{i}}. \tag{1.46}$$

These functions are represented in Figure 1.14. It is interesting to note that Theodorsen's and Jones' functions both tend to 1+0i as $k \to 0$. In other words, the unsteady effects in (1.43) and (1.44) vanish when the oscillation period is large, which is exactly the framework of the quasi-steady assumption (see Section 1.3.1).

The two degree-of-freedom model presented in this section is called a pitch-plunge model. This is the simplest model used to study classical flutter, which involves the interaction of at least two modes.

1.4.2.B The Scanlan model

In civil engineering, the most famous model is due to Scanlan [59], who proposed a two-dimensional (2D) model based on 8 frequency-dependent functions to model the aerodynamic lift and moment considering the vertical and torsional degrees-of-freedom. His first model was later improved [39] introducing 4 additional coefficients to model the aeroelastic drag, and finally improved [38] with a total of 18 frequency-dependent functions to model the aeroelastic behaviour in three dimensions, considering the lateral degree-of-freedom. In bridge engineering, the aerodynamic loads are evaluated at a point located at the intersection of the x and y bending neutral axis, which allows to treat aerodynamic loads like any other static load. This point corresponds to the centroid of the section when the section is symmetric with respect to x and y. The situation is summarized in Figure 1.12. According to the definitive version of the Scanlan model [38], the lift, drag and moment are expressed as

$$l = \frac{1}{2}\rho U^2 B \left(KH_1^* \frac{\dot{h}}{U} + KH_2^* \frac{B\dot{\alpha}}{U} + K^2 H_3^* \alpha + K^2 H_4^* \frac{h}{B} + KH_5^* \frac{\dot{p}}{U} + K^2 H_6^* \frac{p}{B} \right), \tag{1.48a}$$

$$m = \frac{1}{2}\rho U^2 B^2 \left(KA_1^* \frac{\dot{h}}{U} + KA_2^* \frac{B\dot{\alpha}}{U} + K^2 A_3^* \alpha + K^2 A_4^* \frac{h}{B} + KH_5^* \frac{\dot{p}}{U} + K^2 A_6^* \frac{p}{B} \right), \tag{1.48b}$$

$$d = \frac{1}{2}\rho U^2 B \left(KP_1^* \frac{\dot{p}}{U} + KP_2^* \frac{B\dot{\alpha}}{U} + K^2 P_3^* \alpha + K^2 P_4^* \frac{p}{B} + KP_5^* \frac{\dot{h}}{U} + K^2 P_6^* \frac{h}{B} \right), \tag{1.48c}$$

with A_i^*, H_i^* and P_i^* are the Scanlan derivatives —or flutter derivatives—, all functions of the reduced pulsation $K = 2k = \frac{\omega B}{U}$. Once more, it is important to note that these expressions seem to involve a mix between time-dependent functions and frequency-dependent functions — for instance, see $H_1^*\dot{h}$, which should be interpreted as $H_1^*(K)\int_{-\infty}^{+\infty}\dot{h}(t)\exp(-\mathrm{i}\omega t)\,\mathrm{d}t$, i.e. all symbols need to be interpreted in the frequency domain.

Flutter derivatives can be determined experimentally in wind tunnels or numerically either by direct measurement of aerodynamic forces or by integration of the unsteady pressure distribution on the body surface. They are specific to the considered deck section and depend on the average angle of attack. Various methods have been developed for identifying these derivatives, including approaches based on free or forced excitation, using either deterministic or stochastic buffeting inputs. Kernel identification procedures are also valid alternatives, aiming at evaluating the indicial or unit response functions, from which the flutter derivatives may be derived using Fourier analysis. The discussion of these methods goes beyond the scope of this document, but the interested reader may refer to [34] who proposed an in-depth literature review of all existing methods.

The Scanlan model is the most complete linear model so far developed to assess the behaviour of a structure under buffeting actions, covering the unsteady aeroelastic effects and the determination of the critical wind velocities —e.g. [64]. Despite such linear models are unable to incorporate the nonlinear effects inherent to structures undergoing flutter, they however remain well adapted in civil engineering, where structures are generally not allowed to experience large amplitude displacements nor rotations. The model serves therefore to evaluate the critical velocity but not the post-critical behaviour.

The aeroelastic forces in equations (1.48a) to (1.48c) may be expressed under the matrix form

$$\mathbf{f}_{\mathrm{ae}}(t) = \frac{1}{2}\rho U B \begin{bmatrix} KH_1^* & KBH_2^* & KH_5^* \\ KBA_1^* & KB^2A_2^* & KBA_5^* \\ KP_5^* & KBP_2^* & KP_1^* \end{bmatrix} \dot{\mathbf{x}}(t) + \frac{1}{2}\rho U^2 \begin{bmatrix} K^2H_4^* & K^2BH_3^* & K^2H_6^* \\ K^2BA_4^* & K^2B^2A_3^* & K^2BA_6^* \\ K^2P_6^* & K^2BP_3^* & K^2P_4^* \end{bmatrix} \mathbf{x}(t) \tag{1.49}$$

with $\mathbf{x}(t) = \begin{bmatrix} h(t) & \alpha(t) & p(t) \end{bmatrix}^{\mathsf{T}}$ where the operator T refers to the transpose operation. The two matrices introduced have units of damping and stiffness. In civil engineering, these matrices are known as aeroelastic matrices of damping and stiffness,

$$\mathbf{C}_{\mathrm{ae}}(\omega, U) = \frac{1}{2}\rho U B \begin{bmatrix} KH_1^* & KBH_2^* & KH_5^* \\ KBA_1^* & KB^2A_2^* & KBA_5^* \\ KP_5^* & KBP_2^* & KP_1^* \end{bmatrix}, \tag{1.50}$$

$$\mathbf{K}_{\mathrm{ae}}(\omega, U) = \frac{1}{2}\rho U^2 \begin{bmatrix} K^2H_4^* & K^2BH_3^* & K^2H_6^* \\ K^2BA_4^* & K^2B^2A_3^* & K^2BA_6^* \\ K^2P_6^* & K^2BP_3^* & K^2P_4^* \end{bmatrix}. \tag{1.51}$$

This formulation is perfectly compatible with the notation introduced in (1.41), in which case the complex aerodynamic force matrix reads

$$\mathbf{Q}(k) = K^2 \begin{bmatrix} H_4^* + \mathrm{i}H_1^* & B(H_3^* + \mathrm{i}H_2^*) & H_6^* + \mathrm{i}H_5^* \\ B(A_4^* + \mathrm{i}A_1^*) & B^2(A_3^* + \mathrm{i}A_2^*) & B(A_6^* + \mathrm{i}A_5^*) \\ P_6^* + \mathrm{i}P_5^* & B(P_3^* + \mathrm{i}P_2^*) & P_4^* + \mathrm{i}P_1^* \end{bmatrix}. \tag{1.52}$$

Assuming that the structure is exclusively subjected to the aeroelastic force, substituting equation (1.49) into (1.13) results in

$$\left(-\omega^2\mathbf{M}_s + \mathrm{i}\omega\mathbf{C}_s + \mathbf{K}_s\right)\mathbf{X}(\omega) = \mathrm{i}\omega\mathbf{C}_{\mathrm{ae}}(\omega)\mathbf{X}(\omega) + \mathbf{K}_{\mathrm{ae}}(\omega)\mathbf{X}(\omega), \tag{1.53}$$

where the aeroelastic stiffness and damping may be treated exactly like the structural matrices. This equation of motion then becomes

$$\left[-\omega^2\mathbf{M}(\omega) + \mathrm{i}\omega\mathbf{C}(\omega) + \mathbf{K}(\omega)\right]\mathbf{X}(\omega) = \mathbf{0} \tag{1.54}$$

where we have introduced the global system matrices which are expressed as the sum of a structural and an aeroelastic contribution

$$\mathbf{M}(\omega, U) = \mathbf{M}_{\mathrm{s}} - \mathbf{M}_{\mathrm{ae}}(\omega, U), \qquad \mathbf{C}(\omega, U) = \mathbf{C}_{\mathrm{s}} - \mathbf{C}_{\mathrm{ae}}(\omega, U), \qquad \mathbf{K}(\omega, U) = \mathbf{K}_{\mathrm{s}} - \mathbf{K}_{\mathrm{ae}}(\omega, U). \tag{1.55}$$

Although the original authors [59] declared that the added mass effects are negligible because of the low density of the surrounding fluid —air—, matrix $\mathbf{M}_{\mathrm{ae}}(\omega)$ is kept in the following developments in order to make them more general.

1.5 The aeroelastic problem

1.5.1 Without buffeting loads

Equation (1.54) is a homogeneous differential equation that governs a critical stability problem. Its solution defines the critical state, specifically the critical velocity U_{cr}, at which dynamic instability occurs. The wind-speed-dependent properties of the aeroelastic matrices are such that the structure remains stable at subcritical speeds and transitions to instability at the critical velocity, as indicated by the vertical asymptote in Figure 1.11. This behaviour is characteristic of instabilities in general.

A useful analogy can be drawn with Euler buckling. The transverse displacement $w(x)$ of a pinned column, with flexural rigidity EI and subjected to a compressive force P, is governed by a similar homogeneous differential equation[1]

$$EIw''(x) + Pw(x) = 0 \quad \Leftrightarrow \quad (-EI\nu^2 + P)w(\nu) = 0. \tag{1.56}$$

The variable susceptible to trigger the instability is this time the compression load P instead of the wind speed U. This equation admits an infinite set of solutions satisfying the boundary conditions, each corresponding to a distinct buckling mode characterized by a critical load, calculated as an eigenvalue of the problem. For a pinned column of length L, the n-th eigenvalue is given by

$$P_{cr} = \frac{n^2\pi^2 EI}{L^2}. \tag{1.57}$$

The critical load is associated with a particular deformed configuration to which the system transitions instantly from a stable to an unstable behaviour.

The critical equation (1.54) is in fact the aeroelastic equivalent of $(\mathbf{K} - \lambda\mathbf{K}_\sigma)\mathbf{x}$, which models the critical problem (1.56) formulated in space discrete version. While buckling defines the critical instability as the state at which the eigenvalue λ is such that $\det(\mathbf{K} - \lambda\mathbf{K}_\sigma) = 0$, a similar instability occurs when U is such that

$$\det\left[-\omega^2\mathbf{M}(\omega, U) + \mathrm{i}\omega\mathbf{C}(\omega, U) + \mathbf{K}(\omega, U)\right] = 0. \tag{1.58}$$

This is a dynamic instability. It is a different kind of instability. The stable-unstable behaviour is illustrated by the red asymptote of Figure 1.15 for the static instability in (a) and the dynamic instability in (b). Like in Euler buckling, the solution may not be unique, in which case the system admits several critical states. Conversely, since the singular problem is not polynomial (as in the case with integer derivatives), the solution may even not exist if the system is unconditionally stable, i.e flutter-free. Chapter 6 will tackle in detail the solution of this critical problem, and will present a novel and efficient method developed within this Thesis, for solving this homogeneous

[1] In a Finite Element context, this reads $(\mathbf{K} - \lambda\mathbf{K}_\sigma)\mathbf{x} = \mathbf{0}$.

problem. Depending on how the matrices $\mathbf{M}$, $\mathbf{C}$ and $\mathbf{K}$ are affected by U, some degenerated cases can occur. In very simple terms, three well known types of instability can be identified: divergence, galloping and flutter.

First, divergence is a static instability caused by a progressive loss of stiffness as U increases. This phenomenon primarily affects torsional degrees-of-freedom and is commonly referred to as torsional divergence. Since the system mass remains unchanged, the critical state is purely defined by the vanishing of an effective stiffness term. Mathematically, divergence is characterized by the condition:

$$\det\left[\mathbf{K}(U)\right] = \det\left[\mathbf{K}_s - \mathbf{K}_\alpha(U)\right] = 0,$$

which is quite similar to the eigenvalue problem for static buckling. As U approaches the critical value, the loss of stiffness translates into the collapse of a natural frequency to zero, leading to a statically unstable response.

Second, galloping occurs when the aerodynamic damping properties of the system contribute to a net energy input into structural oscillations. This typically happens when the aerodynamic forces do not align with the instantaneous motion of the structure, producing a self-excited oscillation. If the instability primarily affects a mode dominated by displacements transverse to the flow, it is referred to as transverse galloping. Conversely, if the instability involves a torsional mode, it is called torsional galloping. The onset of galloping is associated with a loss of dynamic stability and can be linked to the singularity of the effective damping matrix in the governing equations.

Third, flutter is a more complex instability that arises when both the aerodynamic damping and stiffness terms are affected by U. Unlike divergence and galloping, which can be understood as isolated effects on stiffness or damping, flutter requires a coupling between structural modes. This coupling results in a continuous energy transfer from the surrounding fluid to the structure, surpassing the system's inherent damping capacity and leading to sustained or growing oscillations. By definition, mode coupling with reciprocal energy exchange is a fundamental condition for flutter to occur. A classical example is torsional flutter, where a torsional mode interacts with a bending mode, leading to an energy exchange between a highly damped and an undamped oscillation.

To summarize this important section on aeroelastic forces, the Scanlan model stands as a cornerstone in bridge aerodynamics, offering a rigorous and widely accepted framework for characterizing unsteady aerodynamic forces through flutter derivatives. This semi-empirical approach is particularly practical, as it expresses aerodynamic forces in terms of speed- and frequency-dependent damping and stiffness matrices. Its simplicity and adaptability to various deck profiles have made it indispensable in both research and modern bridge design. However, the main limitation of the model lies in the need to experimentally or numerically determine the flutter derivatives, which are specific to each deck geometry and angle of attack. By formalizing aeroelastic forces into two aeroelastic stiffness and damping matrices, the model frames the equation of motion as a critical problem, whose solutions define the critical states. In the subcritical regime, these forces have no effect unless the structure is excited by an external forcing term, such as the wind loads resulting from wind turbulence. In the sequel, both aeroelastic and buffeting forces will be considered together.

1.5.2 With buffeting loads

While the critical load defined in (1.57) for the elastic buckling problem provides already significant information, the solutions to the homogeneous differential equation provide no insight into the behaviour of the structure before the onset of instability. If a right-hand side is added to equation (1.56) coming for instance from applied end moments, second order effects develop progressively as the compression load P is increased. The black curve in Figure 1.15(a), which models the response of the structure including these effects of the exogenous loading, is not cap-

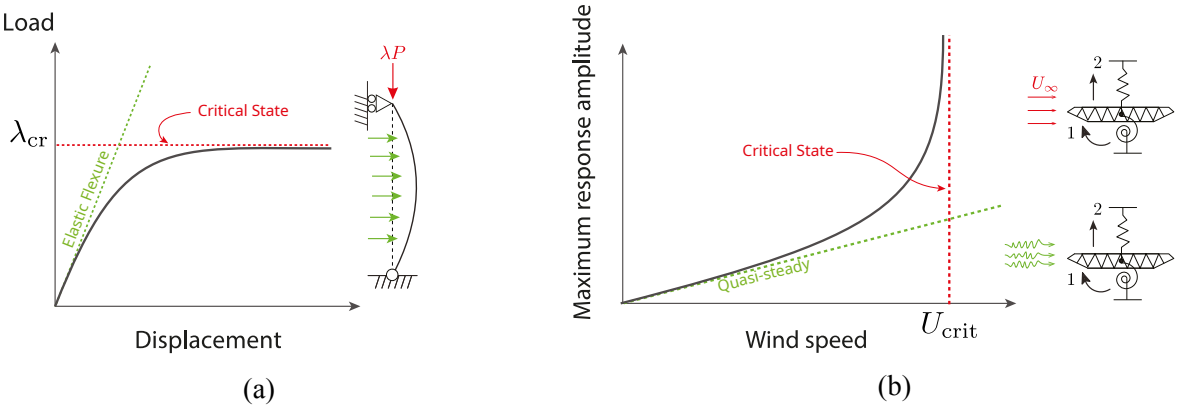

Figure 1.15: Comparison between (a) the Euler buckling instability and (b) the flutter aeroelastic instability.

tured by the critical problem but by a full nonlinear analysis. This makes the difference between bifurcation and divergence.

Similarly, in the aeroelastic context, the solution of (1.54) identifies only critical velocities, without any insight into the aeroelastic structural response at subcritical speeds. The solution of the homogeneous problem presented in the last section leads to the identification of one or several critical states. The determination of critical velocities is however only one part of the design engineer's job, that must also focus on the behaviour of the structure for all wind speeds prior to flutter, ensuring comfort requirements, safety against fatigue, flutter conditions assessment, etc. Beside the classical flutter safety recommendation which ensures that the critical velocity is far enough from the design wind speed [6], some other serviceability or comfort criteria may be based on the maximum allowable structural response and can be specified for instance as an absolute displacement, acceleration or rotation [65]. These serviceability criteria are verified for subcritical wind speeds, under the action of the buffeting forces acting as an additional forcing term on the right hand side of the governing equation (1.12). This is our fundamental motivation for considering the simultaneous action of buffeting and self-excited forces in (1.12). This section is dedicated to presenting the frameworks available for conducting a complete buffeting analysis including unsteady effects. Depending on whether the aerodynamic forces are represented in the time or frequency domain, the analysis can be carried out accordingly in the respective domain.

1.5.2.A Time domain method

The buffeting and unsteady forces are not purely harmonic but random time histories so that closed-form solutions of the equation of motion of the excited system unfortunately do not exist. Instead, buffeting analysis in time domain is conducted by numerically integrating the equations of motion step-by-step, typically using Newmark [66] or Runge-Kutta [67] schemes. This approach requires the determination of a turbulent spatially-coherent wind-fields for the components u, v, and w, which can either be recorded or synthetically generated [4]. With the time histories of fluctuating velocity, the buffeting forces may be calculated using the quasi-steady theory, which remains valid provided the time required for an eddy to cross the bridge deck width is shorter than the characteristic response time of the structure. Self-excited forces are computed as described in Section 1.4.1.

This method involves solving the equations of motion at each time step starting from $t = 0$ to t. The numerical integrators are known to be computationally demanding. Additionally, the convolution product required to account for the self-excited forces must be evaluated at each time step based on the structure's current state, making this operation particularly resource-consuming. To address this problem, [68] proposed an approximation method for the convolution product, considering the typical rational exponential shape of the step response functions to

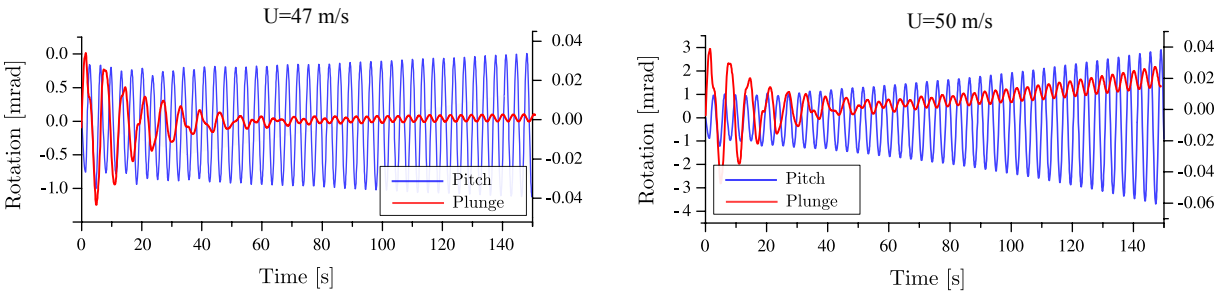

Figure 1.16: Time series of the vertical and torsional response of the Aizhai bridge (a) at critical wind speed and (b) at post-critical wind speed. Adapted from [69].

simplify the computation.

The analysis is typically repeated for a range of reference wind speeds U_{ref} corresponding to expected operational conditions of the bridge. Statistical post-processing of the output time series determines whether the structure satisfies serviceability and comfort requirements. For determining the onset of aeroelastic instability, the wind speed is gradually increased, and the structural response is monitored. A transition from damped to growing oscillations indicates the occurrence of an instability, signifying that the system can no longer dissipate energy effectively and is undergoing dynamic instability. The time series illustrated in Figure 1.16 show the time series of the structural response of the Aizhai bridge obtained by [69] at critical speed and in a post-critical regime. In (a) it may be seen that the oscillations are not damped, and remain of constant amplitude, while in post-critical regime, the system accumulates the energy, and the amplitudes of torsional oscillation grow exponentially.

1.5.2.B Frequency domain method

The structural dynamics of a system subjected to both buffeting and aeroelastic forces, as expressed in (1.13), can be modelled as:

$$\left[-\omega^2\mathbf{M}(\omega,U)+\mathrm{i}\omega\mathbf{C}(\omega,U)+\mathbf{K}(\omega,U)\right]\mathbf{X}(\omega)=\mathbf{F}_{\text{bu}}(\omega). \tag{1.59}$$

where the buffeting forces $F_{\text{bu}}(\omega)$ are calculated as the spectral representation of (1.26), excluding the structural-related terms represented by $\mathbf{A}_{\dot{\mathbf{x}}}$ and $\mathbf{A}_{\mathbf{x}}$, which are now accounted in $\mathbf{C}(\omega)$ and $\mathbf{K}(\omega)$.

The problem formulated in this manner is essentially equivalent to the dynamic response analysis of a buffeting-excited system, with mass, damping, and stiffness properties now dependent on both frequency and wind speed. Here, wind speed will be treated as an input parameter, making the structural properties exclusively frequency-dependent. For all frequencies, the system remains linear with respect to $\mathbf{X}(\omega)$. In the frequency domain, this linearity enables the structural response $\mathbf{X}(\omega)$ to be evaluated as the product of the transfer function $\mathbf{H}_{\text{nod}}(\omega)$ and the buffeting forces $\mathbf{F}_{\text{bu}}(\omega)$:

$$\mathbf{X}(\omega)=\mathbf{H}_{\text{nod}}(\omega)\mathbf{F}_{\text{bu}}(\omega). \tag{1.60}$$

The power spectral density of the displacement $\mathbf{S}_{\mathbf{x}}(\omega)$ is then evaluated from the definition of the PSD [70]

$$\mathbf{S}_{\mathbf{x}}(\omega)=\lim_{T\to\infty}\frac{2\pi}{T}\mathbf{X}(\omega)\mathbf{X}^{*}(\omega)=\mathbf{H}_{\text{nod}}(\omega)\left[\lim_{T\to\infty}\mathbf{F}_{\text{bu}}(\omega)\mathbf{F}_{\text{bu}}^{*}(\omega)\right]\mathbf{H}_{\text{nod}}^{*}(\omega) \tag{1.61}$$

where the superscript * denotes the conjugate-transpose operation. The term inside the brackets is identified as the power spectral density matrix of the buffeting forces, $\mathbf{S}_{F_{\text{bu}}}(\omega)$. Substituting this, the PSD of the structural response becomes:

$$\mathbf{S}_{\mathbf{x}}(\omega)=\mathbf{H}_{\text{nod}}(\omega)\,\mathbf{S}_{F_{\text{bu}}}(\omega)\,\mathbf{H}_{\text{nod}}^{*}(\omega). \tag{1.62}$$

The transfer function matrix $\mathbf{H}_{\text{nod}}(\omega)$ follows the standard form used in structural dynamics, but the inclusion of self-excited forces introduces frequency dependence in the coefficients $\mathbf{M}(\omega)$, $\mathbf{C}(\omega)$, and $\mathbf{K}(\omega)$, which were typically constant matrices:

$$\mathbf{H}_{\text{nod}}(\omega) = \left[-\omega^2\mathbf{M}(\omega) + \mathrm{i}\omega\mathbf{C}(\omega) + \mathbf{K}(\omega)\right]^{-1}. \tag{1.63}$$

The PSD of buffeting forces is evaluated by

$$\mathbf{S}_{\mathbf{F}_{\text{bu}}}(\omega) = \lim_{T\to\infty} \frac{2\pi}{T}\mathbf{F}_{\text{bu}}(\omega)\mathbf{F}^*_{\text{bu}}(\omega). \tag{1.64}$$

Introducing (1.26) with zero mean force $\mathbf{b} = \mathbf{0}$ leads to

$$\mathbf{S}_{F_{\text{bu}}}(\omega) = \mathbf{A}_u\mathbf{S}_u\mathbf{A}_u^\mathsf{T} + \mathbf{A}_w\mathbf{S}_w\mathbf{A}_w^\mathsf{T} + \mathbf{A}_u\mathbf{S}_{uw}\mathbf{A}_w^\mathsf{T} + \mathbf{A}_w\mathbf{S}_{wu}\mathbf{A}_u^\mathsf{T} \tag{1.65}$$

where we have identified $\mathbf{S}_u(\omega)$, $\mathbf{S}_w(\omega)$ and the cross-PSD $\mathbf{S}_{uw}(\omega)$, and introduced the fact that the aerodynamic coefficient matrices are real valued matrices. Because little coupling between u and w is generally observed [15], the last terms are omitted, and

$$\mathbf{S}_{F_{\text{bu}}}(\omega) = \mathbf{A}_u\mathbf{S}_u(\omega)\mathbf{A}_u^\mathsf{T} + \mathbf{A}_w\mathbf{S}_w(\omega)\mathbf{A}_w^\mathsf{T}. \tag{1.66}$$

The motivation for expressing the aerodynamic forces linearly in their stochastic variables u and w in Section 1.3.1 becomes clear in this context. This linear formulation enables the power spectral density of the forces to be obtained as a function of the fluctuating wind speed power spectral densities, $\mathbf{S}_u(\omega)$ and $\mathbf{S}_w(\omega)$, and the aerodynamic force coefficient matrix. Importantly, this approach preserves the Gaussian nature of the turbulence components u and w, which are modelled as Gaussian stochastic processes. Given the Gaussian nature of the buffeting input and the linearity of the system, the structural response $\mathbf{X}(\omega)$ is also Gaussian. Consequently, the response can be fully characterized by its first two statistical moments: the mean and the variance of the displacement. Without this linear formulation, higher-order analyses would be required to characterize the response due to nonlinear loading, significantly increasing the complexity of the solution [44].

The first statistical moment is the mean. Since the stochastic processes u and w are zero-mean, the mean force can be readily identified from (1.26) as $\bar{\mathbf{f}}_{\text{bu}} = \mathbf{b}$. This mean force, generally treated alongside other static loads during design, is crucial in aeroelastic analysis. The static displacement induced by this force affects the flutter derivatives and force coefficients, which are highly dependent on the angle of attack. Using the average angle of attack ensures that the flutter derivatives and force coefficients reflect the structure's average behaviour. The static rotation is obtained by solving a nonlinear system of equations:

$$\mathbf{K}(\omega^* = 0, \alpha_{\text{eff}})\mathbf{x}_{\text{stat}} = \mathbf{b} \tag{1.67}$$

where the nonlinearity arises from the dependence of the stiffness matrix $\mathbf{K}$ on the effective incident angle α_{eff} (see (1.18)), which itself depends on the deck rotation α included in $\mathbf{x}_{\text{stat}}$. This system is solved iteratively. Starting with $\mathbf{x}_0 = \mathbf{K}^{-1}\mathbf{b}$ assuming $\alpha_{\text{app}} = 0$, the process iteratively updates $\mathbf{x}$ using the new α_{app} derived from the current solution until convergence is achieved. The resulting static rotation angle is then held constant throughout the aeroelastic analysis procedure.

The second statistical moment is the variance. It is evaluated from the integral of the unilateral power spectral density. More generally, the covariance matrix is evaluated by integrating the power spectral density matrix. For instance, for displacements,

$$\mathbf{\Sigma}_{\mathbf{x}} = \int_{-\infty}^{+\infty} \mathbf{S}_{\mathbf{x}}(\omega)\,\mathrm{d}\omega. \tag{1.68}$$

This integral is typically computed using standard numerical integration methods, such as Gauss-Lobatto quadrature or, more simply, the trapezoidal rule [71]. The transfer function as well as the power spectral density are however known to exhibit acute resonant peaks whose sharpness depends on the smallness of the damping. As a result, the determination of the covariance matrix (1.68) necessitates the integration of sharp functions, over a broad frequency range to cover the entire energy content of the PSD. This operation is then computationally demanding, especially when large systems are considered.

With the first two statistical moments determined, the Gaussian distribution of the structural responses, in particular the structural displacements, is fully characterized. A peak factor can then be applied to estimate the maximum structural displacement, from which the structural design will be carried out [72].

At the beginning of the section, the wind speed U was considered as a constant parameter. The analysis presented in this section is typically carried out for multiple average wind speeds to characterize the gradual increase of the aeroelastic response of the structure in the design envelop, from wind-off to the instability. The scheme presented here is thus repeatedly executed for increasing wind speeds to produce a response curve such as in Figure 1.15, in which the system response increases as the aeroelastic effects amplify until the onset of instability.

1.5.3 The modal analysis

One efficient way to decrease this computational burden is to use a reduced model, in particular with a Ritz-Galerkin approach [73] which consists in expressing the structural displacement as a linear combination of M modes $\boldsymbol{\phi}_i$ $(i = 1, \ldots, M)$ and associated modal amplitudes $q_i(t)$

$$\mathbf{x}(t) = \sum_{i=1}^{M} \boldsymbol{\phi}_i q_i(t) = \boldsymbol{\Phi}\mathbf{q}(t), \tag{1.69}$$

where, in matrix notation, the matrix $\boldsymbol{\Phi}$ gathers the M columns of ordered modes, and $\mathbf{q}$ is a column vector collecting the modal amplitudes. Equivalently, in frequency domain, this equation reads

$$\mathbf{X}(\omega) = \sum_{i=1}^{M} \boldsymbol{\phi}_i Q_i(\omega) = \boldsymbol{\Phi}\mathbf{Q}(\omega). \tag{1.70}$$

The key idea of the Ritz-Galerkin approach is to represent the structural dynamic response $\mathbf{x}$ as a combination of vibration modes. Each mode $\boldsymbol{\phi}_i$ is characterized by its own mass, natural frequency, and damping ratio and represents an independent vibration pattern; the mode shape.

There is some freedom in choosing this modal basis. The mode shapes can for instance be postulated by an experienced user, who can propose a set of sufficiently different and complete shapes to accurately model any displacement of the structure. The fundamental requirement is that the chosen set of functions satisfies the essential boundary conditions imposed on the displacement —support conditions. However, this approach is likely to result in approximations where the derived displacement may not accurately match the exact structural response.

In classical structural dynamics, where aeroelastic effects are not considered, the most conventional and systematic approach consists in resorting to the undamped normal modes, which are the eigenvectors of the generalized eigenvalue problem:

$$\left(\mathbf{K} - \omega_i^2 \mathbf{M}\right) \boldsymbol{\phi}_i = \mathbf{0} \qquad i = 1, \ldots, M. \tag{1.71}$$

where ω_i represents the circular natural frequency. This method leads to the determination of M real valued modes that are orthogonal with respect to the mass and stiffness matrices. For systems with proportional damping [74], this implies that the original set of N coupled equations of motion with N nodal unknowns is transformed via modal projection into a set of M uncoupled equations with M unknowns. In matrix terms, this transformation results in diagonal

modal matrices of mass, damping and stiffness. These modal matrices may be introduced by substituting (1.70) in typical equation of motions —without aeroelastic effect—,

$$\left[-\omega^2\mathbf{M\Phi} + \mathrm{i}\omega\mathbf{C\Phi} + \mathbf{K\Phi}\right]\mathbf{Q} = \mathbf{F}_{\mathrm{bu}}(\omega), \tag{1.72}$$

and premultiplying by $\mathbf{\Phi}^{\mathsf{T}}$,

$$\left[-\omega^2\mathbf{\Phi}^{\mathsf{T}}\mathbf{M\Phi} + \mathrm{i}\omega\mathbf{\Phi}^{\mathsf{T}}\mathbf{C\Phi} + \mathbf{\Phi}^{\mathsf{T}}\mathbf{K\Phi}\right]\mathbf{Q} = \mathbf{\Phi}^{\mathsf{T}}\mathbf{F}_{\mathrm{bu}}(\omega). \tag{1.73}$$

Here, the matrices of mass $\mathbf{M}^* = \mathbf{\Phi}^{\mathsf{T}}\mathbf{M\Phi}$, damping $\mathbf{C}^* = \mathbf{\Phi}^{\mathsf{T}}\mathbf{C\Phi}$ and stiffness $\mathbf{K}^* = \mathbf{\Phi}^{\mathsf{T}}\mathbf{K\Phi}$ are identified as the projection the nodal matrices into the mode shapes. The strength of modal analysis, associated to systems experiencing proportional damping, lies in the diagonalization of these modal matrices. This diagonal structure simplifies the computation of the transfer function, as it reduces the inversion of the flexibility matrix to a straightforward operation on a diagonal matrix. Moreover, when the applied load has a frequency content in the range of natural frequencies, it is possible to prove that this basis has a fast convergence [75]. Consequently, the dynamic response can be determined with significantly reduced computational effort. As will be discussed later, the use of a modal basis in aeroelastic applications unfortunately does not allow for the diagonalisation of the system matrices.

The second advantage inherent to modal analysis lies in the reduction of the problem size thanks to modal truncation. If M equals to the number of nodes of the structure N, the displacement $\mathbf{x}$ can be exactly represented by the linear combination (1.69). For large models, the vibration modes associated with higher eigenfrequencies typically contribute less to the structural response. In most cases, only a limited number of modes are sufficient to accurately capture the structural dynamics of the deck [76, 77, 78]. For more complex structures, such as cable-supported bridges with multiple support conditions, the number of significant modes may increase to a few dozen [79]. Thus, it is common practice to truncate the modal basis by excluding modes with negligible energy contributions, effectively reducing the number of modes to $M \ll N$. For example, a structure with 10,000 degrees-of-freedom can reasonably be reduced to a system of approximately 20 vibration modes. The number of unknowns, and consequently the size of the system, are reduced by two orders of magnitude. The computational burden is unfortunately not reduced by the same amount, since the aerodynamic loads are established in the nodal basis, so its establishment as well as the projection from the nodal basis to the modal basis is still required at each step of the analysis.

The construction of the modal basis is, however, the price to pay for taking benefit of this large reduction in computation. This advantage becomes indispensable for the buffeting analysis of complex structures, where direct analysis would otherwise lead to important computational time prohibitive at the early design stages where many configurations and combinations variants are studied. In the specific case of aeroelastic systems, the choice of the modal basis legitimates even more discussion than for non-aeroelastic systems due to the speed-dependent nature of the modal properties. While the classical approach relies on the eigenmodes of the undamped dynamic system, it may be entirely reasonable to refine this formulation by incorporating self-excited forces into the modal basis. Since mode shapes evolve with wind speed, the ability of wind-off eigenmodes to accurately represent the structural displacement at high wind speeds U, where self-excited forces dominate, can be questioned. A more sophisticated approach, involving the solution of a homogeneous problem that accounts for speed-dependent aeroelastic matrices, as in (1.54) could thus be considered. However, this raises an additional question: at what wind speed should the modal properties be evaluated? The answer is not straightforward, and several choices are justifiable, such as $U = 0$, $U = U_{\mathrm{crit}}$ or even allowing U to vary, which would require the constitution of one modal basis per wind-speed. What is certain is that aeroelastic damping introduces non-proportional damping into the system. Consequently, the traditional advantage of decoupled equations of motion —achieved by using the wind-off undamped eigenmode basis—

is immediately lost when aeroelastic effects are considered. This naturally leads to the subsequent question: why not directly adopt the damped equations of motion and use the associated complex modes as the modal basis?

At this stage, it too early to provide definitive answers to these questions, but they will be revisited and discussed further in Chapters 3 and 4. What should be emphasized at this point is that conducting a frequency domain buffeting analysis with unsteady effects directly in the nodal basis is impractical. All flutter studies carried out in the frequency domain rely on modal analysis, with the modal basis typically constituted by wind-off eigenmodes derived from the undamped eigenvalue problem (1.71). The method developed in this Thesis is a spectral approach that consistently employs a modal basis. While various choices of modal basis will be explored, the most general form of the modal frequency domain equation of motion is expressed as:

$$\left[-\omega^2\mathbf{M}^*(\omega,U)+\mathrm{i}\omega\mathbf{C}^*(\omega,U)+\mathbf{K}^*(\omega,U)\right]\mathbf{Q}(\omega,U)=\mathbf{\Phi}^{\mathsf{T}}(U)\mathbf{F}_{\mathrm{bu}}(\omega,U). \tag{1.74}$$

where $\mathbf{M}^*(\omega,U)$, $\mathbf{C}^*(\omega,U)$ and $\mathbf{K}^*(\omega,U)$ are introduced as the aeroelastic modal matrices of mass, damping and stiffness and read

$$\mathbf{M}^*(\omega,U)=\mathbf{\Phi}^{\mathsf{T}}(U)\mathbf{M}(\omega,U)\mathbf{\Phi}(U), \tag{1.75-a}$$

$$\mathbf{C}^*(\omega,U)=\mathbf{\Phi}^{\mathsf{T}}(U)\mathbf{K}(\omega,U)\mathbf{\Phi}(U), \tag{1.75-b}$$

$$\mathbf{K}^*(\omega,U)=\mathbf{\Phi}^{\mathsf{T}}(U)\mathbf{C}(\omega,U)\mathbf{\Phi}(U). \tag{1.75-c}$$

Here, the key distinction with usual modal basis is that $\mathbf{\Phi}$ could depend on U.

Instead of directly determining the nodal covariance matrix (1.68), the modal analysis focuses on evaluating the modal covariance matrix

$$\mathbf{\Sigma}_{\mathbf{q}}(U)=\int_{-\infty}^{+\infty}\mathbf{S}_{\mathbf{q}}(\omega,U)\,\mathrm{d}\omega \tag{1.76}$$

and obtain the covariances of nodal displacement by modal superposition

$$\mathbf{\Sigma}_{\mathbf{x}}(U)=\mathbf{\Phi}(U)\mathbf{\Sigma}_{\mathbf{q}}(U)\mathbf{\Phi}^{\mathsf{T}}(U). \tag{1.77}$$

It is interesting to note, that the buffeting and unsteady forces such as presented in Sections 1.3 and 1.4 are always established in nodal basis. The modal forces are then obtained by modal projection. Thus, whether the analysis is carried out in nodal or in modal basis, this aeroelastic model is most often supplemented by a structural model such as a finite element model, especially for cumbersome applications involving complex deck geometries [80].

1.5.4 Solution in time and frequency domains

In Section 1.5.2.A, two families of buffeting analysis methods have been presented: the time domain and frequency domain approaches. The method developed in this Thesis belongs to the frequency domain category, which offers several advantages over time domain analysis.

First of all, excepted in several studies such as [52], the characterisation of aeroelastic forces, including methods based on the indicial responses, always relies on the determination of the flutter derivatives, that are exclusively derived in frequency domain. It seems then natural to stay within this framework for consistency and simplicity. Furthermore, the turbulent forces acting on the structure are also formulated in frequency domain, from their buffeting spectrum. If a time domain method is used, realisations of turbulent wind fields are required, which represents an additional unnecessary task to generate or record the time histories samples. Furthermore, the finite length of those signals induce the subsequent problem of sampling, a well known issue in time domain analysis that is inherent to the use of direct Monte-Carlo simulations [4].

The arguments in favour of frequency domain methods are not only about "comfort". The spectral analysis offers a direct understanding of the dynamic response of the structure. The

contributing modes are easily identified, and clear information may directly be obtained knowing their natural frequencies, resonant peaks, damping and mode shapes. The transfer functions also provide a simple and insightful tool for visualizing and capturing the structural dynamics.

The primary benefit of the frequency domain method relates to its capacity to significantly reduce the computational demands associated with buffeting analysis. In terms of the solutions to the equations of motion, the step-by-step integration approach is considerably slower than taking the Fourier transform of the system, and evaluating a the response $\mathbf{H}(\omega)\mathbf{F}_{\text{bu}}(\omega)$ to determine the output before carrying on an inverse Fourier transform. Furthermore, while the self-excited forces are directly prescribed in the frequency domain, their determination in the time domain necessitates the evaluation of a convolution product, which is a dramatically demanding operation.

The convolutions expressing unsteady wind loads in the time domain make it less straightforward. An efficient method to go around costly numerical estimations of the convolution (especially as time increases), is to recourse to aeroelastic states. By adopting exponential for the modelling of the indicial or impulse response functions of the unsteady loads, it is possible to transform the input and output representation of the wind loads versus displacements as a differential system with these augmented states.

Hence, when performing a modal analysis using time domain methods, the modal generalized forces must be computed by projecting a larger loading matrix onto the modal basis. This projection of nodal loads onto the modal basis is particularly computationally demanding for large structures and with the additional states.

Although this Thesis does not extensively focus on time domain methods, it is essential to acknowledge their indispensability for flutter analysis when structural nonlinearities are present. In cases of nonlinearity, the superposition principle, which underpins the frequency domain analysis, no longer holds. Consequently, frequency domain methods become less appropriate for capturing the structural dynamics. Nonlinearities can arise from various sources, including:

- the formulation of the buffeting forces, such as terms involving $u^2(t)$ or $u(t)w(t)$ for instance, or load coefficients that are highly dependent on the angle of attack;
- the formulation of the aeroelastic forces, particularly when flutter derivatives vary with the angle of attack;
- those originating from material nonlinearities;
- structural geometric nonlinearities such as those resulting from stay cables, hangers, suspension cables.

In such scenarios, time domain methods, employing step-by-step analysis, are the only viable option for capturing the system's behaviour.

Given our objective of developing a fast approximation method for analysing the structural response of aeroelastic oscillators experiencing linear behaviour, we have chosen to focus on frequency domain methods.

1.6 The promise of the Multiple Timescales Spectral Analysis framework

The frequency domain framework offers a powerful and insightful approach for buffeting analysis, particularly when coupled with modal decomposition. Despite its many advantages, the computational cost associated with solving large-scale aeroelastic problems remains relatively significant. This is especially true when integrating the sharp resonant peaks of the power spectral densities associated with lightly damped systems over a wide frequency range. The demand

for computational efficiency becomes relatively pronounced when studying complex structures or performing analyses across multiple wind speeds in the design envelope.

The use of elaborated models is most often reserved to the late stages of a design project, as it requires costly experimental studies as well as high computational demand. Simple models are therefore still highly appreciated by designers at earlier design stages to better capture the dynamic behaviour of the structure, but also for their lightness when several design tasks have to be repeated a large number of times, as required by the iterative nature of the design process. The Background-Resonant decomposition (B/R decomposition) as proposed by Davenport [81] is an example of such simple method used to evaluate the response of a structure to gusty winds, using an analytical decomposition of the response. The inspiration for this work clearly stems from his pioneering studies.

The method proposed in this Thesis, referred to as the background/resonant method, aims to address this problem, proposing an alternative to carry out the integration (1.76). This strategy enables substantial reductions in computational cost by allocating computational effort where it is most impactful: capturing the dominant resonant peaks and efficiently approximating the background contributions, while reducing the number of projection of modal forces.

1.6.1 The background-resonant decomposition for non-aeroelastic oscillators

Davenport introduced in [7, 81] the B/R decomposition framework to separate the wind-induced structural response into two distinct components: the background and resonant contributions, which could then be integrated independently. This decomposition not only provided a clearer understanding of structural dynamics under wind loading but also offered a practical method for simplifying complex computations.

The background/resonant decomposition concept was generalized in a broader theoretical foundation later formalized under the framework of Multiple Timescale Spectral Analysis [82]. This more general theory aims at computing integral with sharp peaks, similar to (1.76), but not necessarily in the context of a modal response. It has been successfully applied in related fields, such as non Gaussian responses [83], nonlinear aerodynamic loading terms [84], or even more recently, wave-loaded structures [85], where a refined decomposition into background, resonant, and inertial components was introduced.

While the core developments and derivations of the new approximation proposed in this Thesis will be presented in detail in subsequent chapters, this introduction focuses on the essential concept of background/resonant decomposition.

1.6.1.A Single-mode oscillators (1964)

Figure 1.17 illustrates, schematically, the decomposition of the response spectrum of a single mode or single degree-of-freedom structure excited by a buffeting load. In this version, the quasi-steady model is used as it corresponds to the context under which Davenport first developed the method. The background component —shown in blue— represents the quasi-static response to low-frequency wind fluctuations, which are spatially coherent and vary smoothly over time. While this component primarily concentrates its energy in the low-frequency range, its slow decay with frequency results in non-negligible higher-frequency contributions, even in the post-resonant regime. This is the reason why, (1.76) must be integrated over a wide frequency range to entirely represent the background contribution. By contrast, the resonant component —drawn in red— depicts the dynamic response driven by higher-frequency wind fluctuations interacting with the structure in its resonant regime.

In the dynamic context, Davenport relied on two major assumptions to formalize the decomposition, namely

- the timescales of the loading and of the system are significantly different. In other words, a distinction is made between the slow dynamics represented by the buffeting loading,

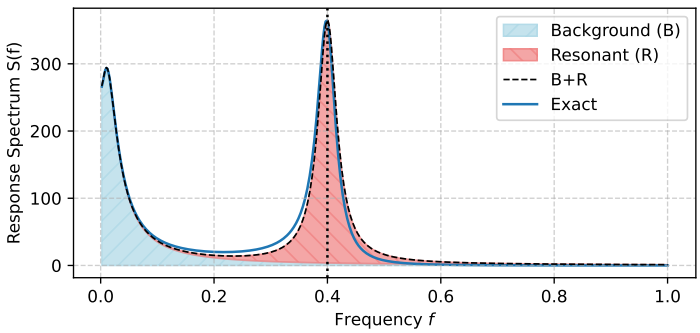

Figure 1.17: Schematic illustration of the background and resonant components in the structural response spectrum. The approximation $B + R$ is almost superposed with the exact response spectrum.

and fast dynamics represented by the natural vibrations of the aeroelastic system. The "centroid" of the power spectral density of the buffeting load shall be substantially lower (5 to 10 times lower) than the natural frequency of the aeroelastic system;

- the structural damping ratio is small, smaller than or of the same order of magnitude as 5%-10%; the quality of the approximation worsens as the damping ratio grows beyond these values.

He then suggested that, for single-mode systems, the response spectrum may be separated into two contributions

$$S_q(\omega) = S_q^B(\omega) + S_q^R(\omega). \tag{1.78}$$

where $S_q^B(\omega)$ and $S_q^R(\omega)$ denote respectively to the background and resonant components of the power spectral density. The two contributions are derived from the formal definition of $S_q(\omega)$

$$S_q(\omega) = |H(\omega)|^2 \, S_{F_{\text{bu}}}(\omega), \tag{1.79}$$

where the transfer function $H(\omega)$ is expressed as

$$H(\omega) = \frac{1}{k}\left[1 - \frac{\omega^2}{\omega_0^2} + 2\mathrm{i}\xi\frac{\omega}{\omega_0}\right]^{-1} \tag{1.80}$$

with ξ referring to the modal damping ratio, and ω_0 the natural frequency of the oscillator. The quasi-static assumption consists in supposing that the loading's frequency content is very low with respect to the resonant frequency, *i.e.* most important contributions come from a domain where $\omega \ll \omega_0$. In this low-frequency region, the transfer function asymptotes to

$$H(\omega) \simeq \frac{1}{k}, \tag{1.81}$$

and the background component of the response spectrum reads accordingly

$$S_q^B(\omega) = \frac{S_{F_{\text{bu}}}(\omega)}{k^2}. \tag{1.82}$$

The corresponding variance is obtained by integration

$$\sigma_{q,B}^2 = \frac{1}{k^2}\int_{-\infty}^{+\infty} S_{F_{\text{bu}}}(\omega)\,\mathrm{d}\omega = \frac{\sigma_{F_{\text{bu}}}}{k^2} \tag{1.83}$$

where $\sigma_{F_{\text{bu}}}$ represents the variance of the modal forces, identified by definition. This expression indeed recalls the static behaviour.

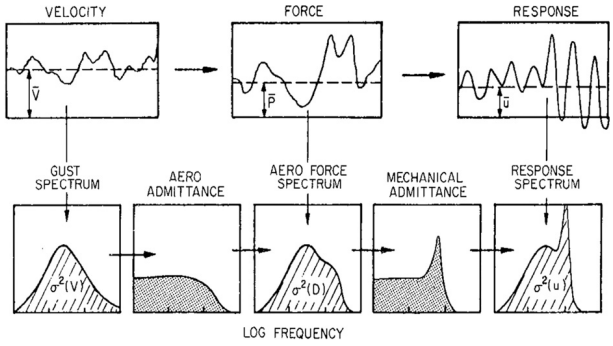

Figure 1.18: Davenport's original idea for determining the structural response to gust

The resonant component is evaluated from (1.78), forming the residual $R(\omega) := S_q(\omega) - S_q^B(\omega)$

$$R(\omega) = S_{F_{\text{bu}}}(\omega)\left(|H(\omega)|^2 - \frac{1}{k^2}\right) = \frac{S_{F_{\text{bu}}}(\omega)}{k^2}\left(\left(1-\frac{\omega^2}{\omega_0^2}\right)^2 + \left(2\xi\frac{\omega}{\omega_0}\right)^2\right)^{-1} - \frac{S_{F_{\text{bu}}}(\omega)}{k^2}. \quad (1.84)$$

This residual is then particularized to the resonant regime, first by introducing the white noise approximation, which consists in approximating the power spectral density by a constant value. Because the PSD of excitation is a smooth function of ω this approximation is particularly adapted to this situation, where most of the energy content is confined into the narrow band of the resonant peak. Negligible variation of the load PSD are expected through this narrow region. This approach was in fact years earlier proposed by [30] in aeronautics applications.

He noticed that, in the neighbourhood of resonance, the first term of has an order of magnitude of $\frac{S_{F_{\text{bu}}}}{k^2}\frac{1}{\xi^2}$ (since $\frac{\omega}{\omega_0} \simeq 1$), which is substantially larger than the second term, and which is therefore neglected.

The resonant component of the PSD reads

$$S_q^R(\omega) \simeq \frac{S_{F_{\text{bu}}(\omega_0)}}{4k^2\xi^2}\frac{1}{\left(\frac{\omega}{\omega_0}-1\right)^2+\xi^2}. \quad (1.85)$$

This result was confirmed by [82]. This result is sometimes found in the litterature with a factor 2, 2π or 4π depending on the excitation PSD scaling convention. The resonant contribution to the variance is then obtained from integration of this function

$$\sigma_{q,R}^2 = \frac{S_{F_{\text{bu}}}(\omega_0)}{k^2}\frac{\pi\omega_0}{2\xi} \quad (1.86)$$

The strength of Davenport's method lies in its ability to analytically integrate these components. This approach is of course incomparably faster than numerical integration methods, which would typically require hundreds of integration points to achieve similar accuracy. By contrast, the white-noise approximation samples the buffeting nodal forces at one single frequency, ω_0. This analytical integration can thus be interpreted as achieving the equivalent of using one integration point (see (1.86)).

1.6.1.B Multiple mode oscillators (2009)

Forty years later, the problem of computing the approximating the resonant resonant of coupled oscillators was tackled in parallel by [79] and [86]. They showed that the modal covariance can sometimes be disregarded during the reconstruction of the nodal displacement, which would correspond to ignoring any modal interaction. The Multiple Timescale Spectral Analysis framework presented by [82] further formalized mathematically the decomposition to possibly coupled

multi-modal systems, providing a first-order expression of the modal covariance Σ_{ij} of modes i and j. The two components are given as:

$$\Sigma_{ij}^{B} = \frac{\Sigma_{ij}^{F_{\mathrm{bu}}}}{k_i k_j} \qquad \text{and} \qquad \Sigma_{ij}^{R} = \frac{1}{k_i k_j} \Re \left\{ S_{F_{\mathrm{bu}},ij}(\omega_{ij})\, \omega_{ij} \frac{\pi(\xi - \mathrm{i}\varepsilon)}{2(\varepsilon^2 + \xi^2)} \right\} \tag{1.87}$$

with $\omega_{ij} = \frac{\omega_i + \omega_j}{2}$ and $\varepsilon = \frac{\omega_j - \omega_i}{\omega_j + \omega_i}$. In this approach, the white noise approximation is also invoked. However, since the PSD could be sampled at either ω_i or ω_j, a compromise is made by evaluating it at a midpoint ω_{ij}, between the resonant peaks. This approximation stays valid as long as ω_i and ω_j are close to each other, which aligns with the expected coupling between modes i and j.

1.6.1.C The MTSA framework (2015)

The Multiple Timescale Spectral Analysis [82] provides a general framework which will serve for all the developments carried out in this Thesis. No matter the context, it consists basically in identifying the regions contributing the most to the response spectrum. Each contribution is individually treated: they are expanded with an approximation function, derived with the perturbation methods [87]. A first contribution to the response spectrum is first captured: the background. For the next steps, this contribution to the response spectrum is removed considering a residual defined as the initial response spectrum where the first contribution approximation is subtracted. A second contributing region is then considered, a local approximation is sought, and a new residual is formed. This scheme is repeated progressively, until the residual is almost zero everywhere, or at least after having addressed all identified peaks of the response.

This process is illustrated in Figure 1.19, on the structural response of a single degree-of-freedom buffeting excited oscillator. There are in total 3 contributions to the response. The first is due to the background response, and the two remaining ones are the resonant response occurring at the natural frequency on the positive and negative sides respectively. Panel (a) represents the spectrum S_q. The first addressed peak is the background, for which the blue curve represents the tailored approximation. In (b), $\hat{S}_q$ illustrates the first residual $\hat{S}_q = S_q - S_b$, and S_{r_1} the approximation tailored to the first resonant contribution. The formation of the second residual $\hat{\hat{S}}_q$ let appear a small residual at ω_0, which will be discarded from the approximation of the response. The third peak is then treated similarly to the second peak, so that all identified contributions are addressed.

One of the requirements to allow for approximating each component independently is the separation of the scales of the problem. Each contribution to the response must be sufficiently distant from another to allow the perturbation method to capture them independently.

This principle, succinctly described here, together with the perturbation method for deriving series expansion of each contribution will be applied on aeroelastic oscillators in Chapters 2, 3 and 4.

1.6.2 Perspective in extension to aeroelastic oscillators

The previous section demonstrated how Davenport's decomposition replaces the numerical integration of sharp response spectra with an approximate analytical method, significantly reducing the computational cost of evaluating variances. The Multiple Timescales Spectral Analysis offers a convenient approach in many other contexts, for instance to estimate the covariance of coupled multiple-degree-of-freedom systems. While the computational effort for evaluating a single variance in a single-degree-of-freedom system is relatively low, the complexity increases substantially for multi-modal systems. The computational load scales with the square of the number of modes, M^2, corresponding to the elements of the covariance matrix, and is further compounded by the operations of modal projection required to compute the buffeting loads in the modal basis.

For large systems, this projection step becomes the primary bottleneck of the analysis. While the time savings may seem minor for a single variance calculation, the cumulative savings become

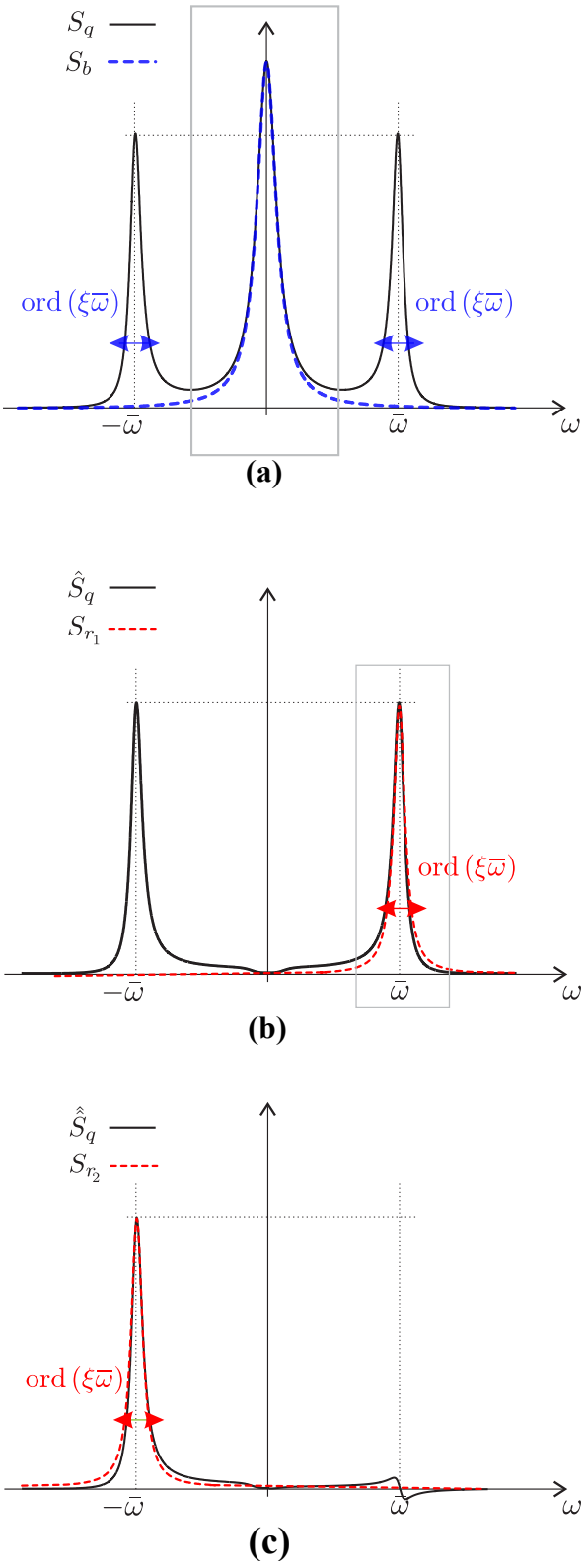

Figure 1.19: Illustration of the principle of the MTSA method on a buffeting excited dynamic oscillator. (a) Response spectrum and approximation of the background, (b) first residual and approximation of the resonant contribution of the positive peak and (c) second residual and approximation of the negative peak.

increasingly significant when determining all $M \times M$ elements of the full covariance matrix of modal responses for systems with large number of degrees-of-freedom N. This advantage is further amplified in aeroelastic systems, where the covariance matrix must be computed across various average wind speeds. By leveraging analytical integration, the potential computational gains become even more pronounced in such scenarios.

1.7 Motivation and objectives

The primary objective of this thesis is to develop an integrated and computationally efficient framework for the early-stage aeroelastic design of long-span bridges. In civil engineering applications, the accurate prediction of flutter instability is essential to ensure both structural safety and serviceability. However, traditional high-fidelity analysis methods remain too resource-intensive for use during the iterative predesign phase. A central aim is therefore to enable a rapid and practical predesign process against flutter, particularly suited to parametric studies and early design iterations. The method developed in this thesis provides a full toolchain for engineers to evaluate the aeroelastic response of a structure across the full wind speed envelope, without requiring a dense numerical sampling of the frequency domain.

This work also seeks to offer a structured alternative to current predesign practices, which—following Eurocode recommendations—typically rely on simplified flat-plate flutter derivatives corrected by empirical factors. By embedding a systematic treatment of the full aeroelastic model—now increasingly accessible through CFD simulations—the proposed method enables the integration of custom aerodynamic data and arbitrary structural configurations. In doing so, it paves the way for more realistic and data-driven evaluations during the preliminary design stage.

A further objective is to provide rapid and sufficiently accurate estimates of key physical quantities that help interpret and refine the dynamic behaviour of bridge decks. These include the separation and quantification of background and resonant components in the response, the evaluation of modal damping ratios, and the estimation of intermodal correlations.

Finally, this thesis aims to remove the need for expert-driven mode selection, often required in reduced-order models. By handling the full-order system from the outset, the method automatically captures all potentially relevant modal interactions. This makes the approach more robust, less dependent on user expertise, and more accessible to non-specialist engineers.

1.8 Outline of the Thesis

The objectives of the work presented in for this Thesis are now clearly defined and can be summarized as follows: extending the background/resonant method to multiple degree-of-freedom aeroelastic oscillators while taking advantage of the significant reduction in computational effort offered by analytical integration.

In Chapter 2 , a single-degree-of-freedom (SDOF) aeroelastic oscillator is developed. This chapter explores the specificities introduced by the frequency-dependence of the aeroelastic matrices, aiming to construct the simplest possible model to establish the foundation for the methodology.

In Chapter 3 , a two-degree-of-freedom (2DOF) aeroelastic model is introduced, focusing on modal interactions and coupling. The 2-mode system is a well-studied benchmark in aeroelastic analysis, particularly the pitch-plunge model, which has been extensively examined in the past. It is revisited here within the MTSA framework. This chapter provides a first attempt at recombining nodal displacements and assessing the method's performance in accurately representing modal correlation coefficients.

In Chapter 4 , the pitch-plunge model is extended to MDOF systems. This chapter aims to develop a robust and systematic approach for performing a comprehensive full-scale buffeting analysis including unsteady effects. While the method builds on the determination of modal

correlation coefficients involving at most two modes at a time, it extends the framework of Chapter 3 to accommodate larger systems. The chapter also emphasizes the importance of extracting the system's modal properties across subcritical wind speeds to ensure a comprehensive aeroelastic analysis.

The increased dimensionality of MDOF systems introduces additional challenges, particularly in collecting and processing the necessary information for flutter and buffeting analysis. To address these difficulties, Chapters 5 and 6 introduce numerical tools designed to streamline the process. Chapter 5 presents a systematic, globally convergent approach for identifying critical velocities within a full-order flutter analysis framework while Chapter 6 focuses on efficiently determining the subcritical modal properties.

With the groundwork now in place and the motivation clearly defined, we are ready to dive into the heart of this Thesis and uncover the details of a novel method for systematic analysis of large MDOF aeroelastic oscillators.

Part I

The Aeroelastic Background/Resonant Decomposition Method

Chapter 2

The single degree-of-freedom (SDOF) aeroelastic oscillator

Before addressing the complexities of multi-degree-of-freedom systems, it is useful to first revisit the SDOF problem to gain insight into the fundamental mechanisms at play. This chapter explores the application of the MTSA approach to an SDOF aeroelastic oscillator, investigating whether Davenport's background/resonant (B/R) decomposition can be meaningfully extended to this context. By examining this simplified case, we establish a foundation for the methodology before considering more intricate modal interactions in higher-dimensional systems. This chapter is not a purely academical demonstration though as in certain situations, the structural response is dominated by a single degree-of-freedom, making a single-degree-of-freedom (SDOF) model a relevant and efficient representation.

In the case of SDOF systems, the equation of motion (1.59) reads

$$\left[-\omega^2 m(\omega, U) + \mathrm{i}\omega c(\omega, U) + k(\omega, U)\right] X(\omega, U) = F_{\mathrm{bu}}(\omega, U). \tag{2.1}$$

The mass $m = m_s - m_{\mathrm{ae}}(\omega)$, damping $c = c_s - c_{\mathrm{ae}}(\omega)$ and stiffness $k = k_s - k_{\mathrm{ae}}(\omega)$ as well as the buffeting force F_{bu} are all scalar functions of U and ω. The static wind force is treated separately in a static analysis, and the buffeting force is considered to be a zero-mean Gaussian process fully characterized by its power spectral density function $S_{F_{bu}}(\omega)$. The response is Gaussian as well, and its power spectral density function is given by

$$S_q(\omega) = |H(\omega, U)|^2 \, S_{F_{bu}}(\omega, U), \tag{2.2}$$

with the transfer function $H(\omega)$ defined as

$$H(\omega, U) = \frac{1}{-\omega^2 m(\omega, U) + \mathrm{i}\omega c(\omega, U) + k(\omega, U)}. \tag{2.3}$$

The variance is obtained by integration

$$\sigma_q^2(U) = \int_{-\infty}^{+\infty} S_q(\omega, U) \, \mathrm{d}\omega. \tag{2.4}$$

In its current and original formulation, the background/resonant decomposition [81] cannot be applied to (2.4) considering the wind-off modal data as it is only valid for structures with constant stiffness and damping. The consideration of aeroelastic systems is incompatible with this assumption, as the self-excited forces are functions of the frequency. One of the implications it that, when the wind velocity increases, the natural frequency of the aeroelastic system might shift off and the damping ratio might also drop. This frequency shifting is illustrated in Figure 2.1, where the response spectrum is represented for two distinct wind speeds. The location of the

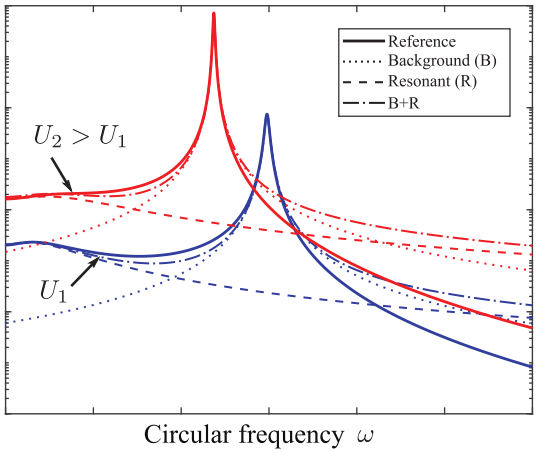

Figure 2.1: Illustration of frequency shifting off and the background/resonant decomposition applied to two response spectra relative to two different wind speeds.

resonance is shifted to the left for the highest velocity, under the action of the self-excited forces. This is one of the new features that the model presented in this chapter should be able to accommodate.

The second feature of aeroelastic oscillators is the possible variation of the aerodynamic damping and stiffness across the resonance peak, since $c(\omega)$ and $k(\omega)$ are functions of the frequency in the aeroelastic problem. This is an important specificity of the considered problem, which differs from the original B/R decomposition, where $c(\omega)$ and $k(\omega)$ were assumed to be constant throughout the frequency range of interest.

In this first SDOF model, we will not consider classical (2-DOF) flutter. Indeed, single-degree-of-freedom models, are inherently unable to fully capture classical flutter, which is fundamentally a coupled instability involving at least two interacting modes. Instead, SDOF models can exhibit other types of aeroelastic instabilities, such as galloping or torsional flutter. Physically, galloping arises due to asymmetric aerodynamic forces acting on a bluff body, leading to self-excited oscillations, while divergence is a static instability that occurs when aerodynamic loads overcome the structural stiffness, causing an unbounded displacement. These instabilities are driven by other physical mechanisms than classical flutter, which is capable of offering dynamic energy exchange between structural modes. Nevertheless, while SDOF models provide valuable insights into certain aeroelastic behaviours, but they are inherently limited in replicating the complex modal interactions that characterize flutter.

Galloping occurs when the wind velocity is such that a negative aerodynamic damping cancels the structural damping, leading to undamped vibrations. The net damping $\bar{\xi}$ is zero at the natural circular frequency ω_0 of the aeroelastic system. The corresponding critical wind velocity $U_{\text{gal.}}$ is obtained by solving

$$c(\omega_0) = c_{\text{s}}(c)_{\text{ae}}(\omega_0(U_{\text{gal.}})) = 0, \tag{2.5}$$

where $\omega_0(U_{\text{gal.}})$ is the natural frequency of the aeroelastic system. The aeroelastic natural frequency will be discussed later. Divergence occurs when the negative aerodynamic stiffness cancels the structural stiffness, so that the total stiffness, henceforth the natural frequency of the aeroelastic system, vanishes. The corresponding critical wind velocity is obtained by solving

$$k(\bar{\omega}) = k_{\text{s}} - k_{\text{ae}}(\bar{\omega}(U_{\text{div.}})) = 0, \tag{2.6}$$

where $\bar{\omega}(U_{\text{div.}})$ is the natural frequency of the aeroelastic system corresponding to wind velocity $U_{\text{div.}}$.

The integral defined in (2.4) does not converge in the sense of Riemann for $U = U_{\text{gal.}}$ since there is a non-integrable singularity located at $\omega = \bar{\omega}(U_{\text{gal.}})$ and it does not converge either

for $U = U_{\text{div.}}$ since there is a non-integrable singularity located at $\omega = 0$. These singularities translate mathematically the occurrence of an instability that can be predicted by solving the critical problem, as intensively discussed in Section 1.4.2.B. Aside from these two particular cases, the integral defined in (2.4) converges for any other wind speed.

2.1 Multiple Timescale Spectral Analysis

In order to simplify the notations, we will treat U as a parameter of the analysis in this section.

2.1.1 Assumptions

An approximate solution is developed under the following assumptions :

- (i) the timescales of the loading and of the system are significantly different. In other words, a distinction is made between the slow dynamics represented by the buffeting loading, and fast dynamics represented by the natural vibrations of the aeroelastic system. The centroid of the power spectral density of the buffeting load shall be substantially lower (5 to 10 times lower) than the natural frequency of the aeroelastic system;

- (ii) the structural damping ratio is small, smaller or of the same order of magnitude as 5%-10%; the quality of the approximation worsens as the damping ratio grows beyond these values;

- (iii) the frequency-dependent stiffness and damping $k(\omega)$ and $c(\omega)$ vary smoothly and moderately in the neighbourhood of the resonance peak of the aeroelastic system. The exact meaning of this assumption will be made clearer after introduction of the dimensionless formulation.

Assumptions (i) and (ii) are the same as in the classical B/R decomposition [82], while assumption (iii) is specific to the current problem. Under these conditions, the general framework of the Multiple Timescale Spectral Analysis can be specialized to get simple solutions. In order to make these assumptions explicit, we define the dimensionless aeroelastic stiffness and damping as

$$\mathcal{K}(\omega) := \frac{k(\omega)}{k_{\text{s}}} = 1 - \frac{k_{\text{ae}}(\omega)}{k_{\text{s}}} \quad , \quad \mathcal{C}(\omega) := \frac{c(\omega)}{c_{\text{s}}} = 1 - \frac{c_{\text{ae}}(\omega)}{c_{\text{s}}} \tag{2.7}$$

which are frequency-dependent and are not necessarily small; in fact the aerodynamic loading can significantly affect the natural frequencies. We also assume that the structural damping ratio ξ_s is a small positive number,

$$\xi_{\text{s}} := \frac{c_{\text{s}}}{2\sqrt{k_s m_s}} \ll 1. \tag{2.8}$$

This is a small parameter of the problem that will be used in the subsequent analysis. It is here explicitly introduced in order to formalize Assumption (ii). With these notations, the frequency response function of the aeroelastic system becomes

$$H(\omega) = \frac{1}{k_{\text{s}}} \left(-\frac{\omega^2}{\omega_{\text{s}}^2} + 2\mathrm{i}\xi_{\text{s}} \frac{\omega}{\omega_{\text{s}}} \mathcal{C}(\omega) + \mathcal{K}(\omega) \right)^{-1}, \tag{2.9}$$

where $\omega_s := \sqrt{k_s/m_s}$ is the natural circular frequency of the structure in wind-off conditions, and $m(\omega)$ is taken equal to 0.

2.1.2 The Background component

The Background component corresponds to the contribution of the variance which is located in the very low frequency range, in the neighbourhood of the centroid of the power spectral density of the buffeting load, see Figure 2.1. In this area, $\omega \ll \omega_{\mathrm{s}}$, the frequency response function of the aeroelastic system is locally approximated by $\hat{H}(\omega) = \left[k_{\mathrm{s}}\mathcal{K}(\omega)\right]^{-1}$, which is obtained by neglecting the dynamics in the system (*i.e.* quasi-static response). The first contribution to the power spectral density of the response is therefore given by

$$S_{q,B}(\omega) = \frac{S_{F_{\mathrm{bu}}}(\omega)}{\left(k_{\mathrm{s}}\mathcal{K}(\omega)\right)^2}, \tag{2.10}$$

and the corresponding variance is expressed as a function of the filtered variance of the buffeting load

$$\sigma_{q,B}^2 = \frac{1}{k_{\mathrm{s}}^2}\int_{-\infty}^{+\infty}\frac{S_{F_{\mathrm{bu}}}(\omega)}{\mathcal{K}^2(\omega)}\mathrm{d}\omega. \tag{2.11}$$

In this expression, $1/\mathcal{K}(\omega)$ can be seen as a frequency response function filtering out the frequency content of the buffeting loading. Since the timescales in $\mathcal{K}(\omega)$ and $S_{F_{\mathrm{bu}}}(\omega)$ might be similar, it is not possible to further simplify this expression. It constitutes the *background* component of the response. Notice that under the quasi-steady assumption, $\mathcal{K}(\omega) \to 1$ and (2.11) degenerates into the usual background component.

The frequency-dependency of the stiffness prevents from evaluating analytically the integral. However, the expected smoothness of the aeroelastic forces makes that this integration is captured by several integration points only. In particular, equation (1.51) establishes that the smoothness of the total stiffness is only conditioned by the variability of flutter derivatives P_i, H_i and A_i for i in $\{1, 2, 5\}$.

Depending on the variability of $k_{\mathrm{ae}}(\omega)$ and the targeted accuracy, the integration of the buffeting forces according to (2.11) can be simplified. Indeed, in cases where the background component plays a secondary role, $\sigma_{q,\mathrm{B}} \ll \sigma_{q,\mathrm{R}}$, its accurate determination is no longer a necessity and the denominator in the expression for $\sigma_{q,\mathrm{B}}$ in (2.11) can be simply replaced by k_{s}^2. This leads to a drastic simplification of the computation of the integral since $\sigma_{q,\mathrm{B}}$ then boils down to the usual quasi-static formulation of Davenport. When this assumption can be made —and this is what is done in the examples below—, the background component does not require any integration point, as buffeting forces must never be evaluated.

2.1.3 The Resonant component

In the variance of the response, defined in (2.4), the background component is trivially added and subtracted. This yields

$$\sigma_q^2 = \sigma_{q,\mathrm{B}}^2 + \int_{-\infty}^{+\infty}\left[S_q(\omega) - S_{q,\mathrm{B}}(\omega)\right]\mathrm{d}\omega. \tag{2.12}$$

The resonant component is then readily identified, as the main component in the residual $S_{q,1}(\omega) := S_q(\omega) - S_{q,\mathrm{B}}(\omega)$, which is also written

$$S_{q,1}(\omega) = \left(\left|H(\omega)\right|^2 - \frac{1}{\left(k_{\mathrm{s}}\mathcal{K}(\omega)\right)^2}\right) S_{F_{\mathrm{bu}}}(\omega). \tag{2.13}$$

Indeed, the main contribution to this residual amounts from the two resonance peaks of the aeroelastic system located in $\pm\bar{\omega}$. Assuming small damping (Assumption (ii)), the resonance

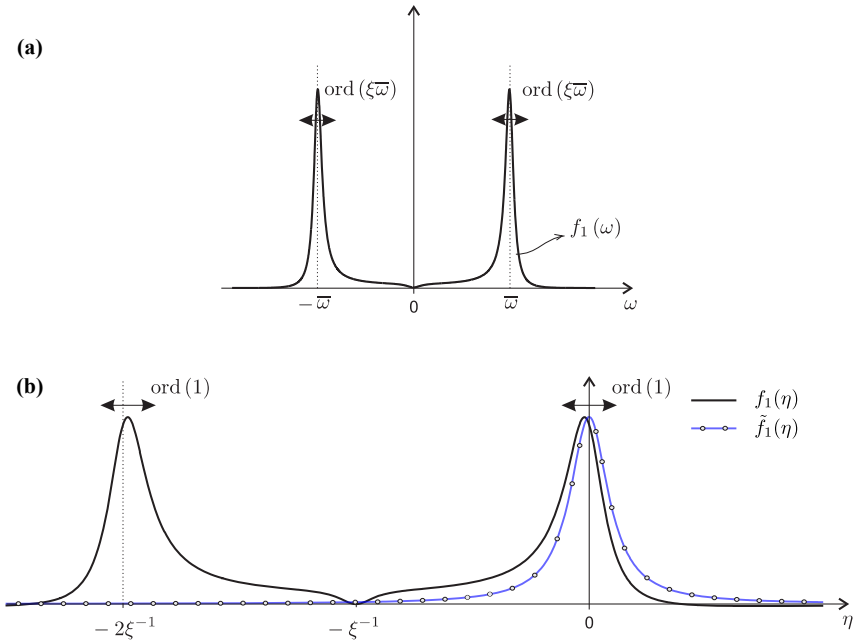

Figure 2.2: Representation of the integrant f_1 and its approximation $\tilde{f}_1$ (a) in the original coordinate ω and (b) in the stretched coordinate η.

frequency of the aeroelastic system (2.9) is defined by

$$-\frac{\bar{\omega}^2}{\omega_s^2} + \mathcal{K}(\bar{\omega}) = 0, \tag{2.14}$$

which is the pole of the frequency response function $H(\omega)$ for negligible damping ratio, see (2.9). Dropping higher order terms, the resonance frequency is therefore defined by $\mathcal{K}(\bar{\omega}) = \bar{\omega}^2/\omega_s^2$. This equation is not difficult to solve; it is nothing but a nonlinear eigenvalue problem. In this SDOF case, it turns into a nonlinear algebraic equation. The unicity of the solution is not guaranteed, multiple poles might exist. Solutions can be determined by an continuation iterative scheme as detailed next in Section 2.1.4. We can also notice that $\bar{\omega}$ is the solution of a problem that is independent of ξ_s. It is therefore independent of the perturbation analysis.

Considering now that $\overline{\omega}$ is known (for a given wind velocity), a stretched coordinate η is introduced to zoom on the resonance peak in the neighbourhood of $\omega = +\bar{\omega}$. This is formalized by writing

$$\omega = \overline{\omega}(1 + \xi_s \eta), \tag{2.15}$$

where $\eta = \mathcal{O}(1)$.

The introduction of a stretched coordinate is a key step in application of the perturbation methods. It allows to focus on the region of interest, here the resonance peak of positive frequency. By picking this abscissa, the second peak relative to the negative component is actually repelled to negative η of order $-1/\xi$, while the treated peak takes place at $\eta = 0$. This situation is described in Figure 2.2, where the function $f_1 = |H(\omega)|^2$ is represented in the original and stretched coordinate systems. We now need to construct a local approximation $\tilde{f}_1$ that accurately represents f_1 for values of the stretched coordinate $\eta = \mathcal{O}(1)$ at most. This approximation should also decrease rapidly in the far field ($\eta \gg 1$) to ensure the convergence of the integral on one side and prevent interactions with other contributions on the other side.

Assuming now that $\mathcal{K}$ and $\mathcal{C}$ are smooth functions in the neighbourhood of $\overline{\omega}$ (Assumption (iii)), they can be expanded as

$$\mathcal{K}(\omega) = \mathcal{K}(\overline{\omega}) + \xi_s \eta \overline{\omega} \partial_\omega \mathcal{K}(\overline{\omega}) + \mathcal{O}\left(\xi_s^2\right), \tag{2.16}$$

$$\mathcal{C}(\omega) = \mathcal{C}(\overline{\omega}) + \xi_s \eta \overline{\omega} \partial_\omega \mathcal{C}(\overline{\omega}) + \mathcal{O}\left(\xi_s^2\right), \tag{2.17}$$

which can be truncated at order ξ_s provided higher order derivatives are small enough to keep the asymptoticness of this series ($\xi_s^i \overline{\omega}^i \partial_\omega^i \mathcal{K}(\overline{\omega}) \ll \mathcal{K}(\overline{\omega})$).

Substituting (2.15), (2.16) and (2.17) into the frequency response function (2.9) leads to

$$\begin{aligned} H[\omega(\eta)] = & \frac{1}{k_s}\Big[-\frac{\overline{\omega}^2}{\omega_s^2}(1+\xi_s\eta)^2 + 2\mathrm{i}\xi_s\frac{\overline{\omega}}{\omega_s}(1+\xi_s\eta)\left(\mathcal{C}(\overline{\omega}) + \xi_s\eta\overline{\omega}\partial_\omega\mathcal{C}(\overline{\omega})\right) + \\ & \mathcal{K}(\overline{\omega}) + \xi_s\eta\overline{\omega}\partial_\omega\mathcal{K}(\overline{\omega}) + \mathcal{O}(\xi_s^2)\Big]^{-1}, \end{aligned} \tag{2.18}$$

or, collecting the likewise powers of ξ_s together,

$$\begin{aligned} H[\omega(\eta)] = & \frac{1}{k_s}\Big[\left(\mathcal{K}(\overline{\omega}) - \frac{\overline{\omega}^2}{\omega_s^2}\right) + \left(-2\eta\frac{\overline{\omega}^2}{\omega_s^2} + 2\mathrm{i}\frac{\overline{\omega}}{\omega_s}\mathcal{C}(\overline{\omega}) + \overline{\omega}\partial_\omega\mathcal{K}(\overline{\omega})\,\eta\right)\xi_s + \\ & + \left(-\eta^2\frac{\overline{\omega}^2}{\omega_s^2} + 2\mathrm{i}\frac{\overline{\omega}}{\omega_s}\left(\mathcal{C}(\overline{\omega}) + \overline{\omega}\partial_\omega\mathcal{C}(\overline{\omega})\right)\eta\right)\xi_s^2 + \mathcal{O}(\xi_s^3)\Big]^{-1}. \end{aligned} \tag{2.19}$$

Remembering the definition (2.14) of $\overline{\omega}$, it is readily seen that the first term drops so that the leading term in the brackets is in ξ_s. It is then decided to truncate the series at order ξ_s, invoking Assumption (ii) again. The local approximation of the frequency response function is therefore expressed, at leading order,

$$\tilde{H}(\omega(\eta)) = \frac{1}{2\xi_s k_s}\left[\left(-\frac{\overline{\omega}^2}{\omega_s^2} + \frac{1}{2}\overline{\omega}\partial_\omega\mathcal{K}(\overline{\omega})\right)\eta + \mathrm{i}\frac{\overline{\omega}}{\omega_s}\mathcal{C}(\overline{\omega})\right]^{-1}. \tag{2.20}$$

This expression is represented as the approximation $\tilde{f}_1(\eta)$ in Figure 2.2(b). It recalls in fact the formulation for a classical single degree-of-freedom system. It captures the order of magnitude of the resonance peak, $\frac{1}{2k_s\xi_s}$ and, at the same time, accounts for the frequency-dependent nature of the stiffness and damping.

The asymptotic analysis that has been performed so far assumes that all quantities other than ξ_s are of order 1. As seen in (2.20), the frequency response function of the aeroelastic system is expressed as a function of the aerodynamic stiffness $\mathcal{K}(\overline{\omega})$ which enters in the definition of $\overline{\omega}$, the aerodynamic damping $\mathcal{C}(\overline{\omega})$ and the gradient of the aerodynamic stiffness $\partial_\omega\mathcal{K}(\overline{\omega})$ in the neighbourhood of the resonance peak. This is precisely to account for the possible non negligible variation of the aerodynamic stiffness across the width of the resonance peak. At leading order, and assuming that $\partial_\omega\mathcal{C}(\overline{\omega}) \sim 1$, this expression also shows that the gradient in the damping $\partial_\omega\mathcal{C}(\overline{\omega})$ is actually repelled to a higher order; this is a consequence of the assumption of small damping ratio. Nevertheless if $\partial_\omega\mathcal{C}(\overline{\omega})$ was much larger than 1, which is a case we have not encountered in the applications that have been studied in this Thesis, it could be possible to enrich the proposed approximation. This approach is summarised in Appendix A, where both the derivatives of $\mathcal{K}(\overline{\omega})$ and $\mathcal{C}(\overline{\omega})$ are included in the approximation.

The substitution of (2.20) into (2.13) indicates that the term $1/(k_s\mathcal{K}(\omega))^2$ can be neglected, so that the residual $\hat{S}_{q,1}$ is approximated by

$$\tilde{S}_{q,1}(\omega(\eta)) = \frac{1}{(2k_s\xi_s)^2}\frac{1}{\left(\frac{\overline{\omega}^2}{\omega_s^2} - \frac{1}{2}\overline{\omega}\partial_\omega\mathcal{K}(\overline{\omega})\right)^2\eta^2 + \left(\frac{\overline{\omega}}{\omega_s}\mathcal{C}(\overline{\omega})\right)^2} S_{F_{\mathrm{bu}}}(\omega(\eta)). \tag{2.21}$$

Assuming that the power spectral density of the buffeting loading does not vary too fast in the neighbourhood of the resonance peak, the white-noise approximation of the excitation PSD may

be formulated as $S_{F_{\mathrm{bu}}}(\omega(\eta)) = S_{F_{\mathrm{bu}}}(\bar{\omega}) + \mathcal{O}(\xi_{\mathrm{s}})$. In this case, this term is seen as a constant with respect to integration along ω. The resonance component is obtained by multiplying $\tilde{S}_{q,1}(\omega(\eta))$ by 2 in order to also take into account the second resonance peaks located at $\omega = -\bar{\omega}$. The resonant contribution to the variance is obtained by integrating the PSD along frequencies

$$\sigma_{q,\mathrm{R}}^2 = 2\int_{-\infty}^{+\infty} \tilde{S}_{q,1}(\omega(\eta))\,\xi_{\mathrm{s}}\overline{\omega}\mathrm{d}\eta. \tag{2.22}$$

This integral accepts a closed form expression since the PSD of the loading is replaced by $S_{F_{\mathrm{bu}}}(\bar{\omega})$. After substitution of (2.21) into (2.22) and some standard calculus, the resonant component is finally given by

$$\sigma_{q,\mathrm{R}}^2 = \frac{S_{F_{\mathrm{bu}}}(\bar{\omega})}{k_{\mathrm{s}}^2}\frac{\pi\omega_{\mathrm{s}}}{2\xi_{\mathrm{s}}\mathcal{C}(\overline{\omega})}\frac{1}{\left|\frac{\overline{\omega}^2}{\omega_{\mathrm{s}}^2} - \frac{\overline{\omega}\partial_\omega\mathcal{K}(\bar{\omega})}{2}\right|}. \tag{2.23}$$

Returning to original variables, the resonant contribution is expressed under a generalized form of the well known resonant contribution for systems with constant mechanical properties,

$$\sigma_{q,\mathrm{R}}^2 = \frac{S_{F_{\mathrm{bu}}}(\bar{\omega})}{k_{\mathrm{s}}^2}\frac{\pi\omega_{\mathrm{s}}}{2\xi_{\mathrm{s}}}\frac{c_{\mathrm{s}}}{c_{\mathrm{s}} - c_{\mathrm{ae}}(\overline{\omega})}\frac{k_{\mathrm{s}}}{\left|k_{\mathrm{s}} - k_{\mathrm{ae}}(\bar{\omega}) + \frac{1}{2}\overline{\omega}\partial_\omega k_{\mathrm{ae}}(\bar{\omega})\right|}. \tag{2.24}$$

The last two factors are indeed equal to 1 in the absence of aerodynamic stiffness and damping. When unsteady aerodynamic loads are included, the damping ratio of the system is affected and is not equal to the structural damping ratio. This justifies the introduction of a new damping ratio that includes the aeroelastic contribution

$$\bar{\xi} := \frac{c_{\mathrm{s}} - c_{\mathrm{ae}}(\overline{\omega})}{2\sqrt{(k_{\mathrm{s}} - k_{\mathrm{ae}}(\bar{\omega}))\,m_s}}. \tag{2.25}$$

The substitution in (2.24) ultimately yields

$$\sigma_{q,\mathrm{R}}^2 = \frac{S_{F_{\mathrm{bu}}}(\bar{\omega})}{(k_{\mathrm{s}} - k_{\mathrm{ae}}(\bar{\omega}))^2}\frac{\pi\bar{\omega}}{2\bar{\xi}}\frac{1}{1 + \frac{1}{2}\frac{\overline{\omega}\partial_\omega k_{\mathrm{ae}}(\bar{\omega})}{k_{\mathrm{s}} - k_{\mathrm{ae}}(\bar{\omega})}} \tag{2.26}$$

which makes it even more obvious that this is a generalization of the well-known B/R decomposition, to systems with smoothly varying mechanical properties, while the smoothly varying buffeting spectra is handled in the same convenient manner as in the original decomposition. The resonant component to the integral (2.4) is then virtually evaluated using one single integration point, located at the natural frequency defined by the leading order equation (2.14).

2.1.4 Summary with dimensional quantities and practical implementation

In summary, the sum of the background and resonant components provides

$$\sigma_q^2 = \sigma_{q,\mathrm{B}}^2 + \frac{S_{F_{\mathrm{bu}}}(\bar{\omega})}{(k_{\mathrm{s}} - k_{\mathrm{ae}}(\bar{\omega}))^2}\frac{\pi\bar{\omega}}{2\bar{\xi}}\frac{1}{1 + \frac{1}{2}\frac{\overline{\omega}\partial_\omega k_{\mathrm{ae}}(\bar{\omega})}{k_{\mathrm{s}} - k_{\mathrm{ae}}(\bar{\omega})}}, \tag{2.27}$$

where in the dimensional version, the eigenvalue of the aeroelastic system is computed by

$$k_{\mathrm{s}} - k_{\mathrm{ae}}(\bar{\omega}) - m_{\mathrm{s}}\bar{\omega}^2 = \mathrm{ord}(\xi_s). \tag{2.28}$$

In practice, the flutter analysis is repeated for several increasing values of the wind speed $\{U^{(n)}\}$, $n \in \mathbb{N}$, starting from $U^{(0)} = 0$ m/s and until a critical state is reached. For each increment in this sequence, a simple iterative method, based on the power method, can be used to compute $\bar{\omega}\left(U^{(n)}\right)$. Starting from the first guess $\bar{\omega}_{(0)} = \bar{\omega}\left(U^{(n-1)}\right)$, or $\bar{\omega}_{(0)} = \omega_{\mathrm{s}}$ when $n = 0$, just a couple

of iterations can be performed at each increment of wind speed in order to converge to the new natural frequency. The iterative scheme is as simple as

$$\bar{\omega}_{(i+1)} = \sqrt{\frac{k_\mathrm{s} - k_\mathrm{ae}\left(\bar{\omega}_{(i)}\right)}{m_\mathrm{s}}}. \tag{2.29}$$

where $k_\mathrm{ae}\left(\bar{\omega}_{(i)}\right)$ is the aerodynamic stiffness corresponding to the frequency $\bar{\omega}_{(i)}$ and wind velocity $U^{(n)}$. This operation is repeated a couple of times until a desired convergence criterion is reached. At this stage, it is recalled that the analysis is performed for $U \leq U_\mathrm{div.}$ so that $k_\mathrm{s} - k_\mathrm{ae}\left(\bar{\omega}_{(i)}\right)$ is indeed positive.

2.2 Algorithmic implementation

This section describes a practical implementation of the algorithm. At this stage, the implemented model is suitable for SDOF models only.

The flow-chart of the solution strategy is shown in Figure 2.3. For a given average wind velocity, the solving process consists of 3 main tasks: the evaluation of the aeroelastic eigen frequency, and that of the background and resonant components. The determination of the eigen frequency of the aerodynamic system relies on an iterative scheme, initiated with the wind-off conditions. Relaxation can be used to improve the convergence of the process. As the wind-off conditions give already an excellent guess of the natural frequency of the aeroelastic system, the convergence is quite straightforward. The resonant component is then evaluated using (2.26), and Scanlan formulation for $k_\mathrm{ae}(\omega), c_\mathrm{ae}(\omega)$ and $\partial_\omega k_\mathrm{ae}(\omega)$. The last step is the determination of the background component, before assembling the two contributions to get the variance at the considered velocity.

All this solving process is embedded in a loop over a range of U, from wind-off to critical conditions.

2.3 Illustrations

This section presents 3 examples of application of the derived decomposition to singe degree-of-freedom torsional aeroelastic oscillators. For this particular displacement, the equation of motion reads

$$\left(-\omega^2 I_\mathrm{s} + 2\xi I_\mathrm{s}\omega_\mathrm{s}(\mathrm{i}\omega) + I_\mathrm{s}\omega_\mathrm{s}^2\right)\Theta\left(\omega\right) = M_\mathrm{se}\left(\omega\right) + M_\mathrm{bu}\left(\omega\right), \tag{2.30}$$

where I_s is the mass moment of inertia per unit length and such that the unsteady moment and the buffeting pitching moment are expressed as

$$\begin{aligned} M_\mathrm{se}\left(\omega\right) &= qB^2\left(\frac{\omega B}{U}\right)^2\left(A_2^*\mathrm{i} + A_3^*\right)\Theta\left(\omega\right), \\ M_\mathrm{bu}\left(\omega\right) &= \frac{qB}{U}\left(\frac{\pi}{2}B\chi\left(\omega\right)\right)W\left(\omega\right). \end{aligned} \tag{2.31}$$

where $\chi(\omega)$ is the real function representing the admittance, weighting the quasi-steady values of buffeting forces in the frequency domain [88] and $W(\omega)$ is the Fourier transform of the vertical wind velocity $w(t)$. In correspondence with the canonical expression of the unsteady forces

$$M_\mathrm{se}\left(\omega\right) = \left(\mathrm{i}\omega c_\mathrm{ae}\left(\omega\right) + k_\mathrm{ae}\left(\omega\right)\right)\Theta\left(\omega\right), \tag{2.32}$$

the aeroelastic stiffness and damping expand as follows

$$\begin{aligned} k_\mathrm{ae}\left(\omega\right) &= qB^2\left(\frac{\omega B}{U}\right)^2 A_3^*\left(\omega\right), \\ c_\mathrm{ae}\left(\omega\right) &= qB^2\frac{B}{U}\left(\frac{\omega B}{U}\right)A_2^*\left(\omega\right). \end{aligned} \tag{2.33}$$

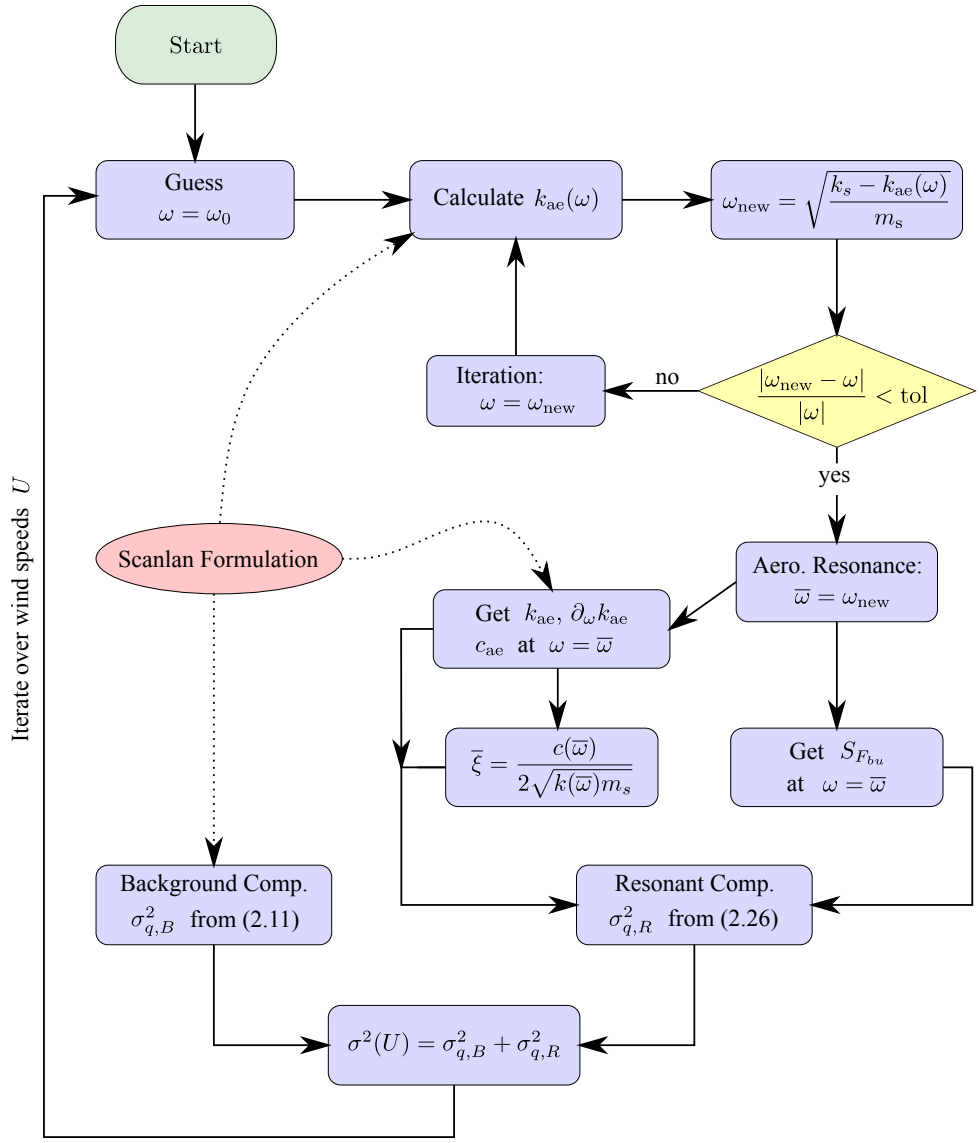

Figure 2.3: Organigram of the aeroelastic analysis performed with the background/resonant decomposition for evaluating the integral of the response spectra. The solving process is embedded in a loop over the average wind speeds.

These latter equations will serve as common basis for all the following illustrations. In these illustrations, the proposed extension of the B/R decomposition will be used to compute the standard deviation of the torsional response; it will also be compared to an accurate result obtained by numerical integration of the power spectral density of the response.

2.3.1 Illustration 1 - Torsional angular response of bridge decks

For this first illustration, the B/R decomposition is applied to the Golden Gate and Tacoma Narrows bridges. For both structures, the flutter derivatives $A_2^*(\omega)$ and $A_3^*(\omega)$ shown in Figure 2.4 as well as other useful data summarised in Table 2.1 are considered (Source: [35, 89, 90, 91]). The aerodynamic stiffness and damping $k_{ae}(\omega)$ and $c_{ae}(\omega)$ are obtained with (2.33) and spline interpolation.

To ensure a safe behaviour against flutter, the variance of the torsional displacement must be calculated for a sufficiently wide range of wind velocities U. The results obtained for the Golden Gate Bridge are shown in Figure 2.5. The power spectral density of the torsional response is

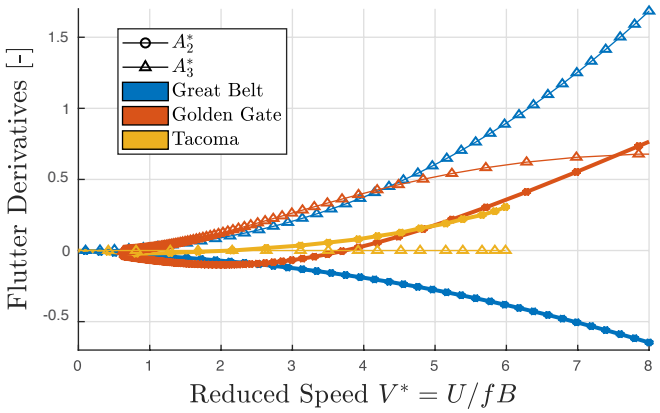

Figure 2.4: Flutter derivatives $A_2^*(\omega)$ and $A_3^*(\omega)$ of the structures considered in Illustrations 1 and 2.

	Golden Gate	**Tacoma**	**Storebaelt**
Moment of Inertia I_s [kg m^2/m]	$4.4 \cdot 10^6$	$177.73 \cdot 10^3$	$2.47 \cdot 10^6$
Natural frequency f_s [Hz]	0.1916	0.20	0.278
Damping Ratio ξ_s [%]	0.5	0.5	0.3
Deck width B [m]	27.43	12.0	31
Aeroelastic Model	Bluff body	Bluff body	Flat Plate
Type of instability	Galloping	Galloping	Divergence

Table 2.1: Structural properties of the structures considered in Illustrations 1 and 2.

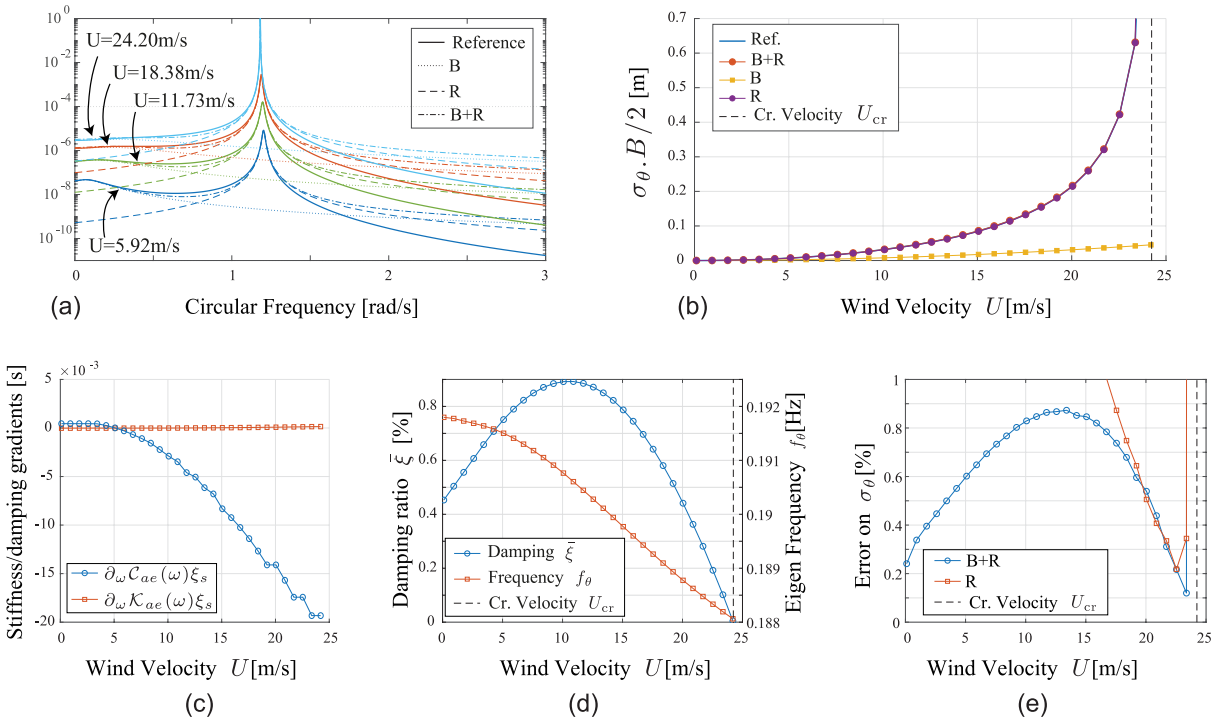

Figure 2.5: Results obtained from background/resonant methods applied to the first illustration (Golden Gate Bridge). (a) PSD and their approximations for different wind velocities. (b) Scaled standard deviations obtained from background component (B), resonant components (R), and the sum of them (B)+(R). (c) Evolution of scaled aeroelastic stiffness and damping gradients with respect to average wind velocity. (d) Damping ratio at resonance with respect to average wind velocity. (e) Error on σ_θ with respect to average wind velocity.

shown in Figure 2.5(a) for several values of U. The exact power spectral density is compared to the power spectral density corresponding to the B/R decomposition —in a log scale. The agreement is very good where the power spectral densities are large. This is also confirmed on Figure 2.5(b) showing the variance of the torsional response, where the proposed method shows a perfect overlay with the reference curve obtained from numerical integration, until the critical wind velocity $U_{cr} \approx 24$ m/s, represented by the dashed line and evaluated with (2.5). The background (B) contribution to the displacement is very low and a quite accurate expression can already be obtained from the resonant component (R) alone. This is justified by the fact that this first illustration corresponds to a torsional galloping, as clearly illustrated from the power spectral densities: the frequency is not affected by the wind velocity but the damping ratio drops to zero when approaching the critical wind velocity. The relative error on the numerically integrated curve does not exceed 1% as illustrated by Figure 2.5(e). Also, the magnitude of the aeroelastic damping and stiffness gradients $\partial_\omega \mathcal{K}(\overline{\omega})$ and $\partial_\omega \mathcal{C}(\overline{\omega})$, plotted as a function of U in Figure 2.5(c), validates the truncation of the series expansions (2.16)-(2.17). Finally, it is observed in Figure 2.5(d) that the structure indeed fails from a galloping instability, since the damping becomes negative at the critical velocity U_{cr}. The value obtained for the critical velocity is corroborated by [89], and matches well the vertical asymptote of the standard deviation of the torsional displacement.

The second example, the first Tacoma Narrows bridge, is widely known for its unstable behaviour [18]. The results obtained for this second example are shown in Figure 2.6. Globally, the structural behaviour is very similar to the one previously discussed, but the critical speed is significantly lower. The instability corresponds again to a torsional galloping. It takes place at a wind velocity of 11.5 m/s, which is consistently obtained either with the formula (2.5) giving the

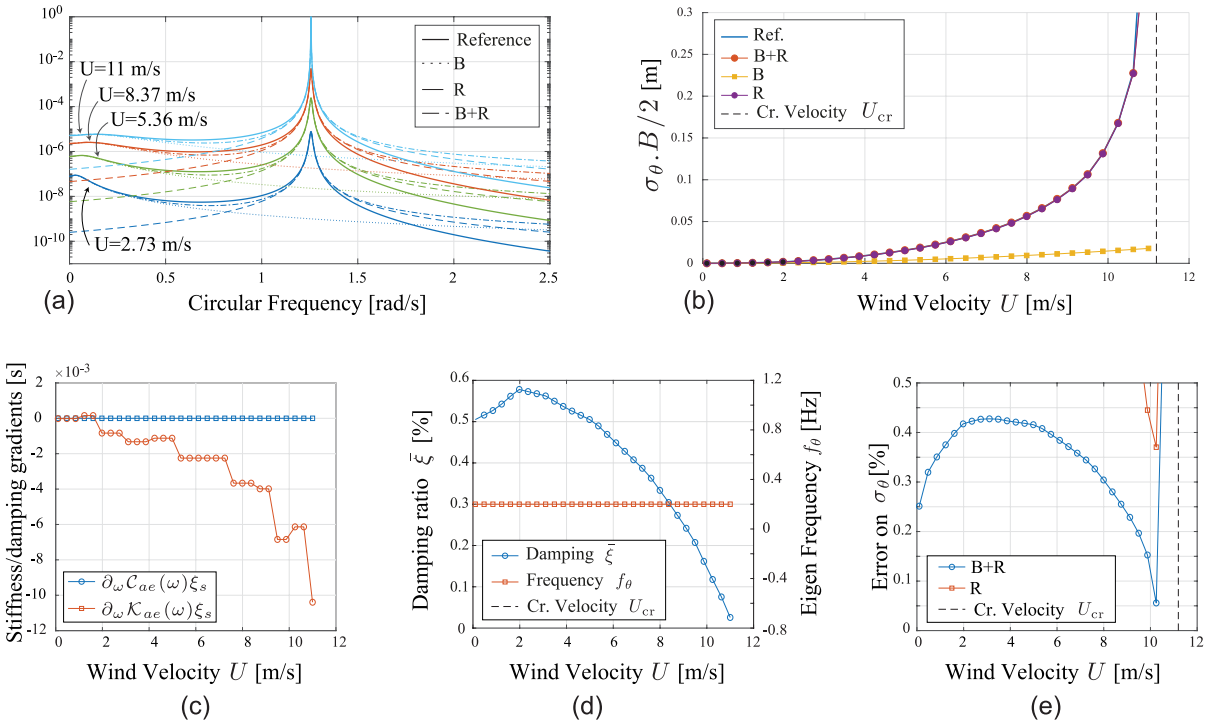

Figure 2.6: Results obtained from background/resonant methods applied to the first illustration (Tacoma Narrows bridge). (a) PSD and their approximations for different wind velocities. (b) Scaled standard deviations obtained from background component (B), resonant components (R), and the sum of them (B)+(R). (c) Evolution of scaled aeroelastic stiffness and damping gradients with respect to average wind velocity. (d) Damping ratio at resonance with respect to average wind velocity. (e) Error on σ_θ with respect to average wind velocity.

critical wind velocity, either by reproducing the complete flutter response $\sigma_\theta(U)$, or when the damping ratio $\bar{\xi}(U)$ estimated with the proposed method reaches zero. It is also consistent with the values provided in [91]. More importantly, the complete flutter response is again accurately captured by the proposed extension of the B/R decomposition; yet, the resonant part of the response is seen to be the most important.

2.3.2 Illustration 2 - Application to the flat plate model

The next example is borrowed from the recent benchmark about flutter analysis of bridges [46]. In that benchmark, a pitch/plunge model of the Storebaelt bridge is studied with the actual structural properties of the bridge but with the aerodynamic properties of a flat plate [57]. In the early stages of the developments of this Thesis, we further reduced this study to the sole torsional dynamics. The aeroelastic deck section is idealized by a flat plate, a simplification which is known to be useful in the prediction of more complex geometries [11] despite its simplicity.

The flutter derivatives are expressed as functions of $F(\omega)$ and $G(\omega)$, respectively the real and imaginary part of Theodorsen's circulation complex function $C(\omega)$. In the following developments, the function is approximated by the analytical formula suggested by Jones [92], that involves a combination of exponential functions.

The flutter derivatives $A_2^*(\omega)$ and $A_3^*(\omega)$ read [46]

$$\begin{aligned} A_2^*(\omega) &= -\frac{\pi}{8}\frac{U}{\omega B}\left(1 - F(\omega) - \frac{4U}{\omega B}G(\omega)\right), \\ A_3^*(\omega) &= \frac{\pi}{2}\left(\frac{U}{\omega B}\right)^2\left(F(\omega) - \frac{\omega B}{4U}G(\omega)\right), \end{aligned} \tag{2.34}$$

so that the aeroelastic stiffness and damping obtained by (2.33) read

$$k_{\text{ae}} = qB^2\frac{\pi}{2}\left(F(\omega) - \frac{\omega B}{4U}G(\omega)\right)$$
$$c_{\text{ae}} = -q\frac{B^3}{U}\frac{\pi}{8}\left(1 - F(\omega) - \frac{4U}{\omega B}G(\omega)\right). \tag{2.35}$$

Before tackling the analysis, it is possible to predict the type of instability based on the knowledge of the flutter derivatives. As shown in Figure 2.4, the damping-related flutter derivative A_2^* is negative, whereas the stiffness-related flutter derivative A_3^* is positive. In other terms, the aeroelastic loading provides additional damping to the structure, while it decreases the total aeroelastic stiffness. Accordingly, the bridge heads towards a divergence instability.

This is confirmed by Figure 2.7(d), showing a marked frequency, where the aeroelastic natural frequency decreases with the wind velocity. Figure 2.7(d) also reveals a marked growth of the net damping ratio $\bar{\xi}$ for increasing velocity, reaching more than 20% for wind velocities larger than 80 m/s, going therefore beyond the scope of assumption (ii). Even so, the proposed analytical solution remains in good agreement with numerical results for small to intermediate values of velocity U, as shown in Figure 2.7(b). As a matter of fact, the power spectral densities and standard deviations are well approximated, with acceptable errors ($< 10\%$) up to a wind velocity of 80 m/s. In the proposed method, the order of magnitude of the error corresponds to the total damping ratio $\bar{\xi}$; in this example, the total damping ratio reaches 20% around 80 m/s which matches the order of magnitude of the error of 10% (the proposed method is therefore more relevant when the instability occurs in galloping-type rather than divergence-type instability, unless lightly damped). Beyond this point, a lack of precision shows up right before the vertical asymptote defining the critical velocity, where a larger discrepancy appears with respect to the numerical solution. Given the magnitude of the damping in this range of velocity, the eigenvalue problem (2.28) needs to be reconsidered by including the damping ratio at leading order.

It is also important to note that the structure does not respond in the background regime. This is fortunate, as the separation between background and resonant timescales diminishes with increasing wind speed. Since this timescale separation is a fundamental assumption of the Multiple Timescale Spectral Analysis used to derive the present approximation, it underscores the need for caution when applying this approach to divergence instabilities at high speeds.

2.3.3 Illustration 3 - Torsional galloping of a bridge deck section of the Third Bosphorus bridge during lifting operations

This application presents another SDOF torsional oscillator. During the Third Bosphorus bridge deck building operations, each segment of the deck was positioned by lifting from a floating platform to the deck level, at a height of 75 meters above sea level. This operation involves a 825 t load to be lifted and last sufficiently long for the deck segment to be submitted to turbulent winds and possible aeroelastic instability [93]. This system is particularly compliant in torsion along the vertical axis, as the strand jacks are relatively close to each other. In these circumstances, the system is particularly sensitive to aeroelastic instabilities and, if no precaution is taken, torsional galloping could be observed with angular displacements larger than 30 degrees in most severe configurations [93]. To ensure a safe lifting process, various configurations were tested using deflectors made of plastic sheeting to partially or fully cover the segment's extremities, mitigating the vortex shedding and the resulting flow pattern and associated wind-induced instabilities.

The deck segment is characterized by a mass $m_{\text{s}} = 825$ t, a width $B = 58.4$ m, and a length $D = 14$ m representing the distance from the rotation centre to each lifting point of the deck segment, see Figure 2.8(a). The strand jacks are separated by 6 m×13.5 m, and the modal

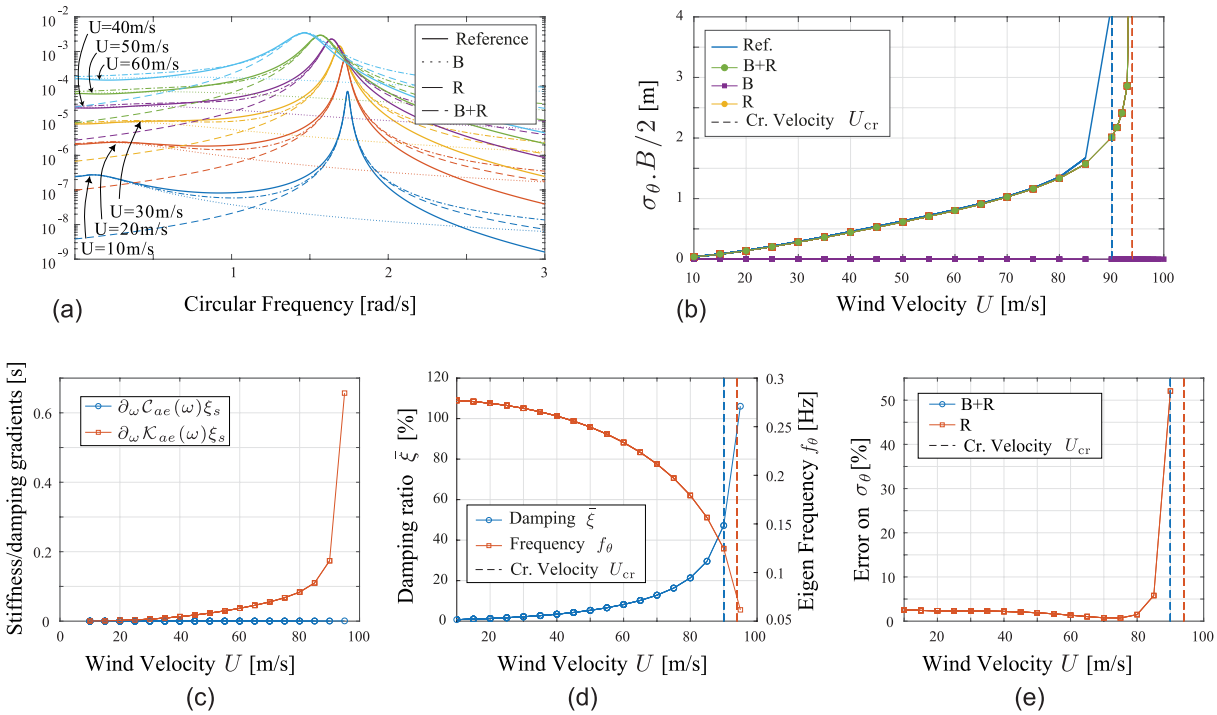

Figure 2.7: Results obtained from background/resonant methods applied to the first illustration (Great Belt Bridge and flat plate aerodynamics). (a) PSD and their approximations for different wind velocities. (b) Scaled standard deviations obtained from background component (B), resonant component (R), and from combinations of them. (c) Scaled aeroelastic stiffness and damping gradients evolution with respect to average wind velocity. (d) Damping ratio at resonance with respect to average wind velocity. (e) Error on σ_θ with respect to average wind velocity.

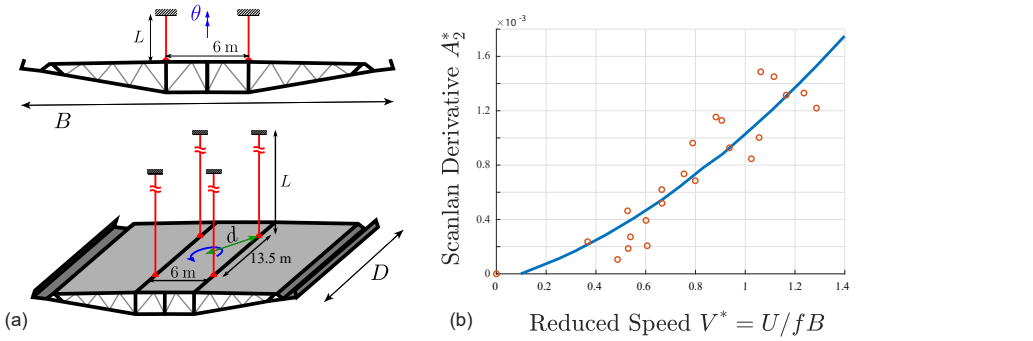

Figure 2.8: (a) View of the deck segment during lifting operation, (b) Flutter derivatives $A_2^*(\omega)$ and $A_3^*(\omega)$ of the Third Bosphorus bridge deck segment (both experimental data and fitting are taken from [93])

	Segment BB3
Cable length L [m]	100
Torsional radius d [m]	7.39
Segment mass m_s [Kg]	$8.25 \cdot 10^5$
Eigen Frequency f_s [m]	0.031
Damping Ratio ξ_s [%]	0.2
Type of instability	Galloping

Table 2.2: Modal parameters for the segment deck during lifting operation

parameters are shown in Table 2.2. The stiffness in torsion is calculated by

$$k_\theta = \frac{m_\mathrm{s} g d^2}{L},$$

where g is the acceleration of gravity, $L \in \{0, 100\}$ m is the length of the lifting cables and $d = 7.4$ m the distance from the strand jacks to the centre of rotation of the segment. This stiffness is computed from the pendulum-like stiffness $m_\mathrm{s} g/L$ of a single cable; for a unit rotation of the deck, $\theta = 1$, the displacement of the anchorages is equal to d which gives after multiplication by the pendulum-like stiffness and the lever arm d, the torsional moment corresponding to a unit rotation.

The Scanlan derivatives of each deck segment have been determined by experimental testing at the University of Liège [93]; this study has revealed that the wind velocity does not affect the eigen frequency and thus, the stiffness. The derivative A_3^* is therefore negligible. The structural properties are summarised in Table 2.2, and the only remaining flutter derivative of interest, A_2^*, is shown in Figure 2.8(b) as a function of the reduced velocity $V^* = U/fB$. Following the quasi-steady theory, the buffeting forces are described by

$$F_\mathrm{b} = \left(\frac{1}{2}\rho U B \frac{\mathrm{d}C_\mathrm{M}}{\mathrm{d}\theta}\right)^2 S_\mathrm{w}(\omega), \tag{2.36}$$

where $\mathrm{d}C_\mathrm{M}/\mathrm{d}\theta = -0.02$ is the derivative of the moment coefficient with respect to the torsional coordinate θ. This value has been determined with stationary tests on a rigid bridge deck segment mounted on a high frequency force balance at the University of Liège; it is also consistent with the torsional coefficients measured on cantilever bridges under construction [94].

The analysis is repeated for several values of wind velocity up to critical state as shown in Figure 2.9. The superimposed power spectral densities of Figure 2.9(a) are fully centred on 0.18 Hz, showing that no frequency shifting occurs with increasing wind speed, due to the negligible aeroelastic stiffness. Therefore this is an example of pure torsional galloping. Because the scaled damping gradient $\partial_\omega \mathcal{C}(\overline{\omega})\xi_\mathrm{s}\overline{\omega}$ is of order 10^{-3}, its contribution to the transfer function is of order 10^{-6} and can clearly be neglected in front of $\mathcal{O}(\xi_\mathrm{s})$ terms, as it was assumed in (2.20). Again, the background/resonant decomposition provides an excellent estimation of the standard deviation of the torsional coordinate, with a relative error constantly lower than 0.3%. The vertical asymptote in the neighbourhood of the critical regime takes place around 12 m/s, which is also the velocity at which the aeroelastic damping equals the structural damping, see Figure 2.9(d); this is also consistent with available results in the literature [93].

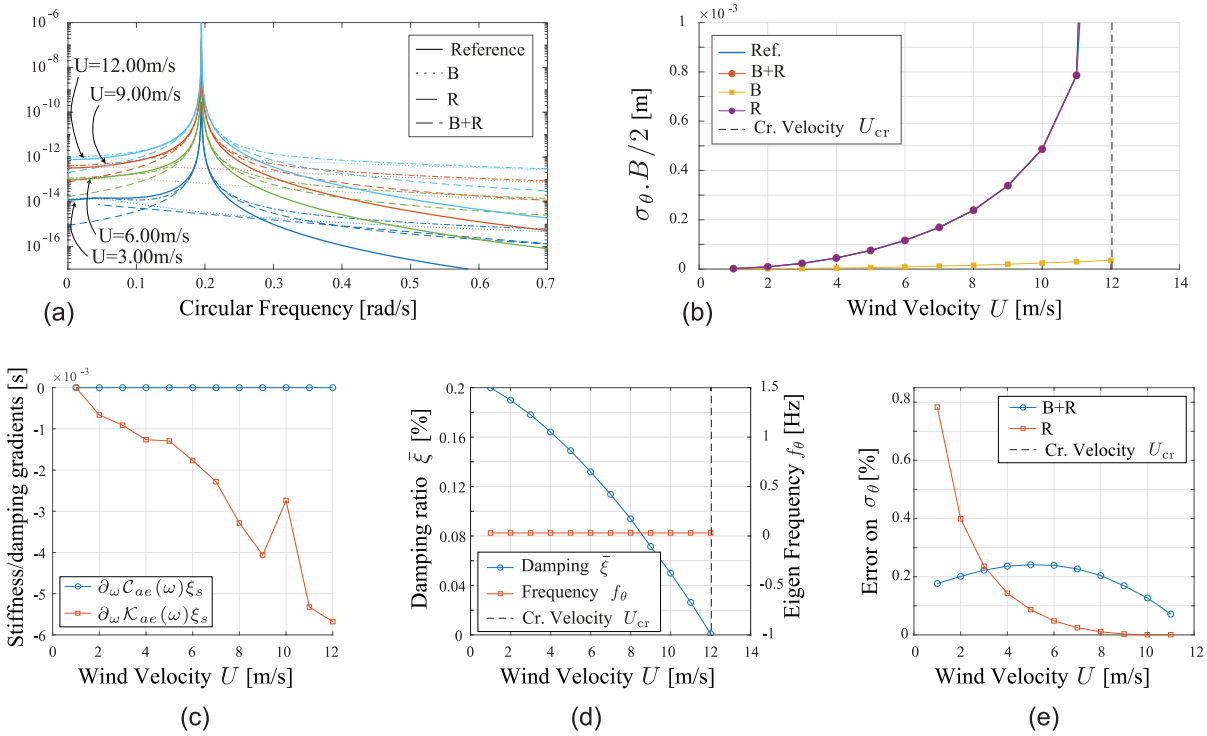

Figure 2.9: Results obtained from background/resonant methods applied to the third illustration (Bosphorus Bridge deck segment). (a) PSD and their approximations for different wind velocities. (b) Scaled standard deviations obtained from background component (B), resonant components (R), and the sum of them (B)+(R). (c) Evolution of scaled aeroelastic stiffness and damping gradients with respect to average wind velocity. (d) Damping ratio at resonance with respect to avg. wind velocity. (e) Error on σ_θ with respect to avg. wind velocity.

2.4 Perspectives on the extension to MDOF models

The successful development of this SDOF model represents a key milestone in establishing a complete methodology for MDOF systems. At this stage, it is useful to assess the efficiency of the method and evaluate its performance in terms of the trade-off between accuracy and computational cost compared to other approaches.

As first discussed in Section 1.6.2, the benefits of the proposed B/R decomposition method become naturally truly significant when applied to MDOF systems. While the computational savings for SDOF models remain relatively modest, the situation changes drastically when multiple modes are involved. In MDOF systems, the computational cost increases not only with the number of wind velocities but also with the number of modes, making the projection of buffeting forces onto the modal basis a major demanding task. This challenge becomes particularly critical when a fine resolution of the transition to instability is required. In the context of a preliminary design, brute-force numerical integration and their important associated computational burden quickly become impractical, reinforcing the interest (semi-)analytical methods such as the B/R decomposition.

In a standard linearized buffeting force model, the wind force at each node is expressed as a linear transformation of the local wind velocity, as given in (1.26). Consequently, the power spectral density (PSD) of the nodal buffeting forces, derived in (1.66), requires a projection of the wind speed PSD matrix $\mathbf{S_u}$ onto the aerodynamic force coefficient matrix $\mathbf{A_u}$. The PSD matrix of the modal forces then involves a double projection —first onto $\mathbf{A_u}$ and then onto the mode shape matrix $\mathbf{\Phi}$— resulting in

$$\mathbf{S}_{\mathbf{F}^*_{\text{bu}}}(\omega) = \mathbf{\Phi}^T \mathbf{A}_u \mathbf{S_u} \mathbf{A}_u^T \mathbf{\Phi}. \tag{2.37}$$

For large systems, where both $\mathbf{A}_u$ and $\mathbf{\Phi}$ can be considerably sizeable, this double projection process significantly increases the computational burden, making the evaluation of the PSD matrix of the modal forces particularly time-consuming.

In short, for large MDOF structures, the computational cost of modal analysis is primarily dictated by the number of frequencies at which the PSD $\mathbf{S}_{\mathbf{F}^*_{\text{bu}}}$ must be sampled—that is, the number of required projections as given in (2.37). Since each projection involves costly matrix operations, a reduction of the number of sampling points directly translates into significant computational savings. Consequently, the number of integration points needed for the evaluation of the modal covariance matrix serves as a useful relative measure of the CPU load required for a full flutter analysis.

With the first aeroelastic oscillator model now established, it becomes possible to compare the computational efficiency of the proposed method to more conventional approaches. To this end, three numerical strategies are explored in the remainder of this section to evaluate these integrals, each offering a different balance between accuracy and computational cost:

- Classical trapezoidal integration: This method applies a uniform discretization over the frequency range and typically requires a large number of points to accurately capture the sharp resonant peaks of the spectrum.
- Adaptive integration: By dynamically adjusting the integration mesh, this approach reduces the number of required points while ensuring accurate peak resolution, thereby mitigating unnecessary computational expense.
- Background/resonant decomposition-based integration: The proposed method leverages an analytical treatment of the background and resonant components, drastically reducing the number of necessary integration points and, in turn, the computational burden.

By comparing these approaches, the objective is to assess the computational efficiency of the background/resonant decomposition and provide and quantitative measure of this computational advantage to be expected when tackling large-scale aeroelastic analyses.

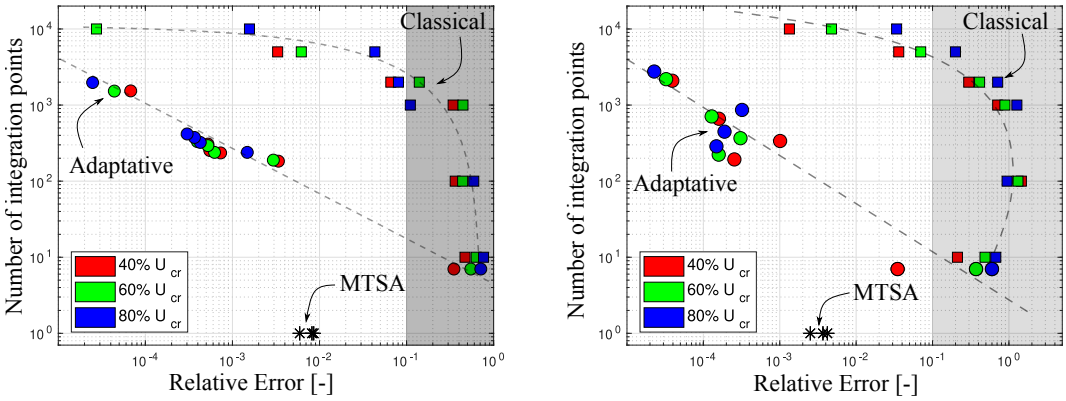

(a) Golden Gate bridge

(b) Tacoma Narrow's bridge

Figure 2.10: Evolution of the number of integration points with the relative error for the three considered methods (classical=trapezoidal).

For this purpose, flutter analyses were re-conduced on the Tacoma Narrow's and Golden Gate bridges presented in Section 2.3.1, using the three previously described integration techniques. The algorithm used for the adaptive integration method is given in Appendix B. The results are presented in Figure 2.10, were the number of integration points required to satisfy a given relative precision is represented for the two usual numerical methods (trapezoidal scheme and adaptative integration) and the MTSA approach. Several dataset of integration parameters have been considered to produce a variation in the relative error which is calculated with respect to a reference solution obtained from a classical trapezoidal integration method with a mesh of 50,000 points uniformly spaced between 0 and 10 Hz (i.e. 62.8 rad/s). For the reference solution, the integration mesh was kept constant for all considered wind speeds, but that used with the adaptive integration method was updated to account for the frequency shift.

The results for the Golden Gate bridge are shown in Figure 2.10(a). The square symbols, associated with the trapezoidal scheme, indicate that this classical integration method requires a minimum of 10,000 integration points to get a relative error of the order of the percent for all wind speeds. For 1,000 points and below, the error is already way too large and the function is not accurately represented. However, with 1,000 points smartly distributed using an adaptive integration method, the standard deviation is accurately calculated with an error lower than 0.01%. A good compromise can be found around 100 points, where the error is of the order of the percent again. This method reduces the number of integration points required by a factor 100, approximatively. The performance of this adaptive integration method is of course conditioned by the efficiency of the refinement algorithm and also by the parameters passed by the user —for instance the initial mesh. Usage of other adaptive integration scheme than the algorithm presented in the Appendix B might therefore lead to similar trends but slightly different numbers. The last cluster of points represented in Figure 2.10 refers to the B/R decomposition (MTSA) and suggests an error below 1% while being limited a single sampling point, at resonance. This method appears now to be incontestably the best compromise number of points/accuracy.

The second case study, the Tacoma Narrow's bridge, behaves very similarly to the Golden Gate bridge such that most of results are globally the same. In Figure 2.10(b), the same tendencies as in the previous applications are observed regarding the relative error. A number of 100 integration points are required to accurately integrate the PSD using an adaptive method, and 10.000 points at least should be used if a uniform mesh is used. The MTSA approach provides accurate standard deviation with an error lower than 0.5%, slightly lower than in the Golden Gate bridge illustration.

2.5 Conclusion on SDOF model

In this chapter, the background/resonant decomposition was extended to the aeroelastic analysis of SDOF systems, where the stiffness and damping of the system changes with frequency and wind speed.

The assumption of a single-degree-of-freedom motion in (2.1) limits the applicability of this model to purely SDOF systems or, to MDOF systems with uncoupled modal responses. In the latter case, the analysis is conducted mode by mode —if multiple modes are excited— where the nodal mass, damping, and stiffness are replaced by their modal homologues.

Important assumptions have been formulated in the establishment of this model. Namely, the clear separation between the buffeting loading and the natural frequencies of the aeroelastic system, a small damping ratio ξ_s, and smoothly varying aeroelastic stiffness and damping. The hypotheses are those required by the Multiple Timescale Spectral Analysis framework, which has been used in this context to derived a closed form expression for the variance of the response expressed as a sum of background and resonant components. It is shown that the background component takes a slightly different form than non aeroelastic formulation [81], since the energy of the buffeting loading is low-pass filtered and not just translated in a quasi-static manner. Also the resonant component assumes a form that is very similar to the classical decomposition, with the differences that the quantities related to the natural frequency of the structural system are moved to the natural frequency of the aeroelastic system and that there is an additional coefficient in the expression, taking care of the possible non negligible change in the aeroelastic stiffness in the neighbourhood of the natural frequency of the aeroelastic system.

The proposed method is tested on three realistic examples. It has shown accurate results with an error lower than 1% in most cases. Torsional galloping is accurately captured since it meets the assumptions of the model; torsional divergence of the flat plate is also well represented but until approximately 90% of the critical wind velocity since the damping ratio is too large beyond that point.

Divergence instabilities in systems with significant background contributions are expected to be difficult to capture with this model due to the necessity of a clear separation between background and resonant timescales. At higher wind speeds, the frequency shift associated with divergence instabilities was found to deteriorate this timescale separation, even when it was well observed in wind-off conditions.

The performance of the B/R decomposition method was assessed through comparative studies, evaluating the trade-off between the number of integration points and accuracy. The results demonstrated that the MTSA method reduced the number of sampling points by a factor of 10,000 compared to classical integration methods and by a factor of 100 compared to a more advanced adaptive integration technique, without compromising the accuracy of the predictions. This significant reduction is highly promising for extending the method to coupled systems.

While the current discussion has been centred on single-degree-of-freedom systems, the true challenge lies in extending these principles to MDOF systems, where modal interactions increase complexity and the computational cost grows with the size of the problem. The promising results obtained in this section will serve as a motivation for extending the current model to MDOF systems, adapted to efficiently handle multi-modal coupling. This naturally leads to the next chapter, which focuses on the role of modal inter-coupling by examining two-degree-of-freedom models. This intermediate step is essential before tackling full MDOF systems, as it allows us to analyse how the background/resonant decomposition performs when multiple modes interact.

Chapter 3

The 2DOF model

In the previous chapter, a first model was derived to predict the aeroelastic behaviour of single-DOF oscillators or uncoupled modal systems. Number of modern large-scale projects are however beyond the scope of application of this model, which remains unable to incorporate the modal coupling induced by aerodynamic loads on bridge decks [38, 95, 96, 97].

This chapter contributes to filling this gap, and improve this formulation by focusing on the effect of modal coupling using a 2 degree-of-freedom model. In the context of aeroelasticity, this model takes most often the form of a pitch-plunge model, which allows to capture the fundamental interaction between bending and torsional modes. This interaction is essential for describing key features of classical flutter instability, where energy exchange between orthogonal modes is the central key to accumulating the wind energy.

After the single-degree-of-freedom model, this 2DOF model constitutes the intermediate step for building the complete and rapid analysis for assessing stability of large-scale structures submitted to aeroelastic and buffeting loading.

Aeroelastic analyses are typically performed in a modal framework, as it provides a natural basis for describing the system's dynamic response and identifying dominant mode interactions. Additionally, working in a modal basis significantly reduces the problem size. Beyond these advantages, the methodology developed in this chapter specifically leverages the modal basis to simplify the equations of motion by minimizing coupling terms. While perfect decoupling occurs in systems with proportional damping, aeroelastic systems exhibit non-proportional damping due to aerodynamic loads, preventing full diagonalization. Despite their relatively smaller order of magnitude when solving the problem in a modal basis, these coupling terms will have to be taken into account.

As it will be formalized later, the modal basis used in this chapter is constructed from the wind-on eigenmodes. Consequently, the structural equations in the modal basis,

$$\left[-\omega^2\mathbf{M}^*(\omega,U)+\mathrm{i}\omega\mathbf{C}^*(\omega,U)+\mathbf{K}^*(\omega,U)\right]\mathbf{Q}(\omega,U)=\mathbf{\Phi}^{\mathsf{T}}\mathbf{F}_{\mathrm{bu}}(\omega,U), \tag{3.1}$$

which were given in (1.74), cannot be further simplified as $\mathbf{\Phi}$ is well dependent of the wind speed U. This choice of wind-on eigenmodes will be in depth discussed together with the construction of the modal basis in Section 3.1. Note that throughout this chapter, the wind speed U will also be treated as an input parameter. To simplify notation, it might also be omitted.

The chapter is structured as follows: In Section 3.1 the modal basis used in this chapter is presented, and the problems associated with the consideration of aeroelastic matrices are discussed. Section 3.2 presents the simplification of the equations for systems with weakly coupled matrices, while Section 3.3 derives the approximate solution using the MTSA method. Section 3.4 summarizes and discusses the developments before applying them to a case study in Section 3.7.

3.1 The modal basis

Starting from the equation of motion in modal basis (3.1), the generalized modal amplitudes $\mathbf{Q}^*(\omega)$ can be expressed by introducing the modal transfer function matrix $\mathbf{H}^*(\omega)$ and the generalized modal buffeting forces $\mathbf{F}^*_{\text{bu}}(\omega)$

$$\mathbf{Q}^*(\omega) = \mathbf{H}^*(\omega)\mathbf{F}^*_{\text{bu}}(\omega). \tag{3.2}$$

with

$$\mathbf{H}^*(\omega) = \left[-\omega^2\mathbf{M}^*(\omega) + \mathrm{i}\omega\mathbf{C}^*(\omega) + \mathbf{K}^*(\omega)\right]^{-1}. \tag{3.3}$$

Because the problem will be entirely solved in the modal basis, the superscript * used to designate modal quantities will be dropped for the sake of clarity.

One of the advantages of using a modal basis in structural dynamics is its ability to uncouple the equations of motion. However, the inclusion of aeroelastic contributions to the stiffness and damping matrices introduces several problems:

- **Problem #1:** Aeroelastic matrices are neither symmetric nor Hermitian.
- **Problem #2:** Aerodynamic damping does not follow the proportional damping assumption.
- **Problem #3:** Aeroelastic matrices depend on the wind speed in a parametric manner
- **Problem #4:** Aeroelastic matrices are frequency-dependent in the unsteady loading model.

The following section examines these issues in detail and outlines the approach adopted in this Thesis to address them.

3.1.1 Problem # 1: Asymmetric aeroelastic matrices

The asymmetry of the aeroelastic matrices can be addressed by introducing left and right eigenvectors [98]. In linear algebra, the left eigenvector $\mathbf{u}_i$ and the right eigenvector $\mathbf{v}_i$ corresponding to the i-th eigenvalue λ_i of a general non-Hermitian complex matrix $\mathbf{A}$ are defined as the solutions of

$$\mathbf{u}_i^{\mathsf{T}}\mathbf{A} = \lambda_i\mathbf{u}_i^{\mathsf{T}}, \tag{3.4a}$$

$$\mathbf{A}\mathbf{v}_i = \lambda_i\mathbf{v}_i. \tag{3.4b}$$

Since transposition does not affect the eigenvalues of a matrix, the left eigenvectors of $\mathbf{A}$ can be characterized as the conjugate right eigenvectors of the conjugate-transposed matrix $\mathbf{A}^*$. Indeed, conjugating and transposing (3.4a),

$$\mathbf{A}^*\overline{\mathbf{u}}_i = \overline{\lambda}_i\overline{\mathbf{u}}_i, \tag{3.5}$$

and noting that the eigenvalues of a Hermitian matrix are real, we conclude that $\overline{\mathbf{u}}_i = \mathbf{v}_i$ by comparing (3.4b) and (3.5). In the particular case of real symmetric matrices, the same reasoning shows that the left and right eigenvectors are identical.

The interest of left and right eigenvectors lies in their biorthogonality property [99]. Postmultiplying (3.4a) by $\mathbf{v}_j$ and premultiplying (3.4b), rewritten $\mathbf{A}\mathbf{v}_j = \lambda_j\mathbf{v}_j$, by $\mathbf{u}_i^{\mathsf{T}}$ and subtracting the equations gives

$$(\lambda_i - \lambda_j)\mathbf{u}_i^{\mathsf{T}}\mathbf{v}_j = 0. \tag{3.6}$$

If $\lambda_i \neq \lambda_j$, this equation establishes the biorthogonality relation between $\mathbf{u}_i$ and $\mathbf{v}_i$, expressing that the left and right eigenvectors respectively related to distinct eigenvalues λ_i and λ_j are mutually orthogonal. However, there is no orthogonality between $\mathbf{u}_i$ and $\mathbf{u}_j$, nor between $\mathbf{v}_i$

and $\mathbf{v}_j$. This implies that the left and right eigenvectors are not mutually orthogonal between themselves.

In the case of real symmetric matrices ($\mathbf{v}_i = \mathbf{u}_i$) or complex hermitian matrices ($\mathbf{v}_i = \overline{\mathbf{u}}_i$), this equation degenerates into $\mathbf{u}_i^{\mathsf{T}}\mathbf{u}_j = 0$ and $\mathbf{u}_i^{*}\mathbf{u}_j = 0$, when $\lambda_j \neq \lambda_i$. In this case, the biorthogonality property degenerates into the usual orthogonality property: all the modes corresponding to distinct eigenvalues are mutually orthogonal. This is precisely that property that allows to diagonalize the symmetric modal matrix in classical dynamics of structures. Biorthogonality then applies to general matrices, while orthogonality applies to symmetric or hermitian matrices.

Formally written, the biorthogonality relation (3.6) is translated for all modes by introducing a diagonal matrix $\mathbf{D}$,

$$\mathbf{U}^{\mathsf{T}}\mathbf{V} = \mathbf{D} \tag{3.7}$$

with $\mathbf{U} = \begin{bmatrix}\mathbf{u}_1 & \dots & \mathbf{u}_m\end{bmatrix}$ and $\mathbf{V} = \begin{bmatrix}\mathbf{v}_1 & \dots & \mathbf{v}_m\end{bmatrix}$ are the eigenmode matrices, left and right respectively. This relation remains valid for any general matrix with nondegenerate eigenvalues. The left and right eigenvectors are sometimes normalized such that $\mathbf{D}$ is equal to the identity matrix, in which case $\mathbf{U}$ and $\mathbf{V}$ are said to be biorthonormal, $\mathbf{U}^{\mathsf{T}}\mathbf{V} = \mathbb{I}$, but nothing prevents to use any other convention to normalize the left and right eigenvectors independently. Expressing the definition of right eigenvalue problem (3.4b) for all modes

$$\mathbf{A}\mathbf{V} = \mathbf{V}\mathbf{\Lambda}. \tag{3.8}$$

where $\mathbf{\Lambda} = \operatorname{diag}(\lambda_1, \dots, \lambda_m)$ is a diagonal matrix gathering the nondegenerate eigenvalues of $\mathbf{A}$. Multiplying by $\mathbf{U}^{\mathsf{T}}$ gives

$$\mathbf{U}^{\mathsf{T}}\mathbf{A}\mathbf{V} = \mathbf{U}^{\mathsf{T}}\mathbf{V}\mathbf{\Lambda} = \mathbf{D}\mathbf{\Lambda} \tag{3.9}$$

where the right-hand side is a diagonal matrix because both $\mathbf{\Lambda}$ and $\mathbf{D}$ are diagonal. Hence, thanks to the biorthogonality for $\mathbf{U}$ and $\mathbf{V}$, a diagonal form was found for $\mathbf{A}$ by projecting it onto $\mathbf{U}$ and $\mathbf{V}$.

In structural dynamics, the above theory can be used considering eigenvalue problem with $\lambda = \omega^2$. A common approach for constituting a modal basis is to use the mode shapes of the undamped system, in which case the left and right eigenvectors are obtained by solving

$$\left[\mathbf{K} - \omega_i^2\mathbf{M}\right]\boldsymbol{\phi}_i^R = \mathbf{0}, \tag{3.10a}$$

$$\boldsymbol{\phi}_i^{L,\mathsf{T}}\left[\mathbf{K} - \omega_i^2\mathbf{M}\right] = \mathbf{0}. \tag{3.10b}$$

To keep it simple at this stage, the nodal matrices of mass, damping and stiffness are assumed to be constant: the problem associated with the frequency-dependence of these matrices and its consequence on the diagonality will be discussed later in Section 3.1.3. The solution of (3.10) leads to the complete set of solutions $(\omega_i, \boldsymbol{\phi}_i^R, \boldsymbol{\phi}_i^L)$ with $i = 1, \dots, M$ corresponding to the M mode shapes of the system. The structural matrices are then projected into the modal basis formed by the right and left eigenvectors, which are assembled in the column-ordered matrices $\mathbf{\Phi}^R$ and $\mathbf{\Phi}^L$. This projection results in the modal matrices

$$\mathbf{K}^* = \mathbf{\Phi}^{L,\mathsf{T}}\mathbf{K}\mathbf{\Phi}^R, \quad \mathbf{C}^* = \mathbf{\Phi}^{L,\mathsf{T}}\mathbf{C}\mathbf{\Phi}^R, \quad \mathbf{M}^* = \mathbf{\Phi}^{L,\mathsf{T}}\mathbf{M}\mathbf{\Phi}^R. \tag{3.11}$$

The biorthogonality conditions can be demonstrated in a similar manner in this context. Premultiplying (3.10a), rewritten $\left[\mathbf{K} - \omega_j^2\mathbf{M}\right]\boldsymbol{\phi}_j^R = \mathbf{0}$, by $\boldsymbol{\phi}_i^{L,\mathsf{T}}$

$$\boldsymbol{\phi}_i^{L,\mathsf{T}}\mathbf{K}\boldsymbol{\phi}_j^R = \omega_j^2\boldsymbol{\phi}_i^{L,\mathsf{T}}\mathbf{M}\boldsymbol{\phi}_j^R \tag{3.12}$$

and postmultiplying (3.10b) by $\boldsymbol{\phi}_j^R$

$$\boldsymbol{\phi}_i^{L,\mathsf{T}}\mathbf{K}\boldsymbol{\phi}_j^R = \omega_i^2\boldsymbol{\phi}_i^{L,\mathsf{T}}\mathbf{M}\boldsymbol{\phi}_j^R. \tag{3.13}$$

Subtracting (3.13) to (3.12) yields

$$(\omega_i^2 - \omega_j^2)\boldsymbol{\phi}_i^{L,\mathsf{T}}\mathbf{M}\boldsymbol{\phi}_j^R = 0 \tag{3.14}$$

For nondegenerate eigenvalues the following biothogonality conditions are observed

$$\boldsymbol{\phi}_i^{L,\mathsf{T}}\mathbf{M}\boldsymbol{\phi}_j^R = 0 \qquad \text{and} \qquad \boldsymbol{\phi}_i^{L,\mathsf{T}}\mathbf{K}\boldsymbol{\phi}_j^R = 0. \tag{3.15}$$

The biorthogonality property in this modal basis is such that each column of the right eigenvector matrix $\boldsymbol{\Phi}^R$ is orthogonal, in the metric of the mass and stiffness matrices, to all columns of left eigenvector matrix $\boldsymbol{\Phi}^L$, excepted to its corresponding one. Consequently, if $\mathbf{K}^*$ and/or $\mathbf{M}^*$ are non-symmetric matrices with constant coefficients and have nondegenerate eigenvalues, their projections $\mathbf{K}$ and $\mathbf{M}$ become diagonal when using such an undamped modal basis. Moreover, if the damping is proportional to the mass and stiffness matrices, the resulting modal damping matrix $\mathbf{C}^*$ is also diagonal, leading to a fully uncoupled system of equations of motion.

Using two sets of eigenmodes instead of a single one effectively doubles the computational effort required to construct the modal basis. However, this additional cost is necessary for achieving simultaneous diagonalization of any undamped system characterized by constant, non-symmetric mass and stiffness matrices with nondegenerate eigenvalues and subjected to proportional damping.

3.1.2 Problem #2: the non-proportional damping

The second problem introduced by aeroelastic forces in the constitution of a modal basis reside in the aeroelastic damping, which is inherently not proportional. As a result, the modal basis constructed from the undamped dynamic system is unable to diagonalize the damping matrix, preventing a full decoupling of the equations of motion. In a standard approach, where PSD are numerically integrated to obtain covariance matrices, this is not a real limitation. However in the approach used in the following, it is necessary to keep coupling terms in the modal basis as low as possible. To address this issue, one possible approach is to construct the modal basis directly from the damped system.

A common strategy for achieving this diagonalization is the formulation of the equations of motion in state-space representation. This approach has been successfully applied in various fields, including hydro-mechanically loaded floating structures, where damping primarily originates from added mass effects and is similarly non-proportional [85], but also in bridge flutter analysis [95]. The key idea is to transform the second-order system (1.12) into a first-order system by introducing the trivial identity $\dot{\mathbf{x}} = \dot{\mathbf{x}}$, leading to the following augmented formulation:

$$\begin{bmatrix} \mathbf{I} & \mathbf{0} \\ \mathbf{C} & \mathbf{M} \end{bmatrix} \begin{bmatrix} \dot{\mathbf{x}} \\ \ddot{\mathbf{x}} \end{bmatrix} + \begin{bmatrix} \mathbf{0} & \mathbf{I} \\ \mathbf{K} & \mathbf{0} \end{bmatrix} \begin{bmatrix} \mathbf{x} \\ \dot{\mathbf{x}} \end{bmatrix} = \begin{bmatrix} \mathbf{0} \\ \mathbf{f}_{\text{bu}} + \mathbf{f}_{\text{se}} \end{bmatrix} \tag{3.16}$$

By introducing the state-space modal coordinates $\mathbf{q} = \begin{bmatrix} \mathbf{x}^\mathsf{T}, & \dot{\mathbf{x}}^\mathsf{T} \end{bmatrix}^\mathsf{T}$, the system takes the compact first-order form:

$$\mathbf{A}\dot{\mathbf{q}} + \mathbf{B}\mathbf{q} = \mathbf{0}. \tag{3.17}$$

This formulation is structurally identical to the eigenvalue problem in (3.10), meaning that the same process used to construct a modal basis can be applied here. As a result, the projection of the system matrices $\mathbf{A}$ and $\mathbf{B}$ into the state-space modal basis leads to a diagonalized representation. This state-space approach provides a general framework for performing modal analysis in non-proportionally damped systems and is widely used in structural dynamics of systems characterized by fluid-structure interaction, concentrated energy dissipative system such TMD, and gyroscopic effects [100]. The system has two disadvantages: the use of a state-space modal basis results in the introduction of additional states, and the physical insight that is so highly

regarded when considering the undamped modal basis is immediately lost. While the vertical displacement shape of a mode remains easy to interpret, its first derivative—associated with the velocity field— offers indeed a less intuitive physical description.

The developments presented in this work aim to enable the rapid and straightforward evaluation of buffeting response as a function of wind speed U. Since the intended users are design engineers, it is essential to preserve a clear physical interpretation throughout the process. To maintain this interpretability, a different strategy, retaining the physical meaning of the initial modal basis, is adopted. Instead of reformulating the problem in state-space form as in equation (3.16), the eigenmodes of the damped eigenvalue problem will be considered. The damped eigenvalue problem is directly solved for the complex eigenvalues λ_i and their associated right eigenvectors $\boldsymbol{\phi}_i^R$

$$\left[\lambda_i^2\mathbf{M} + \lambda_i\mathbf{C} + \mathbf{K}\right]\boldsymbol{\phi}_i^R = \mathbf{0}. \tag{3.18}$$

Similarly, the left eigenvectors $\boldsymbol{\phi}_i^L$ are obtained by solving:

$$\boldsymbol{\phi}_i^{L,\mathsf{T}}\left[\lambda_i^2\mathbf{M} + \lambda_i\mathbf{C} + \mathbf{K}\right] = \mathbf{0}. \tag{3.19}$$

Each eigen triplet $(\lambda_i, \boldsymbol{\phi}_i^R, \boldsymbol{\phi}_i^L)$ characterizes a vibration mode. Both the eigenvalues λ_i and modes $\boldsymbol{\Phi}_i^R$, $\boldsymbol{\Phi}_i^L$ are complex quantities. The damped natural frequency is given by

$$\omega_i = \Im(\lambda_i), \tag{3.20}$$

while the modal damping ratio is obtained as

$$\xi_i = \frac{\Re(\lambda_i)}{|\lambda_i|}. \tag{3.21}$$

Pre-multiplying (3.18) by $\boldsymbol{\phi}_j^{L,\mathsf{T}}$ and post-multiplying (3.19), where j is used instead of i, by $\boldsymbol{\phi}_i^R$, then subtracting the equations yields

$$(\lambda_i^2 - \lambda_j^2)\boldsymbol{\phi}_j^{L,\mathsf{T}}\mathbf{M}\boldsymbol{\phi}_i^R + (\lambda_i - \lambda_j)\boldsymbol{\phi}_j^{L,\mathsf{T}}\mathbf{C}\boldsymbol{\phi}_i^R = \mathbf{0}. \tag{3.22}$$

If $i \neq j$, this equation can be simplified as follows,

$$(\lambda_i + \lambda_j)\boldsymbol{\phi}_j^{L,\mathsf{T}}\mathbf{M}\boldsymbol{\phi}_i^R + \boldsymbol{\phi}_j^{L,\mathsf{T}}\mathbf{C}\boldsymbol{\phi}_i^R = \mathbf{0}. \tag{3.23}$$

This equation cannot be further simplified. While the (bi)orthogonality property of undamped mode shapes allows for the diagonalization of the mass and stiffness matrices, the use of damped mode shapes does not enable the simultaneous diagonalization of the mass, damping, and stiffness matrices. However, adopting a damped modal basis still provides a key advantage: the equations of motion are lightly coupled. Intuitively, it would indeed not be surprising that the consideration of the damping when determining the mode shapes of the modal basis adds an important information regarding the equations of motion. We will see how this almost diagonal form can be used to evaluate the FRF matrix. This idea of complex eigenmodes basis was already investigated by [101] but orthogonality with respect to mass and stiffness matrices was observed by neglecting the damping matrix.

The main drawback of this damped basis is the increased computational effort required to construct the modal basis, as it now involves complex eigenvalues and complex eigenmodes. This also doubles the size of the generalized eigenvalue problem.

The developments presented here assume constant matrices $\mathbf{M}$, $\mathbf{C}$, and $\mathbf{K}$. In aeroelasticity, however, these matrices are frequency-dependent, introducing an additional complexity addressed in the next section.

3.1.3 Problem #3: Frequency-dependent properties

In general for aeroelastic systems, the eigenvalue problems (3.19) and (3.18) are non-polynomial. The nonlinearity of the problem originates from the quadratic λ term, but also from the frequency-dependence of both the stiffness, damping and mass matrices $\mathbf{K}(\omega)$, $\mathbf{C}(\omega)$ and $\mathbf{M}(\omega)$, that are most often defined by means of flutter derivatives, which are inherently frequency-dependent

$$\left[\lambda^2\mathbf{M}(\lambda) + \lambda\mathbf{C}(\lambda) + \mathbf{K}(\lambda)\right]\boldsymbol{\phi}^R = \mathbf{0} \tag{3.24}$$

$$\boldsymbol{\phi}^{L,\mathsf{T}}\left[\lambda^2\mathbf{M}(\lambda) + \lambda\mathbf{C}(\lambda) + \mathbf{K}(\lambda)\right] = \mathbf{0}. \tag{3.25}$$

Therefore, this problem may be characterized as a quadratic eigenvalue problem with frequency-dependent coefficient. If the solution of a quadratic eigenvalue problem with constant coefficient is quite straightforward using the augmented state-space formulation detailed in Section 3.1.2, the solution of a system with frequency-dependent properties is more complicated. An option is to recourse to augmented aeroelastic states, which is possible when flutter derivatives can be represented as rational fractions [51]. A more general framework is considered here and a more general approach requiring an iterative procedure is needed.

Focusing for instance on the i-th mode, the aeroelastic matrices are first evaluated at the corresponding natural frequency, as an initial guess. The eigenvalue problem is then solved for $(\lambda_i, \boldsymbol{\phi}_i^R, \boldsymbol{\phi}_i^L)$, and a new frequency is evaluated from λ_i. This new frequency is then used to evaluate the aeroelastic matrices and a new frequency is determined. The iterations are repeated until convergence *i.e.* (3.24) and (3.25) are verified up to desired accuracy. At this time, one mode has been treated. This process is carried out to treat all the modes consecutively. At the end, M distinct eigenvalues are determined.

The frequency-dependence of the coefficients in the quadratic eigenvalue problem presents a fundamental challenge: equation (3.24) can only be satisfied on a mode-by-mode basis, as the aeroelastic matrices are evaluated at a single frequency at a time. When (3.24) holds for mode i, the aeroelastic matrices are computed at λ_i. However, if the (i, j) element of the modal projection represents the interaction between two modes i and j, it is unclear which eigenvalue should be used to evaluate the aeroelastic matrices.

Unfortunately, this issue cannot be mitigated through adjustments to the modal basis itself. One thing is sure, the frequency-dependence nature of the aeroelastic matrices makes that it exists no modal basis for which the equation of motion can be diagonalized.

3.1.4 Problem #4: Speed-dependent properties

The aeroelastic matrices are speed-dependent, and so are the system matrices, and the eigenvalues and eigenvectors. To take the benefits from the nearly diagonal form proposed by the consideration of the above presented modal basis, the eigenmodes must be updated at each wind speed. They form a different basis for each wind velocity which is called the wind-on modal basis, by opposition to the wind-off modal basis that is constituted without considering the aeroelastic effects.

The quasi-diagonal form of the projected dynamic flexibility matrix is however not completely altered if the exact eigenvectors corresponding to the considered wind speed are not used. Indeed, since the perfect diagonalization is anyway not possible, small variations of the eigenmodes with respect to their actual values should not consequently affect the quasi-diagonal shape of the matrix. For this reason, the eigenvectors used in the modal basis may be approximated, and for instance evaluated by interpolation on a pre-calculated mesh.

Therefore, prior to the buffeting analysis, the eigenmodes are calculated for a set of chosen wind speeds. The eigenmodes are interpolated on this grid. When constituting the interpolation grid, the eigenmodes can be evaluated at the same time with the aeroelastic eigenfrequencies and damping, which must be observed to characterize the aeroelastic behaviour prior to critical

speed. The critical system (3.24) is then be solved anyway for (λ_i), so the determination of the associated eigenmode $\boldsymbol{\phi}_i^R$ can be carried out for free at the same time. The process, aiming at determining the speed-dependent modal properties of the system will be referred to as pre-flutter analysis in this Thesis. It will be the topic of Chapter 5 where an arc-length continuation based algorithm will be presented. By now, it is assumed that the wind-on basis can be obtained for any desired wind velocity.

3.1.5 Summary

The last four sections have introduced several modal bases, including the wind-off undamped and damped modal bases, with and without left eigenvectors, as well as wind-on modal bases. These alternatives have been explored to improve the classical wind-off undamped modal basis, as they offer particular advantages in addressing the specific properties of aeroelastic matrices, which are generally nonsymmetric, speed-dependent, and frequency-dependent. The primary motivation behind examining multiple modal bases is to achieve the most diagonalized form of the equations of motion, thereby facilitating the application of the methodology developed in this Thesis.

While these refinements are not strictly necessary for the method to function, they provide an optimal framework for its implementation. At this stage, it is sufficient to acknowledge that the problem is formulated in a modal basis and that different choices can enhance the representation of the equations of motion. The selection of the most suitable modal basis will be further examined in Section 3.6.1 and revisited in Chapter 4.

Regardless of the chosen modal basis, it is crucial to recognize that the modal bases used in this particular context differ in several key aspects from those commonly used in classical structural dynamics. Notably, it should be emphasized that

- The classical orthogonalization property between two different eigen modes is no more observed as soon as frequency-dependent matrices are considered. This means that $K_{ij}^*(\omega) = \boldsymbol{\phi}_i^{L,T}\mathbf{K}(\omega)\boldsymbol{\phi}_j^R \neq 0$ and $M_{ij}^*(\omega) = \boldsymbol{\phi}_i^{L,T}\mathbf{M}(\omega)\boldsymbol{\phi}_j^R \neq 0$ are no longer diagonal, even if $\omega = \omega_i$ or $\omega = \omega_j$.

- However, in the sequel, we will assume that the off-diagonal elements $\boldsymbol{\phi}_i^{L,T}\mathbf{M}(\omega_i)\boldsymbol{\phi}_j^L$, $\boldsymbol{\phi}_i^{L,T}\mathbf{K}(\omega_i)\boldsymbol{\phi}_j^L$ and $\boldsymbol{\phi}_i^{L,T}\mathbf{C}(\omega_i)\boldsymbol{\phi}_j^L$ are assumed to remain small compared to the diagonal elements. This assumption is referred to a *small coupling assumption*.

- The following statement is always observed

$$\boldsymbol{\phi}_i^{L,\mathsf{T}}\left[-\omega_i^2 M_{ii}(\omega_i) + \mathrm{i}\omega_i C_{ii}(\omega_i) + K_{ii}(\omega_i)\right]\boldsymbol{\phi}_i^R = 0. \tag{3.26}$$

  Its proof is left for Appendix C.2.

The small coupling assumption introduced earlier is a direct consequence of the modal projection of the equations of motion. Using a modal basis is essential, as a diagonal form cannot be obtained in a nodal basis. A well-chosen modal basis provides a significant advantage, as we will see that the degree of diagonality of $\mathbf{M}^*(\omega)$, $\mathbf{C}^*(\omega)$ and $\mathbf{K}^*(\omega)$ in the neighbourhood of ω_i and ω_j directly affects the accuracy of the method.

3.2 The small modal coupling assumption

In the modal basis, the power spectral density matrix of the response processes reads

$$\mathbf{S}_q(\omega) = \mathbf{H}(\omega)\,\mathbf{S}_p(\omega)\,\overline{\mathbf{H}}^T(\omega) \tag{3.27}$$

where $\mathbf{S}_p(\omega)$ is the power spectral density matrix of generalized forces $\mathbf{S}_p(\omega) = \mathbf{\Phi}_L^{\mathsf{T}} \mathbf{S}_{F_{\text{bu}}}(\omega) \mathbf{\Phi}_L$ and $\mathbf{H}(\omega)$ is the modal transfer function matrix defined in (3.3). We also define the dynamic flexibility

$$\mathbf{J}(\omega) = \mathbf{H}^{-1}(\omega) = \mathbf{K}(\omega) + \mathrm{i}\omega\mathbf{C}(\omega) - \omega^2\mathbf{M}(\omega). \tag{3.28}$$

Under the small coupling assumption, the structural matrices can be split into their leading diagonal elements and their small off-diagonal coupling terms

$$\begin{aligned} \mathbf{K}(\omega) &= \mathbf{K}_d(\omega) + \mathbf{K}_o(\omega) \\ \mathbf{C}(\omega) &= \mathbf{C}_d(\omega) + \mathbf{C}_o(\omega) \\ \mathbf{M}(\omega) &= \mathbf{M}_d(\omega) + \mathbf{M}_o(\omega) \end{aligned} \tag{3.29}$$

where the $_d$ subscript indicates diagonal matrices and the $_o$ subscript indicates matrices with zeros on the diagonal — i.e. obtained by subtracting $\mathbf{K}_d$ to $\mathbf{K}$. The same applies for the dynamic flexibility that reads

$$\mathbf{J}(\omega) = \mathbf{J}_d(\omega) + \mathbf{J}_o(\omega) \tag{3.30}$$

where

$$\mathbf{J}_d(\omega) = \mathbf{K}_d(\omega) + \mathrm{i}\omega\mathbf{C}_d(\omega) - \omega^2\mathbf{M}_d(\omega) \tag{3.31}$$

and

$$\mathbf{J}_o(\omega) = \mathbf{K}_o(\omega) + \mathrm{i}\omega\mathbf{C}_o(\omega) - \omega^2\mathbf{M}_o(\omega). \tag{3.32}$$

The modal coupling is quantified by the relative magnitude of the coupling matrix $\mathbf{J}_o(\omega)$ with respect to the diagonal matrix $\mathbf{J}_d(\omega)$. For slightly coupled systems, a first order approximation of the transfer matrix was proposed in [79], which avoids inversion of a full matrix,

$$\mathbf{H}(\omega) \simeq \mathbf{H}_d(\omega) - \mathbf{H}_d(\omega)\mathbf{J}_o(\omega)\mathbf{H}_d(\omega) = \mathbf{H}_d(\omega)(\mathbf{I} - \mathbf{J}_o(\omega)\mathbf{H}_d(\omega)) \tag{3.33}$$

where $\mathbf{H}_d(\omega) = \mathbf{J}_d^{-1}(\omega)$. The proof of this is detailed in Appendix C.1. This approximation states that the transfer matrix $\mathbf{H}(\omega)$ is equal to the diagonal transfer matrix $\mathbf{H}_d(\omega)$ that would have been obtained by assuming the uncoupled system, plus a correction $-\mathbf{H}_d(\omega)\mathbf{J}_o(\omega)\mathbf{H}_d(\omega)$ that introduces the effect of coupling through the off-diagonal terms gathered in $\mathbf{J}_o(\omega)$. This correction constitutes the first order correction in the series expansion of $\mathbf{H}(\omega)$ for small out-of-diagonal elements. It is noticed that this formulation for $\mathbf{H}(\omega)$ does not require any full matrix inversion. Indeed, $\mathbf{H}_d(\omega)$ is the only matrix to be inverted, but this matrix is diagonal which significantly reduces the computational burden. In this case, we have the diagonal terms

$$H_{d,i}(\omega) = \left[K_{d,i}(\omega) + \mathrm{i}\omega C_{d,i}(\omega) - \omega^2 M_{d,i}(\omega)\right]^{-1} \tag{3.34}$$

and all other terms of $\mathbf{H}_d(\omega)$ are strictly equal to zero. Besides, it offers a simple understanding of the coupled response as a product of two transfer matrices and a coupling matrix $\mathbf{J}_o(\omega)$.

Equation (3.33) relies on the single assumption that $\mathbf{J}(\omega)$ is slightly coupled and remains accurate as long as this hypothesis is verified, even if no quantitative characterization of the matrix coupling rate has been provided so far. This is left for Appendix C.1, where the spectral radius of the matrix $\mathbf{H}_d\mathbf{J}_o$ is proven to be a trustful scalar characterization of the matrix coupling,

$$\rho(\mathbf{J}) = \max_i \left[\, |\mathrm{eig}(\mathbf{H}_d\mathbf{J}_o)| \,\right]. \tag{3.35}$$

This indicator $\rho(\mathbf{J})$ will be referred to as *diagonality index* of $\mathbf{J}(\omega)$, and can be seen as an order of magnitude of the upper bound error committed when truncating the series expansion (3.33) at first order [102]. Because $\mathbf{J}(\omega)$ is a function of ω, the diagonality index is itself a functional of ω.

The substitution of the first order approximation of the transfer function (3.33) into the power spectral density matrix (3.27) yields

$$\mathbf{S}_q(\omega) \simeq \mathbf{H}_d(\omega)\left(\mathbf{I} - \mathbf{J}_o(\omega)\,\mathbf{H}_d(\omega)\right)\mathbf{S}_p(\omega)\left(\mathbf{I} - \overline{\mathbf{H}}_d(\omega)\,\overline{\mathbf{J}}_o^T(\omega)\right)\overline{\mathbf{H}}_d(\omega). \tag{3.36}$$

Expanding the right hand side leads to

$$\mathbf{S}_q(\omega) \simeq \mathbf{S}_q^{\mathrm{I}}(\omega) + \mathbf{S}_q^{\mathrm{II}}(\omega) + \overline{\mathbf{S}_q^{\mathrm{II}}}^{\mathsf{T}}(\omega) + \mathbf{S}_q^{\mathrm{III}}(\omega) \tag{3.37}$$

with

$$\left|\begin{array}{ll} \mathbf{S}_q^{\mathrm{I}}(\omega) & = \mathbf{H}_d(\omega)\,\mathbf{S}_p(\omega)\,\overline{\mathbf{H}}_d(\omega) \\ \mathbf{S}_q^{\mathrm{II}}(\omega) & = -\mathbf{H}_d(\omega)\,\mathbf{J}_o(\omega)\,\mathbf{S}_q^{\mathrm{I}} \\ \mathbf{S}_q^{\mathrm{III}}(\omega) & = \mathbf{H}_d(\omega)\,\mathbf{J}_o(\omega)\,\mathbf{S}_q^{\mathrm{I}}\overline{\mathbf{J}}_o^T(\omega)\,\overline{\mathbf{H}}_d(\omega) = -\mathbf{S}_q^{\mathrm{II}}\overline{\mathbf{J}}_o^T(\omega)\,\overline{\mathbf{H}}_d(\omega). \end{array}\right. \tag{3.38}$$

This expression shows that an approximate solution for the power spectral density matrix of the modal response can be calculated without any full matrix inversion, based on $\mathbf{H}_d$, $\mathbf{J}_o$ and $\mathbf{S}_p(\omega)$ only. The single assumption used so far is the first order expansion of the transfer matrix $\mathbf{H}(\omega)$ proposed in (3.33), which is supported by the small coupling approximation. Intuitively, because the flexibility matrix $\mathbf{J}(\omega)$ is mostly diagonal, the product of $\mathbf{H}_d\mathbf{J}_o$ is small compared to $\mathbf{H}_d^2$. It is therefore tempting to drop the last three terms of (3.37). A more rigorous approach based on perturbations methods presented in Appendix C.1.1 shows that only the last term is significantly smaller than the others and can therefore be dropped. Furthermore, to close this section, the following expression is held for (3.37)

$$\mathbf{S}_q(\omega) \triangleq \mathbf{S}_q^{\mathrm{I}}(\omega) + \mathbf{S}_q^{\mathrm{II}}(\omega) + \overline{\mathbf{S}_q^{\mathrm{II}}}^{\mathsf{T}}(\omega). \tag{3.39}$$

3.3 Multiple Timescale Approximation

This section is dedicated to the derivation of the background and resonant components of the response power spectral density, and contains therefore exclusively the mathematical developments. We invite the reader to refer to Section 3.4 where some intermediate results are schematically illustrated.

As previously introduced, the Multiple Timescale Spectral Analysis is a technique used to derive approximations to solutions of perturbed problems. It consists physically in separating two —or more— phenomena of well separated timescales. In the present case, wind turbulence and dynamics of the structure define still respectively the low and high frequency phenomena. This hypothesis of separated timescales is used to derive local approximations of the power spectral densities in the low and higher frequency ranges. So far, the concept is identical to the methodology developed in Chapter 2.

The output power spectral densities are split into two contributions: the background $\mathbf{S}_q^B(\omega)$ and resonant $\mathbf{S}_q^R(\omega)$ components

$$\mathbf{S}_q(\omega) \simeq \mathbf{S}_q^B(\omega) + \mathbf{S}_q^R(\omega). \tag{3.40}$$

Consequently, after integration, the variance of the response reads

$$\mathbf{\Sigma}_q \simeq \mathbf{\Sigma}_q^B + \mathbf{\Sigma}_q^R. \tag{3.41}$$

In the next sections the derivation of the two contributions $\mathbf{\Sigma}_{q,B}$ and $\mathbf{\Sigma}_{q,R}$ to the variance of the system are presented separately.

3.3.1 Derivation of the background component

Starting from (3.39) and substituting approximations for $\mathbf{H}_d(\omega)$ in the vicinity of the origin —i.e. at much lower frequencies than those associated to the resonant peaks— defines a rather smooth function of ω representing the background component of the structural response. An approximate expression is first found for $\mathbf{H}_d(\omega)$ starting from (3.34) and introducing the eigen frequency of the uncoupled system $\omega_{d,i}^2 = K_{d,i}/M_{d,i}$

$$H_{d,i}(\omega) = \frac{1}{K_{d,i}(\omega)} \left[1 + 2\mathrm{i}\xi_{d,i}(\omega)\frac{\omega}{\omega_{d,i}} - \frac{\omega^2}{\omega_{d,i}^2} \right]^{-1} \tag{3.42}$$

with $\xi_{d,i}(\omega) = C_{d,i}(\omega)/(2\sqrt{K_{d,i}(\omega)M_{d,i}(\omega)})$ referring to the damping ratio in the i-th mode assuming an uncoupled behaviour. The background response constitutes the response of the system in the very low frequency range, in the neighbourhood of the centroid of the power spectral density of the excitation, that is where $\omega \ll \omega_{d,i}$. Under this hypothesis, the diagonal FRF matrix and the off diagonal dynamic flexibility take quite simple expressions

$$H_{d,i}(\omega) = K_{d,i}^{-1}(\omega) \quad ; \quad J_{o,ij}(\omega) = K_{o,ij}(\omega). \tag{3.43}$$

These two equations are substituted in (3.38) to build the background component of the response PSD. The first term of (3.38) reads

$$S_{q,ij}^{B,\mathrm{I}}(\omega) = H_{d,i}(\omega)\, S_{p,ij}(\omega)\, \overline{H}_{d,j}(\omega) \simeq \frac{S_{p,ij}(\omega)}{K_{d,i}(\omega)K_{d,j}(\omega)}. \tag{3.44}$$

This expression cannot be further simplified as this requires the knowledge of the aeroelastic stiffness $\mathbf{K}_{\mathrm{ae}}(\omega)$ while these are dependent on experimentally derived flutter derivatives. The background component of the variance is therefore calculated by numerical integration of the previous equation

$$\Sigma_{B,ij}^{\mathrm{I}} = \int_{-\infty}^{+\infty} \frac{S_{p,ij}(\omega)}{K_{d,i}(\omega)K_{d,j}(\omega)}\, \mathrm{d}\omega. \tag{3.45}$$

The evaluation of this integral is much less resource consuming than integrating (3.27), that requires the integration of a very sharp function. Here, the integrand $S_{q,ij}^{B,\mathrm{I}}(\omega)$ is a smoother function of ω and the amount of integration points required to perform its accurate integration is drastically reduced, lightening the integration process. If the aeroelastic stiffness is such that it can be assumed to be constant at low frequency, the background component is even simpler thanks to the definition of the variance of the excitation and reads

$$\Sigma_{B,ij}^{\mathrm{I}} = \frac{\Sigma_{p,ij}}{K_{d,i}(0)K_{d,j}(0)}. \tag{3.46}$$

Stepping back to the second term of (3.38) and plugging in (3.43) in it leads to

$$\Sigma_{B,ij}^{\mathrm{II}} = -\int_{-\infty}^{+\infty} \sum_k \frac{K_{o,ik}(\omega)}{K_{d,i}(\omega)\, K_{d,j}(\omega)\, K_{d,k}(\omega)} S_{p,kj}(\omega)\, \mathrm{d}\omega, \tag{3.47}$$

where the integrand defines $S_{q,ij}^{B,\mathrm{II}}$, the background component of the second term of (3.38). Illustrations of the PSDs $S_{q,ij}^{B,\mathrm{I}}$ and $S_{q,ij}^{B,\mathrm{II}}$ are provided in Figure 3.2. Again, this equation can be simplified if the aeroelastic stiffness is supposed constant in the background region so that

$$\Sigma_{B,ij}^{\mathrm{II}} = -\sum_k \frac{K_{o,ik}(0)}{K_{d,i}(0)\, K_{d,j}(0)\, K_{d,k}(0)} \Sigma_{p,kj}. \tag{3.48}$$

With these approximations, and considering that the third term in (3.39) is the complex conjugate of the second, the background approximation of $S^B_{q,ij}(\omega)$ reads

$$S^B_{q,ij}(\omega) = \frac{1}{K_{d,i}(\omega)K_{d,j}(\omega)} S_{p,ij}(\omega) - \sum_k \frac{K_{o,ik}(\omega) + K_{o,ki}(\omega)}{K_{d,i}(\omega)\, K_{d,j}(\omega)\, K_{d,k}(\omega)} S_{p,kj}(\omega), \tag{3.49}$$

and the corresponding variance is

$$\mathbf{\Sigma}_B = \mathbf{\Sigma}^{\mathrm{I}}_B + \mathbf{\Sigma}^{\mathrm{II}}_B + \overline{\mathbf{\Sigma}}^{\mathrm{II}\,\mathsf{T}}_B = \mathbf{\Sigma}^{\mathrm{I}}_B + 2\mathbf{\Sigma}^{\mathrm{II}}_B \tag{3.50}$$

because $\mathbf{\Sigma}^{\mathrm{II}}_B$ is a real and symmetric matrix.

3.3.2 Derivation of the resonant component

Considering the residual

$$\mathbf{S}^{\mathrm{Res}}_q(\omega) = \mathbf{S}_q(\omega) - \mathbf{S}^B_q(\omega) \tag{3.51}$$

and substituting (3.39) and the background component (3.49) gives

$$\begin{aligned} S^{\mathrm{Res}}_{q,ij}(\omega) = S^{\mathrm{I}}_{q,ij} &- \frac{1}{K_{d,i}(\omega)K_{d,j}(\omega)} S_{p,ij}(\omega) \\ &+ S^{\mathrm{II}}_{q,ij} + \sum_k \frac{K_{o,ik}(\omega)}{K_{d,i}(\omega)\, K_{d,j}(\omega)\, K_{d,k}(\omega)} S_{p,kj}(\omega) \\ &+ \overline{S}^{\mathrm{II}\;\mathsf{T}}_{q,ij} + \sum_k \frac{K_{o,ki}(\omega)}{K_{d,i}(\omega)\, K_{d,j}(\omega)\, K_{d,k}(\omega)} S_{p,kj}(\omega). \end{aligned} \tag{3.52}$$

This residual can be seen as the superposition of 3 residuals that have no energy in the low frequency zone, and their main component arises from the region in the neighbourhood of the resonance peaks of the aeroelastic system. We shall develop each of these 3 terms separately, substituting a local approximation of $\mathbf{H}_d(\omega)$ and $\mathbf{J}_o(\omega)$ following the spirit of the Multiple Timescale Analysis.

3.3.2.A Stretching of variable

The methodology described in [82] suggests that the stretching should take the form $\omega = \omega_{ij}(1 + \varepsilon\eta_{ij})$. This would however complicate the derivation. Instead, we found that using momentarily 3 coordinates makes it easier. Three different stretched coordinates will be used to zoom in the neighbourhood of the poles of the uncoupled system. They are chosen as

$$\omega = \omega_i\,(1 + \varepsilon\delta\eta_i) \tag{3.53}$$

$$\omega = \omega_j\,(1 + \varepsilon\delta\eta_j) \tag{3.54}$$

$$\omega = \omega_{ij}\,(1 + \varepsilon\delta\eta_{ij}) \tag{3.55}$$

with $\omega_{ij} = (\omega_i + \omega_j)/2$ and chosen to be η_i, η_j and η_{ij} the three stretched variables ranging from $-\infty$ to $+\infty$. These changes of variables are chosen to be compatible, which means that (3.53), (3.54) and (3.55) are the same so that one can be used instead of another, indifferently, to give the same results. The use of 3 instead of a single change of variable as in the standard MTSA method allows considerable simplifications in the analytical developments presented below. In the 3 changes of variable, the parameter ε plays the role of a stretching parameter. The product $\varepsilon\delta$ corresponds to the order of magnitude of a zone extending over the two resonance peaks

$$\delta\varepsilon = \sqrt{\frac{1}{2}\left(\xi_i^2 + \xi_j^2\right) + \left(\frac{\omega_j - \omega_i}{\omega_i + \omega_j}\right)^2}. \tag{3.56}$$

This formulation is a personal choice translating the motivation of the stretching. It envelopes the maximum of 2 things: the relative distance between the natural frequencies and the width of the peaks in the FRFs, closely proportional to the damping ratio. The closer the eigenfrequencies ω_i and ω_j and/or the lower the damping, the larger the stretching on the resonant regime. Figure 3.1 illustrates the stretching on the resonant regime, for various relative magnitudes of the parameters ξ_i, ξ_j and $\frac{\omega_j-\omega_i}{\omega_i+\omega_j}$.

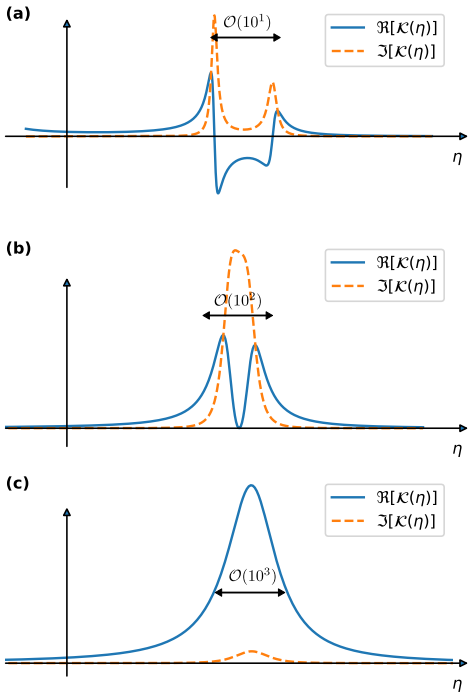

Figure 3.1: Illustration of the stretching on the kernel $\mathcal{K}[\omega(\eta)] = H_i[\omega(\eta)]\overline{H}_j[\omega(\eta)]$ depending on the stretching parameter $\delta\varepsilon$. (a) The peaks are well distinct if $\{\xi_i,\ \xi_j\} \lesssim \frac{\omega_j-\omega_i}{\omega_i+\omega_j}$ and gets progressively closer as the ratio $\frac{\omega_j-\omega_i}{\omega_i+\omega_j}$ decreases to zero, see (b). In (c), the two peaks are coalescing, $\frac{\omega_j-\omega_i}{\omega_i+\omega_j} \lesssim \{\xi_i,\ \xi_j\}$. These examples can be generated with $m_i = 1$ kg, $\omega_i = 1$ rad s^{-1} , (a) $\varepsilon = 0.2$, $\xi_i = \xi_j = 0.03$, (b) $\varepsilon = 0.02$, $\xi_i = \xi_j = 0.02$ and (c) $\varepsilon = 0.001$, $\xi_i = \xi_j = 0.03$.

3.3.2.B Asymptotic expansion of the system matrices

In a very general manner, a matrix can be expanded as a series around a given point ω_0 as follows

$$A_{ij}(\omega) = A_{ij}(\omega_0) + \partial_\omega A_{ij}(\omega_0)(\omega - \omega_0) + \mathcal{O}\left[(\omega - \omega_0)^2\right] \tag{3.57}$$

with $\partial_\omega A_{ij} = \dfrac{\partial A_{ij}}{\partial \omega}$. In particular, if $\omega_0 = \omega_{ij}$, one gets after substituting (3.55)

$$A_{ij}(\eta_{ij}) = A_{ij}(\omega_{ij}) + \partial_\omega A_{ij}(\omega_{ij})\omega_{ij}\delta\eta_{ij}\varepsilon + \mathcal{O}\left(\varepsilon^2\right). \tag{3.58}$$

Restarting from (3.57) in the particular cases of $j = i$ and $i = j$ and using respectively the first and second changes of variable (3.53) and (3.54), we also have

$$A_{ii}(\eta_i) = A_{ii}(\omega_i) + \partial_\omega A_{ii}(\omega_i)\omega_i\delta\eta_i\varepsilon + \mathcal{O}\left(\varepsilon^2\right) \tag{3.59}$$

and

$$A_{jj}(\eta_j) = A_{jj}(\omega_j) + \partial_\omega A_{jj}(\omega_j)\omega_j\delta\eta_j\varepsilon + \mathcal{O}\left(\varepsilon^2\right). \tag{3.60}$$

In particular, this linearization of $\mathbf{A}(\omega)$ can be executed for $\mathbf{M}(\omega)$, $\mathbf{C}(\omega)$ and $\mathbf{K}(\omega)$ provided that these are smooth functions of ω, which expects therefore from aeroelastic matrices $\mathbf{M}_{\text{ae}}(\omega)$, $\mathbf{C}_{\text{ae}}(\omega)$ and $\mathbf{K}_{\text{ae}}(\omega)$ to be smooth functions of ω.

3.3.2.C Asymptotic expansion of diagonal transfer function, and dynamic flexibility

Substituting the linear expansion (3.58) for $\mathbf{M}$, $\mathbf{C}$ or $\mathbf{K}$ and the stretching (3.53) in (3.34) leads to the following expression

$$\begin{aligned} H_{d,i}^{-1}(\eta_i) = K_{d,i}(\omega_i) &+ \partial_\omega K_{d,i}(\omega_i)\omega_i\eta_i\delta\varepsilon \\ &+ \mathrm{i}\omega_i(1+\delta\varepsilon\eta_i)\left(C_{d,i}(\omega_i) + \partial_\omega C_{d,i}(\omega_i)\omega_i\eta_i\delta\varepsilon\right) \\ &- \omega_i^2(1+\delta\varepsilon\eta_i)^2(M_{d,i}(\omega_i) + \partial_\omega M_{d,i}(\omega_i)\omega_i\eta_i\delta\varepsilon) + \mathcal{O}(\varepsilon^2). \end{aligned} \tag{3.61}$$

If we assume that the structure is lightly damped at the aeroelastic resonance, the damping $C_{d,i}(\omega_i)$ can be expressed as a function of the small parameter ε, that is

$$C_{d,i}(\omega_i) = 2\chi_{d,i}\omega_i M_{d,i}(\omega_i)\varepsilon \tag{3.62}$$

where $\chi_{d,i}$ is a parameter of order 1, at most. The same assumption is made for $\partial_\omega C_{d,i}(\omega_i)$, supposing therefore

$$\partial_\omega C_{d,i}(\omega_i) = 2\partial_\omega\chi_{d,i}\omega_i M_{d,i}(\omega_i)\varepsilon. \tag{3.63}$$

Substituting (3.62) and (3.63) in (3.61), and considering (3.26) yields, at leading order

$$H_{d,i}^{-1}(\eta_i) = \varepsilon\omega_i\left[\mathrm{i}\chi_{d,i} + \delta\eta_i(\partial_\omega K_{d,i}(\omega_i)) - \omega_i(2M_{d,i}(\omega_i) + \omega_i\partial_\omega M_{d,i}(\omega_i))\right]. \tag{3.64}$$

This equation shows that the diagonal transfer functions are of the order of $\mathcal{O}(\varepsilon^{-1})$, under the considered assumptions. This is consistent with other applications of the MTSA method in dynamics of structures [82] and translates the fact that, at resonance, the height of the resonance peak is of order $\varepsilon^{-1} \sim \xi^{-1}$. From (3.64), we can now back substitute our changes of variable (3.53), (3.62) and (3.63) to get a linear expression in ω for $H_{d,i}$

$$\begin{aligned} H_{d,i}^{-1}(\omega) \simeq \mathcal{H}_{d,i}^{-1}(\omega) \triangleq &\left[\partial_\omega K_{d,i}(\omega_i) - \omega_i(2M_{d,i}(\omega_i) + \omega_i\partial_\omega M_{d,i}(\omega_i))\right]\omega \\ &+ \omega_i\left[\mathrm{i}\,C_{d,i}(\omega_i) - \partial_\omega K_{d,i}(\omega_i) + \omega_i(2M_{d,i}(\omega_i) + \omega_i\partial_\omega M_{d,i}(\omega_i))\right]. \end{aligned} \tag{3.65}$$

This latter expression constitutes our asymptotic expansion of the diagonal transfer function valid in the vicinity of the resonant peak ω_i. The same process is used to derive the series expansion near the second peak of the response ω_j, so that

$$\begin{aligned} H_{d,j}^{-1}(\omega) \simeq \mathcal{H}_{d,j}^{-1}(\omega) \triangleq &\left[\partial_\omega K_{d,j}(\omega_j) - \omega_j(2M_{d,j}(\omega_j) + \omega_j\partial_\omega M_{d,j}(\omega_j))\right]\omega \\ &+ \omega_j\left[\mathrm{i}\,C_{d,j}(\omega_j) - \partial_\omega K_{d,j}(\omega_j) + \omega_j(2M_{d,j}(\omega_j) + \omega_j\partial_\omega M_{d,j}(\omega_j))\right]. \end{aligned} \tag{3.66}$$

Similarly, the dynamic flexibility may be expanded in series introducing in (3.28) the linearization (3.58) particularized with $\mathbf{A} = \mathbf{M}$, $\mathbf{K}$ and $\mathbf{C}$. The small damping assumptions $C_{ij} = 2\chi_{ij}\omega_{ij}M_{ij}\varepsilon$ and $\partial_\omega C_{ij} = 2\partial_\omega\chi_{ij}\omega_{ij}M_{ij}\varepsilon$ show that the damping terms are of order $\mathcal{O}(\varepsilon)$ at most —considering the fact that $M_{ij}(\omega)$ and $\partial_\omega M_{ij}(\omega)$ are at most of order $\mathcal{O}(1)$, even if more likely of order $\mathcal{O}(\varepsilon)$. The dynamic flexibility matrix then becomes

$$\begin{aligned} J_{ij}(\eta) = K_{ij}(\omega_{ij}) &- \omega_{ij}^2 M_{ij}(\omega_{ij}) \\ &+ \omega_{ij}\left[\partial_\omega K_{ij}(\omega_{ij})\delta\eta_{ij} + \mathrm{i}\chi_{ij} - \omega_{ij}\left(2\omega_{ij}\omega M_{ij}(\omega_{ij})\delta\eta_{ij} + \partial_\omega M_{ij}(\omega_{ij})\delta\eta_{ij}\omega_{ij}\right)\right]\varepsilon \\ &+ \mathcal{O}(\varepsilon^2). \end{aligned} \tag{3.67}$$

Equation (3.26) does not cancel the two first terms of the previous equation. This quantity is however expected to be small when $\omega_j \simeq \omega_i$ ($\omega_{ij} \simeq \omega_i$) because $K_{ij}(\omega_{ij}) - \omega_{ij}^2 M_{ij}(\omega_{ij})$ is exactly (3.26) but with $\omega_{ij} = \omega_i$. The quantity $K_{ij}(\omega_{ij}) - \omega_{ij}^2 M_{ij}(\omega_{ij})$ is small and can therefore be assumed of order $\mathcal{O}(\varepsilon)$. The previous series expansion can not be further simplified, so that

after truncating at leading order and stepping back to the unstretched coordinate system, the dynamic flexibility finally reads

$$J_{ij}(\omega) \simeq \mathcal{J}_{ij}(\omega) \triangleq K_{ij}(\omega_{ij}) + \omega_{ij}\left[\mathrm{i}C_{ij}(\omega_{ij}) - \partial_\omega K_{ij}(\omega_{ij}) + M_{ij}(\omega_{ij})\omega_{ij} + \partial_\omega M_{ij}(\omega_{ij})\omega_{ij}^2\right] + \left[\partial_\omega K_{ij}(\omega_{ij}) - 2M_{ij}(\omega_{ij})\omega_{ij} - \partial_\omega M_{ij}(\omega_{ij})\omega_{ij}^2\right]\omega. \quad (3.68)$$

3.3.2.D Asymptotic expansion of the resonant component of the PSD

The resonant component is derived from the residual (3.52) made up of 3 contributions, substituting for ω a stretched coordinate allowing to zoom in the zone of primary interest, where most of the energy of the residual is localized. Each of them will be treated separately in this section, after noting that they all consist in a difference of two terms, where the second is systematically two orders of magnitude lower than the first in the region of interest. And since a leading order approximation is sought, these 3 terms can be relinquished.

$$S_{q,ij}^{\mathrm{Res}}(\omega) \simeq S_{q,ij}^{\mathrm{I}}(\omega) + S_{q,ij}^{\mathrm{II}}(\omega) + \overline{S}_{q,ij}^{\mathrm{II}\,\mathsf{T}}(\omega). \quad (3.69)$$

The first component of the residual (3.69), can be expressed by substituting the series expansions of (3.65) and (3.66), which provides the first part of the resonant component

$$S_{q,ij}^{R,\mathrm{I}}(\omega) = \mathcal{H}_{d,i}(\omega)S_{p,ij}(\omega)\overline{\mathcal{H}}_{d,j}(\omega). \quad (3.70)$$

For lightly damped structures such as those encountered in most of civil engineering applications, the resonance peaks are very sharp. For this reason, the power spectral density of the excitation may be replaced by its value at resonance. In the context of the MTSA method, this hypothesis was popularized by Davenport [81] and is known as *white noise approximation*, recalled in Section 1.6.1.A

$$S_{q,ij}^{R,\mathrm{I}}(\omega) = \mathcal{H}_{d,i}(\omega)S_{p,ij}(\omega_{ij})\overline{\mathcal{H}}_{d,j}(\omega). \quad (3.71)$$

In case of M degree-of-freedom (MDOF) applications, it is suggested [82, 96] to replace $S_{p,ij}(\omega_{ij})$ by $1/2\left[S_{p,ij}(\omega_i) + S_{p,ij}(\omega_j)\right]$, which allows limiting the evaluation of the modal force PSD to all natural frequencies rather than to all possible combinations of arithmetic means, reducing hence the number projections of the modal forces to a smaller amount of frequencies (about M times).

The second component is obtained similarly using (3.65), (3.66) and (3.68) in the second term of (3.69)

$$S_{q,ij}^{R,\mathrm{II}}(\omega) = -\mathcal{H}_{d,i}(\omega)\sum_k \left[\mathcal{J}_{o,ik}(\omega)\mathcal{H}_{d,k}(\omega)S_{p,kj}(\omega_{kj})\right]\overline{\mathcal{H}}_{d,j}(\omega), \quad (3.72)$$

where $\mathcal{J}_{o,ij} = (1-\delta_{ij})\mathcal{J}_{ij}$ with δ_{ij} is the Kronecker delta symbol. $\mathbf{J}_o$ contains therefore the out-of-diagonal element of $\mathbf{J}$. The resonant component is finally obtained by superposition of the 3 components

$$S_{q,ij}^{R}(\omega) = S_{q,ij}^{R,\mathrm{I}}(\omega) + S_{q,ij}^{R,\mathrm{II}}(\omega) + \overline{S}_{q,ij}^{R,\mathrm{II}\,\mathsf{T}}(\omega) \quad (3.73)$$

where the third is readily obtained by transposing and conjugating (3.72). The PSDs $S_{q,ij}^{R}(\omega)$, $S_{q,ij}^{R,\mathrm{I}}(\omega)$ and $S_{q,ij}^{R,\mathrm{II}}(\omega) + \overline{S}_{q,ij}^{R,\mathrm{II}\,\mathsf{T}}(\omega)$ are illustrated in Figure 3.2 (c). A schematic example of background and resonant decomposition is also illustrated in Figure 3.2 (a).

3.3.2.E Derivation of the resonant component of the co-variance of modal responses

The resonant component of the co-variance of modal responses is obtained by integration of the PSD over the frequencies

$$\Sigma_{ij}^{R} = \int_{-\infty}^{+\infty}\left[S_{q,ij}^{R,\mathrm{I}}(\omega) + S_{q,ij}^{R,\mathrm{II}}(\omega) + \overline{S}_{q,ij}^{R,\mathrm{II}\,\mathsf{T}}(\omega)\right]\mathrm{d}\omega. \quad (3.74)$$

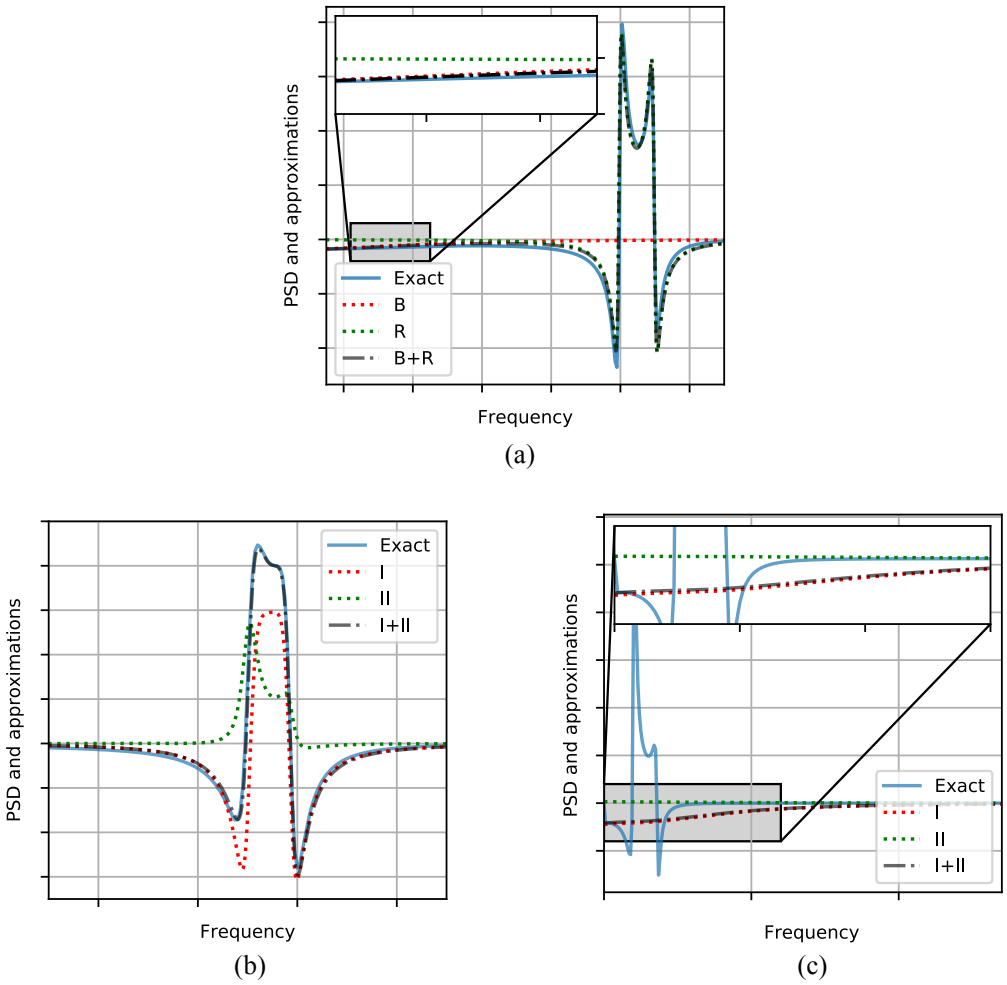

Figure 3.2: Schematic illustration of the components of the power spectral densities of the response. (a) Background (B) and Resonant Component (R) and approximation (B+R) (b) Decomposition of the resonant component of the approximation (I+II) in two terms I and II referring to $S_q^{\mathrm{I},R}(\omega)$ and $S_q^{\mathrm{II},R}(\omega) + \overline{S}_q^{\mathrm{II},R^{\mathsf{T}}}$, respectively. (c) Decomposition of the background component of the approximation (I+II) in two terms I and II referring respectively to $S_q^{\mathrm{I},B}(\omega)$ and $S_q^{\mathrm{II},B}(\omega) + \overline{S}_q^{\mathrm{II},B^{\mathsf{T}}}$.

Cauchy's theorem is used to calculate the corresponding variances. The terms I and II of the integrand admits respectively 2 and 3 poles, easily determined from the series expansion $\mathcal{H}_{d,i}(\omega)$, $\mathcal{H}_{d,j}(\omega)$ and $\mathcal{H}_{d,k}(\omega)$. These two PSDs can therefore be factored as follows

$$S_{q,ij}^{R,\mathrm{I}}(\omega) = \frac{\omega_i\omega_j}{4\kappa_i\kappa_j(\omega - p_i)(\omega - \overline{p}_j)} S_{p,ij}(\omega_{ij}) \tag{3.75}$$

and

$$S_{q,ij}^{R,\mathrm{II}}(\omega) = -\sum_{\substack{k \\ k\neq i}} \frac{\omega_i\omega_j\omega_k}{8\kappa_i\kappa_k\kappa_j(\omega - p_i)(\omega - \overline{p}_j)(\omega - p_k)} S_{p,kj}(\omega_{kj})\mathcal{J}_{o,ik}(\omega) \tag{3.76}$$

where $p_i = \omega_i\left(1 + \mathrm{i}\xi_{d,i}\right)$ refers to the complex poles of $\mathcal{H}_{d,i}(\omega)$ and where

$$\kappa_i = K_{d,i}(\omega_i) + \frac{1}{2}\omega_i\left(\partial_\omega K_{d,i}(\omega_i) - \omega_i^2\partial_\omega M_{d,i}(\omega_i)\right). \tag{3.77}$$

The poles of $\mathcal{H}_{d,i}(\omega)$ and $\mathcal{H}_{d,j}(\omega)$ are characterized by a positive complex part. Therefore, the first and second parts of the resonant component admit respectively one and two poles of positive complex part, namely p_i for $S_{q,ij}^{R,\mathrm{I}}(\omega)$ and p_i and p_k for $S_{q,ij}^{R,\mathrm{II}}(\omega)$. Starting from the factored forms (3.75) and (3.76), the residues of the integrands are easily evaluated at these poles of first order:

$$\operatorname*{Res}_{\omega=p_i}\left[S_{q,ij}^{R,\mathrm{I}}(\omega)\right] = \lim_{\omega\to p_i}(\omega - p_i)S_{q,ij}^{R,\mathrm{I}}(\omega) = \frac{\omega_i\omega_j}{4\kappa_i\kappa_j}\frac{S_{p,ij}(\omega_{ij})}{(p_i - \overline{p}_j)}, \tag{3.78}$$

$$\operatorname*{Res}_{\omega=p_i}\left[S_{q,ij}^{R,\mathrm{II}}(\omega)\right] = \lim_{\omega\to p_i}(\omega - p_i)S_{q,ij}^{R,\mathrm{II}}(\omega) = -\sum_{\substack{k \\ k\neq i}} \frac{\omega_i\omega_j\omega_k}{8\kappa_i\kappa_j\kappa_k}\frac{S_{p,kj}(\omega_{kj})}{(p_i - p_k)(p_i - \overline{p}_j)}\mathcal{J}_{o,ik}(\omega_{ij}), \tag{3.79}$$

$$\operatorname*{Res}_{\omega=p_k}\left[S_{q,ij}^{R,\mathrm{II}}(\omega)\right] = \lim_{\omega\to p_k}(\omega - p_k)S_{q,ij}^{R,\mathrm{II}}(\omega) = -\sum_{\substack{k \\ k\neq i}} \frac{\omega_i\omega_j\omega_k}{8\kappa_i\kappa_j\kappa_k}\frac{S_{p,kj}(\omega_{kj})}{(p_k - p_i)(p_k - \overline{p}_j)}\mathcal{J}_{o,ik}(\omega_{ij}). \tag{3.80}$$

Equation (3.74) is then integrated using the Cauchy's residue theorem. Each contribution (3.78) or (3.79) and (3.80) is integrated as

$$\int_{-\infty}^{+\infty} S_q(\omega)\,\mathrm{d}\omega = 2\mathrm{i}\pi\sum_k \mathrm{Res}, \tag{3.81}$$

where $\sum_k \mathrm{Res}$ is the residual (3.78) for integrating (3.71) and the sum of (3.79) and (3.80) for integrating (3.72).

At this stage however, the result is still a complex number as we only focused on resonance peaks located in the positive frequency range. The same operations must be repeated to integrate also the peaks of the response power spectral density in the negative frequency range. The response PSD have however a symmetric real part, and an asymmetric imaginary part, so that the contribution of the negative frequencies to the variances and covariances may simply be obtained by adding respectively to (3.78), (3.79), and (3.80) their complex conjugates. Accounting for positive and negative frequency ranges and the definition of the poles yields

$$\Sigma_{ij}^{R,\mathrm{I}} = \frac{\pi\omega_i\omega_j}{\kappa_i\kappa_j}\Re\left\{\frac{\mathrm{i}S_{p,ij}(\omega_{ij})}{(p_i - \overline{p}_j)}\right\} \tag{3.82}$$

and

$$\Sigma_{ij}^{R,\mathrm{II}} = -\sum_{\substack{k \\ k\neq i}} \frac{\omega_i\omega_j\omega_k}{2\kappa_i\kappa_j\kappa_k}\Re\left\{\frac{\mathrm{i}S_{p,kj}(\omega_{ij})\mathcal{J}_{o,ik}(\omega_{ij})}{(p_i - p_k)(p_i - \overline{p}_j)} + \frac{\mathrm{i}S_{p,kj}(\omega_{ij})\mathcal{J}_{o,ik}(\omega_{ij})}{(p_k - p_i)(p_k - \overline{p}_j)}\right\}. \tag{3.83}$$

Finally, the resonant component is obtained by (3.74) with $\boldsymbol{\Sigma}^{R,\mathrm{II}}$ a real and symmetric matrix, which produces

$$\Sigma_{ij}^{R} = \Sigma_{ij}^{R,\mathrm{I}} + 2\Sigma_{ij}^{R,\mathrm{II}}. \tag{3.84}$$

This last expression was the missing piece of (3.41) to evaluate the modal response of the structure, and closes this section dedicated to the derivation of the approximate solution.

3.4 Summary and discussion

The establishment of the solution (3.41) is the result of several hypotheses. The first was formulated to obtain a series expansion of the transfer function matrix $\mathbf{H}(\omega)$, valid for slightly coupled matrices. This series was truncated at first order, resulting in the approximate expression (3.33) for $\mathbf{H}(\omega)$ demanding no full matrix inversion. Accordingly, the power spectral density matrix of the modal response was obtained in (3.37), depicting the sum of 4 components where one was found to be significantly smaller than the others, and therefore dropped in (3.39). The 3 remaining components are exclusively described by three matrices: the power spectral density matrix of modal forces $\mathbf{S}_p(\omega)$, the diagonal matrix $\mathbf{H}_d(\omega)$ and the off-diagonal matrix $\mathbf{J}_o(\omega)$ for which asymptotic expansions were searched, in both the low and the high frequency regions, following the principle of the Background/Resonant decomposition of the modal PSD. The local expansions of $\mathbf{H}_d(\omega)$ and $\mathbf{J}_o(\omega)$ in the resonant regions are conditioned upon one important assumption: the relative distance between the two natural frequencies of the aeroelastic system and the damping ratio must be small . This hypothesis is formulated along with the small damping assumption, which is observed in most locally undamped slender structures. As a result, the proposed method is designed to be accurate for lightly damped structures with close natural frequencies, potentially experiencing modal coupling. The method covers also structures with distant resonant peaks: in this case, the covariances are less accurately estimated, but are to small to affect the recombined nodal displacements. There is therefore very little interest in the determination of the covariances for those cases, as they are to small to affect the nodal recombined variance [96].

These local approximations are plugged in (3.39) defining the background $\mathbf{S}_q^B(\omega)$ and resonant $\mathbf{S}_q^R(\omega)$ contributions to the response PSD. A synthetic decomposition of a response PSD into a background and resonant components is shown in Figure 3.2 (a). The 3 contributions to the background and the 3 contributions to the resonant component of the response PSD are respectively illustrated in a schematic example in Figure 3.2 (a) and (b).

The last step of the method is the derivation of the covariance matrix as the integral of the response power spectral densities. The background component of the covariance matrix is obtained from numerical integration. The need for a numerical integration method is the consequence of the presence of $K_{d,i}(\omega)$ for which no global approximation can be made through the whole frequency range. However, the background component is quite a smooth function, and its integration is accurately performed with a few integration points in contrast to what the integration of the response PSD would have required. Accordingly, the number of integration points, and consequently projection of the modal forces $\mathbf{S}_p(\omega)$ is significantly reduced [103]. Despite the presented method still necessitates the use of numerical integration, its interest remains evident when we know that the modal projection constitutes a highly consuming operation in a large FEM model [104].

On the other hand, the resonant component depicts most of its energy in sharp resonant peaks, where the aeroelastic matrices, supposed smooth functions of the frequency, can be locally approached by series expansions. The resonant component can therefore be analytically integrated using the Cauchy's residue theorem yielding (3.84).

The superposition of the background and resonant components yields the covariance matrix of the structural response (3.41), which quantifies the modal behaviour of the structure in a probabilistic context.

This expression constitutes the generalization of the several existing models. Indeed, particularizing the $M \times M$ PSD (3.39) with $M = 1$ to degenerate into a SDOF model leads to $S_q^{\mathrm{II}}(\omega) = 0$ and reduces the approximation of the variance of the response (3.41) to its first component only

$$\Sigma_q \simeq \Sigma_q^B + \Sigma_q^R = \Sigma_q^{B,\mathrm{I}} + \Sigma_q^{R,\mathrm{I}}. \tag{3.85}$$

Simplifying (3.45) and (3.82) with $i = j$, and noting that $p_j - \overline{p}_i = 2\xi_{d,i}\omega_i$, the approximation

reads

$$\Sigma_q^B + \Sigma_q^R = \int_{-\infty}^{+\infty} \frac{S_{p,ij}(\omega)}{K_{d,i}^2(\omega)}\,\mathrm{d}\omega + \frac{\pi\omega_i}{\kappa_i^2}\frac{S_{p,ij}(\omega_i)}{2\xi_{d,i}} \tag{3.86}$$

which corresponds to the response of the SDOF aeroelastic oscillator [105], with the only difference that the quadratic term $[\partial_\omega k_i(\omega_i)]^2$ was neglected, and the modal mass taken constant.

This equation may be furthermore simplified in wind-off conditions in which case $\kappa_i = K_{d,i}(\omega_i)$. Noting that the variance of the buffeting is by definition $\sigma_p^2 = \int_{-\infty}^{+\infty} S_p(\omega)\,\mathrm{d}\omega$, the approximation degenerates as follows

$$\Sigma_q^B + \Sigma_q^R = \frac{\sigma_p^2}{K_{d,i}^2} + \frac{\pi\omega_i}{K_{d,i}^2}\frac{S_{p,ij}(\omega_i)}{2\xi_{d,i}}. \tag{3.87}$$

This last formulation corresponds exactly to the Davenport's Background/Resonant decomposition of the structural response to a gusty wind [81]. The approximation established in this chapter can then be seen as the extension of his model to MDOF aeroelastic oscillators.

3.5 User guide

This section provides a concise summary of the equations required to implement the background/resonant decomposition. It is intended as a practical reference for users who wish to reconstruct the solution based on the methodology developed in this work. Only the essential steps and expressions are reported, without further derivation or discussion. It is meant to serve as a quick-access reference for implementation, containing only the final expressions derived throughout the manuscript.

User Guide for the Developer

1. Evaluate the B contributions from (3.45) or (3.46) (contribution I) and from (3.47) or (3.48) (contribution II):

$$\Sigma^{\mathrm{I}}_{B,ij} = \int_{-\infty}^{+\infty} \frac{S_{p,ij}(\omega)}{K_{d,i}(\omega)K_{d,j}(\omega)}\,\mathrm{d}\omega$$

$$\Sigma^{\mathrm{II}}_{B,ij} = -\int_{-\infty}^{+\infty} \sum_{k} \frac{K_{o,ik}(\omega)}{K_{d,i}(\omega)\,K_{d,j}(\omega)\,K_{d,k}(\omega)} S_{p,kj}(\omega)\,\mathrm{d}\omega$$

2. The B component is then obtained added the two contributions according to (3.50)

$$\boldsymbol{\Sigma}_B = \boldsymbol{\Sigma}^{\mathrm{I}}_B + 2\boldsymbol{\Sigma}^{\mathrm{II}}_B$$

3. Evaluate the R contributions $\boldsymbol{\Sigma}^{R,\mathrm{I}}$ from (3.82) and $\boldsymbol{\Sigma}^{R,\mathrm{II}}$ (3.83):

$$\Sigma^{R,\mathrm{I}}_{ij} = \frac{\pi\omega_i\omega_j}{\kappa_i\kappa_j}\Re\left\{\frac{\mathrm{i}S_{p,ij}(\omega_{ij})}{(p_i-\overline{p}_j)}\right\}$$

$$\Sigma^{R,\mathrm{II}}_{ij} = -\sum_{\substack{k\\k\neq i}} \frac{\omega_i\omega_j\omega_k}{2\kappa_i\kappa_j\kappa_k}\Re\left\{\frac{\mathrm{i}S_{p,kj}(\omega_{ij})\mathcal{J}_{o,ik}(\omega_{ij})}{(p_i-p_k)(p_i-\overline{p}_j)} + \frac{\mathrm{i}S_{p,kj}(\omega_{ij})\mathcal{J}_{o,ik}(\omega_{ij})}{(p_k-p_i)(p_k-\overline{p}_j)}\right\}$$

with

- ω_i is the eigenfrequency of mode i of the damped uncoupled aeroelastic system
- $p_i = \omega_i(1+\mathrm{i}\xi_{d,i})$
- $\xi_{d,i}(\omega) = C_{d,i}(\omega)/(2\sqrt{K_{d,i}(\omega)M_{d,i}(\omega)})$
- $\kappa_i = K_{d,i}(\omega_i) + \frac{1}{2}\omega_i\left(\partial_\omega K_{d,i}(\omega_i) - \omega_i^2\partial_\omega M_{d,i}(\omega_i)\right)$ from (3.77).
- $\omega_{ij} = \frac{1}{2}(\omega_i+\omega_j)$
- $\mathcal{J}_{o,ij} = (1-\delta_{ij})\mathcal{J}_{ij}$
- $\mathcal{J}_{ij}$ from (3.68):

$$\begin{aligned}\mathcal{J}_{ij}(\omega) = K_{ij}(\omega_{ij}) + \omega_{ij}\left[\mathrm{i}C_{ij}(\omega_{ij}) - \partial_\omega K_{ij}(\omega_{ij}) + M_{ij}(\omega_{ij})\omega_{ij} + \partial_\omega M_{ij}(\omega_{ij})\omega_{ij}^2\right]\\ + \left[\partial_\omega K_{ij}(\omega_{ij}) - 2M_{ij}(\omega_{ij})\omega_{ij} - \partial_\omega M_{ij}(\omega_{ij})\omega_{ij}^2\right]\omega\end{aligned}$$

4. Add the B and R components according to (3.41)

$$\boldsymbol{\Sigma}_q = \boldsymbol{\Sigma}^B_q + \boldsymbol{\Sigma}^R_q$$

3.6 Illustrations

3.6.1 Presentation of the case study

The selected case study is adapted from the benchmark investigated in [46] about flutter analysis of bridge decks. This benchmark proposed to assess the aeroelastic stability of the Storebaelt bridge with its actual structural properties but using a 2DOF pitch-plunge model, as shown in Figure 3.3. Because the structure was proven to fail in an uncoupled torsional divergence instability [46], some of the real structural properties were modified here to ensure good timescale separation and to artificially induce a coupled instability on which the efficiency of the Background/Resonant decomposition can be assessed. The plunge eigenfrequency $f_{s,0}$ is set to 0.2 Hz to allow the resonant component to bring a significant contribution to the response. Since the focus of this chapter is more on the demonstration that simplified formula can be used to determine the coupled response, we consider a single wind velocity ($U = 30$ m/s) and vary $f_{s,1}$ in order to investigate the various conditions under which coupling can be more or less important. Therefore, the plunge natural frequency $f_{s,1}$ is taken as a variable, ranging from 0.15 to 0.25 Hz. The response of the structure is evaluated for each pair of frequencies $(f_{s,0}, f_{s,1})$. All the parameters used in the present example have been summarized in Table 3.1.

The aeroelastic behaviour was also slightly modified using the Theodorsen flat plate model [57], where the aeroelastic damping terms were rescaled by a factor $\beta \in \{0.1, 1\}$ allowing values smaller than one to meet the small coupling assumption across the entire frequency range. Indeed, in the resonant regime, the flexibility matrix is close to singular and the coupling terms of the aeroelastic damping become increasingly dominant as one tends to critical speed, harming the fundamental assumption of slightly coupled matrix formulated in Section 3.2. In order to validate our developments in an ideal framework, the parameter β is first chosen equal to 0.1, that is, the aeroelastic damping terms are decreased to 10% of their actual value. The case of the original formulation of the aeroelastic damping, $\beta = 1$, will be investigated in a second stage, in the dedicated Section 3.6.4.

Applied to a 2-DOF pitch/plunge model and neglecting the added mass effects, equation (1.49) is particularized with $\mathbf{x}^{\mathsf{T}}(t) = \begin{bmatrix}\theta(t) & h(t)\end{bmatrix}$ and

$$\mathbf{M}_{\text{ae}} = \mathbf{0} \tag{3.88}$$

$$\mathbf{C}_{\text{ae}}(\omega) = \frac{1}{2}\rho\beta U B \left(\frac{2\pi}{V^*}\right) \begin{bmatrix} H_1 & BH_2 \\ BA_1 & B^2A_2 \end{bmatrix} \tag{3.89}$$

$$\mathbf{K}_{\text{ae}} = \frac{1}{2}\rho U^2 B \left(\frac{2\pi}{V^*}\right)^2 \begin{bmatrix} H_4/B & H_3 \\ A_4 & BA_3 \end{bmatrix} \tag{3.90}$$

where $H_1^*, H_2^*, H_3^*, H_4^*$ and $A_1^*, A_2^*, A_3^*, A_4^*$ are the flutter derivatives as described by Scanlan [106] and are all functions of the reduced velocity $V^* = U/fB$. These functions are evaluated analytically from [57], and in a first step, reduced by $\beta = 0.1$. They are represented in Figure 3.4 (a) and (b).

The modal basis considered in this application is a wind-on modal basis, composed of the eigenmodes obtained by solving the damped eigenvalue problem. These modes are inherently complex, making the buffeting force and modal response power spectral density matrices complex as well. As a result, some of the intermediate results formulated in the previous section no longer hold. To address this, instead of using the full complex mode shapes, only the real part of each component is retained, while the imaginary part is discarded. At first glance, this choice may seem counter-intuitive, especially since other, simpler modal bases with real-valued eigenmodes could have been considered. However, as demonstrated later in Section 3.6.3, even without the imaginary part, this approach significantly impacts the accuracy of the method. The eigenmodes

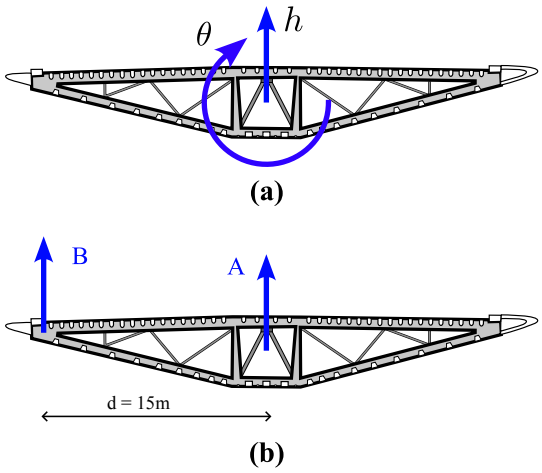

Figure 3.3: (a) Schematic of a pitch (θ) - plunge (h) model of a bridge deck. (b) Identification of the points A and B, where the vertical displacement is monitored (both are located at mid-span).

Parameters	**Values**	**Units**
Deck width B	31	[m]
Moment of Inertia I_s	24.7×10^6	[kg.m^2/m]
Deck mass m_s	227.4×10^3	[kg]
Natural frequency $f_{s,0}$ (pitch)	0.2	[Hz]
Natural frequency $f_{s,1}$ (plunge)	$\in [0.15; 0.25]$	[Hz]
Structural Damping Ratios $\xi_{s,\theta}$ and $\xi_{s,h}$	0.6	[%]

Table 3.1: Parameters for the proposed case study. All the parameters are measured in wind-off conditions ($U = 0$ m/s). Variable $\xi_{s,\theta}$ and $\xi_{s,h}$ refer respectively to the structural damping in pitch and plunge motion.

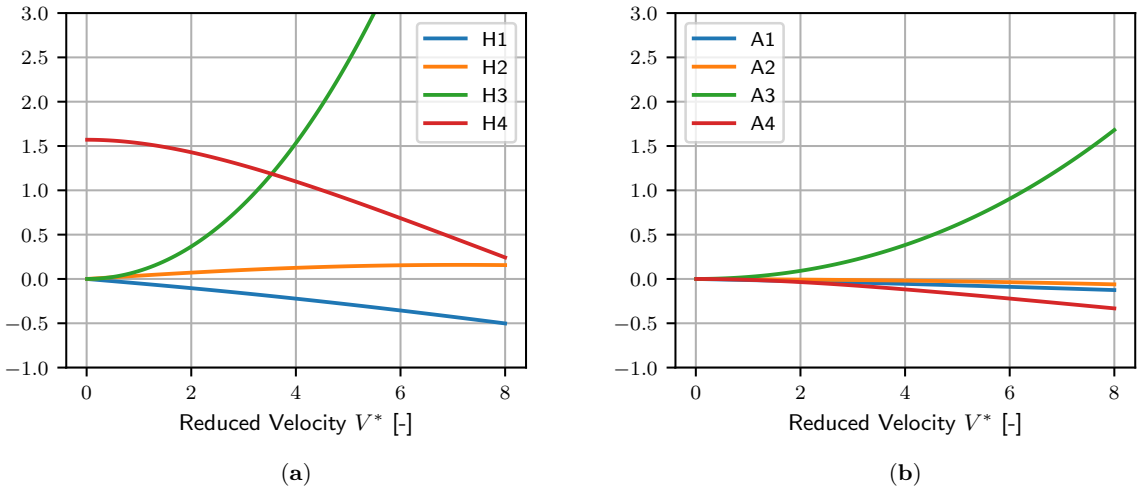

Figure 3.4: Scanlan's derivatives used in the aeroelastic model. (a) A's derivatives, (b) H's derivatives. The derivatives A_1, A_2, H_1 and H_2 comprise the rescaling made on the aeroelastic damping.

of this wind-on modal basis, used for the parametric analysis, are illustrated for $U = 30$ m/s in Figure 3.5. The case of fully complex eigenmodes requires several modifications to the theory presented in this chapter and will be investigated separately in Chapter 4 . This modal basis is used to project the equations (3.89) and (3.90) to get the generalized modal matrices used in the following of the section.

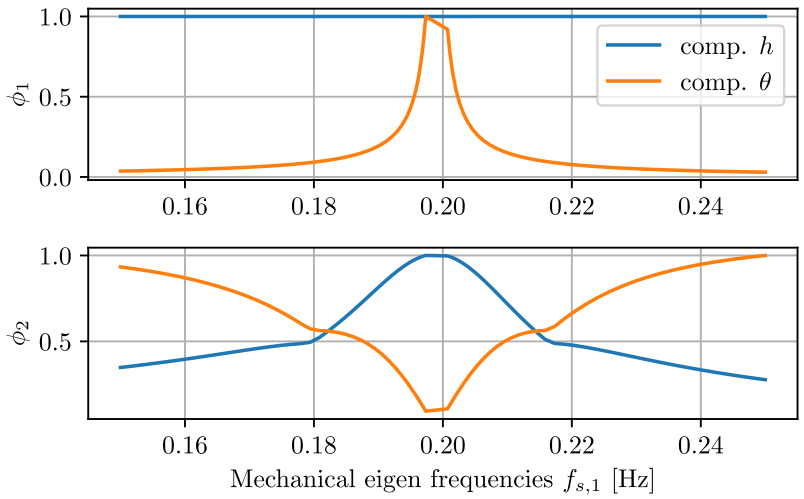

Figure 3.5: Eigenmodes of the wind-on modal basis at 30 m/s

A quick look at the diagonality index $\rho(\mathbf{J})$ represented in Figure 3.6(b) is enough to convince that the case $\beta = 0.1$ meets well the requirements of the small coupling assumption. This index is also represented in Figure 3.6(a) for three particular cases of the parametric study, each having a different pitch frequency $f_{s,1}$. In principle, the shape of $\rho(\mathbf{J})$ depicts two peaks, corresponding respectively to the two eigenvalues f_1 and f_2, localising the frequencies at which the aeroelastic terms have the most significant influence on the total stiffness and damping. When the wind off natural frequencies $f_{s,0}$ and $f_{s,1}$ are close, these peaks become coalescent as shown by the green —and orange— curve. Because the expansion (3.33) is exploited in the resonant frequency range, it is recommended, for conservativeness, to ensure that the diagonality index $\rho(\mathbf{J})$ is small enough when evaluated in both f_1 and f_2, for instance $\rho(\mathbf{J}) \lesssim 0.1$. This restricts the check of the diagonality index magnitude to two single chosen frequencies instead of across the entire frequency range. Figure 3.6(b) shows $\rho(\mathbf{J})$ for all the datasets considered in the parametric study, with $f_{s,1}$ ranging from 0.15 to 0.25 Hz. Without surprise, the largest indexes are obtained for cases with close eigenfrequencies, as coupling terms are there the most significant, but are bounded to about 10%, which indicates that the magnitude of the truncated quadratic terms are of order of $0.1^2 = 1\%$.

3.6.2 Results

As introduced in the previous section, the second natural frequency is taken as a variable parameter ranging from 0.15 to 0.25 Hz. In total, 80 values have been sampled in this range, and therefore, the analysis is conducted for 80 different pairs of wind-off natural frequencies $(f_0,\ f_1)$. Each combination is represented by one point in Figures 3.7, 3.8, 3.9 and 3.10. Note that since several data modifications have been made from the initial statement [46], results must be compared with care.

Figure 3.7(a) also shows a red dashed line at 30 m/s materializing the average wind velocity at which the structure will be assessed indicating that all points considered are subcritical ($U_{\text{cr}} >$ 30 m/s). The critical velocities decrease gradually as $f_{0,1}$ approaches 0.2 Hz, which is an expected

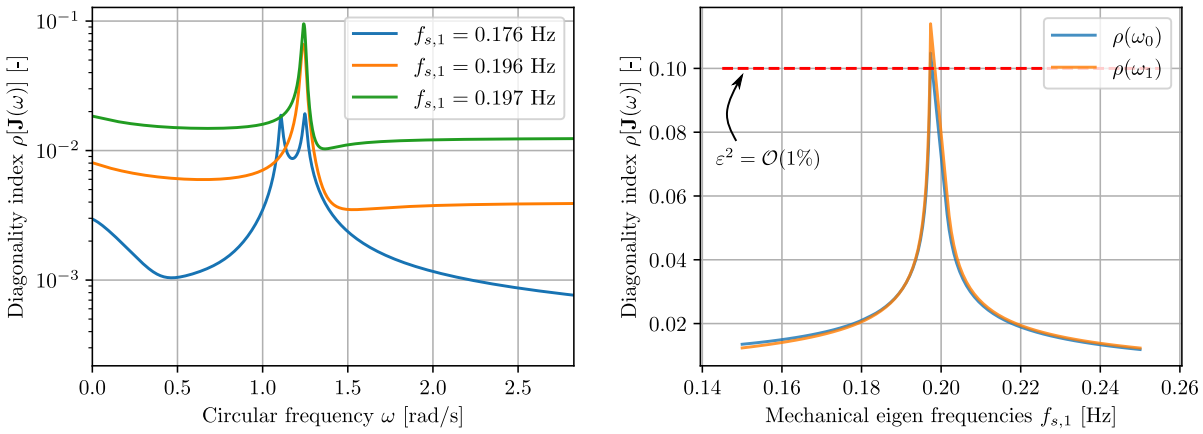

Figure 3.6: Diagonality index $\rho(\mathbf{J})$ (a) as a function of ω for three particular pitch natural frequencies $f_{s,0}$, and (b) for all points of the parametric study, evaluated in the aeroelastic eigenvalues ω_0 or ω_1.

behaviour as the modal coupling is more important as the eigen frequencies are closer. In addition, since the instability is here instigated by frequency matching, fewer aeroelastic effects —and thus lower wind speeds— are required to match the eigen frequencies. The zone defined by frequencies higher than 0.2 Hz is characterized by an unconditionally flutter safe behaviour.

A similar asymptotic behaviour is observed in Figure 3.7(b), which shows the evolution of the modal damping ratios at 30 m/s with the mechanical frequency of the second mode f_1. The closer $f_{s,1}$ to 0.2 Hz, the lower the critical velocity and therefore, at fixed considered speed $U = 30$ m/s, the more important the aeroelastic effects. This explains why the damping ratio deviates from its wind-off values as $f_{s,1}$ approaches 0.2 Hz.

Figure 3.8 (a) and (b) show the modal variance of the structural response in the two modes. Again, an asymptote is well marked when $f_{s,0} = f_{s,1} = 0.2$ Hz for the same reason as discussed previously. The exact variance of the response is evaluated from the integration of the modal response power spectral density (3.27), using a very fine frequency mesh of 10^5 points uniformly distributed in the range $[0^+;\ 10$ Hz$]$. The MTSA solution is obtained from direct application of (3.41). Both approaches are in excellent agreement. This is also confirmed by the relative errors in (c) and (d) with respect to the exact variances that never seriously exceed the 1% reference value. The same order of magnitude was obtained for the relative error committed on the variances in the SDOF model developed in [105], where a very similar MTSA approach was used.

The covariance $\Sigma_{\theta h}$ obtained with the exact and MTSA methods are represented in Figure 3.9. Again, a good match between the two approaches is observed, in spite of some slight deviations observed when $f_{s,1}$ is near 0.2 Hz. Indeed, the points located on the immediate left of the asymptote have a critical speed lower than those a bit further, and are therefore subjected to more aeroelastic effects, so that the resulting coupling terms are there greater as one gets closer to 0.2 Hz, which violates the requirements of the small coupling assumption of Section 3.2, and consequently the accuracy of the series expansion (3.33).

The correlation coefficient plays a role of primary interest in modal response recombination [96]. It is mathematically expressed by

$$\rho_{ij} = \frac{\Sigma_{ij}}{\sqrt{\Sigma_{ii}\Sigma_{jj}}}. \tag{3.91}$$

The nodal variance is obtained by modal superposition. We assumed earlier $\mathbf{x}(t) = \sum_i \boldsymbol{\phi}_i^R q_i(t)$,

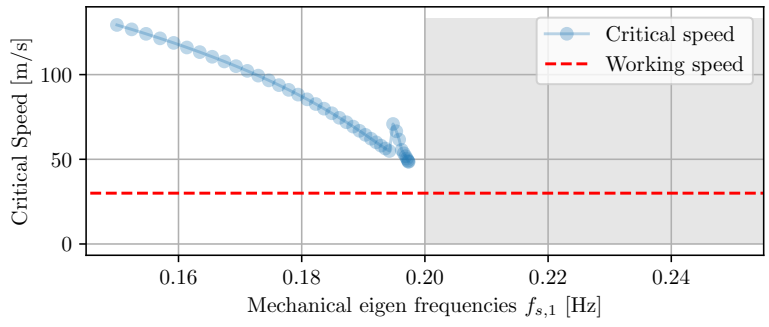

(a)

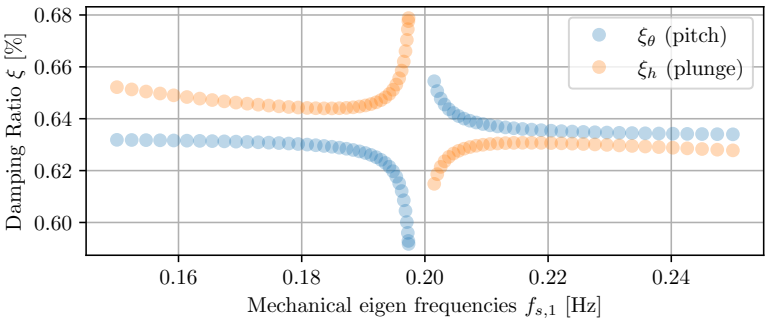

(b)

Figure 3.7: (a) Evolution of the critical velocities with respect to the wind-off second mode natural frequency $f_{s,1}$. The gray area is unconditionally stable (flutter velocity is infinity). (b) Evolution of the modal damping ratios for pitching and plunging motion at 30 m/s.

which gives

$$\Sigma_{x,ij} = \sum_m \sum_n \Phi^R_{im} \Sigma_{mn} \Phi^R_{nj} \tag{3.92}$$

where $\mathbf{\Phi}^R = \begin{bmatrix} \boldsymbol{\phi}^R_1 & \cdots & \boldsymbol{\phi}^R_N \end{bmatrix}$ gathers all modes ordered by columns. This double sum can be split into 2 contributions [96] to better highlight the influence of the modal correlation coefficients,

$$\Sigma_{x,ij} = \sum_m \Phi^R_{im} \Phi^R_{jm} \Sigma_{mm} + \sum_m \sum_{\substack{n \\ n \neq m}} \Phi^R_{im} \Phi^R_{jn} \rho_{mn} \sqrt{\Sigma_{mm} \Sigma_{nn}} \tag{3.93}$$

The first sum accounts only for the diagonal elements of the covariance matrix, and is known to enter in the famous *square root of the sum of the square* recombination process (SRSS). When all terms of the covariance matrix are considered during the recombination, the process is referred to as *complete quadratic combination* (CQC). In the second term appears the correlation coefficient ρ_{mn}. Its magnitude, bounded to $[-1; 1]$ quantifies directly the importance of the contribution of the correlation between the modes m and n to the nodal variance. The SRSS is basically a CQC neglecting all the correlation coefficients, and should therefore be recommended only if all modes of the basis are indeed uncorrelated. However, it remains sometimes preferred to CQC as it does not require the evaluation of the full covariance matrix, but only its diagonal elements reducing the computational demand of the operation [96, 107].

Figure 3.9(c) illustrates the evolution of the correlation coefficient with respect to $f_{s,1}$, along with the absolute error compared to the exact value. The MTSA method once again provides an accurate estimation of the actual correlation coefficients across the entire $f_{s,1}$ range. A notable asymptote appears at 0.2 Hz, where modal correlation is particularly significant. In this region, the coefficients are estimated with an error of approximately 1% to 2%.

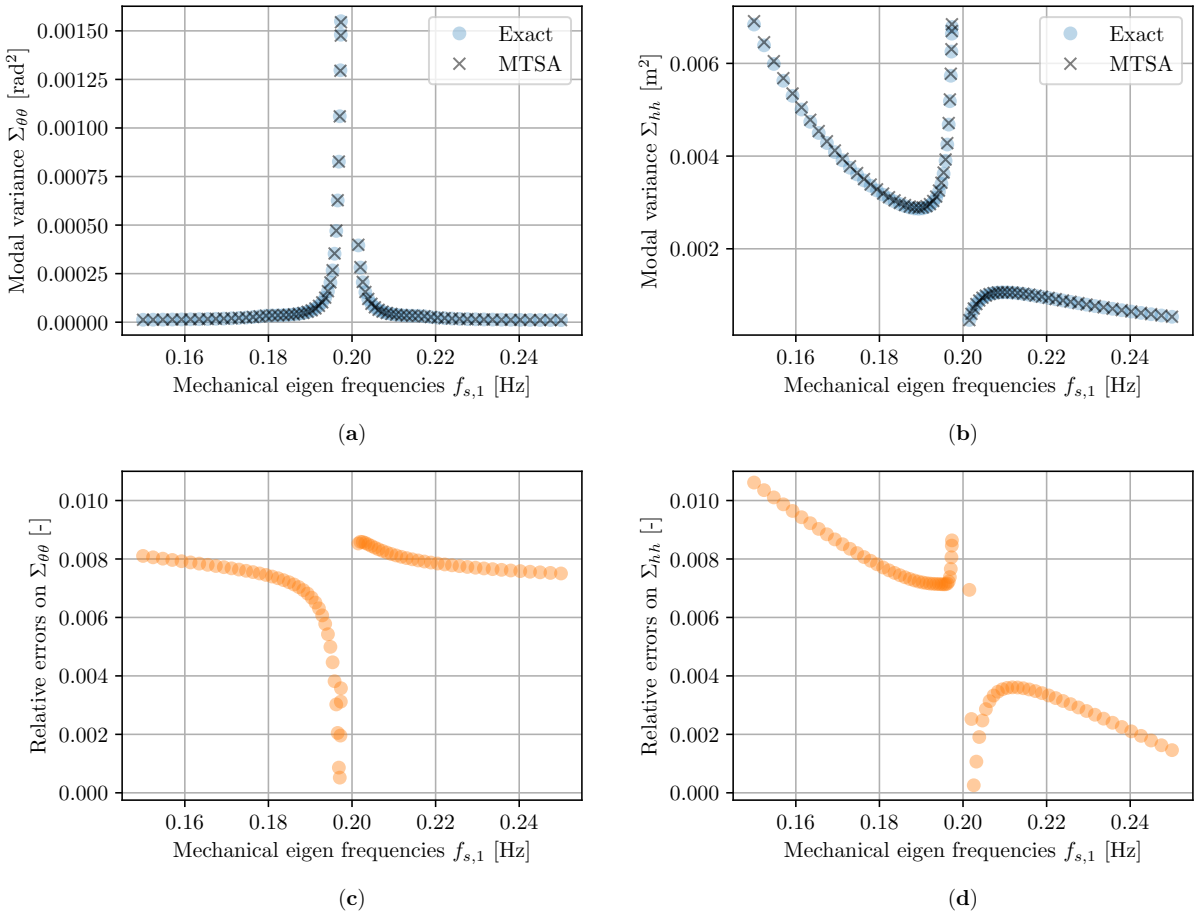

Figure 3.8: Evolution of the modal variances for pitch (a) and plunge (b), and associated relative errors with respect to the exact solution (c) and (d). Results obtained for $\beta = 0.1$, and $U = 30$ m/s.

Figure 3.10 presents the nodal variances at points A and B, located at the center of the deck and 15 meters from the center, respectively, as shown in Figure 3.3(b). The variances are computed using either the Complete Quadratic Combination (CQC) or the Square Root of the Sum of Squares (SRSS) method, with both the exact and MTSA covariance of modal coordinates. This results in three different approximations, in addition to a reference solution (CQC with exact variances).

For values of $f_{s,1}$ outside the range $[0.19, 0.21]$ Hz, all three approximations—SRSS with exact variances, and both SRSS and CQC with MTSA variances—closely match the reference solution at point A, with errors consistently below 1%, regardless of the chosen method. However, within the range $[0.19, 0.21]$ Hz, the SRSS approach fails to capture modal coupling, leading to errors exceeding 10% as $f_{s,1}$ approaches 0.2 Hz. In contrast, the CQC MTSA method maintains a high level of accuracy throughout This trend is also evident in Figure 3.10(c), which shows that using CQC instead of SRSS significantly improves the approximation. The error remains within 1% to 2% for the CQC MTSA method, whereas the SRSS-based approaches exhibit errors exceeding 20% near 0.2 Hz.

Similarly, Figure 3.10(b) shows the nodal variance at point B, once again highlighting the strong agreement between the CQC predictions and the reference solution. The error distribution in Figure 3.10(d) confirms that the CQC method maintains an accuracy of approximately 1% across the entire $f_{s,1}$ range, except in the interval $[0.19, 0.21]$ Hz, where errors associated with SRSS combinations exceed 10%. This coincides with the region of higher correlation coef-

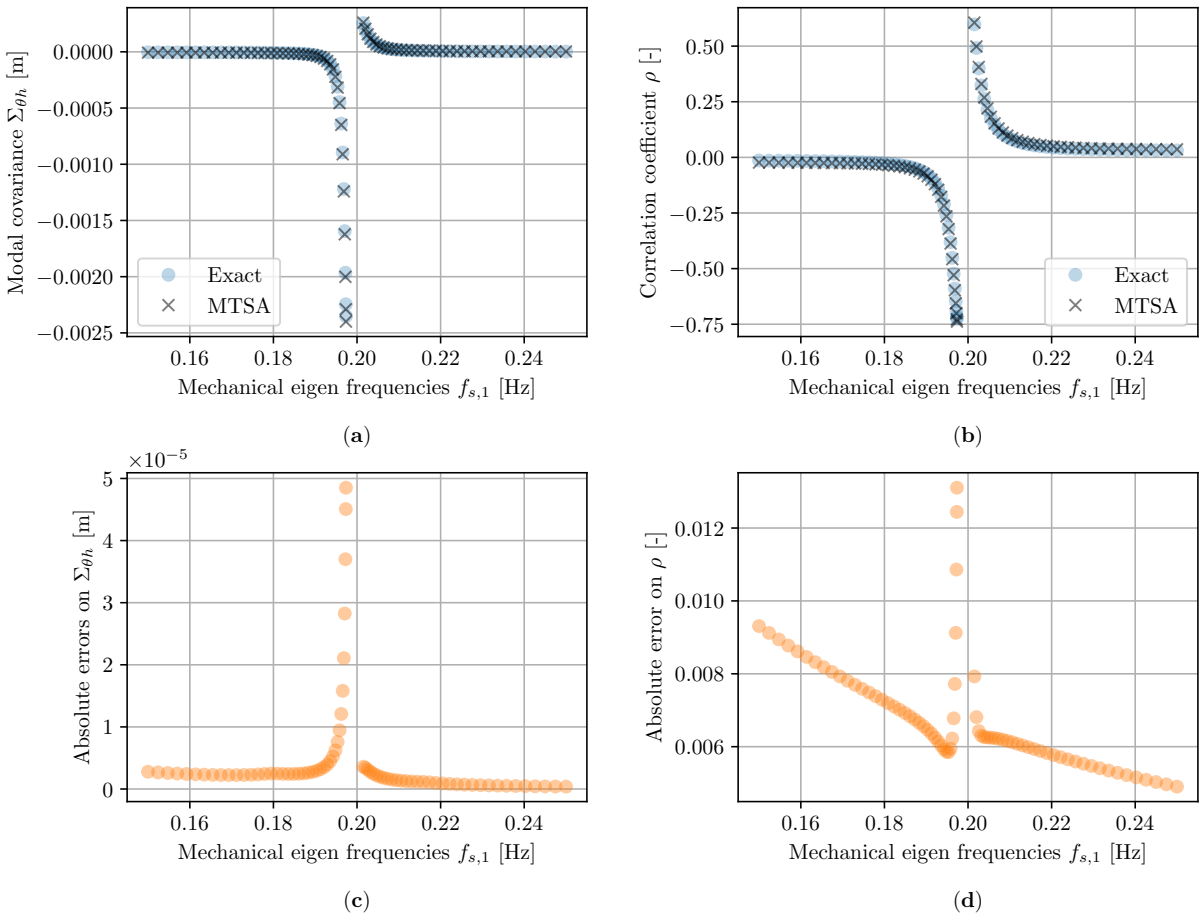

Figure 3.9: (a) Evolution of the modal covariance for the exact solution and the MTSA approximation with respect to the wind-off pitch eigenfrequency $f_{s,1}$. (b) Correlation coefficients for the exact solution and MTSA approximation with respect to the wind-off plunge eigenfrequency $f_{s,1}$. (c) Absolute errors in modal covariances estimated using the MTSA method compared to exact covariances. (d) Error in correlation coefficients when using the MTSA method. Results are obtained for $\beta = 0.1$ and $U = 30$ m/s.

ficients, as seen in Figure 3.9(b), reinforcing the preference for CQC over SRSS in such cases. The advantage of the method presented in this work is particularly evident here: the semi-analytical formulation greatly accelerates covariance estimation, allowing CQC recombination to be performed nearly as efficiently as SRSS, while maintaining an error below 1

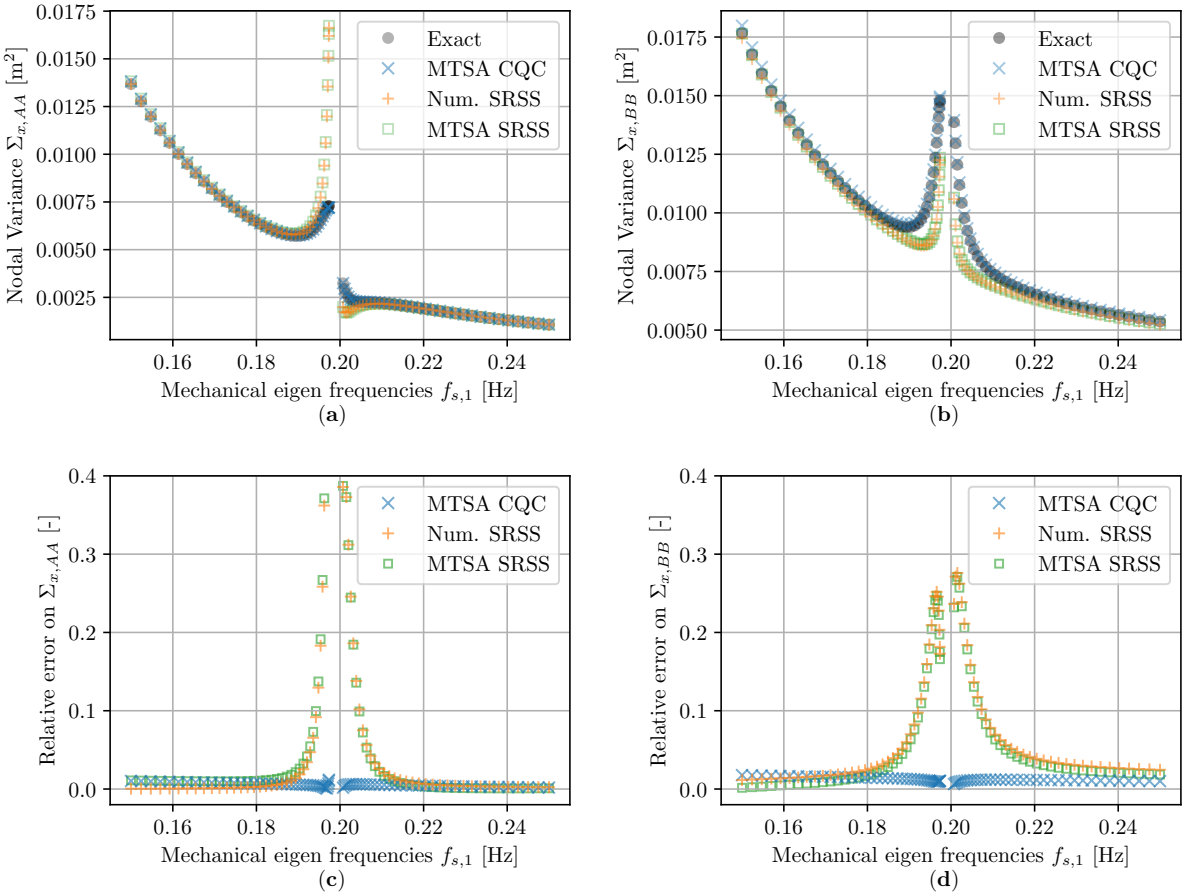

Figure 3.10: Nodal variances obtained from integration of the exact solution, from a CQC or SRSS recombination process with the exact solution or MTSA approximation: (a) vertical displacement in A (b) vertical displacement in B. Error committed on the exact nodal variance using an SRSS recombination with the exact solution, or using a SRSS or CQC with the MTSA approximation: (c) vertical displacement in A, (d) vertical displacement in B. Results obtained for $\beta = 0.1$, and $U = 30$ m/s.

3.6.3 The effect of the modal basis

The results presented in the previous section were obtained using the real projection of the eigenmodes obtained from the damped eigenvalue problem. This choice, though somewhat arbitrary, has the advantage of nearly diagonalizing the equations of motion while providing real-valued eigenmodes, which offers a simpler interpretation of the mode shapes. However, one might wonder: what if a simpler wind-off modal basis, derived from the undamped eigenvalue problem, was used instead? This section compares the performance of such a wind-off modal basis with the previously considered wind-on basis.

As shown in Figure 3.11, the diagonality index increases by a factor of approximately 3 in the disturbed region (when $f_{s,1}$ is around 0.2 Hz) when using the wind-off modal basis. The diagonality index is there about 5%. Additionally, the peak of $\rho(\mathbf{J})$ near 0.2 Hz appears less

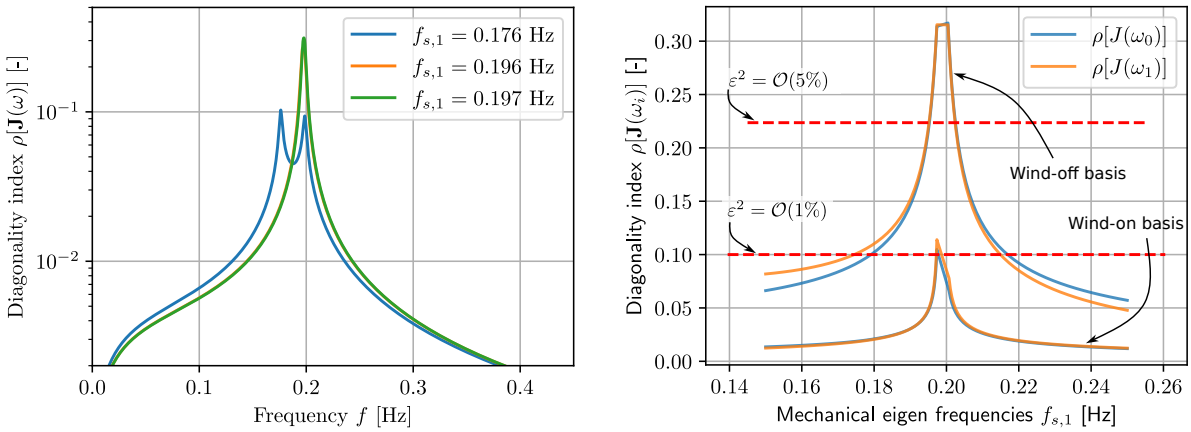

Figure 3.11: (a) Diagonality index $\rho(\mathbf{J})$ as a function of ω for three particular pitch natural frequencies $f_{s,1}$, considering the undamped wind-off eigenmodes, and (b) Comparison of the diagonality index for all points of the parametric study for the two considered modal bases.

pronounced than in the wind-on case. Above $\rho(\mathbf{J}) = 5\%$, the linearization of the PSD matrix using the small coupling assumption is expected to introduce significant deviations from the actual values.

Indeed, Figure 3.12 (a) shows that the wind-off modal basis provides accurate results outside the frequency range $[0.18, 0.22]$, where the diagonality index is small enough. However, around 0.2 Hz, severe deviations are observed, while the wind-on basis remains highly reliable in this region. For the displacement at point A, the relative error in Figure 3.12 (c) rapidly reaches 10%, suggesting that the wind-off modal basis should be avoided near this singularity. In contrast, the wind-on basis is particularly accurate in this region. A similar trend is observed in Figure 3.12 (d): although the error for the wind-on modal basis remains below 2%, the wind-off modal basis provides a lower error for the displacement at point B outside of the asymptotic region characterized by large diagonality index.

Overall, for this application, the wind-off modal basis generally yields less accurate results, limiting the applicability of the method to structures with light aeroelastic loading. A key observation is that the choice of modal basis directly influences the diagonality index and can significantly impact the method's efficiency. Therefore, selecting an appropriate modal basis is crucial when applying the proposed approximation method.

3.6.4 Results with original aeroelastic damping formulation

The results discussed in the previous section rely on a modified formulation of the aeroelastic damping where the actual aeroelastic damping was rescaled by a factor $\beta = 0.1$ so that the modal coupling introduced by the unsteady loading remained limited. The parametric study is thus repeated, considering $\beta = 1$ (*i.e.* the intended unsteady loading) and an average wind speed $U = 20$ m/s. All other parameters given in Table 3.1 remain unchanged.

The diagonality index is first examined in Figure 3.13 and compared with the reference value $\sqrt{0.05}$, which corresponds to cases where the terms of order ϵ neglected in (3.33) may contribute up to 5% of the leading-order terms. Points exceeding this value are more likely to exhibit deviations of 5% or more on the response PSD and hence on the response covariances. For most of the parametric study, the diagonality index ranges from 0.1 to 0.25 but reaches significantly higher values near eigenfrequencies, sometimes exceeding 1. In these frequency regions, the small-coupling assumption no longer holds, as $\rho(\mathbf{J}) = \mathcal{O}(1)$, leading to less accurate approximations.

Figure 3.14 illustrates the variance of the modal displacements and the associated errors with respect to the exact solution. The same asymptotic behaviour is obtained around $f_{s,1} = 0.2$ Hz:

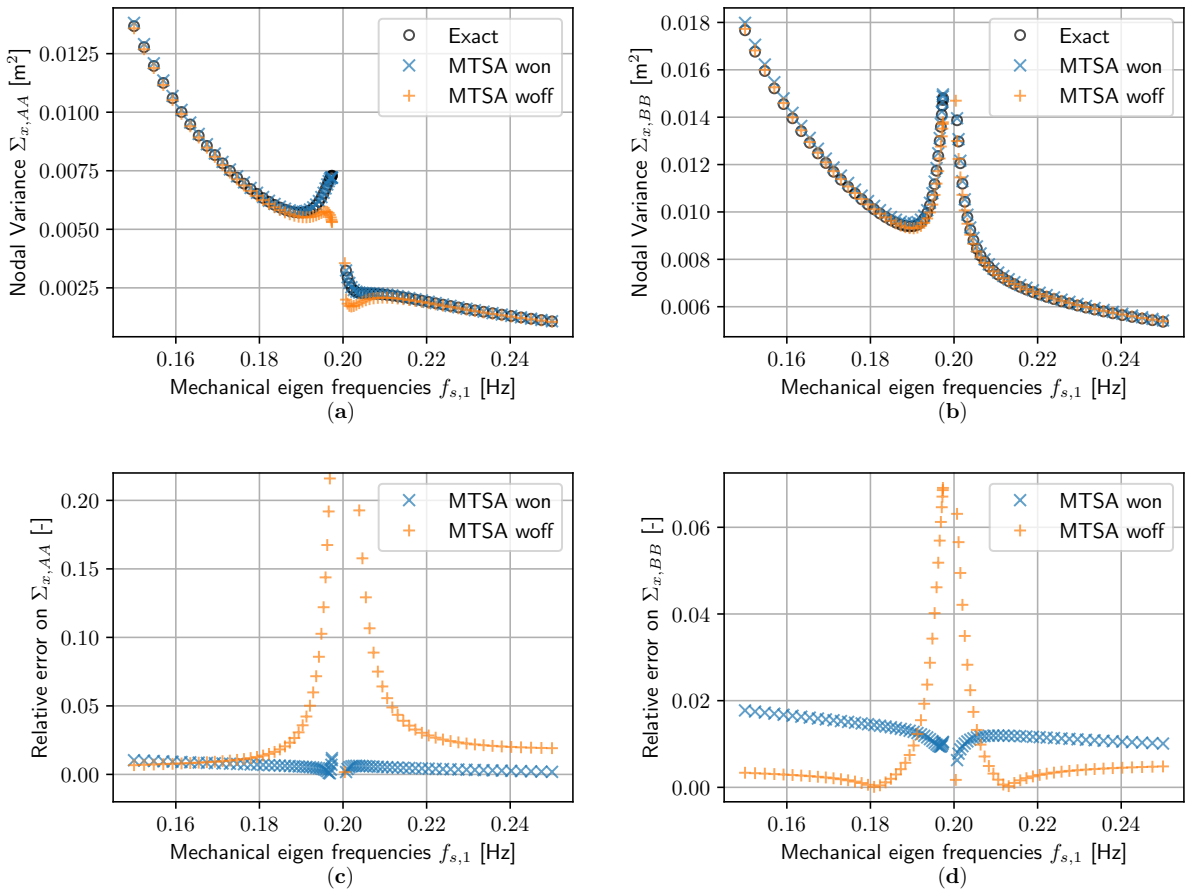

Figure 3.12: Comparison of the nodal variances of the vertical displacement in point A and B obtained using a wind-off undamped eigenmodes modal basis (woff), and a wind-on damped eigenmodes modal basis (won). Results obtained for $\beta = 0.1$, and $U = 30$ m/s.

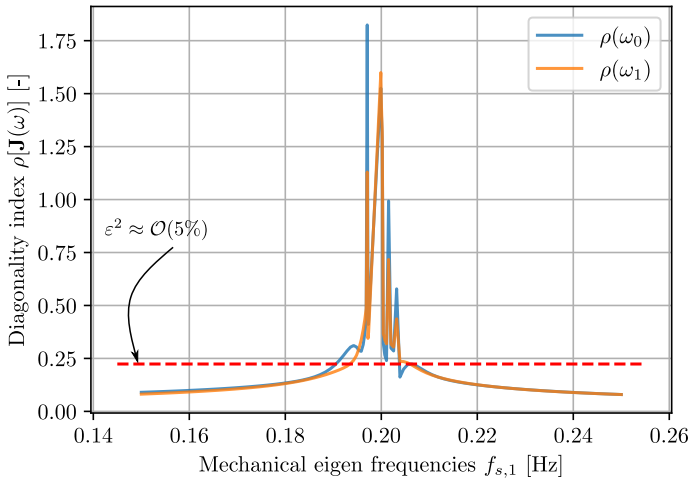

Figure 3.13: Diagonality index in ω_0 or ω_1 for all dataset of the parametric study with $\beta = 1$, and $U = 20$ m/s.

far enough from the singularity, the errors are somewhat higher or even comparable to those obtained in the case $\beta = 0.1$, but increase progressively as $f_{s,1}$ tends to 0.2 Hz to reach 10%, and finally exceeds 30% for the closest points to the asymptote. The MTSA method also predicts negative variances in Figure 3.14(b), which is of course impossible. This troubling and undesirable result is the consequence of the truncation of the term $\mathbf{S}_q^{\mathrm{III}}(\omega)$ in (3.37), supposed negligible when referring to the small coupling hypothesis. Without this truncation, the quadratic term $\mathbf{S}_q^{\mathrm{III}}(\omega)$ together with the three other terms defining (3.37) would have established a complex quadratic form for approximating $\mathbf{S}_q(\omega)$, whose integral would have necessarily been real and positive. The results obtained using a variant of the method presented here, by including the last term $\mathbf{S}_q^{\mathrm{III}}(\omega)$ in the series expansion of $\mathbf{S}_q(\omega)$ is presented in Section C.3. It is seen there that all variances are well strictly positive, even though the quality of the approximations provided for $f_{s,1} \in [0.19,\ 21]$ is not significantly more accurate.

The previous observations made on the variances are globally transposable to the covariances and the correlation coefficients (see Figure 3.15), for which the errors on the reference solution follow a very similar pattern. Apart from the points where $f_{s,1}$ is very close to 0.2 Hz, the correlation coefficient is estimated with a reasonable absolute error of 1 or 2%, and 5% in the worst cases. For the highly correlated responses, the MTSA method also returns correlation coefficients outside the interval $[-1, 1]$. This is again related to the importance of the diagonality index which is well above 25% in this region, rendering the MTSA approximation unreliable. In those cases however, the corresponding exact correlation coefficient is very close to 1 or -1, so that the predictions could be slightly improved if bounded to 1 or -1.

The displacement variances at points A and B (Figure 3.16) show that for $f < 0.2$ Hz, all methods perform well, with errors around 1%. The numerical SRSS method is slightly more accurate in this range, though CQC provides comparable results. Near $f = 0.2$ Hz, the error is large due to the importance of the coupling. SRSS methods are unable to capture the coupled response. The MTSA method does not provide better results in this range due to the magnitude of the diagonality index. At higher frequencies, the structure responds in the single vertical mode $\boldsymbol{\phi}_1$, and the 3% error aligns with the modal variance observed in Figure 3.14(b).

The displacement at point B is represented by two significantly coupled modes, which explains why SRSS methods offer a very poor representation of this structural motion. Outside of the zone centred on 0.2 Hz characterized by high diagonality index, the MTSA CQC performs quite well with an error of the order of 1%.

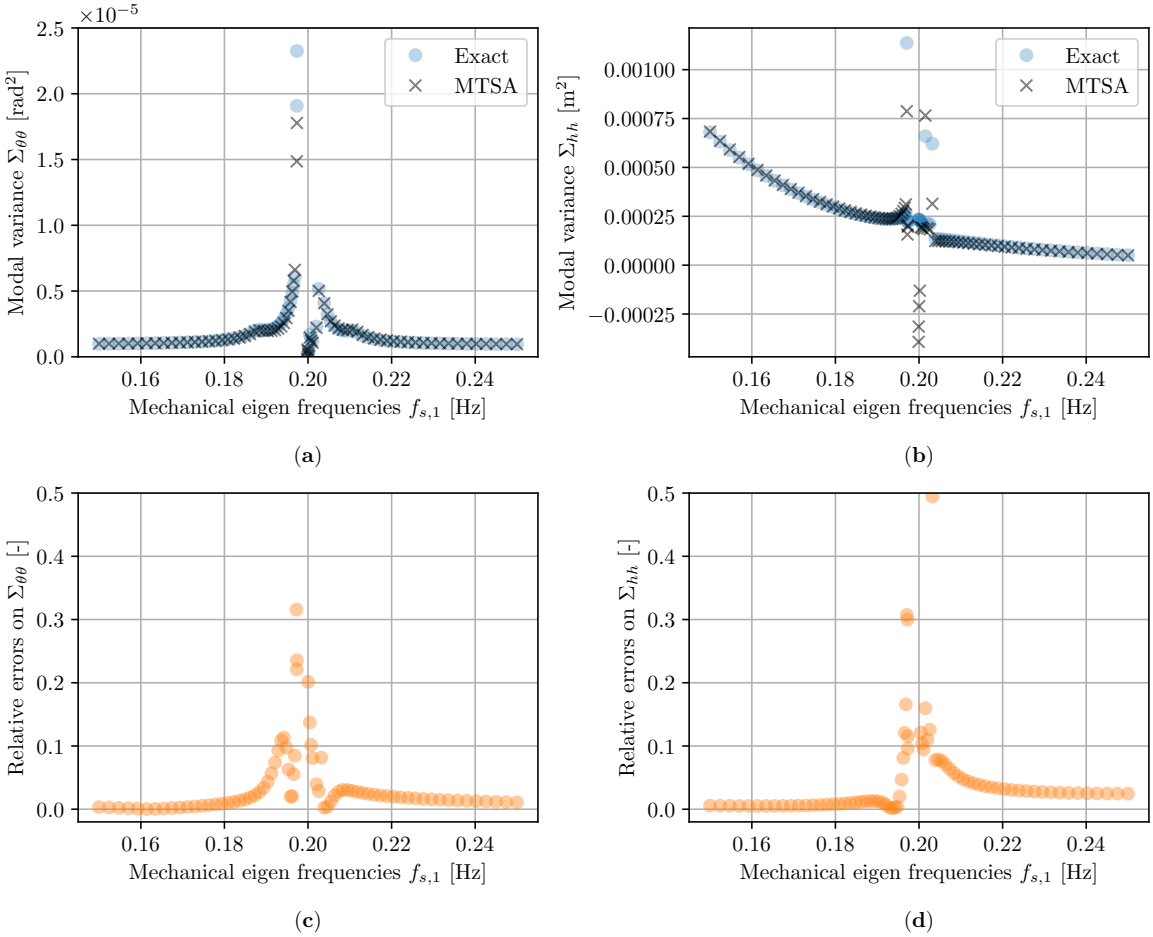

Figure 3.14: Evolution of the modal variances for pitch (a) and plunge (b), and associated relative errors with respect to the exact solution (c) and (d). Results obtained for $\beta = 1$, at $U = 20$ m/s.

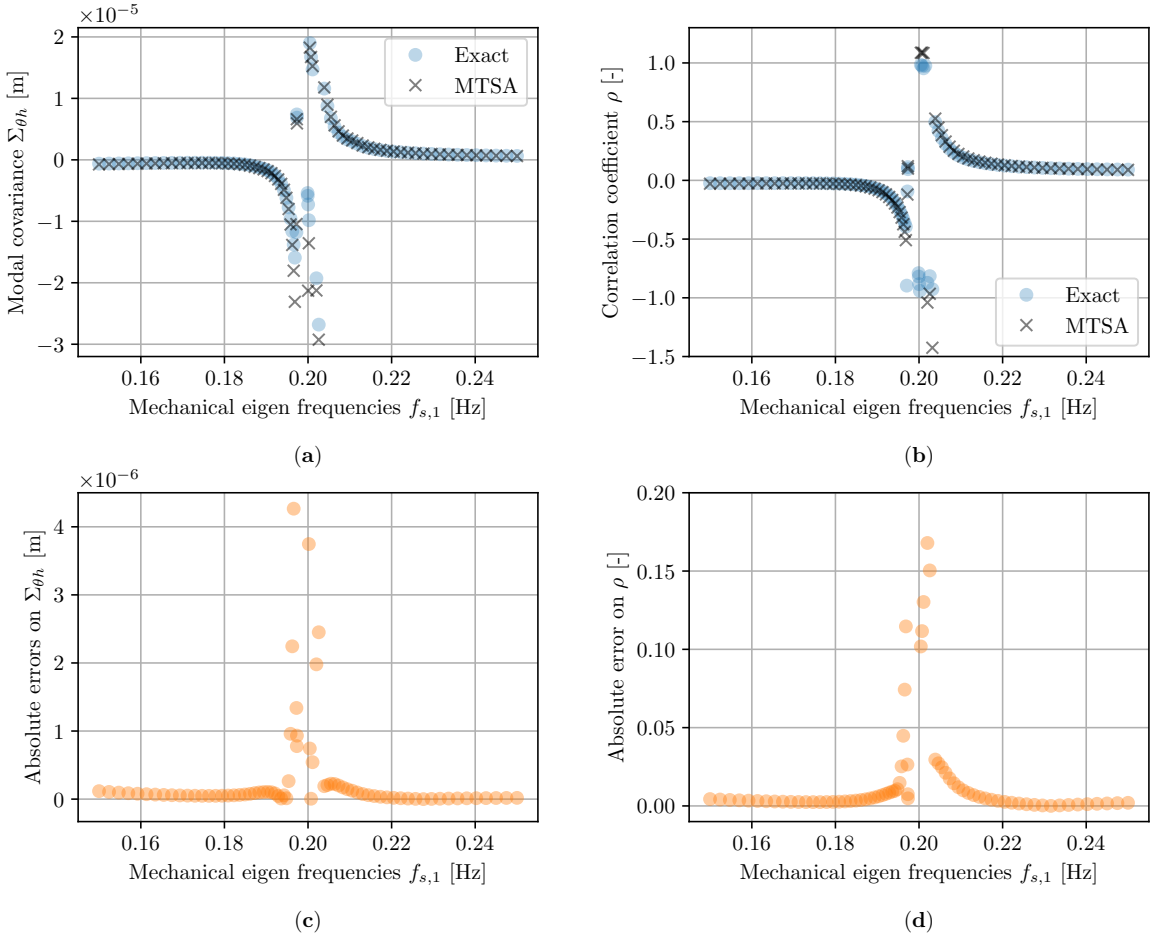

Figure 3.15: (a) Evolution of the modal covariance for the exact solution, and the MTSA approximation with respect to the wind-off pitch eigen frequency $f_{s,1}$. (b) Correlation coefficients for the exact solution, and MTSA approximation with respect to the wind-off plunge eigen frequency $f_{s,1}$. (c) Evolution with the $f_{s,1}$ of the absolute errors on modal covariances evaluated with the MTSA method on exact covariances. (d) Error committed on the exact correlation coefficients when using the MTSA method. Results obtained for $\beta = 1$, at $U = 20$ m/s.

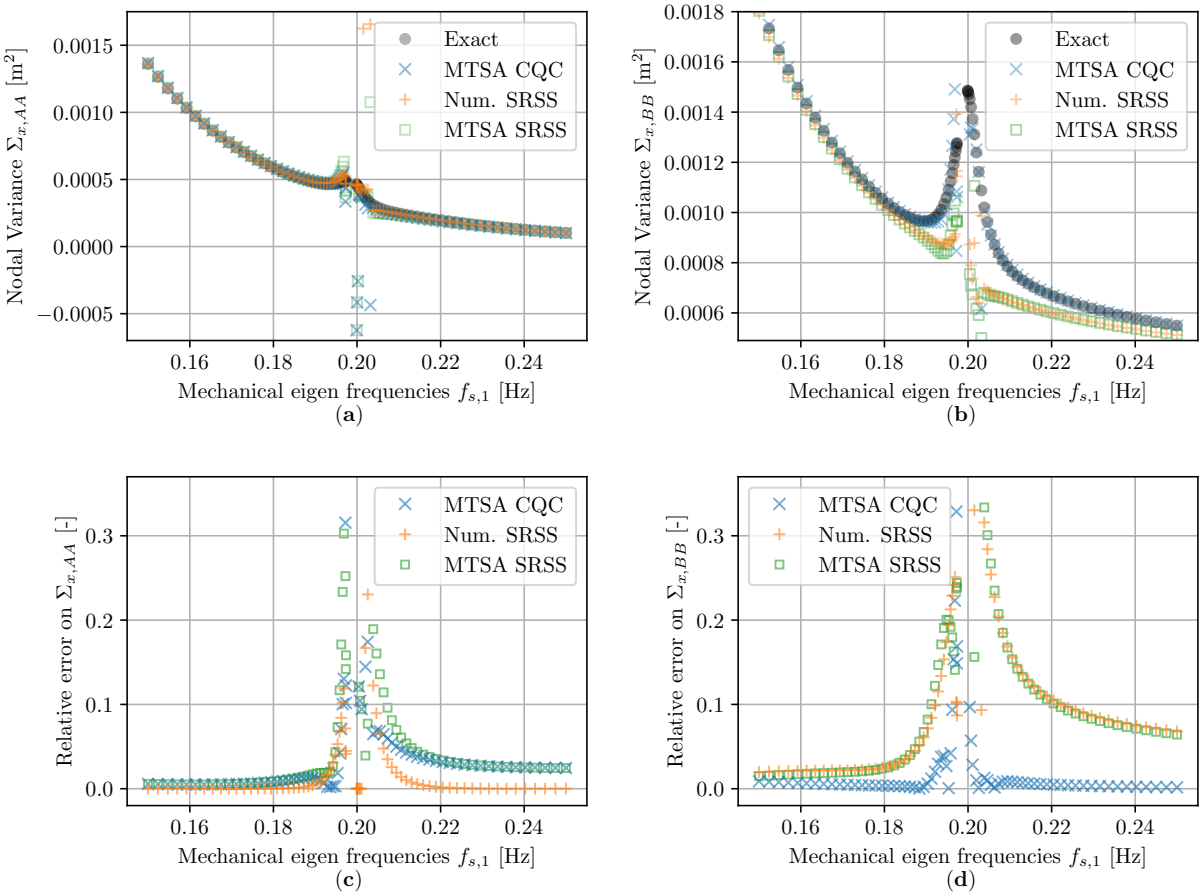

Figure 3.16: Nodal variances obtained from integration of the exact solution, from a CQC or SRSS recombination process with the exact solution or MTSA approximation: (a) vertical displacement in A (b) vertical displacement in B. Error committed on the exact nodal variance using an SRSS recombination with the exact solution, or using a SRSS or CQC with the MTSA approximation: (c) vertical displacement in A, (d) vertical displacement in B. Results obtained for $\beta = 1$, at $U = 20$ m/s.

3.7 Conclusion

This chapter introduced a 2DOF model for the aeroelastic analysis of simple structures, extending the SDOF model from Chapter 2 to bimodal systems incorporating the intermodal coupling effects, which are fundamental for many modern structures. In bridge flutter analysis, this model is typically applied as a pitch/plunge system, where the mass matrix remains independent of frequency.

The method hinges on several assumptions. First, the separation of dynamic timescales and the small damping assumption, both of which were introduced in the previous chapter. Then, the key new assumption is the slight coupling of the system, which allows for the linearization of the inverse of the transfer function without requiring an explicit matrix inversion, which should have been carried out numerically. The pseudo inverse is calculated by a succession of uncoupled problems which can be inverted and analysed with simple analytical formulas. The model provides a semi-analytical approach to evaluate response covariances, which are decomposed into background and resonant components. Each of these components consists of three contributions of *a priori* comparable magnitude, derived from the asymptotic expansion of the slightly coupled flexibility matrix.

To reduce the computational cost of flutter analysis, the model is formulated in a modal basis. Several modal bases have been introduced and classified into two categories: wind-off and wind-on modal bases. The wind-off basis consists of eigenmodes computed in wind-off conditions, ignoring aeroelastic effects, while the wind-on basis includes eigenmodes computed at a given wind speed, accounting for unsteady aeroelastic contributions to stiffness and damping. Additionally, eigenmodes can be derived from either the damped or undamped eigenvalue problem —in wind-off or wind-on conditions. The undamped problem yields real-valued eigenmodes, whereas the damped problem results in complex eigenmodes. Due to the assumptions made in this chapter, the presented theory is however restricted to real-valued modes, but will be later relaxed.

The method was tested on a pitch-plunge model of the Storebaelt Bridge with a modified aeroelastic model, in the form of a parametric study of the plunge natural frequency. It demonstrated good accuracy in estimating the response covariance and correlation coefficients, with errors remaining below 1%. The modal variances were approximated with similar or even greater accuracy. Additionally, modal displacements were recombined to evaluate displacements at two specific points on the deck section at mid-span, using both CQC and SRSS recombinations with exact and approximate variances.

The same case was also analysed using the actual aeroelastic model of a flat plate, where the method continued to provide reliable estimates of (co)variances and correlation coefficients, provided the system remained only weakly coupled. The intensity of the modal coupling was also proven to be effectively quantified by a scalar indicator, the diagonality index, introduced as the spectral radius of a matrix derived from the exact dynamic flexibility $\mathbf{J}(\omega)$. The second illustration showed that the quality of the estimation was directly conditioned by this index, which, beyond 25%, predicts severe deviations from the exact solution.

The choice of the modal basis was also shown to significantly impact the diagonality index and, consequently, the accuracy of the method. Comparing the results obtained from the undamped wind-off eigenmodes with those of damped wind-on eigenmodes, it was found that the wind-on modal basis improved the diagonality index by a factor of three near the singularity, leading to better approximation quality. This highlights the need for careful selection of the modal basis when applying this method.

The extension of the B/R decomposition to a 2DOF aeroelastic system with modal coupling is successful, providing a simple semi-analytical expression for the covariance of modal responses. It constitutes a computationally efficient tool for engineers conducting iterative flutter design or parametric studies at early design stages. However, the benefit of this method for simple 2DOF models remains limited since a 2DOF pitch-plunge model runs in seconds on a computer today.

Its true potential lies in extending it to MDOF aeroelastic systems as explored in [38, 108, 109, 110], enabling systematic assessment of all possible modal interactions in structures subject to multimodal flutter, where computational cost remains a critical factor.

Chapter 4

The MDOF model

In Chapter 3, an extension of the background/resonant decomposition to 2DOF modal aeroelastic oscillators was presented. The pitch-plunge model with buffeting loading may be appreciated by practitioners because it runs rapidly and provides quick results in a few minutes or seconds, which is quite suitable when multiple iterations are required on the problem parameters at early design stages. This model however suffers from two serious disadvantages. First, it assumes that the pitching and heaving modes shapes are fully coherent along the span. This single-noded discretization is also preventing to model varying properties along the span, such as non-uniform section geometry, skewed or sheaved wind profile, spatial wind coherence, ... The second drawback is that two modes may not always be sufficient to capture and model all the aeroelastic energy involved in the system, even if the two modes are adequately selected. Indeed, over the last decades, numbers of applications have demonstrated that the 2D coupled flutter analysis was not sufficient to accurately predict their aeroelastic response [38, 76, 111, 112, 113]. This is particularly evident in cases where the out-of-plane transverse motion must be considered [76, 114], in which case a horizontal mode is supplemented to the selected heaving and pitching modes to build a 3D flutter analysis. More generally, higher modes may bring significant contribution and may thus require consideration, as presented in [111, 112, 113]. This issue does not only affect the critical velocity but also the behaviour of the system prior to flutter, for instance considering the curve veering phenomenon [115].

For these complex applications, the detailed aeroelastic behaviour is generally covered by a small number of modes, typically ranging from a few pairs to a dozen. One way to keep the computational loads as low as possible is to restrict the number of modes in the analysis, incorporating only the aeroelastically responding ones. As it was the case for 2DOF applications, the quality of the conducted flutter analysis is hence conditioned by the selection of the modes considered in the analysis. This selection is largely based on the experience of the designer to identify the aeroelastic responding modes among the modal basis, considering their aeroelastic sensitivity, their orthogonality and their eigenfrequencies. The complexity of this selection process increases thus with the number of modes under consideration, and is certainly not a trivial process especially for complex modern structures exhibiting modes shapes sometimes far from being sinusoidal. To prevent any issue pertaining to the identification of aeroelastic responding modes, it is often preferred to incorporate all the modes of the basis in the flutter analysis. This approach is designated as a full-mode or full-order flutter analysis, and is considered at the price of an increase in computational load [77, 78, 112]. This is particularly emphasized here as we target the entire buffeting response for many wind velocities, from $U = 0$ m/s to the critical wind velocity.

Although a full-order flutter analysis involving up to 50 modes remains computationally feasible, its cost becomes increasingly significant when the procedure must be repeated multiple times —such as during iterative design phases. In such contexts, full-scale analyses may consume substantial time and resources on a day-to-day basis. This is precisely where the approximation

developed in this thesis proves valuable: it offers a notable reduction in computational cost for high-order flutter analyses, with only a minor trade-off in accuracy. As discussed in Section 1.6, the performance gains enabled by this approach grow with the size of the system, making it particularly well-suited for large MDOF configurations.

In essence, the extension of the proposed method to MDOF systems remains conceptually consistent with the 2DOF case. The approach continues to rely on approximating the covariance matrix by addressing two-by-two modal interactions. While the covariance matrix grows in size due to the additional modes considered, the underlying methodology remains unchanged beside that each mode may potentially be coupled with all the other modes, while coupling was limited to the only two existing modes of the 2DOF approach. Therefore, for each element of the covariance matrix Σ_{ij}, the interaction between modes i and j is considered, but also the possible interactions between mode j and all the other modes $k = 1, \ldots, M$. This matter will be discussed later in this chapter.

Compared to the previous chapters, the treatment of MDOF systems causes additional difficulty due to their increased dimensionality. As shown earlier, the background/resonant decomposition method relies on several key inputs —namely, the aeroelastic eigenvalues, eigenmodes, and the critical velocity— which must be determined with care as the size of the system grows. Specific efforts were thus dedicated to the development of numerical tools for the systematic computation of both the subcritical behaviour and critical state. While the subcritical (buffeting) response is analyzed in this chapter, Chapter 5 introduces a method to track the evolution of the modal properties with wind speed, and Chapter 6 focuses on the generation of critical maps to assess system stability. Additionally, some transversal aspects related to the practical implementation of the B/R method for large MDOF systems are covered by this chapter, notably in Section 4.4.

The distribution of the aeroelastic eigenfrequencies introduces another significant problem. Unlike 2DOF systems, where the only two eigenfrequencies are often considered close to each other (otherwize the analysis looses its interest), MDOF systems can exhibit a much broader frequency spectrum. In the 2DOF case, the local approximation of the flexibility matrix was validated over a restricted frequency band, where series expansions offered trustful local approximations. However, this linearization must now hold over a considerably wider range. This increased dispersion of eigenfrequencies necessitates a reconsideration of certain assumptions and intermediate results derived for 2DOF systems, as they may no longer be valid for large MDOF structures. One such aspect is the expansion of the dynamic flexibility, $J_{d,i}(\omega)$. To address this, an alternative expansion is proposed in Section 4.2 to better accommodate the wider frequency range. White-noise approximation is the second assumption rendered incompatible by this broader frequency range. This approximation invoked in the evaluation of the structural response assumes that the wind buffeting modal force is constant across the frequency range of interest. While this is reasonable for narrow frequency bands restricted to sharp resonant peaks, it becomes problematic when applied over wider ranges, especially for systems with low fundamental natural frequencies considering the exponential decay of the power spectral density at higher frequencies. An alternative to the white-noise approximation for system with broad frequency spectra will be discussed in Section 4.4.1.

Finally, another important consideration in applying the background/resonant decomposition, as established in the previous Chapter 3, concerns the diagonality of the flexibility matrix, monitored using the diagonal index. An efficient way to reduce it lies in the choice of the modal basis. Until now, we have superficially investigated the interest of a wind-on eigenmode basis, but relied exclusively real mode shapes. However, alternative choices could further decouple the modal equations, which is necessary for a better conditioning of the MTSA formulation. Several options, including wind-off or wind-on eigenmodes and real or complex eigenmodes, will be explored in detail in Section 4.6.4.

4.1 The complex modal forces

In Chapter 3, we have assumed that the modal force PSD matrix was real. The wind spectrum and coherence functions being real valued, the nodal forces are indeed always real in the case of of buffeting excitations. However, if a complex modal basis is considered, the result of modal projection becomes accordingly complex. While Chapter 3 has highlighted the interest of using such complex mode shapes for a better diagonalization of the system matrices, the assumption of real valued modal forces prevented the use of such complex modal basis. This assumption may be dropped by reformulating (3.36), rewritten

$$\mathbf{S}_q(\omega) = \big[\mathbf{H}_d(\omega) - \mathbf{H}_d(\omega)\mathbf{J}_o(\omega)\mathbf{H}_d(\omega)\big]\mathbf{S}_p(\omega)\big[\mathbf{H}_d(\omega) - \mathbf{H}_d(\omega)\mathbf{J}_o(\omega)\mathbf{H}_d(\omega)\big]^*, \tag{4.1}$$

as follows

$$\mathbf{S}_q(\omega) = \mathbf{S}_q^{\mathrm{I}}(\omega) + \mathbf{S}_q^{\mathrm{II},A}(\omega) + \mathbf{S}_q^{\mathrm{II},B}(\omega) + \mathbf{S}_q^{\mathrm{III}}(\omega), \tag{4.2}$$

with

$$\left|\begin{aligned}
\mathbf{S}_q^{\mathrm{I}}(\omega) &= \mathbf{H}_d(\omega)\mathbf{S}_p(\omega)\overline{\mathbf{H}}_d(\omega) && \text{(4.3a)}\\
\mathbf{S}_q^{\mathrm{II},A}(\omega) &= -\mathbf{H}_d(\omega)\mathbf{J}_o(\omega)\mathbf{H}_d(\omega)\mathbf{S}_p(\omega)\overline{\mathbf{H}}_d(\omega) && \text{(4.3b)}\\
\mathbf{S}_q^{\mathrm{II},B}(\omega) &= -\mathbf{H}_d(\omega)\mathbf{S}_p(\omega)\overline{\mathbf{H}}_d(\omega)\mathbf{J}_o^*(\omega)\overline{\mathbf{H}}_d(\omega) && \text{(4.3c)}\\
\mathbf{S}_q^{\mathrm{III},A}(\omega) &= \mathbf{H}_d(\omega)\mathbf{J}_o(\omega)\mathbf{S}_p(\omega)\overline{\mathbf{H}}_d(\omega)\mathbf{J}_o^*(\omega)\overline{\mathbf{H}}_d(\omega) && \text{(4.3d)}
\end{aligned}\right.$$

The only difference with (3.39) is that $\mathbf{S}_q^{\mathrm{II}}(\omega) = \mathbf{S}_q^{\mathrm{II},A}(\omega) + \mathbf{S}_q^{\mathrm{II},B}(\omega)$ can no longer be expressed as the sum of two complex conjugate terms. In this way, $\mathbf{S}_q(\omega)$ can be expressed with a complex modal basis. This development is a first order expansion of the response PSD: $\mathbf{S}_q^{\mathrm{I}}$ being $\mathcal{O}(1)$, $\mathbf{S}_q^{\mathrm{II}}$ being $\mathcal{O}(\varepsilon)$ and $\mathbf{S}_q^{\mathrm{III},A}$ being $\mathcal{O}(\varepsilon^2)$. Even though it contains one second order term, it is however incomplete to be a full quadratic expansion of $\mathbf{S}_q$.

Following the modification of the expansion of the response PSD matrix, the expressions of the background and resonant approximation of the response detailed in chapter 3 must be updated. They are expressed as the sum of the three terms

$$\boldsymbol{\Sigma}_{q,R} = \boldsymbol{\Sigma}_R^{\mathrm{I}} + \boldsymbol{\Sigma}_R^{\mathrm{II},A} + \boldsymbol{\Sigma}_R^{\mathrm{II},B}, \qquad \boldsymbol{\Sigma}_{q,B} = \boldsymbol{\Sigma}_B^{\mathrm{I}} + \boldsymbol{\Sigma}_B^{\mathrm{II},A} + \boldsymbol{\Sigma}_B^{\mathrm{II},B} \tag{4.4}$$

where

$$\Sigma_{B,ij}^{\mathrm{I}} = \int_{-\infty}^{+\infty} \frac{S_{F_{\mathrm{bu}},ij}(\omega)}{K_{d,i}(\omega)\overline{K}_{d,j}(\omega)}\,\mathrm{d}\omega, \tag{4.5}$$

$$\Sigma_{B,ij}^{\mathrm{II},A} = -\sum_k \int_{-\infty}^{+\infty} \frac{J_{o,ik}(\omega)S_{F_{\mathrm{bu}},kj}(\omega)}{K_{d,i}(\omega)K_{d,k}(\omega)\overline{K}_{d,j}(\omega)}\,\mathrm{d}\omega \tag{4.6}$$

and

$$\Sigma_{B,ij}^{\mathrm{II},B} = -\sum_k \int_{-\infty}^{+\infty} \frac{S_{F_{\mathrm{bu}},ki}(\omega)\overline{J}_{o,jk}(\omega)}{K_{d,i}(\omega)\overline{K}_{d,k}(\omega)\overline{K}_{d,j}(\omega)}\,\mathrm{d}\omega. \tag{4.7}$$

The resonant components will later be updated to incorporate later modifications discussed in the next sections.

4.2 Quadratic expansion of the diagonal flexibility matrix

4.2.1 Motivations

So far, an approximation of the diagonal flexibility $J_{d,i}(\omega)$ was found in (3.65), stretching the circular frequency ω in the neighbourhood of the resonant peak related to ω_i, by introducing

the small parameter ε, and truncating the result at leading order. An estimation of uncoupled frequency response matrix was then straightforwardly obtained by inverting this diagonal matrix. Let us now assume that the estimation approximates the actual frequency response matrix with an error ϵ, an other arbitrarily small number. In particular, focusing on the i-th component, the approximation $\mathcal{H}_{d,i}(\omega)$ is given by

$$\mathcal{H}_{d,i}(\omega) = \frac{1}{(1+\epsilon_i)J_{d,i}(\omega)} = \frac{1}{(1+\epsilon_i)}H_{d,i}(\omega). \tag{4.8}$$

Noting that the series expansion

$$\frac{1}{1+\varepsilon} = 1 - \varepsilon + \varepsilon^2 + \mathcal{O}(\varepsilon^3), \tag{4.9}$$

the diagonal transfer function (4.8) may be expressed at first order as

$$\mathcal{H}_{d,i}(\omega) = (1-\epsilon_i)H_{d,i}(\omega) \tag{4.10}$$

Equivalently, we consider that the off-diagonal elements of the flexibility matrix $J_{o,ij}$ are evaluated by $\mathcal{J}_{o,ij}(\omega)$ with a similar error

$$\mathcal{J}_{o,ij}(\omega) = (1+\epsilon_{ij})J_{o,ij}(\omega). \tag{4.11}$$

It is evident that, in reality, ϵ_i is a variable of ω, as the error committed on the exact $J_{d,i}$ is likely not constant over the whole frequency range. However, to ease the discussion, we will assume it is the case as it does not impact the final discussion. The approximations (4.8) and (4.11) are used to estimate the resonant component of the response spectra $\mathbf{S}_q^{R,\mathrm{I}}$, $\mathbf{S}_q^{R,\mathrm{II}}$ and $\mathbf{S}_q^{R,\mathrm{III}}$ in (4.3). Focusing on the second contribution $\mathbf{S}_q^{R,\mathrm{II},A}(\omega)$, an approximation $\mathcal{S}_{q,ij}^{R,\mathrm{II},A}(\omega)$ is found by substituting (4.8) and (4.11) in (4.3b)

$$\mathcal{S}_{q,ij}^{R,\mathrm{II},A} = \sum_k^M (1-\epsilon_i)H_{d,i}(\omega)\,(1+\epsilon_{ik})J_{o,ik}\,(1-\epsilon_k)H_{d,k}(\omega)S_{p,kj}(\omega)(1-\epsilon_j)\bar{H}_{d,j}(\omega). \tag{4.12}$$

Introducing ϵ a small number and Ξ_i, Ξ_j^k, Ξ_k^k and Ξ_{ik}^k four order-one parameters such as $\epsilon_i = -\Xi_i\epsilon$, $\epsilon_j = -\Xi_j^k\epsilon$, $\epsilon_k = -\Xi_k^k\epsilon$ and $\epsilon_{ij} = \Xi_{ik}^k\epsilon$, Equation (4.12) can be rewritten as

$$\mathcal{S}_{q,ij}^{R,\mathrm{II},A} = \sum_k^M (1+\Xi_i^k\epsilon)(1+\Xi_j^k\epsilon)(1+\Xi_k^k\epsilon)(1+\Xi_{ik}^k\epsilon)H_{d,i}(\omega)\bar{H}_{d,j}(\omega)H_{d,k}(\omega)J_{o,ik}(\omega)S_{p,kj}(\omega). \tag{4.13}$$

Expanding the products leads to the following series in ϵ

$$\begin{aligned}\mathcal{S}_{q,ij}^{R,\mathrm{II},A} = \sum_k^M \Big[1 + (\Xi_i^k + \Xi_j^k + \Xi_k^k + \Xi_{ik}^k)\epsilon + \left[\Xi_i^k(\Xi_j^k + \Xi_k^k + \Xi_{ik}^k) + \Xi_j^k(\Xi_k^k + \Xi_{ik}^k) + \Xi_k^k\Xi_{ik}^k\right]\epsilon^2 \\ + \left[\Xi_i^k\Xi_j^k(\Xi_k^k + \Xi_{ik}^k) + (\Xi_i^k + \Xi_j^k)\Xi_k^k\Xi_{ik}^k\right]\epsilon^3 + \Xi_i^k\Xi_j^k\Xi_k^k\Xi_{ik}^k\epsilon^4\Big]H_{d,i}(\omega)\bar{H}_{d,j}(\omega)H_{d,k}(\omega)J_{o,ik}(\omega)S_{p,kj}(\omega),\end{aligned} \tag{4.14}$$

where the first term may be seen as an amplification factor applied on the k-th contribution to PSD $S_{q,ij}^{R,\mathrm{II},A}(\omega)$ as expressed in (4.3b). This series can be truncated at first order to give

$$\mathcal{S}_{q,ij}^{R,\mathrm{II},A} = S_{q,ij}^{R,\mathrm{II},A} + \sum_k^M \Big[(\Xi_i^k + \Xi_j^k + \Xi_k^k + \Xi_{ik}^k)\epsilon\Big]H_{d,i}(\omega)\bar{H}_{d,j}(\omega)H_{d,k}(\omega)J_{o,ik}(\omega)S_{p,kj}(\omega). \tag{4.15}$$

where it is clear that the amplification factor $(\Xi_i^k+\Xi_j^k+\Xi_k^k+\Xi_{ik}^k)$ represents a first order truncated relative error committed on the k-th contribution of the sum of the exact PSD. This equation

shows that the acknowledgment a relative error of order ϵ on $H_{d,i}(\omega)$ and $J_{o,ik}(\omega)$, results in a relative error of order 4ϵ committed on each of the k terms of the sum of (4.3b).

But things are even worse when considering the results of the sum over the k terms. In a worst situation, each of these k terms has the same order of magnitude and thus brings similar contributions to $S^{R,\mathrm{II},A}_{q,ij}$, the relative error committed on $S^{R,\mathrm{II}}_{q,ij}$ then grows with the number of considered modes and is of order $4M\epsilon$, which is by far unacceptable. Hopefully, this assumption is not realistic. They are few reasons for this.

First, all modes of the structure will not be excited at the same time. As a consequence, large variations in magnitude of the PSD of the generalized modal forces must be expected. For instance, turbulence length scale can be such that only symmetric loads are excited. Also, the absence of coupling between mode i and k suffices to annihilate the k-th contribution since $J_{o,ik} = 0$.

Furthermore, as the number of modes M increases, they usually spread over an increasingly large frequency range. Depending on the distance between $\omega_{d,i}$, $\omega_{d,j}$ and $\omega_{d,k}$, the structural transfer functions, the aerodynamic admittance and the buffeting spectrum act as filters decreasing or amplifying one or another contribution whose energy distribution is not uniform over the frequency range. For instance, if we consider two distinct modes i and j with eigenfrequencies $\omega_{d,i}$ and $\omega_{d,j}$, the product $H_{d,i}(\omega)H_{d,j}(\omega)$ will be much smaller if $|\omega_{d,i} - \omega_{d,j}| \gg \frac{(\omega_{d,i}+\omega_{d,j})}{2}\frac{(\xi_i+\xi_j)}{2}$[1] than if $\omega_{d,i} \approx \omega_{d,j}$, especially if the structure is lightly damped because the two resonant regimes do not interfere. Additionally, since each contribution to the sum (4.15) is weighted by $S_{p,kj}(\omega)$, the k-th contribution with $k \gg 1$ and consequently with larger $\omega_{d,k} \gg \omega_{d,1}$ will be significantly smaller due to the exponential decay of the aerodynamic admittance, and that of the of the wind buffeting spectrum.

All these reasons show that only few values of k will contribute significantly to (4.3b), but it is difficult to identify them a priori, given the number of criteria to consider. As a consequence, the relative error $4M\varepsilon$ should be seen as a hypothetical upper bound of the relative error. A much reasonable, despite non conservative, estimate of this error could be obtained by replacing M by the number of significant contributors to the sum (4.3b), even though this number is impossible to determine a priori and may only be obtained after evaluation of each of the k contributions.

Although the number of contributors reduces to two or three, the resulting maximum relative error is of order $\mathcal{O}(10\varepsilon)$. This arguments fed our first motivation to relinquish the first-order expansion for approximating the dynamic flexibility, and using a higher order expansion.

Our second, equally, if not more compelling motivation to consider higher order approximations for $J_{d,i}(\omega)$ and $J_{o,ij}(\omega)$ arises also from this broader frequency range inherent to MDOF systems. Without considering aeroelastic effects, the dynamic flexibility is inherently a quadratic function of ω. While aeroelastic effects introduce variations, the overall shape of the impedance function generally maintains its quadratic nature. This behaviour contrasts sharply with the linear expansion adopted in Chapter 3 to approximate $J_{d,i}(\omega)$ and $J_{o,ij}(\omega)$. Although insignificant in 2DOF models, the discrepancy becomes more pronounced in MDOF systems, as the approximation is no longer confined to the vicinity of two closely spaced eigenfrequencies but instead extends over a broader frequency span, typically around 1 Hz. This linearization is fundamentally inadequate for capturing the quadratic behaviour of $J_{d,i}(\omega)$ and $J_{o,ij}(\omega)$ far from the point where the linearization was performed. Consequently, the decay of the transfer function $H_{d,i}(\omega)$ with frequency is insufficiently steep, leading to artificial residual energy being incorporated into $H_{d,i}(\omega)$ at high frequencies.

This problem is illustrated on a generic and minimalistic example in Figure 4.1 where the flexibility function $J_{d,i}(\omega)$ and its inverse $H_{d,i}(\omega)$ obtained with the exact and linearized formulations are compared, as a function of a dimensionless frequency $r = \omega/\omega_{d,0}$ with $\omega_{d,0}$ representing

[1] The distance between two frequencies could also be compared to the width of the resonant peak at half-power. In the case of SDOF harmonic oscillators, the width of the resonant peak is characterized using the quality factor $Q = 1/2\varepsilon$ giving $\Delta\omega = \omega_d/Q = 2\xi\omega_d$.

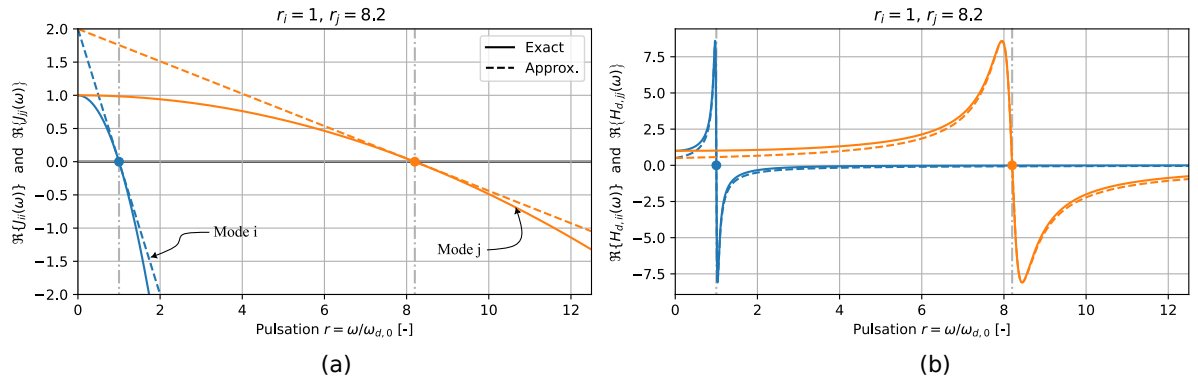

Figure 4.1: (a) Dynamic flexibility functions $J_{d,i}(\omega)$ and (b) Transfer functions $H_{d,i}(\omega)$ for mode i and j using exact and linearized formulations. This figure can be reproduced with $\omega_{d,0} = 2$ rad s^{-1}, $r_i = 1$, $r_j = 8.2$, $k_i = k_j = 1$ N m^{-1} and $\xi_i = \xi_j = 0.3\%$. No aeroelastic effects.

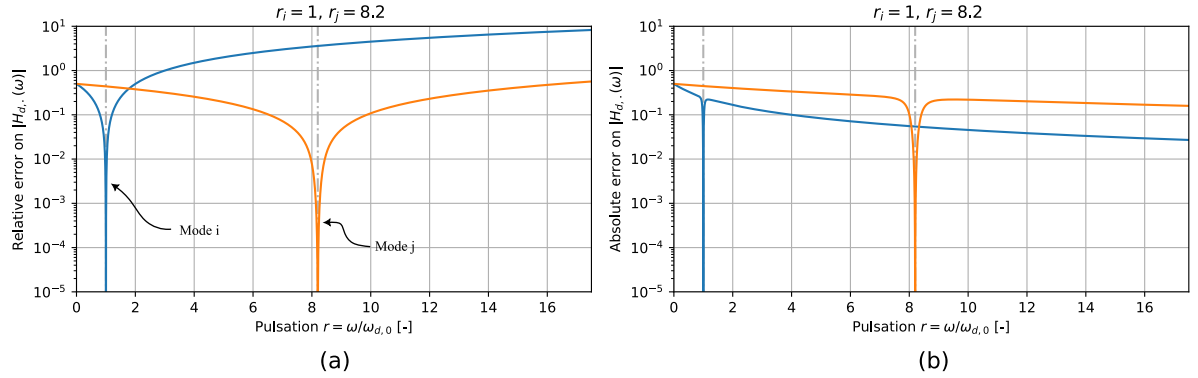

Figure 4.2: (a) Relative and (b) Absolute error on $J_{d,\cdot}(\omega)$ and $H_{d,\cdot}(\omega)$ for mode i and j using a first-order approximation. This figure can be reproduced with $\omega_{d,0} = 2$ rad s^{-1}, $r_i = 1$, $r_j = 8.2$, $k_i = k_j = 1$ N m^{-1} and $\xi_i = \xi_j = 0.3\%$. No aeroelastic effects.

the uncoupled fundamental eigenfrequency taken here equal to 2 rad/s. Two modes i and j are represented, respectively characterized by $r_i = \frac{\omega_{d,i}}{\omega_{d,0}} = 1$ and $r_j = \frac{\omega_{d,j}}{\omega_{d,0}} = 8.2$. The caption of the Figure summarizes the parameters used to reproduce this example. Close to the eigenfrequency of mode j *i.e.* around $r = 8.2$, the linear approximation of $J_{d,j}$ is quite trustful. But next to the fundamental eigenfrequency around $r \approx 1$, severe deviations are observed. Using this approximation for $H_{d,j}$ to approximate the response PSD would result in underestimating the actual energy in the region where $r < r_j$ and overestimating where $r > r_j$. Since the dynamic flexibility has always the same concavity due to the positiveness of the modal mass, linear approximation for $J_{d,i}$ will always results in underestimating the energy at lower frequencies while introducing residual energy at higher frequencies. This behaviour is also exposed in Figure 4.2, which shows the absolute and relative errors. While the errors remain low in the immediate vicinity of the eigenfrequency, they increase rapidly as the frequency moves further away, which is of course an expected behaviour. The absolute error decreases with increasing frequency, aligning with the decay of the transfer function. However, the relative error grows with r, translating the systematic underestimation or overestimation of the actual transfer function at frequencies far from the linearization point.

At this stage, after having compared $H_{d,\cdot}(\omega)$[2]and its approximation in Figure 4.1(b) and Figure 4.2(a), we may still be convinced that the linear approximation is convenient for our needs, and could be plugged straight in the response PSDs to build our approximation. However, this

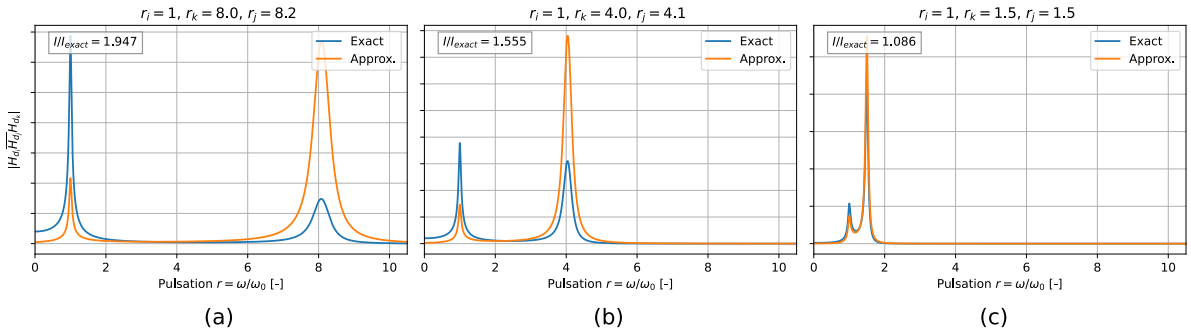

Figure 4.3: Comparison of $H_{d,i}(\omega)H_{d,k}(\omega)\bar{H}_{d,j}(\omega)$, obtained with exact and first order approximation for $H_{d,\cdot}(\omega)$. This figure can be reproduced with $\omega_{d,0} = 2\ \mathrm{rad\,s^{-1}}$, $r_i = 1$, $r_k = 8$, $r_j = 8.2$, $k_i = k_k = k_j = 1\ \mathrm{N\,m^{-1}}$ and $\xi_i = \xi_j = 0.3\%$. No aeroelastic effects.

would be forgetting the error accumulation arising when several approximations for $H_{d,i}$ and $J_{o,ij}$ are used together in a same product, for instance in (4.15). Figure 4.3 represents the product $H_{d,i}(\omega)H_{d,k}(\omega)\bar{H}_{d,j}(\omega)$ using the exact and first-order approximations for $H_{d,i}(\omega)$ and illustrates then how the separation between $\omega_{d,i}$, $\omega_{d,j}$ and $\omega_{d,k}$ may degrade the quality of the approximation of a single term of (4.15). The same synthetic data have been used to generate this example, and are detailed in the figure caption. This product is represented for three different triplets (r_i, r_k, r_j) to model various separations of the eigenfrequencies. In (a), modes i and j are well separated with $r_i = 1$ and $r_j = 8.2$, showcasing a dramatic overestimation of the first peak and an even worse underestimation of the second peak around $r = 8$. This is the result of the aforementioned over- and underestimations. In (b), this separation is reduced by 2, and the same conclusion holds regarding the quality of the approximation that remains very poor in the top left corner. In (c) the separation is significantly lower, and a better estimate is obtained. For each graph, the ratio between I and I_{exact}, respectively the integrals of the two functions, is shown top left, and demonstrates well how the exact integral of one term of (4.3b) could be badly approached if a first order approximation was used, if the resonant regimes are distant.

It is finally interesting to observe that this issue applies also for the terms of $S^{R,\mathrm{I}}_{q,ij}(\omega)$, albeit to a lesser extent. To illustrate this, the product $H_{d,i}(\omega)\bar{H}_{d,j}(\omega)$ is shown in Figure 4.4 for the same datasets. The same conclusion could globally hold for the approximations but the deviations seem less pronounced, and the integral is well better approximated. This is explained by the fact that $S^{R,\mathrm{I}}_{q,ij}(\omega)$ is a first-order term and does not accumulate errors, unlike higher-order terms such as $S^{R,\mathrm{II}}_{q,ij}(\omega)$.

The illustrations of Figure 4.3 and Figure 4.4 are based on synthetic examples incorporating no aeroelastic effects, in which case a quadratic expansion exactly reproduces the diagonal flexibility $J_{d,i}(\omega)$. It is important to note that this quadratic formulation of the impedance function will not exactly represent $\mathbf{J}_d$ with the aeroelastic matrices. This is because the matrices $\mathbf{M}_{\text{ae}}$, $\mathbf{C}_{\text{ae}}$ and $\mathbf{K}_{\text{ae}}$ are linearized around a single chosen point, whereas the aeroelastic matrices themselves may exhibit some significant nonlinearity. Consequently, the quadratic approximation can deviate substantially from the actual behaviour far from the expansion point, especially if notable aeroelastic variations occur in the intervening range.

4.2.2 The quadratic expansion

The approach described in this section is similar to that formalized in Section 3.3.2. It extends to any combination (i, j) the development that had been presented for the 2DOF model. The

[2]The notation $H_{d,\cdot}$ refers generically to either $H_{d,i}$, $H_{d,k}$, or $H_{d,j}$. Equivalently, $J_{d,i}$ is used to refer either to $J_{d,i}$, $J_{d,k}$, or $J_{d,j}$

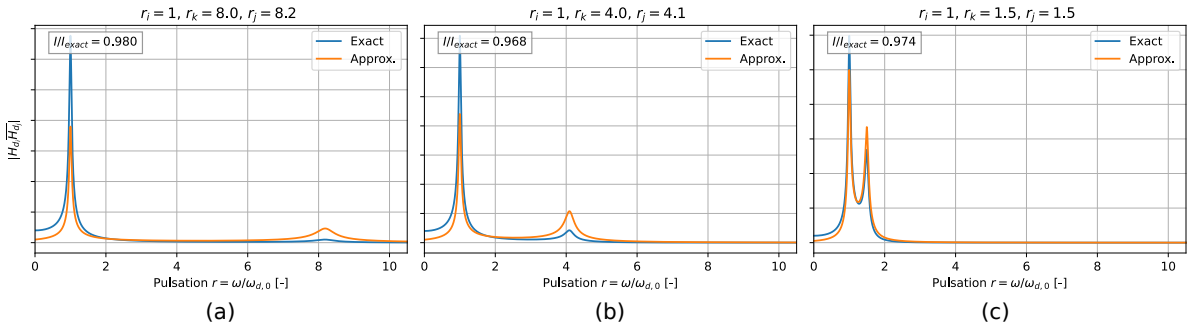

Figure 4.4: Comparison of $H_{d,i}(\omega)\bar{H}_{d,j}(\omega)$, obtained with exact and first order approximation for $H_{d_{,\cdot}}(\omega)$.

intermediate results are succinctly provided to extend the previous formulation to quadratic formulation.

The aeroelastic matrices can be linearized around a chosen circular frequency ω_{ij}

$$A_{ij}(\omega) = A_{ij}(\omega_{ij}) + \partial_\omega A_{ij}(\omega_{ij})(\omega - \omega_{ij}) + \mathcal{O}\left[(\omega - \omega_{ij})^2\right]. \tag{4.16}$$

The dynamic flexibility reads

$$J_{ij}(\omega) = -\omega^2 M_{ij}(\omega) + \mathrm{i}\omega C_{ij}(\omega) + K_{ij}(\omega). \tag{4.17}$$

Applying (4.16) to linearize the total matrices of mass $\mathbf{M}$, damping $\mathbf{C}$ and stiffness $\mathbf{K}$ gives

$$\begin{aligned} J_{ij}(\omega) = -\omega^2\left[M_{ij}(\omega_{ij}) + (\omega - \omega_{ij})\,\partial_\omega M_{ij}(\omega_{ij})\right] + \mathrm{i}\omega\left[C_{ij}(\omega_{ij}) + (\omega - \omega_{ij})\,\partial_\omega C_{ij}(\omega_{ij})\right] \\ + K_{ij}(\omega_{ij}) + (\omega - \omega_{ij})\,\partial_\omega K_{ij}(\omega_{ij}). \end{aligned} \tag{4.18}$$

Introducing the stretching $\omega = \omega_{ij}(1 + \varepsilon_{ij}\delta\eta)$

$$\begin{aligned} J_{ij}(\omega) = -\partial_\omega M_{ij}(\omega_{ij})\delta^3\varepsilon_{ij}^3\omega_{ij}^3 + \delta^2\eta^2\varepsilon_{ij}^2\omega_{ij}^2\left[\mathrm{i}\partial_\omega C_{ij}(\omega_{ij}) - M_{ij}(\omega_{ij}) - 2\partial_\omega M_{ij}(\omega_{ij})\omega_{ij}\right] \\ + \delta\varepsilon_{ij}\eta\left[\mathrm{i}C_{ij}(\omega_{ij})\omega_{ij} + \partial_\omega K_{ij}(\omega_{ij})\omega_{ij} + \mathrm{i}\partial_\omega C_{ij}(\omega_{ij})\omega_{ij}^2 - 2M_{ij}\omega_{ij}^2 - \partial_\omega M_{ij}(\omega_{ij})\omega_{ij}^3\right] \\ + K_{ij}(\omega_{ij}) + \mathrm{i}C_{ij}(\omega_{ij})\omega_{ij} - M_{ij}(\omega_{ij})\omega_{ij}^2. \end{aligned} \tag{4.19}$$

This series is truncated at second order to give

$$\begin{aligned} J_{ij}(\omega) = \delta^2\eta^2\varepsilon_{ij}^2\omega_{ij}^2\left[\mathrm{i}\partial_\omega C_{ij}(\omega_{ij}) - M_{ij}(\omega_{ij}) - 2\partial_\omega M_{ij}(\omega_{ij})\omega_{ij}\right] \\ + \delta\varepsilon_{ij}\eta\left[\mathrm{i}C_{ij}(\omega_{ij})\omega_{ij} + \partial_\omega K_{ij}(\omega_{ij})\omega_{ij} + \mathrm{i}\partial_\omega C_{ij}(\omega_{ij})\omega_{ij}^2 - 2M_{ij}\omega_{ij}^2 - \partial_\omega M_{ij}(\omega_{ij})\omega_{ij}^3\right] \\ + K_{ij}(\omega_{ij}) + \mathrm{i}C_{ij}(\omega_{ij})\omega_{ij} - M_{ij}(\omega_{ij})\omega_{ij}^2. \end{aligned} \tag{4.20}$$

In aeroelasticity, the third order terms are anyway zero since the added mass effect are neglected. This truncation is then realized without loss of accuracy. Equivalently, stepping back to the original coordinate system, equation (4.20) reads

$$\begin{aligned} J_{ij}(\omega) = \left[\mathrm{i}\,\partial_\omega C_{ij}(\omega_{ij}) - M_{ij}(\omega_{ij}) - 2\partial_\omega M_{ij}(\omega_{ij})\omega_{ij}\right]\omega^2 + \\ \left[\mathrm{i}\,C_{ij}(\omega_{ij}) + \partial_\omega K_{ij}(\omega_{ij}) + \omega_{ij}\left[-\mathrm{i}\,\partial_\omega C_{ij}(\omega_{ij}) + 3\,\partial_\omega M_{ij}(\omega_{ij})\,\omega_{ij}\right]\right]\omega + a_{ij,0}(\omega). \end{aligned} \tag{4.21}$$

The small damping assumption may also be invoked, such that the damping is expressed using the small parameter ε_{ij} and a variable $\chi_{ij} = \mathcal{O}(1)$, $C_{ij} = \chi_{ij}\varepsilon_{ij}$, and equivalently $\partial_\omega C_{ij} = \mathrm{d}\chi_{ij}\varepsilon_{ij}$.

In this case, equation (4.20) becomes

$$J_{ij}(\omega) = \epsilon^2\delta^2\eta_{ij}^2\left(-2\partial_\omega M_{ij}(\omega_{ij})\omega_{ij}^3 + \mathrm{i}\omega_{ij}(\chi_{ij} + \mathrm{d}\chi_{ij}\omega_{ij})/(\delta\eta_{ij} - M_{ij}(\omega_{ij})\omega_{ij}^2\right) + \epsilon\delta\eta_{ij}\left(\partial_\omega K_{ij}(\omega_{ij})\omega_{ij} + (-M_{ij}(\omega_{ij}))\omega_{ij}^3 - 2M_{ij}(\omega_{ij})\omega_{ij}^2 + \mathrm{i}\chi_{ij}\omega_{ij}/(\delta\eta_{ij})\right) + K_{ij}(\omega_{ij}) - M_{ij}(\omega_{ij})\omega_{ij}^2. \tag{4.22}$$

In the unstretched coordinate system

$$\begin{aligned} J_{ij}(\omega) = \big[&-2\partial_\omega M_{ij}(\omega_{ij})\omega_i - M_{ij}(\omega_{ij})\big]\omega^2 \\ &+ \big[\mathrm{i}C_{ij}(\omega_{ij}) + \omega_i\left[3\partial_\omega M_{ij}(\omega_{ij})\omega_i + \mathrm{i}\partial_\omega C_{ij}(\omega_{ij})\right] + \partial_\omega K_{ij}(\omega_{ij})\big]\,\omega \\ &+ \big[K_{ij}(\omega_{ij}) - \omega_i\left[\partial_\omega K_{ij}(\omega_{ij}) + \omega_i(\partial_\omega M_{ij}(\omega_{ij})\omega_i + \mathrm{i}\partial_\omega C_{ij}(\omega_{ij}))\right]\big]. \end{aligned} \tag{4.23}$$

Noting that $H_{d,i}(\omega) = J_{ii}^{-1}(\omega)$ and $J_{o,ij} = J_{ij}(\omega)(1-\delta_{ij})$ where δ_{ij} is the delta Kronecker symbol, these expressions can be used in (4.3) to evaluate the different resonant components of the response power spectral density.

In a very general manner, the dynamic flexibility at first or second order can be expressed in the form

$$J_{ij}(\omega) = a_{ij,2}\omega^2 + a_{ij,1}\omega + a_{ij,0}. \tag{4.24}$$

The analytical expressions of the coefficients $a_{ij,k}$ for $k \in \{0,1,2\}$ for linear and quadratic formulations with or without small damping assumption of the dynamic flexibility are summarized in Table 4.1. Equation (4.24) can be factorized using its two zeroes

$$J_{ij}(\omega) = a_{ij,2}(\omega - p_{ij,1})(\omega - p_{ij,2}) \tag{4.25}$$

with

$$p_{ij,1} = \frac{-a_{ij,1} - \sqrt{a_{ij,1}^2 - 4a_{ij,2}a_{ij,0}}}{2a_{ij,2}} \quad \text{and} \quad p_{ij,2} = \frac{-a_{ij,1} + \sqrt{a_{ij,1}^2 - 4a_{ij,2}a_{ij,0}}}{2a_{ij,2}}. \tag{4.26}$$

From this factorized form of the dynamic flexibility, and the definition of the residual,

$$\operatorname*{Res}_{z=z_0} f(z) = \lim_{z\to z_0}(z - z_0)\,f(z_0), \tag{4.27}$$

the residuals of $\mathbf{S}_q^{\mathrm{I}}$ are evaluated using (4.3a),

$$\operatorname*{Res}_{\omega=p_{ii,1}} S_{ij}^{\mathrm{I}}(\omega) = S_{p,ij}(\omega^*)\left[a_{ii,2}\bar{a}_{jj,2}(p_{ii,1} - p_{ii,2})(p_{ii,1} - \bar{p}_{jj,1})(p_{ii,1} - \bar{p}_{jj,2})\right]^{-1} \tag{4.28a}$$

$$\operatorname*{Res}_{\omega=p_{ii,2}} S_{ij}^{\mathrm{I}}(\omega) = S_{p,ij}(\omega^*)\left[a_{ii,2}\bar{a}_{jj,2}(p_{ii,2} - p_{ii,1})(p_{ii,2} - \bar{p}_{jj,1})(p_{ii,2} - \bar{p}_{jj,2})\right]^{-1} \tag{4.28b}$$

$$\operatorname*{Res}_{\omega=p_{jj,1}} S_{ij}^{\mathrm{I}}(\omega) = S_{p,ij}(\omega^*)\left[a_{ii,2}\bar{a}_{jj,2}(\bar{p}_{jj,1} - p_{ii,1})(\bar{p}_{jj,1} - p_{ii,2})(\bar{p}_{jj,1} - \bar{p}_{jj,2})\right]^{-1} \tag{4.28c}$$

$$\operatorname*{Res}_{\omega=p_{jj,2}} S_{ij}^{\mathrm{I}}(\omega) = S_{p,ij}(\omega^*)\left[a_{ii,2}\bar{a}_{jj,2}(\bar{p}_{jj,2} - p_{ii,1})(\bar{p}_{jj,2} - p_{ii,2})(\bar{p}_{jj,2} - \bar{p}_{jj,1})\right]^{-1}. \tag{4.28d}$$

The residuals of $\mathbf{S}_q^{\mathrm{II},A}$ are equivalently evaluated from (4.3b)

$$\begin{aligned} \operatorname*{Res}_{\omega=p_{ii,1}} S_{ij}^{\mathrm{II},A}(\omega) = {} & J_{ik}(p_{ii,1})\delta_{ij}\,S_{p,kj}(\omega^*) \\ & /\left[a_{ijk,2}(p_{ii,1} - p_{ii,2})(p_{ii,1} - p_{kk,1})(p_{ii,1} - p_{kk,2})(p_{ii,1} - \bar{p}_{jj,1})(p_{ii,1} - \bar{p}_{jj,2})\right] \end{aligned} \tag{4.29a}$$

$$\begin{aligned} \operatorname*{Res}_{\omega=p_{ii,2}} S_{ij}^{\mathrm{II},A}(\omega) = {} & J_{ik}(p_{ii,2})\delta_{ij}\,S_{p,kj}(\omega^*) \\ & /\left[a_{ijk,2}(p_{ii,2} - p_{ii,1})(p_{ii,2} - p_{kk,1})(p_{ii,2} - p_{kk,2})(p_{ii,2} - \bar{p}_{jj,1})(p_{ii,2} - \bar{p}_{jj,2})\right] \end{aligned} \tag{4.29b}$$

Denomination	**Order**	**Assumptions**	**Coefficients**
F0	$\mathcal{O}(\varepsilon^0)$	Gradient-free Const. aero. matrices	$a_{ij,2} = -M_{ij}(\omega_{ij})$ $a_{ij,1} = \mathrm{i}\, C_{ij}(\omega_{ij})$ $a_{ij,0} = K_{ij}(\omega_{ij})$
F1A	$\mathcal{O}(\varepsilon^1)$	Small Damping Linear aero. matrices	$a_{ij,2} = 0$ $a_{ij,1} = \partial_\omega K_{ij}(\omega_{ij}) - \omega_i(2M_{ij}(\omega_{ij}) + \partial_\omega M_{ij}(\omega_{ij})\omega_i)$ $a_{ij,0} = K_{ij}(\omega_{ij}) + \omega_i(\mathrm{i}C_{ij}(\omega_{ij}) - \partial_\omega K_{ij}(\omega_{ij}) + \omega_i(M_{ij}(\omega_{ij}) + \partial_\omega M_{ij}(\omega_{ij})\omega_i))$
F1B	$\mathcal{O}(\varepsilon^1)$	Linear aero. matrices	$a_{ij,2} = 0$ $a_{ij,1} = \mathrm{i}C_{ij}(\omega_{ij}) + \partial_\omega K_{ij}(\omega_{ij}) - \omega_i(-\mathrm{i}\partial_\omega C_{ij}(\omega_{ij}) + 2M_{ij}(\omega_{ij}) + \partial_\omega M_{ij}(\omega_{ij})\omega_i)$ $a_{ij,0} = K_{ij}(\omega_{ij}) + \omega_i(-\partial_\omega K_{ij}(\omega_{ij}) + \omega_i(-\mathrm{i}\partial_\omega C_{ij}(\omega_{ij}) + M_{ij}(\omega_{ij}) + \partial_\omega M_{ij}(\omega_{ij})\omega_i))$
F2A	$\mathcal{O}(\varepsilon^2)$[a]	Small Damping Linear aero. matrices	$a_{ij,2} = -2\partial_\omega M_{ij}(\omega_{ij})\omega_i - M_{ij}(\omega_{ij})$ $a_{ij,1} = \mathrm{i}C_{ij}(\omega_{ij}) + \omega_i\left[3\partial_\omega M_{ij}(\omega_{ij})\omega_i + \mathrm{i}\partial_\omega C_{ij}(\omega_{ij})\right] + \partial_\omega K_{ij}(\omega_{ij})$ $a_{ij,0} = K_{ij}(\omega_{ij}) - \omega_i\left[\partial_\omega K_{ij}(\omega_{ij}) + \omega_i(\partial_\omega M_{ij}(\omega_{ij})\omega_i + \mathrm{i}\partial_\omega C_{ij}(\omega_{ij}))\right]$
F2B	$\mathcal{O}(\varepsilon^2)$[a]	Linear aero. matrices	$a_{ij,2} = \mathrm{i}\,\partial_\omega C_{ij}(\omega_{ij}) - M_{ij}(\omega_{ij}) - 2\partial_\omega M_{ij}(\omega_{ij})\omega_{ij}$ $a_{ij,1} = \mathrm{i}\, C_{ij}(\omega_{ij}) + \partial_\omega K_{ij}(\omega_{ij}) + \omega_{ij}\big[-\mathrm{i}\,\partial_\omega C_{ij}(\omega_{ij}) + 3\,\partial_\omega M_{ij}(\omega_{ij})\,\omega_{ij}\big]$ $a_{ij,0} = K_{ij}(\omega_{ij}) - \omega_{ij}(\partial_\omega K_{ij}(\omega_{ij}) + \partial_\omega M_{ij}(\omega_{ij})\omega_{ij}^2)$

[a] The second derivatives of the aeroelastic matrices have been neglected. These terms are potentially of order $\mathcal{O}(\varepsilon^2)$ and should have been included to get an exact expansion of $\mathcal{O}(\varepsilon^2)$..

Table 4.1: Analytical expressions of the coefficients of the dynamic flexibility expressed according to (4.24) for the linear or quadratic formulations with and without small damping assumption. The quadratic gradient-free formulation is obtained assuming $\partial_\omega K_{ij}(\omega_{ij}) = \partial_\omega C_{ij}(\omega_{ij}) = 0$.

$$\underset{\omega=p_{kk,1}}{\text{Res}}\; S_{ij}^{\text{II},A}(\omega) = J_{ik}(p_{kk,1})\delta_{ij}\, S_{p,kj}(\omega^*) \Big/ \left[a_{ijk,2}(p_{kk,1}-p_{ii,1})(p_{kk,1}-p_{ii,2})(p_{kk,1}-p_{kk,2})(p_{kk,1}-\bar{p}_{jj,1})(p_{kk,1}-\bar{p}_{jj,2})\right] \tag{4.29c}$$

$$\underset{\omega=p_{kk,2}}{\text{Res}}\; S_{ij}^{\text{II},A}(\omega) = J_{ik}(p_{kk,2})\delta_{ij}\, S_{p,kj}(\omega^*) \Big/ \left[a_{ijk,2}(p_{kk,2}-p_{ii,1})(p_{kk,2}-p_{ii,2})(p_{kk,2}-p_{kk,1})(p_{kk,2}-\bar{p}_{jj,1})(p_{kk,2}-\bar{p}_{jj,2})\right] \tag{4.29d}$$

$$\underset{\omega=\bar{p}_{jj,1}}{\text{Res}}\; S_{ij}^{\text{II},A}(\omega) = (\bar{J}_{ik}(\bar{p}_{jj,1})\delta_{ij}\, S_{p,kj}(\omega^*) \Big/ \left[a_{ijk,2}(\bar{p}_{jj,1}-p_{ii,1})(\bar{p}_{jj,1}-p_{ii,2})(\bar{p}_{jj,1}-p_{kk,1})(\bar{p}_{jj,1}-p_{kk,2})(\bar{p}_{jj,1}-\bar{p}_{jj,2})\right] \tag{4.29e}$$

$$\underset{\omega=\bar{p}_{jj,2}}{\text{Res}}\; S_{ij}^{\text{II},A}(\omega) = (\bar{J}_{ik}(\bar{p}_{jj,2})\delta_{ij}\, S_{p,kj}(\omega^*) \Big/ \left[a_{ijk,2}(\bar{p}_{jj,2}-p_{ii,1})(\bar{p}_{jj,2}-p_{ii,2})(\bar{p}_{jj,2}-p_{kk,1})(\bar{p}_{jj,2}-p_{kk,2})(\bar{p}_{jj,2}-\bar{p}_{jj,1})\right] \tag{4.29f}$$

with $a_{ijk,2} = a_{ii,2}a_{kk,2}\bar{a}_{jj,2}$, and the residuals of $\mathbf{S}_q^{\text{II},B}$ are evaluated from (4.3c)

$$\underset{\omega=p_{ii,1}}{\text{Res}}\; S_{ij}^{\text{II},B}(\omega) = \bar{J}_{jk}(p_{ii,1})\delta_{ij}\, S_{p,ik}(\omega^*) \Big/ \left[b_{ijk,2}(p_{ii,1}-p_{ii,2})(p_{ii,1}-\bar{p}_{kk,1})(p_{ii,1}-\bar{p}_{kk,2})(p_{ii,1}-\bar{p}_{jj,1})(p_{ii,1}-\bar{p}_{jj,2})\right] \tag{4.30a}$$

$$\underset{\omega=p_{ii,2}}{\text{Res}}\; S_{ij}^{\text{II},B}(\omega) = \bar{J}_{jk}(p_{ii,2})\delta_{ij}\, S_{p,ik}(\omega^*) \Big/ \left[b_{ijk,2}(p_{ii,2}-p_{ii,1})(p_{ii,2}-\bar{p}_{kk,1})(p_{ii,2}-\bar{p}_{kk,2})(p_{ii,2}-\bar{p}_{jj,1})(p_{ii,2}-\bar{p}_{jj,2})\right] \tag{4.30b}$$

$$\underset{\omega=\bar{p}_{kk,1}}{\text{Res}}\; S_{ij}^{\text{II},B}(\omega) = \bar{J}_{jk}(\bar{p}_{kk,1})\delta_{ij}\, S_{p,ik}(\omega^*) \Big/ \left[b_{ijk,2}(\bar{p}_{kk,1}-p_{ii,1})(\bar{p}_{kk,1}-p_{ii,2})(\bar{p}_{kk,1}-\bar{p}_{kk,2})(\bar{p}_{kk,1}-\bar{p}_{jj,1})(\bar{p}_{kk,1}-\bar{p}_{jj,2})\right] \tag{4.30c}$$

$$\underset{\omega=\bar{p}_{kk,2}}{\text{Res}}\; S_{ij}^{\text{II},B}(\omega) = \bar{J}_{jk}(\bar{p}_{kk,2})\delta_{ij}\, S_{p,ik}(\omega^*) \Big/ \left[b_{ijk,2}(\bar{p}_{kk,2}-p_{ii,1})(\bar{p}_{kk,2}-p_{ii,2})(\bar{p}_{kk,2}-\bar{p}_{kk,1})(\bar{p}_{kk,2}-\bar{p}_{jj,1})(\bar{p}_{kk,2}-\bar{p}_{jj,2})\right] \tag{4.30d}$$

$$\underset{\omega=\bar{p}_{jj,1}}{\text{Res}}\; S_{ij}^{\text{II},B}(\omega) = (\bar{J}_{jk}(\bar{p}_{jj,1})\delta_{ij}\, S_{p,ik}(\omega^*) \Big/ \left[b_{ijk,2}(\bar{p}_{jj,1}-p_{ii,1})(\bar{p}_{jj,1}-p_{ii,2})(\bar{p}_{jj,1}-\bar{p}_{kk,1})(\bar{p}_{jj,1}-\bar{p}_{kk,2})(\bar{p}_{jj,1}-\bar{p}_{jj,2})\right] \tag{4.30e}$$

$$\underset{\omega=\bar{p}_{jj,2}}{\text{Res}}\; S_{ij}^{\text{II},B}(\omega) = (\bar{J}_{jk}(\bar{p}_{jj,2})\delta_{ij}\, S_{p,ik}(\omega^*) \Big/ \left[b_{ijk,2}(\bar{p}_{jj,2}-p_{ii,1})(\bar{p}_{jj,2}-p_{ii,2})(\bar{p}_{jj,2}-\bar{p}_{kk,1})(\bar{p}_{jj,2}-\bar{p}_{kk,2})(\bar{p}_{jj,2}-\bar{p}_{jj,1})\right] \tag{4.30f}$$

with $b_{ijk,2} = a_{ii,2}\bar{a}_{kk,2}\bar{a}_{jj,2}$.

In these expressions, ω^* refers to the particular pulsation at which the power spectral density of the modal forces are evaluated.

After having identified the poles of the integrands S_{ij}^{I}, $S_{ij}^{\text{II},A}$ and $S_{ij}^{\text{II},B}$ located in upper part of the complex plane and having evaluated the corresponding residuals, the integrals are calculated analytically using the Cauchy's residue theorem adding all the residues

$$\int_{-\infty}^{+\infty} f(\omega)\,\mathrm{d}\omega = 2\mathrm{i}\pi \sum_k \text{Res}_k\left[f(z)\right]. \tag{4.31}$$

4.3 Quadratic expansion of the response PSD

In the same spirit as in Section 4.2 where a quadratic expansion of the diagonal flexibility matrix was presented, a higher order expansion of the response power spectral density was also investigated. Indeed, if the diagonal transfer function matrices $\mathbf{H}_d(\omega)$ are second order expansions, it is legitimate to push the expansion (4.1) of $\mathbf{S}_q(\omega)$ to a quadratic formulation as

well. Such a quadratic formulation of $\mathbf{S}_q(\omega)$ allows for a better representation of the response power spectral density at higher diagonality indices.

To derive this quadratic expansion, the transfer function matrix $\mathbf{H}(\omega)$ is first expanded as a quadratic series (see Appendix C.1)

$$\mathbf{H}_c(\omega) = \mathbf{H}_d(\omega) - \mathbf{H}_d(\omega)\mathbf{J}_o(\omega)\mathbf{H}_d(\omega) + \mathbf{H}_d(\omega)\mathbf{J}_o(\omega)\mathbf{H}_d(\omega)\mathbf{J}_o(\omega)\mathbf{H}_d(\omega) + \mathcal{O}(\varepsilon^3). \tag{4.32}$$

The first term is $\mathcal{O}(1)$, the second is $\mathcal{O}(\varepsilon)$ and the third is $\mathcal{O}(\varepsilon^2)$. Plugging this equation into (3.27) leads to

$$\mathbf{S}_q = \mathbf{S}_q(\omega) = \mathbf{S}_q^{\mathrm{I}}(\omega) + \mathbf{S}_q^{\mathrm{II},A}(\omega) + \mathbf{S}_q^{\mathrm{II},B}(\omega) + \mathbf{S}_q^{\mathrm{III}}(\omega) + \mathcal{O}(\varepsilon^3) \tag{4.33}$$

with

$$\mathbf{S}_q^{\mathrm{III}}(\omega) = \mathbf{H}_d\mathbf{J}_o\mathbf{H}_d\mathbf{S}_q\mathbf{H}_d^*\mathbf{J}_o^*\mathbf{H}_d^* + \mathbf{H}_d\mathbf{J}_o\mathbf{H}_d\mathbf{J}_o\mathbf{H}_d\mathbf{S}_q\mathbf{H}_d^* + \mathbf{H}_d\mathbf{S}_q\mathbf{H}_d^*\mathbf{J}_o^*\mathbf{H}_d^*\mathbf{J}_o^*\mathbf{H}_d^*. \tag{4.34}$$

At first glance, these three terms appear to be integrable analytically using the Cauchy theorem, in a similar manner to what was done in Chapter 3 , with the only difference being the presence of two additional factors —and thus two additional residues— compared to $\mathbf{S}_q^{\mathrm{II},A}$ or $\mathbf{S}_q^{\mathrm{II},B}$. The first term in (4.34), noted $\mathbf{S}_q^{\mathrm{III},A}$ can indeed be treated accordingly. However, the situation becomes significantly more complex for the last two terms. For instance, the second term of (4.34) expressed in index notation is

$$S_{q,ij}^{\mathrm{III},B}(\omega) = \sum_k \sum_l H_{d,i}J_{o,ik}H_{d,k}J_{o,kl}H_{d,l}S_{q,lj}\bar{H}_{d,j}. \tag{4.35}$$

The particular element of this double sum with $i = l$ is expressed as

$$H_{d,i}^2 J_{o,ik}H_{d,k}J_{o,ki}S_{q,ij}\bar{H}_{d,j}. \tag{4.36}$$

In this case, the first factor appears squared, introducing one second-order pole, whereas previous derivations only involved first-order poles. The evaluation of residues for such integrands introduces prohibitive mathematical challenges. Given these difficulties, this approach was ultimately deemed impractical and was not pursued further. The linear formulation of the response power spectral density such as considered so far is thus finally kept.

4.4 Practical recommendations for implementation of the solution

4.4.1 The white-noise approximation

As stated in the introduction of this chapter, the distribution of aeroelastic eigenfrequencies in a wide frequency band poses a significant challenge in accurately representing the response power spectral density. Beyond the issues already discussed, this frequency spread also affects the validity of the white-noise approximation especially for cross power spectral densities. This limitation can be illustrated using the first-order term $\mathbf{S}q^{\mathrm{I}}(\omega)$ in the approximation of the response PSD:

$$S_{q,ij}^{\mathrm{I}} = H_{d,i}(\omega)S_{p,ij}(\omega_{ij})\bar{H}_{d,j}(\omega) \tag{4.37}$$

where the modal buffeting forces are approximated using the white-noise assumption. When modes i and j have close eigenfrequencies, this assumption is reasonable, as the modal force PSD typically varies smoothly within the resonant range. Since the dominant frequency content of (4.37) is concentrated around ω_i and ω_j, it can be reasonably well approximated as constant in this narrow range. Whether the PSD is computed at ω_i, ω_j, or the mean frequency $\omega_{ij} = \frac{1}{2}(\omega_i +$

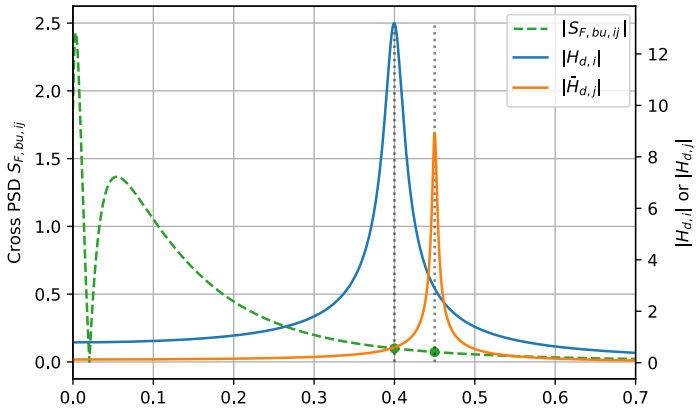

(a) Modal buffeting forces and inverse of the diagonal flexibility $H_{d,.} = J_{d,.}^{-1}$

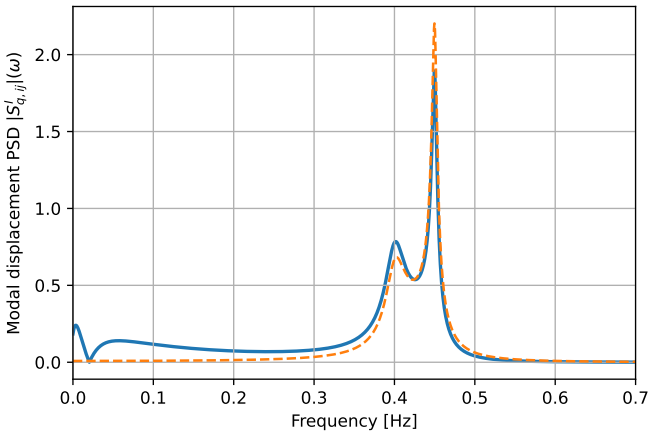

(b) Successful application of the white-noise approximation on the power spectral density

Figure 4.5: White-noise decomposition of the modal response PSD applied to $S_{q,ij}$ with close eigenfrequencies $\omega_i \approx \omega_j$. Synthetic example generated with $f_i = 0.4$ Hz, $f_j = 0.45$ Hz, $\xi_i = 3\%$, $\xi_j = 0.7\%$, $\frac{m_i^*}{m_j^*} = 0.2$.

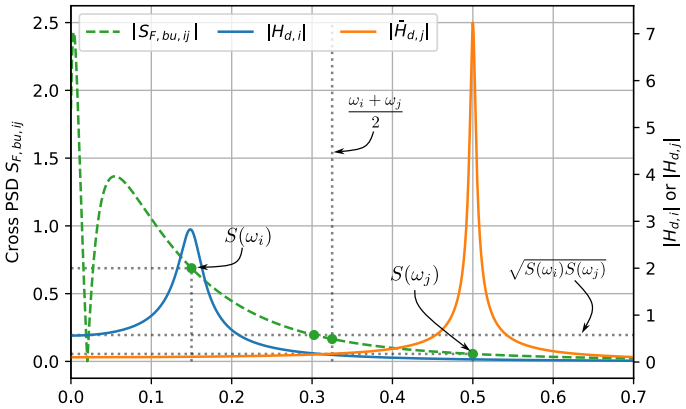

(a) Modal buffeting forces and inverse of the diagonal flexibility $H_{d,.} = J_{d,.}^{-1}$

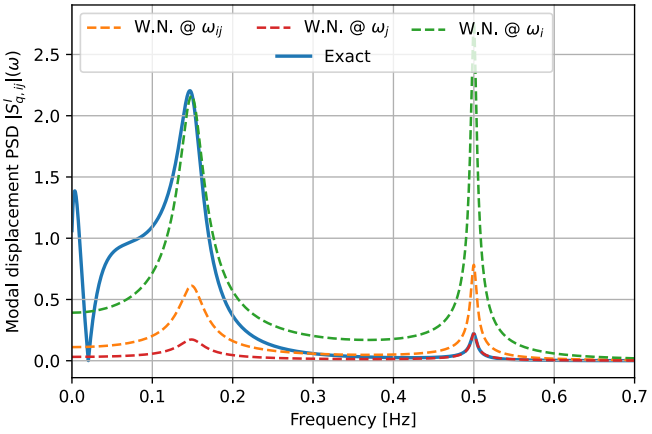

(b) Consequence of the white-noise approximation strategies on representation of the power spectral density.

Figure 4.6: White-noise decomposition of the modal response PSD. Synthetic example generated with $f_i = 0.15$ Hz, $f_j = 0.5$ Hz, $\xi_i = 10\%$, $\xi_j = 0.7\%$, $\frac{m_i^*}{m_j^*} = 2$.

ω_j), the resulting approximation remains accurate. This scenario is illustrated in Figure 4.5, where the PSD exhibits minimal variation across the resonant frequencies in (a), leading to a close match between the approximated and exact modal response PSD in (b).

When two modes have widely separated eigenfrequencies, i.e., $\omega_{d,i} \ll \omega_{d,j}$, the power spectral density (PSD) can exhibit a significant drop between the two resonance peaks, as shown in Figure 4.6 (a). In such cases, the white-noise approximation may provide a poor representation of the modal buffeting PSD, with its accuracy decreasing as the ratio ω_i/ω_j becomes smaller. The frequency at which the PSD is calculated has a crucial impact on the accuracy of the response spectrum representation.

As schematically illustrated in Figure 4.6 (b), evaluating the PSD at the lower eigenfrequency provides an accurate representation of the first resonant peak but leads to a substantial overestimation of the higher-frequency peak, resulting in an overall overestimation of the (co-)variance. Conversely, evaluating the PSD at the highest eigenfrequency underestimates both the PSD and the covariance, making this approach non-conservative. The trade-off between accuracy at different peaks suggests the need for a compromise. Following the approach introduced in Chapter 3, two alternative strategies can be considered: (i) performing the white-noise approximation at the average eigenfrequency $\frac{1}{2}(\omega_i + \omega_j)$, or (ii) using the geometric mean of the modal force PSD values, $\sqrt{S(\omega_i)S(\omega_j)}$. The resulting response PSDs using the three strategies are illustrated in Figure 4.6 (b).

Given that large MDOF systems typically have widely spread eigenfrequencies, this observation implies that the elements $S^{\mathrm{I}}_{q,ij}$ with $i \ll j$ are inherently less accurately represented than those with $i \approx j$. However, this conclusion cannot be directly extended to $\mathbf{S}_q$ without also considering the contributions of $\mathbf{S}^{\mathrm{II},A}_q$ and $\mathbf{S}^{\mathrm{II},B}_q$, which both involve summations over all modes:

$$S^{\mathrm{II},A}_{q,ij}(\omega) = -\sum_k H_{d,i}(\omega) J_{o,ik}(\omega) H_{d,k}(\omega) S_{p,kj}(\bar{\omega}) \bar{H}_{d,j}(\omega), \tag{4.38a}$$

$$S^{\mathrm{II},B}_{q,ij}(\omega) = -\sum_k H_{d,i}(\omega) S_{p,ik}(\bar{\omega}) \bar{H}_{d,k}(\omega) \bar{J}_{o,jk}(\omega) \bar{H}_{d,j}(\omega). \tag{4.38b}$$

Intuition drawn from Figure 4.5 and 4.6 suggests applying the white-noise approximation with $\bar{\omega} = \omega_{kj} = \frac{\omega_k+\omega_j}{2}$[3], as this choice provides the best balance of accuracy across the entire frequency range. While this approach is optimal for representing $S^{\mathrm{I}}_{q,kj} = H_{d,k}(\omega) S_{p,kj}(\omega) \bar{H}_{d,j}(\omega)$, practical implementation reveals that setting $\bar{\omega} = \frac{\omega_i+\omega_j}{2}$ remains the most suitable option for accurately capturing each contribution of $S^{\mathrm{II}}_{q,ij}$.

This preference arises from the filtering effect introduced by the terms $H_{d,i}(\omega)J_{o,ik}(\omega)$ in $S^{\mathrm{II},A}_{q,ij}(\omega)$. As a result, most of the energy content in $S^{\mathrm{II},A}_{q,ij}(\omega)$ is governed by contributions where $\omega_k \approx \omega_i$ and/or $\omega_k \approx \omega_j$. The summation in (4.38) is therefore primarily influenced by these marginal contributions. However, it is important to note that the conditions $\omega_k \approx \omega_i$ or $\omega_k \approx \omega_j$ alone are not sufficient for dominance, as additional factors such as the representation of the buffeting spectrum and modal interactions also play a role.

To illustrate this discussion, Figure 4.7 presents the k-th element of $S^{\mathrm{II},A}_{q,ij}(\omega)$. In (a), the modal buffeting forces were sampled at $\frac{\omega_k+\omega_j}{2}$, whereas in (b), they were sampled at $\frac{\omega_i+\omega_j}{2}$. In both cases, the energy content in the vicinity of ω_k is negligible, meaning that its accuracy has little influence on the overall integral. However, the dominant frequency content is captured much more effectively in (b) than in (a), as the PSD of the excitation is better represented precisely where the energy contribution is most significant.

As a consequence of the above recommendation, an important warning should be given for implementing the background/resonant decomposition to MDOF systems: recursive formulations

[3]Or, alternatively, the PSD $S_{p,kj}(\bar{\omega})$ can be approximated using the geometric mean $\sqrt{S_{p,kj}(\omega_i)S_{p,kj}(\omega_j)}$

should be avoided when evaluating $S^{\mathrm{II}}_{q,ij}(\omega)$. While, in theory, expressions such as

$$S^{\mathrm{II},A}_{q,ij}(\omega) = -\sum_k H_{d,i}(\omega) J_{o,ik}(\omega) S^{\mathrm{I}}_{q,jk}(\omega) \tag{4.39}$$

and

$$S^{\mathrm{II},B}_{q,ij}(\omega) = -\sum_k \bar{S}^{\mathrm{I}}_{q,ki}(\omega) \bar{J}_{o,jk}(\omega) \bar{H}_{d,j}(\omega), \tag{4.40}$$

could be used alternatively to (4.3b) and (4.3c) to compute $\mathbf{S}^{\mathrm{II},A}_q$ and $\mathbf{S}^{\mathrm{II},B}_q$ by iteratively building upon $\mathbf{S}^{\mathrm{I}}_q$, doing so introduces compounding errors in the frequency selection. Each term in these summations inherently relies on an approximation of S^{I}_q, which itself depends on a chosen sampling frequency. Since S^{II}_q involves a second layer of summation over all modal contributions, propagating an initial frequency choice across recursive steps may lead to a cumulative misrepresentation of the dominant spectral content. For this reason, equations (4.38a) and (4.38b) are preferred to (4.39) and (4.40) to ensure that each contribution remains properly weighted where the spectral energy is most significant.

While the white-noise approximation provides a simple and computationally efficient way to estimate the modal buffeting PSD, its accuracy may not always be satisfactory for coupling terms and especially for modes with widely separated eigenfrequencies. A natural alternative is to relax the assumption of a constant PSD and instead allow it to vary smoothly across the frequency range. For instance, a linear or quadratic interpolation scheme could be employed [82], using available data points such as $\mathbf{S}_p(\omega_i)$, $\mathbf{S}_p(\omega_j)$, and $\mathbf{S}_p(\omega_k)$ to construct a more representative approximation. This would modify the expressions of the previously computed residues, as $S_{p,ik}$ would be replaced by the interpolated function. Although this approach introduces additional complexity, it remains relatively straightforward to implement and could offer improved accuracy in cases where the white-noise approximation is in default. However, this alternative has not been tested in the present work.

This section has illustrated the consequences of the white-noise approximation on the modal response power spectral density. The identified limitations affect only the cross-terms contributions of the PSD, corresponding to modes with well-separated eigenfrequencies. It is important to emphasize that, although the PSD of modal responses is a key intermediate result, an exact representation of each cross-term is not strictly necessary for accurately predicting the nodal variances, which are mostly contributed by modal variances. Ultimately, it is the nodal variances that carry physical relevance. If the covariance between two modes contributing minimally to the overall response is badly captured, inaccuracies in its estimation may have negligible impact on the final variance values. This is because the cross elements of the covariance matrix are smaller than the product of the standard deviation (a consequence of Cauchy-Schwarz theorem). While this section shows that a more refined approximation could improve the representation of the PSD's cross-terms beyond what is achieved under the white-noise assumption, the relevance of such improvements should be assessed in terms of their effect on nodal variances. This point will be revisited later in the chapter through the analysis of correlation coefficients.

4.4.2 The expansion of $J_{o,ij}(\omega)$

The question of selecting an appropriate frequency for evaluating the response power spectral density also arises when expanding the flexibility function $J_{o,ij}$. While the white-noise approximation simplifies the PSD by assuming a flat spectral distribution, the expansion of $J_{o,ij}$ introduces frequency-dependence through a second-order Taylor development, as given in equation (4.21). In this context, the choice of the expansion frequency becomes crucial to ensure local accuracy, particularly in the frequency range where the modal interaction is most significant. No though, that this frequency selection impacts only the S^{II}_q component of the response, in contrast with the white-noise assumption, which affects both S^{I}_q and S^{II}_q.

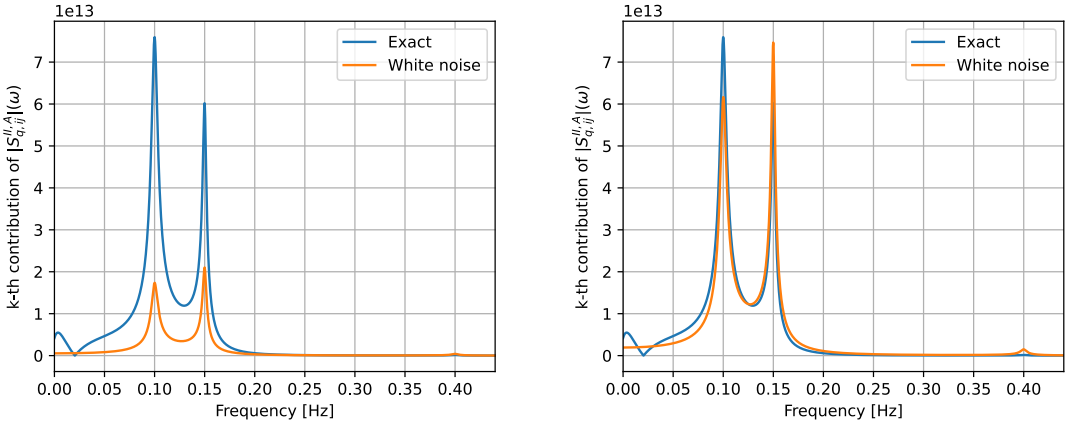

(a) With $S\left(\bar{\omega} = \frac{\omega_k+\omega_j}{2}\right)$ (b) With $S\left(\bar{\omega} = \frac{\omega_i+\omega_j}{2}\right)$

Figure 4.7: Illustration of the white-noise decomposition for $S^{\mathrm{II},A}_{q,ij}(\omega)$. Schematic example generated with $f_i = 0.1$ Hz, $f_j = 0.15$ Hz, $f_k = 0.4$ Hz, ξ_i =3%, $\xi_j = 1.2\%$, $\xi_k = 0.7\%$. In this fictive example $J_{o,ik}$ is set equal to 1.

In practice, a consistent strategy involves expanding $J_{o,ik}$ around $\omega_{ij} = (\omega_i + \omega_j)/2$, rather than around $\omega_{ik} = (\omega_i + \omega_k)/2$, as done in equation (4.16). This choice ensures a better approximation within the frequency band that carries the dominant energy exchange between modes i and j.

4.5 User guide

This section provides a concise summary of the equations required to implement the background/resonant decomposition. It is intended as a practical reference for users who wish to reconstruct the solution based on the methodology developed in this work. Only the essential steps and expressions are reported, without further derivation or discussion. It is meant to serve as a quick-access reference for implementation, containing only the final expressions derived throughout this chapter.

User Guide for the Developer

1. Evaluate the B contributions from (4.5) for contribution I, (4.6) for contribution II, A and from (4.7) for contribution II, B:

$$\Sigma^{\mathrm{I}}_{B,ij} = \int_{-\infty}^{+\infty} \frac{S_{F_{\mathrm{bu}},ij}(\omega)}{K_{d,i}(\omega)\overline{K}_{d,j}(\omega)}\,\mathrm{d}\omega,$$

$$\Sigma^{\mathrm{II},A}_{B,ij} = -\sum_k \int_{-\infty}^{+\infty} \frac{J_{o,ik}(\omega)S_{F_{\mathrm{bu}},kj}(\omega)}{K_{d,i}(\omega)K_{d,k}(\omega)\overline{K}_{d,j}(\omega)}\,\mathrm{d}\omega$$

$$\Sigma^{\mathrm{II},B}_{B,ij} = -\sum_k \int_{-\infty}^{+\infty} \frac{S_{F_{\mathrm{bu}},ki}(\omega)\overline{J}_{o,jk}(\omega)}{K_{d,i}(\omega)\overline{K}_{d,k}(\omega)\overline{K}_{d,j}(\omega)}\,\mathrm{d}\omega.$$

2. The B component is then obtained added the three contributions according to (4.4)

$$\boldsymbol{\Sigma}_{q,B} = \boldsymbol{\Sigma}^{\mathrm{I}}_{B} + \boldsymbol{\Sigma}^{\mathrm{II},A}_{B} + \boldsymbol{\Sigma}^{\mathrm{II},B}_{B}$$

3. Choose one formulation in Table 4.1 (F1A, linear and small damping is recommended).

4. Evaluate the poles of $S^{\mathrm{I}}_{R,q,ij}$, from (4.26)

$$p_{ll,1} = \frac{-a_{ll,1} - \sqrt{a_{ll,1}^2 - 4a_{ll,2}a_{ll,0}}}{2a_{ll,2}} \qquad \text{and} \qquad p_{ll,2} = \frac{-a_{ll,1} + \sqrt{a_{ll,1}^2 - 4a_{ll,2}a_{ll,0}}}{2a_{ll,2}}$$

   with $l = i$ and $l = j$. The $a_{ll,m}$ elements $m = \{0, 1, 2\}$ are given in Table 4.1. In total 4 poles, possibly duplicated, must be calculated. Discard the poles that are located below the real axis of the complex plane.

5. Evaluate the residuals corresponding to the non-discarded poles from (4.28). Multiply them by $2\mathrm{i}\pi$, and sum them all to get $\Sigma^{\mathrm{I}}_{R,q,ij}$.

6. Evaluate the poles of $S^{\mathrm{II,A}}_{R,q,ij}$, from (4.26) with $l = i$, $l = j$ and $l = k$. The $a_{ll,m}$ elements $m = \{0, 1, 2\}$ are given in Table 4.1. In total 6 poles, possibly duplicated, must be calculated. Discard the poles that are located below the real axis of the complex plane.

7. Evaluate the residuals corresponding to the non-discarded poles from (4.28). Multiply them by $2\mathrm{i}\pi$, and sum them all to get $\Sigma^{\mathrm{II,A}}_{R,q,ij}$.

8. Repeat the process described in 6. and 7. with the poles of $S^{\mathrm{II,B}}_{R,q,ij}$ to get $\Sigma^{\mathrm{II,B}}_{R,q,ij}$

9. Evaluate the R component by superimposing the three contributions from (4.4)

$$\boldsymbol{\Sigma}_{q,R} = \boldsymbol{\Sigma}^{\mathrm{I}}_{R} + \boldsymbol{\Sigma}^{\mathrm{II},A}_{R} + \boldsymbol{\Sigma}^{\mathrm{II},B}_{R}$$

10. Add the B and R components according to (3.41)

$$\boldsymbol{\Sigma}_{q} = \boldsymbol{\Sigma}_{q,B} + \boldsymbol{\Sigma}_{q,R}$$

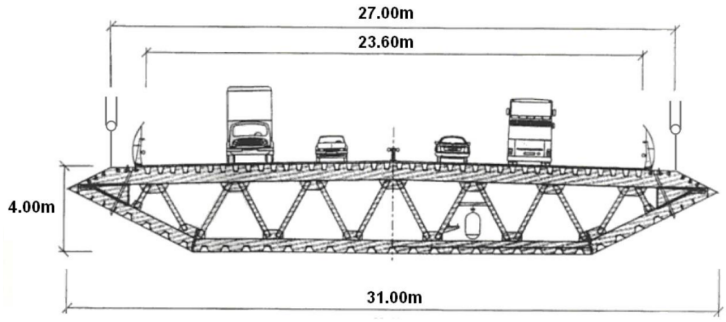

Figure 4.8: Deck section. Figure taken from [42].

4.6 Illustration

4.6.1 Presentation of the benchmark

The IABSE Task Group 3.1 Benchmark [42] is the third in a series of aeroelastic benchmark studies aimed at validating numerical methods for predicting the stability and buffeting response of long-span bridges. It builds upon previous benchmarks —also discussed previously in this Thesis— that focused on simpler systems, first considering a SDOF model and later extending to 2DOF systems. This final benchmark addresses the full bridge response, accounting for multi-modal coupling effects in a 12-mode representation.

The case study is based on the Storebælt East Bridge, a long-span suspension bridge in Denmark. The bridge deck is modelled using a finite element approach, retaining the first 12 structural modes, which include lateral, vertical, and torsional components. Aerodynamic forces are modelled using wind tunnel-derived aerodynamic derivatives, and the response is evaluated under both steady wind conditions and turbulent buffeting loads. For certain flutter derivatives, the quasi-steady coefficients have been used instead of proper wind tunnel measurements.

The structure under investigation is a three-span suspension bridge with a total length L_{tot}, a central span L_{main}, and two symmetric side spans L_{side}. The bridge deck is modelled as a beam-like structure, discretized using a series of nodal degrees-of-freedom representing vertical, lateral, and torsional motions. The key geometrical properties are provided in Table 4.2. A schematic representation of the bridge model, including the discretization into finite elements, is provided in Figure 4.9, while the cross section is detailed in Figure 4.8.

Table 4.2: Geometrical properties of the bridge

Parameter	**Value**
Total bridge length, L_{tot}	2696 m
Main span length, L_{main}	1626 m
Side span length, L_{side}	572 m
Deck width, B	31 m

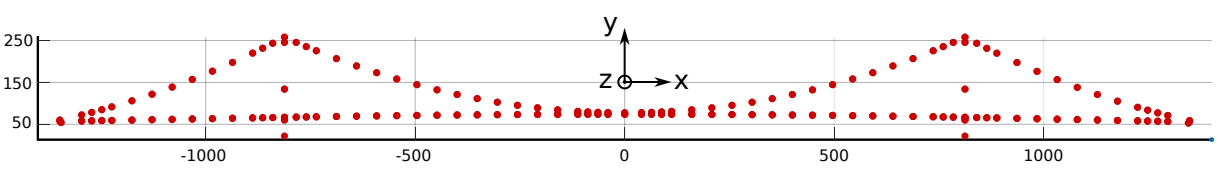

Figure 4.9: Schematic of the bridge structure and nodal discretization. Adapted from [42].

4.6.1.A The FEM model

The bridge deck is discretized using $N_{\text{elem}} = 70$ finite elements, each incorporating two nodes, and five degrees-of-freedom per node: vertical displacement h, lateral displacement p, torsional displacement α, and their respective slopes $\partial h/\partial x$ and $\partial p/\partial x$.

The structural mass matrix is derived from the modal masses given in Table 4.3. The stiffness matrix is accordingly calculated with the modal mass and the associated eigenfrequencies. A Rayleigh damping is then assumed to produce the structural damping matrix. All these matrices are constructed in modal basis.

The aeroelastic stiffness and damping matrices are obtained from the self-excited forces using the finite element method detailed in Appendix D. The modal projection of the assembled global matrices $\mathbf{C}_{\text{ae}}$ and $\mathbf{K}_{\text{ae}}$ along with the modal structural matrices $\mathbf{M}_{\text{s}}^{*}$, $\mathbf{C}_{\text{s}}^{*}$ and $\mathbf{K}_{\text{s}}^{*}$ are used to compute the modal wind-on properties of the structure.

4.6.1.B Modal Properties

The modal properties are given in the benchmark statement [42]. The main modal data is summarized in Table 4.3. The eigenmodes of the system are illustrated in Figure 4.11. All the modes have been considered in the present analysis.

Table 4.3: Modal properties of the first 12 modes

Mode	Mode Type	Eigenfrequency [Hz]	Modal Mass [kg]	Damping Ratio [%]
1	Horizontal 1st	0.0521	1.7424e+07	0.3
2	Vertical 1st	0.0839	1.8231e+07	0.3
3	Vertical 2nd	0.0998	1.6682e+07	0.3
4	Horizontal 2nd	0.1179	1.8981e+07	0.3
5	Vertical 3rd	0.1317	1.2559e+07	0.3
6	Vertical 4th	0.1345	2.1215e+07	0.3
7	Vertical 5th	0.1827	1.7402e+07	0.3
8	Horizontal 3rd	0.1866	2.4313e+07	0.3
9	Torsional 1st	0.2784	1.6827e+09	0.3
10	Vertical 6th	0.2815	1.6538e+07	0.3
11	Torsional 2nd	0.3833	1.9232e+09	0.3
12	Vertical 7th	0.3975	1.7269e+07	0.3

4.6.1.C Aerodynamic Model

Aerodynamic buffeting forces are modelled using the quasi-steady theory, with wind turbulence velocity fields defined by a von Kármán spectrum and coherence decay functions. A Davenport's formulation was used for the admittance function. Their properties are summarized in Table 4.4. The power spectral density of the resulting forces is constructed following the methodology also presented in Appendix D.

The self-excited forces are modelled using a combination of quasi-steady coefficients and unsteady aerodynamic derivatives obtained from wind tunnel experiments. The aerodynamic loads —comprising lift, drag, and pitching moment— are applied at each node of the bridge deck. Wind tunnel measurements provide the flutter derivatives A_i^* and H_i^* for $i \in \{1, 2, 3, 4\}$, while the quasi-steady coefficients are used for the remaining derivatives, specifically H_i^* and A_i^*

for $i \in \{5, 6\}$ and P_i^* for $i \in \{1, 2, 3, 4, 5, 6\}$. Consequently, $P_4^* = P_6^* = H_6^* = A_6^* = 0$. The non-zero flutter derivatives are depicted in Figure 4.10.

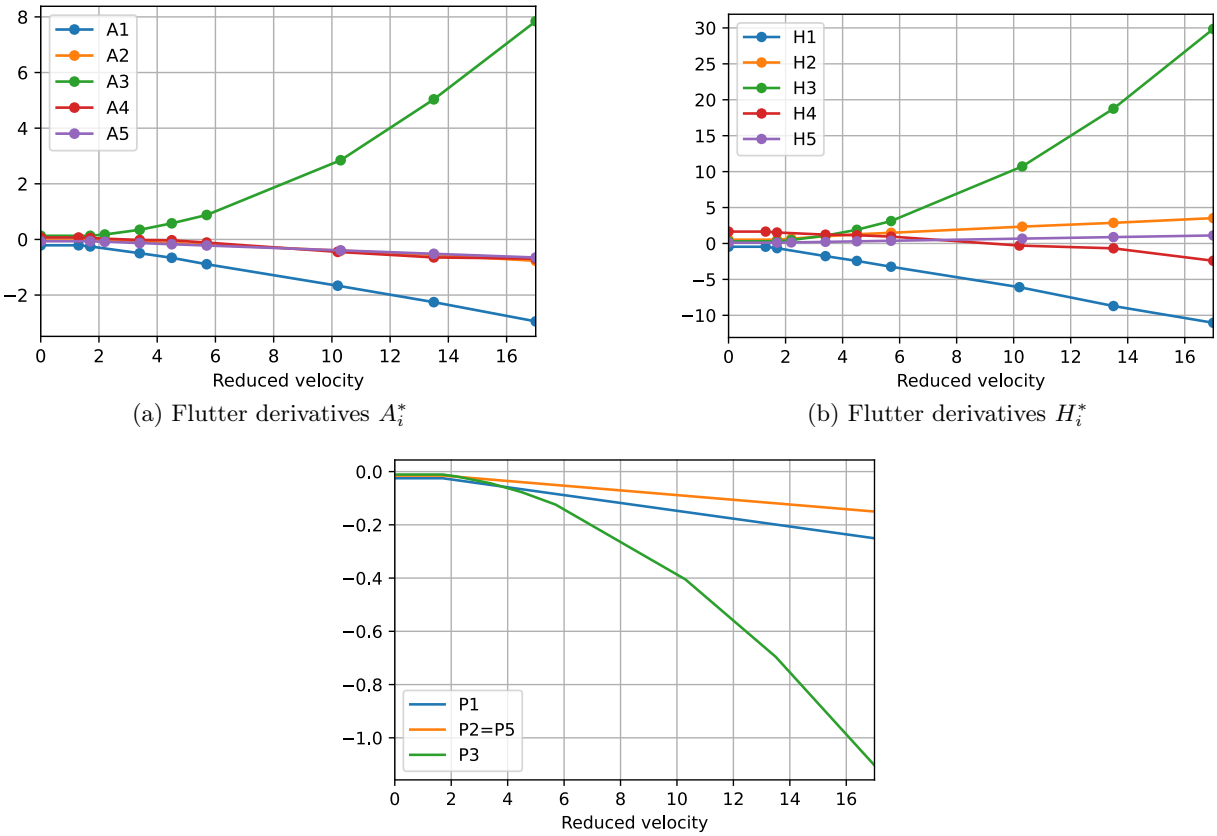

(a) Flutter derivatives A_i^*

(b) Flutter derivatives H_i^*

(c) Flutter derivatives P_i^*

Figure 4.10: Aerodynamic derivatives as a function of the reduced velocity. All non mentioned derivatives are zero.

Table 4.4: Wind turbulence properties used in the buffeting analysis

Parameter	**Value**
Longitudinal turbulence intensity, I_u	10%
Vertical turbulence intensity, I_w	5%
Integral length scale, L_u^x	200 m
Integral length scale, L_u^y	20 m
Coherence coefficients C_{ux}/C_{uz}	10/10 [-]
Coherence coefficients C_{wx}/C_{wz}	6.5/3 [-]
PSD of $u(t)$ and $w(t)$	Von Karman [116]
Admittance $A(f^*)$	$2/(7f^*)^2(7f^* - 1 + \exp(-7f^*))$
Air density ρ	1.22 kg m^{-3}

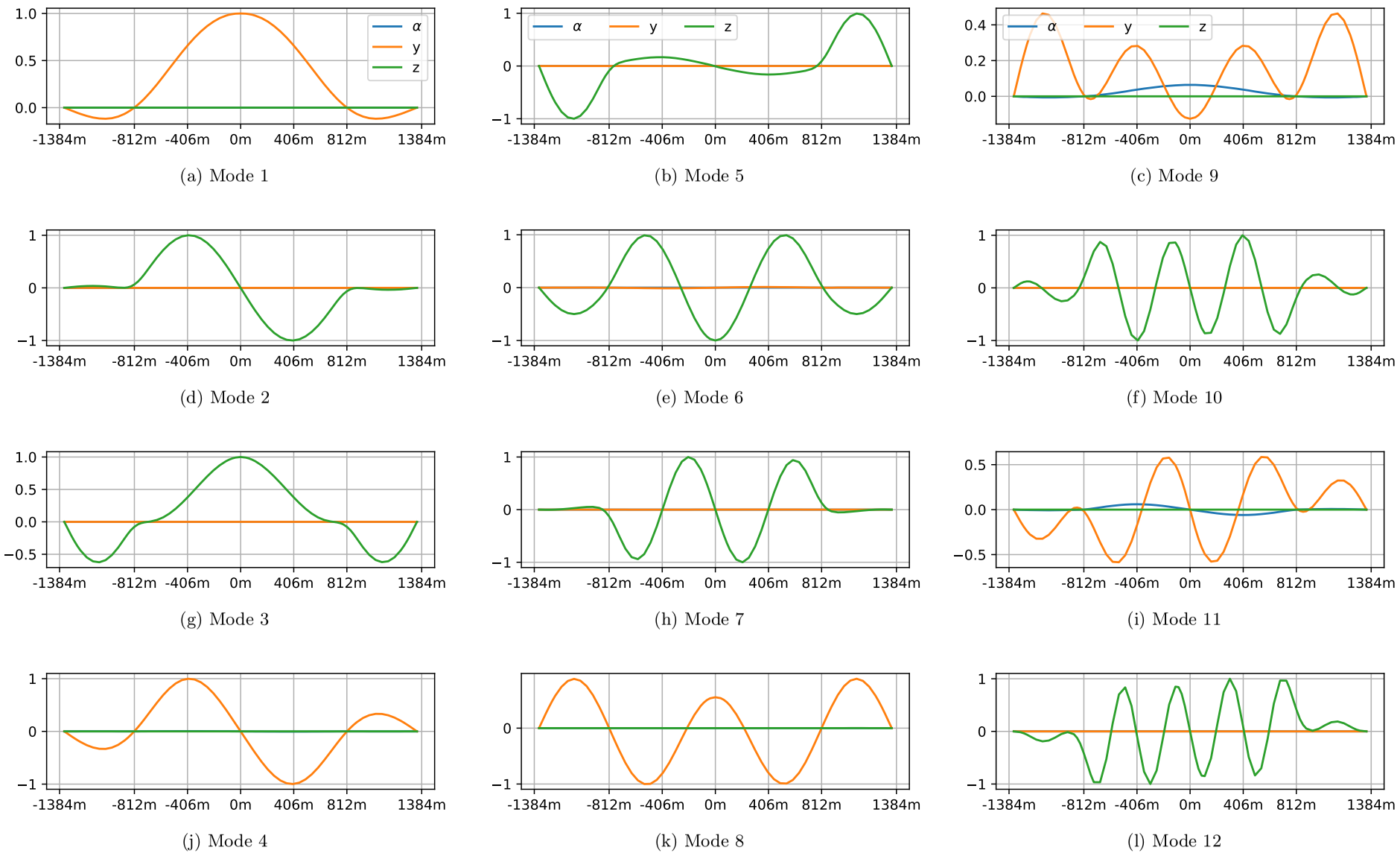

(a) Mode 1 (b) Mode 5 (c) Mode 9

(d) Mode 2 (e) Mode 6 (f) Mode 10

(g) Mode 3 (h) Mode 7 (i) Mode 11

(j) Mode 4 (k) Mode 8 (l) Mode 12

Figure 4.11: Structural modes in wind-off conditions.

4.6.2 Results

The determination of the critical velocity is discussed in detail in chapter 6, section 6.2.2. The value obtained is 69.9 m/s, which corresponds quite well to the averaged value of 68.8 m/s provided by [42].

4.6.2.A Modal results

Figure 4.12 presents the aeroelastic modal properties of the system in the subcritical regime. Chapter 5 will explain how these quantities have been obtained. In (a), the aeroelastic eigenfrequencies remain nearly constant across the wind speed range, except for torsional modes 9 and 11, which exhibit significant variations in their natural frequencies. The evolution of the total damping, shown in (b), follows an almost linear trend with wind speed. However, modes 9 and 11 deviate from this behaviour: mode 9 follows a curved trend and reaches zero just below 70 m/s, while mode 11 exhibits a similar trend but does not reach zero within the considered wind speed range.

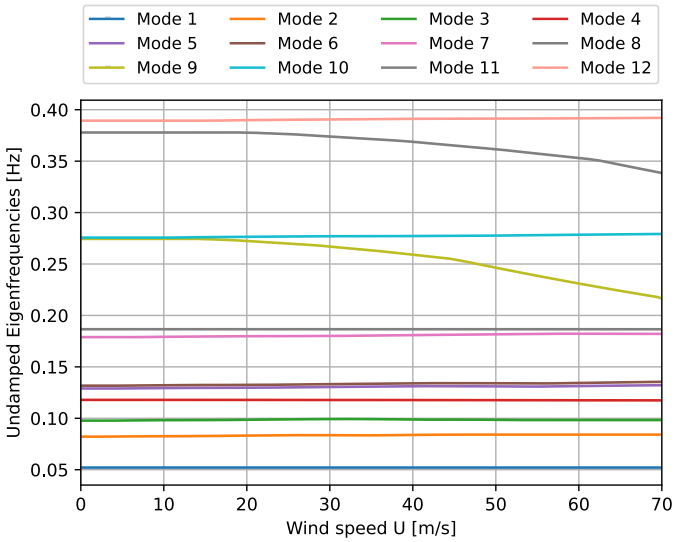

(a) Evolution of the undamped aeroelastic eigenfrequencies f_i with wind speed U.

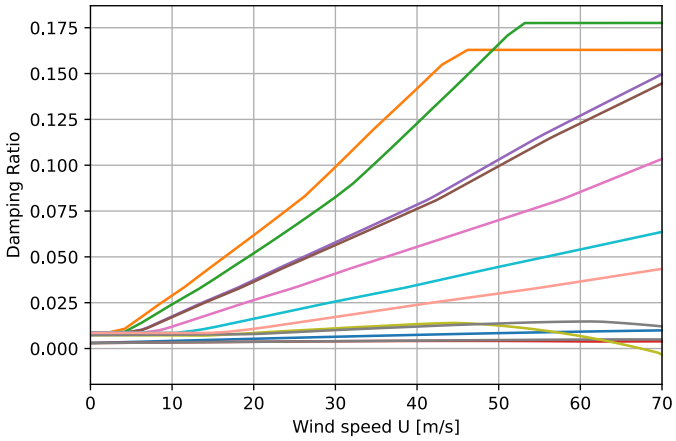

(b) Evolution of the aeroelastic damping ξ_i with wind speed U.

Figure 4.12: Aeroelastic modal properties of the structure prior to instability.

The wind-on eigenmodes have also been computed using the wind-off eigenmode basis. The MAC (Modal Assurance Criterion) number of right wind-on eigenvectors and wind-off eigenmodes

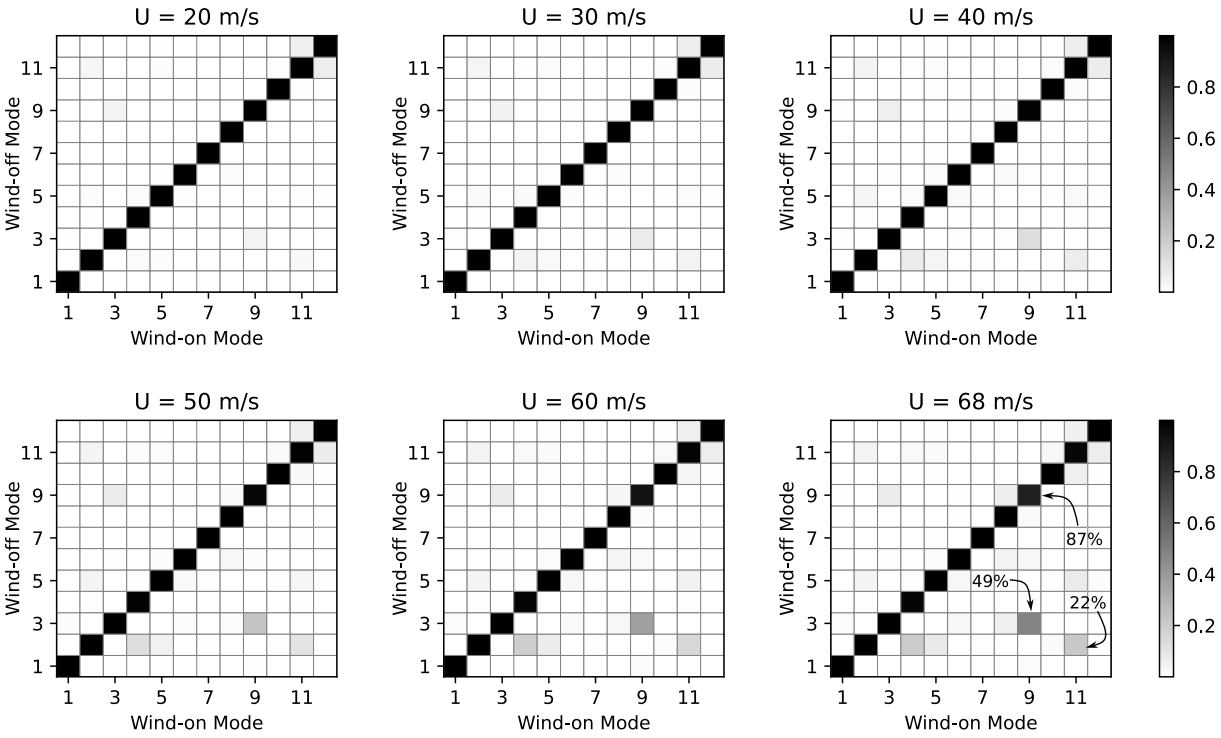

Figure 4.13: MAC numbers of the wind-on eigenmodes $\mathbf{\Phi}_R$ for different wind speeds U.

are represented in Figure 4.13 for different wind speeds. This number quantifies the correlation between two mode shapes, providing a measure of their similarity. It is defined for two vectors, $\mathbf{x}$ and $\mathbf{y}$, as

$$\mathrm{MAC}(\mathbf{x},\mathbf{y}) = \frac{\mathbf{x}^\mathsf{T}\mathbf{y}}{\sqrt{\mathbf{x}^\mathsf{T}\mathbf{x}}\sqrt{\mathbf{y}^\mathsf{T}\mathbf{y}}}. \tag{4.41}$$

The MAC values range from 0 to 1, where 1 indicates identical mode shapes and 0 indicates orthogonal mode shapes. For complex mode shapes, the MAC number is computed in absolute value to ensure a real-valued indicator. Here, it is used to assess the similarity between the wind-on eigenmodes and their wind-off counterparts. In this section, the considered wind-off modal basis is made up of the right eigenvectors solution of the wind-off damped eigenvalue problem, while the wind-on modal basis is established with the left and right eigenvectors solution of wind-on aeroelastic damped eigenvalue problem. Additional modal bases will later be considered, but their characteristics will be explained in detail at that time.

As observed in Figure 4.13, the presence of a strong diagonal across all wind speeds indicates that most wind-on modes keep a high correlation with their corresponding wind-off modes, meaning that the mode shapes remain merely unchanged despite the influence of aeroelastic effects. However, the presence of isolated off-diagonal points suggests localized mode interactions, where certain modes exchange characteristics with neighbouring modes as the wind speed increases.

This phenomenon is particularly noticeable at higher wind speeds, for instance in the 11th column, where the wind-on mode shape exhibits strong similarities with wind-off modes 2 and 11, but also, to a lesser extent, with wind-off modes 5 and 10. A similar interaction can be observed for wind-on mode 9, which couples contributions from wind-off modes 3 and 9 (bending and torsion). These off-diagonal terms serve as indicators of emerging aeroelastic instabilities, particularly involving wind-on modes 9 and 11. Their increasing interaction with other modes, depicting modal coupling, is a typical precursor to the onset of classical flutter.

Several modal power spectral densities are illustrated at $U = 45$ m/s in Figure 4.14 using either the wind-off modal basis in (a) or the wind-on modal basis in (b). The solid blue curve represents the exact modal power spectral density, while the dashed blue curve corresponds to the

MTSA approximation. The red and green dotted curve respectively represent the contributions $S^{\mathrm{I}}_{q,ij}(\omega)$ and $S^{\mathrm{II}}_{q,ij}(\omega)$ within the approximated MTSA method. The last curve, obtained using the approximation (4.2) with exact formulations for $H_{d,i}(\omega)$, $J_{o,ij}(\omega)$ and the exact PSD of the modal forces $S_{p,ij}(\omega)$ represents the theoretical limit of accuracy that the MTSA method could theoretically reach if $\mathbf{J}(\omega)$ were perfectly reproduced. In this section, linear formulations are used to approximate $J_{d,i}(\omega)$ and $J_{o,ij}(\omega)$.

It is important to note that the use of the term "exact" to refer to the blue curve may be misleading. This curve corresponds to the reference solution obtained via spectral analysis, without any of the additional assumptions that may underlie the other curves presented in Figure 4.14. This reference solution can be compared to the one published in [42], which compiles the results submitted by various contributors to the benchmark.

Figure 4.16 shows a comparison between my own result and the reference curve from [42]. A rescaling factor of 4π was applied to ensure consistency between the different scaling conventions used for the power spectral density. The reference curve in [42] represents an averaged outcome derived from a statistical treatment of all submitted contributions.

As seen in Figure 4.16, both approaches show excellent agreement. In what follows, the term "exact" will be used to refer to my own solution to the benchmark problem. However, this terminology should not be interpreted as implying that the proposed solution is superior to that provided in [42]; is simply used for greater convenience and control over the data handling throughout the study.

The PSD of mode 2 is well captured in both modal bases, although the wind-off modal basis slightly underestimates the resonance peak. However, all approximation methods suffer from an incomplete background/resonant separation, causing an excess of background energy in the post-resonant regime and leading to an overestimation of the PSD at higher frequencies. This issue also appears in the PSD of mode 3, which has a slightly higher resonant frequency. In this case, the estimation using the wind-off modal basis is slightly less accurate. For these two modes, the first-order correction, represented by the green curve, remains smaller when using the wind-on modal basis than with the wind-off modal basis.

The separation of these two components can be characterized by the ratio of their centroid frequencies, $r = f^*_R/f^*_B$. When this ratio is close to one —or worse, $r < 1$— background and resonant dynamics interfere, as observed for mode 2 in Figure 4.17(a) and (b). Conversely, when $r \gg 1$, a clear separation of timescales is achieved, as illustrated in (c) for mode 9, which has a significantly higher eigenfrequency.

The separation of background and resonant components is a fundamental hypothesis underlying the present method, and severe discrepancies are expected when $f^*_R/f^*_B \ll 3$. While this issue is highlighted here for mode 2, it similarly affects modes 3 and 5, which have slightly higher eigenfrequencies and still exhibit interference between background and resonant dynamics.

For mode 9, the PSD is perfectly captured by the approximation in the wind-on modal basis, benefiting from a complete separation of background and resonant response components. Conversely, the wind-off modal basis significantly underestimates the resonance peak, a consequence of the modal coupling occurring at this speed. The discrepancy becomes even more pronounced at $U = 65$ m/s, near the critical velocity, where the wind-off approximation completely fails to capture the resonance of this mode. In contrast, the wind-on modal basis continues to provide an accurate PSD estimation. This deviation is directly related to the high magnitude of the diagonality index at high wind speed, which quantifies the extent of modal coupling. In the case of the wind-off modal basis, the indicator exceeds 0.3, where the wind-on modal basis maintains a relatively low level across the entire frequency range (see later, in Figure 4.22).

The modal variances calculated using both the wind-off and wind-on modal bases are illustrated in Figure 4.18 for three wind speeds: $U = 35$, 45, and 55 m/s. The associated relative errors on the exact variance obtained from the integration of the exact response modal PSD, are indicated in percent above each bar.

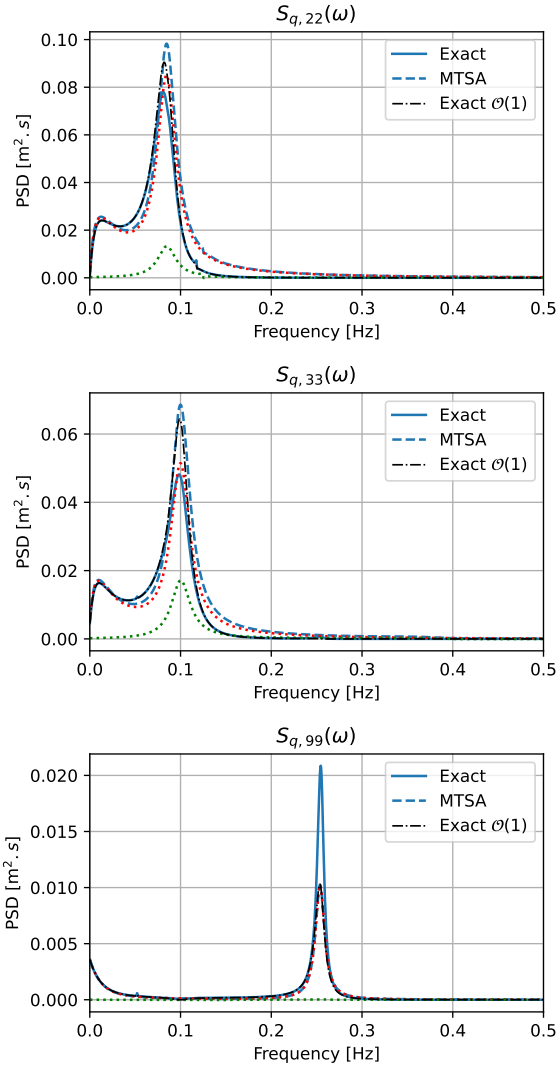

(a) Wind-off modal basis (1), undamped mode shapes with $\Phi_L = \Phi_R$

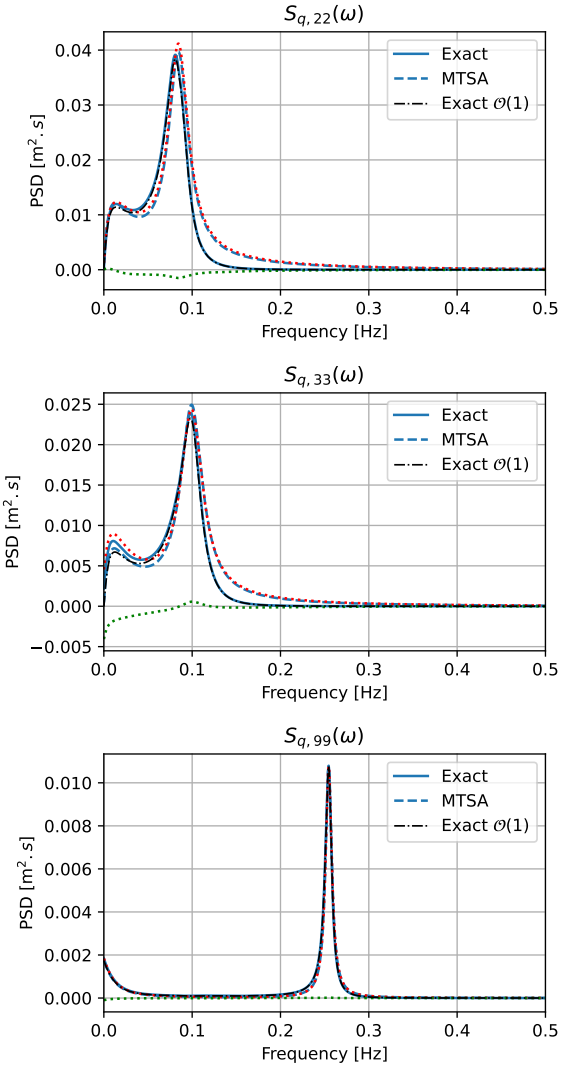

(b) Wind-on modal basis (6) with $\Phi_L \neq \Phi_R$

Figure 4.14: Selected modal response PSD at $U = 45$ m/s. The red and green dotted curves represent respectively the contributions of $S^{\mathrm{I}}_{q,ij}(\omega)$ and $S^{\mathrm{II}}_{q,ij}(\omega)$ to the approximated MTSA method.

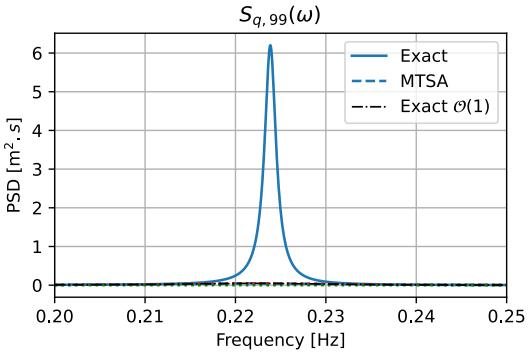

(a) Wind-off modal basis with undamped mode shapes with $\Phi_L = \Phi_R$

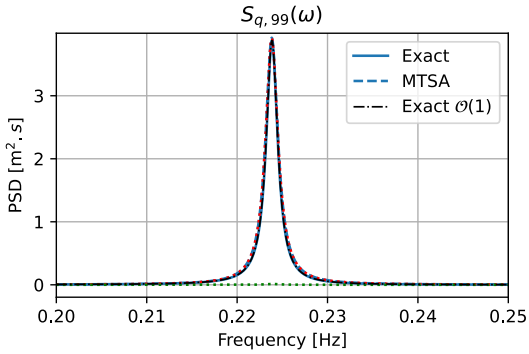

(b) Wind-on modal basis with $\Phi_L \neq \Phi_R$

Figure 4.15: Sower spectral density of modal response in mode 9 at $U = 65$ m/s.

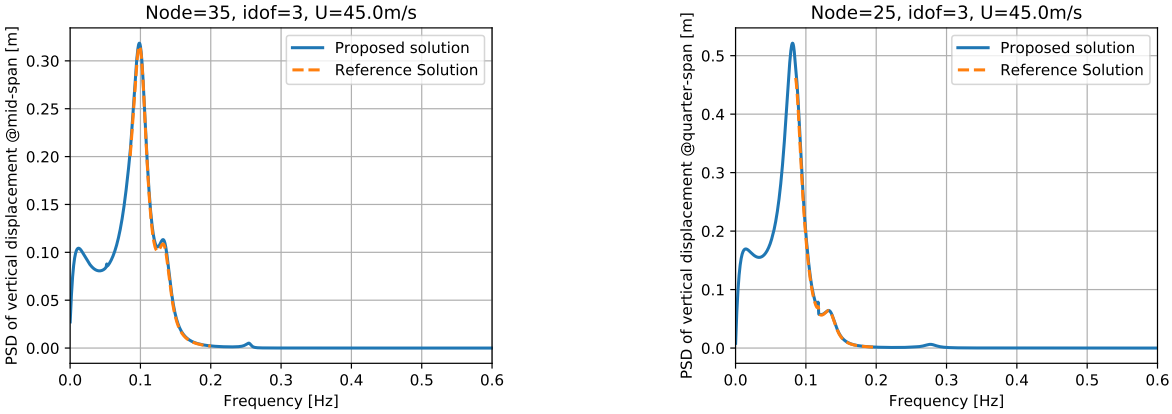

(a) Vertical displacement at mid-span

(b) Vertical displacement at quarter-span

Figure 4.16: Comparison of the reference solution provided by [42] (reference solution), and my personal result on the benchmark (proposed solution). A rescaling factor 4π was applied to harmonize the PSD scaling convention.

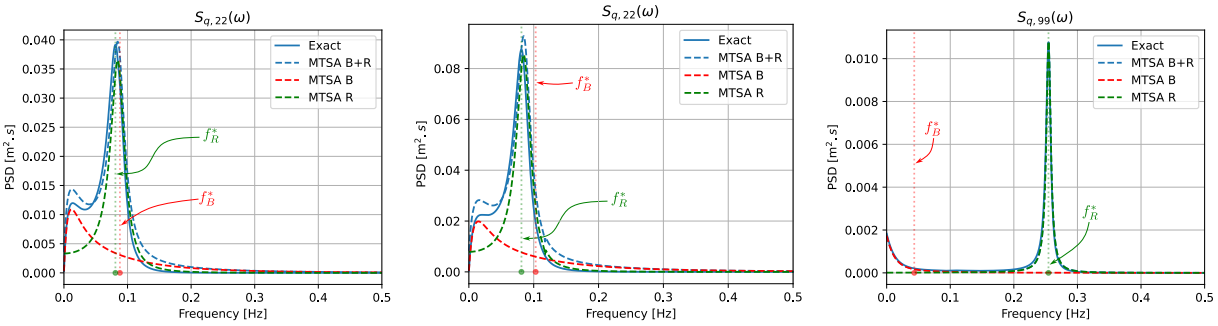

(a) Mode 2, $U = 45$ m/s, incomplete separation ($f_B^*/f_R^* = 0.92$)

(b) Mode 2, $U = 55$ m/s, incomplete separation ($f_B^*/f_R^* = 0.79$)

(c) Mode 9, $U = 45$ m/s, full separation ($f_B^*/f_R^* = 5.8$)

Figure 4.17: Illustration of the Background and Resonant interaction for selected PSDs and wind speeds and characterization of the background/resonant separation.

For $U = 35$ m/s, the MTSA method generally provides a good approximation of the variances, with relative errors remaining below 10%. At $U = 55$ m/s, the maximum relative error increases, except for modes 2, 3, and 9, which exhibit significantly higher errors compared to the others. The discrepancies for modes 2 and 3 can be partially attributed to the incomplete separation between the background and resonant components, as illustrated in the PSDs in Figure 4.14. Meanwhile, the errors associated with modes 3 and 9 are primarily due to the increasing modal coupling between these two modes.

At $U = 65$ m/s, corresponding to 95% of the critical speed, the wind-off modal basis produces inaccurate results, with relative errors exceeding 60%. In contrast, the wind-on modal basis still provides reasonable estimates, with errors around 15%. This behaviour was anticipated based on Figure 4.15(a), where the MTSA method fails to capture the resonant peak, leaving only the background component (which is not visible in the graphical window) as the sole energetic contribution considered in the approximation.

The correlation coefficients ρ_{ij} based on the covariances $\Sigma_{q,ij}$ obtained from the exact and MTSA methods are illustrated in Figure 4.19 for the wind-off modal basis, and in Figure 4.20 for the wind-on modal basis. Each line of the Figure corresponds to one wind velocity. The left column of the Figure depicts the correlation evaluated with the exact integration, the central

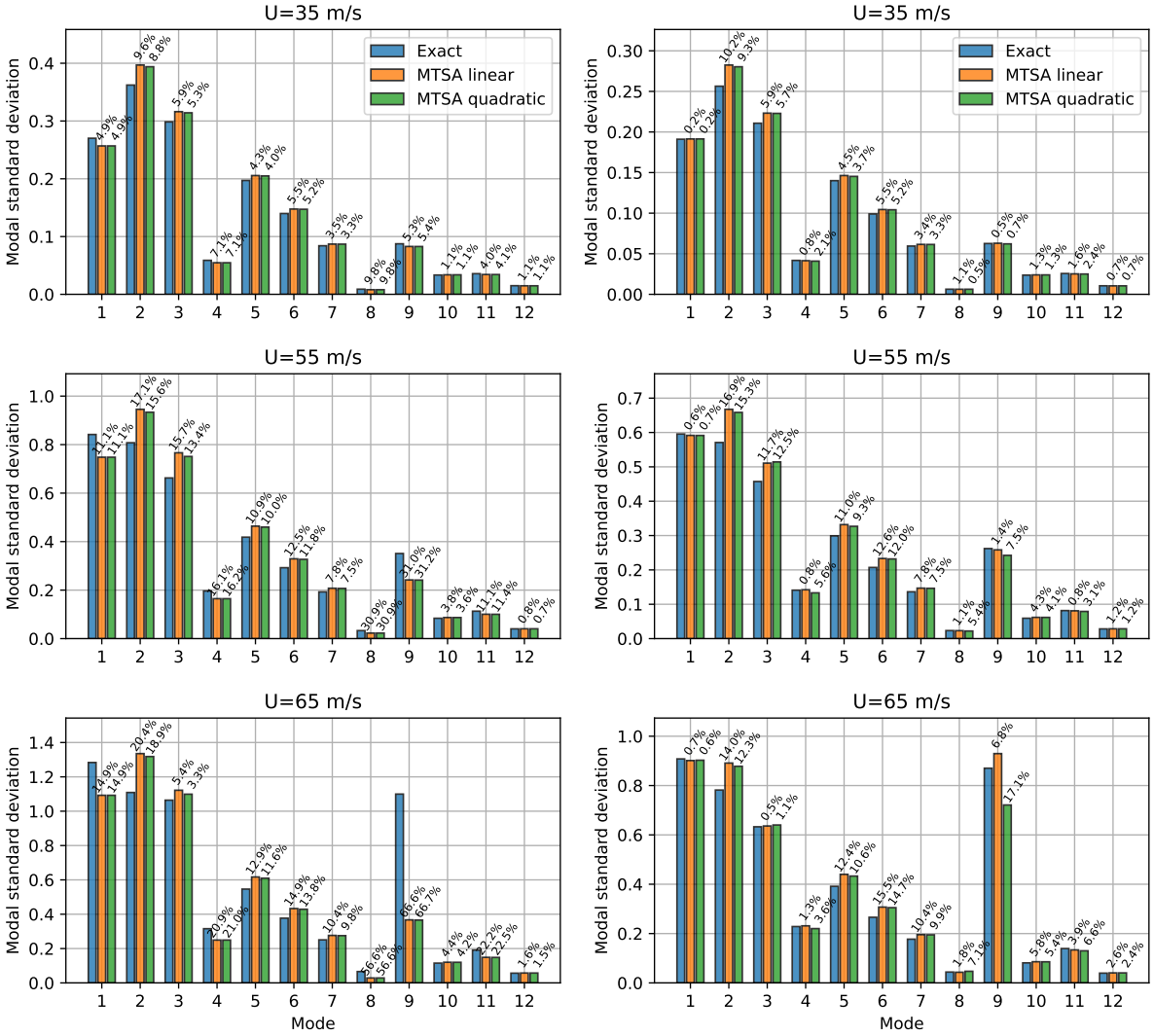

(a) Wind-off modal basis, with undamped mode shapes and $\Phi_L = \Phi_R$

(b) Wind-on modal basis with $\Phi_L \neq \Phi_R$

Figure 4.18: Standard deviation of the modal displacement at three different wind speeds.

column the coefficients calculated from the MTSA method and in the right column, the absolute errors between these two results. For visualisation purposes of the colour scale, the diagonal elements of the correlation coefficients matrices have been set to 0 (even though equal to 1).

Globally, the shape of the correlation coefficient matrix at low wind speed is well reproduced for both modal bases, even though the absolute error matrix is less populated for the wind-on modal basis than for the wind-off. The maximal absolute error on the exact correlation coefficient is roughly 10% in the wind-off modal basis drops to 3% for the wind-on modal basis. Close to flutter, the calculated error of 31% confirms that the wind-off modal basis is less accurate at those speeds, since the maximal error of 3% is achieved by the wind-on modal basis.

To put the importance of the absolute error committed on the correlation coefficients in perspective with the relative errors committed on the exact variances presented in Figure 4.18, the contributions of the errors on the modal variances and on the modal correlation coefficients can be emphasized on the representation of the nodal variances, which is one of the ultimate point of interest of the dynamic study. Let's consider an arbitrary nodal displacement z, expressed as the superposition of two modal displacements, this displacement is expressed as

$$z = \alpha q_1 + \beta q_2. \tag{4.42}$$

The variance of the nodal displacement z is given by

$$\sigma_z^2 = \alpha^2 \sigma_{q_1}^2 + \beta^2 \sigma_{q_2}^2 + 2\alpha\beta\rho\, \sigma_{q_1}\sigma_{q_2}. \tag{4.43}$$

Assuming that the correlation coefficient ρ is evaluated by the MTSA method with an absolute error $\Delta\rho$, and similarly that the modal variances are approximated with an absolute error $\Delta\sigma_q$, the approximation of the nodal variances $\tilde{\sigma}_z$ reads

$$\tilde{\sigma}_z^2 = (\sigma_z + \Delta\sigma_z)^2 = \alpha^2(\sigma_{q_1} + \Delta\sigma_{q_1})^2 + \beta^2\left(\sigma_{q_2} + \Delta\sigma_{q_2}\right)^2 + 2\alpha\beta\left(\rho + \Delta\rho\right)\sigma_{q_1}\sigma_{q_2} \tag{4.44}$$

Or, assuming $\Delta\sigma_z \ll 1$, the error on the variance $\Delta\sigma_z^2 + 2\sigma_z\Delta\sigma_z \approx 2\sigma_z\Delta\sigma_z$, and (4.44) becomes

$$2\sigma_z\Delta\sigma_z = \alpha^2\left[\Delta\sigma_{q_1}\left(\Delta\sigma_{q_1} + 2\sigma_{q_1}\right)\right] + \beta^2\left[\Delta\sigma_{q_2}\left(\Delta\sigma_{q_2} + 2\sigma_{q_2}\right)\right] + 2\alpha\beta\Delta\rho\,\sigma_{q_1}\sigma_{q_2}. \tag{4.45}$$

Hence, the error committed on the nodal variance is composed of several terms including one proportional to the error on the modal variances, one proportional the squared-root of the error on the modal variance and one last proportional to the error committed on the correlation coefficient. Focusing particularly on the latter term, assuming that the errors on the modal variances are zero

$$2\sigma_z\Delta\sigma_z = 2\alpha\beta\Delta\rho\,\sigma_{q_1}\sigma_{q_2}. \tag{4.46}$$

The associated relative error is

$$\frac{\Delta\sigma_z}{\sigma_z} = \frac{\Delta\rho\,\sigma_{q_1}\sigma_{q_2}}{\sigma_{q_1}^2 + \sigma_{q_2}^2 + 2\rho\sigma_{q_1}\sigma_{q_2}} = \frac{\Delta\rho\gamma}{1 + \gamma^2 + 2\Delta\rho\gamma} \tag{4.47}$$

with $\gamma = \alpha\sigma_{q_1}/\beta\sigma_{q_2}$. Differentiating this function with respect to γ, and equating to zero gives

$$(1 + \gamma^2 + 2\Delta\rho\gamma) = 2\gamma^2 + 2\Delta\rho\gamma, \tag{4.48}$$

for which $\gamma^2 = 1$ is the solution. This indicates that the relative error on the nodal variance is maximal when $\gamma^2 = 1$ or when $\alpha^2\sigma_{q,1}^2 = \beta^2\sigma_{q,2}^2$. When $\gamma = 1$, the relative error (4.47) becomes

$$\frac{\Delta\sigma_z}{\sigma_z} = \frac{\Delta\rho}{2(1 + \Delta\rho)} \sim \frac{\Delta\rho}{2}. \tag{4.49}$$

An important conclusion can be drawn from this last equation. Even if the relative error in the correlation coefficient is large such as sometimes observed in Figure 4.19, its actual impact on

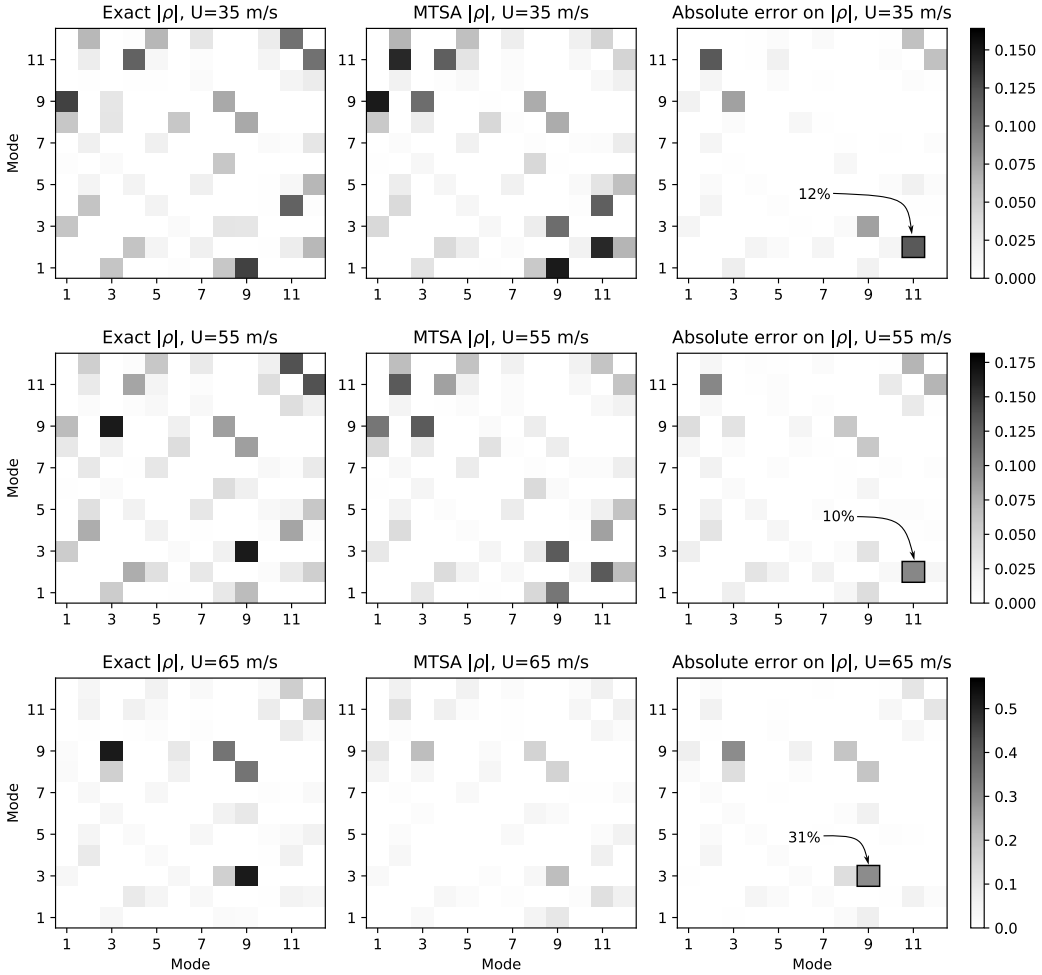

Figure 4.19: Exact and approximated correlation coefficients, and absolute error on the correlation coefficients evaluated at different wind speeds using a wind-off modal basis and a linear flexibility.

the nodal variance depends on the relative contribution of the interacting modes to the overall structural response. Furthermore, since $\Delta\sigma_z \to 0$ when $\gamma \to 0$ or $\gamma \to \infty$, if a particular mode has a low participation factor (i.e., it contributes little to the total displacement energy), then even a significant error in its correlation coefficient will have a negligible effect on the nodal variance. This naturally reduces the practical impact of correlation errors.

Thus, a large error in the correlation coefficient does not necessarily translate into a significant error in the nodal variance because the impact is modulated by modal participation factors. Even tough the reasoning was hold considering only two modes, practical cases (including this one) show that mode interactions are typically limited to a few dominant modes. Therefore, while the correlation error should be minimized, its practical influence on structural response may remain limited in many cases, so that inaccurate representations of the modal correlation coefficients should not be sufficient to quantify the efficiency of a method. Instead, the assessment of accuracy should be based on the result of primary interest: the nodal variances.

4.6.2.B Nodal results

Figure 4.21 presents the torsional, transverse, and vertical displacements along the deck for $U = 35$, 45, and 55 m/s, as obtained using the MTSA and exact methods.

The torsional behaviour is accurately reproduced by the MTSA wind-on method, which closely follows the exact curve at all wind speeds, with an error on the order of one percent.

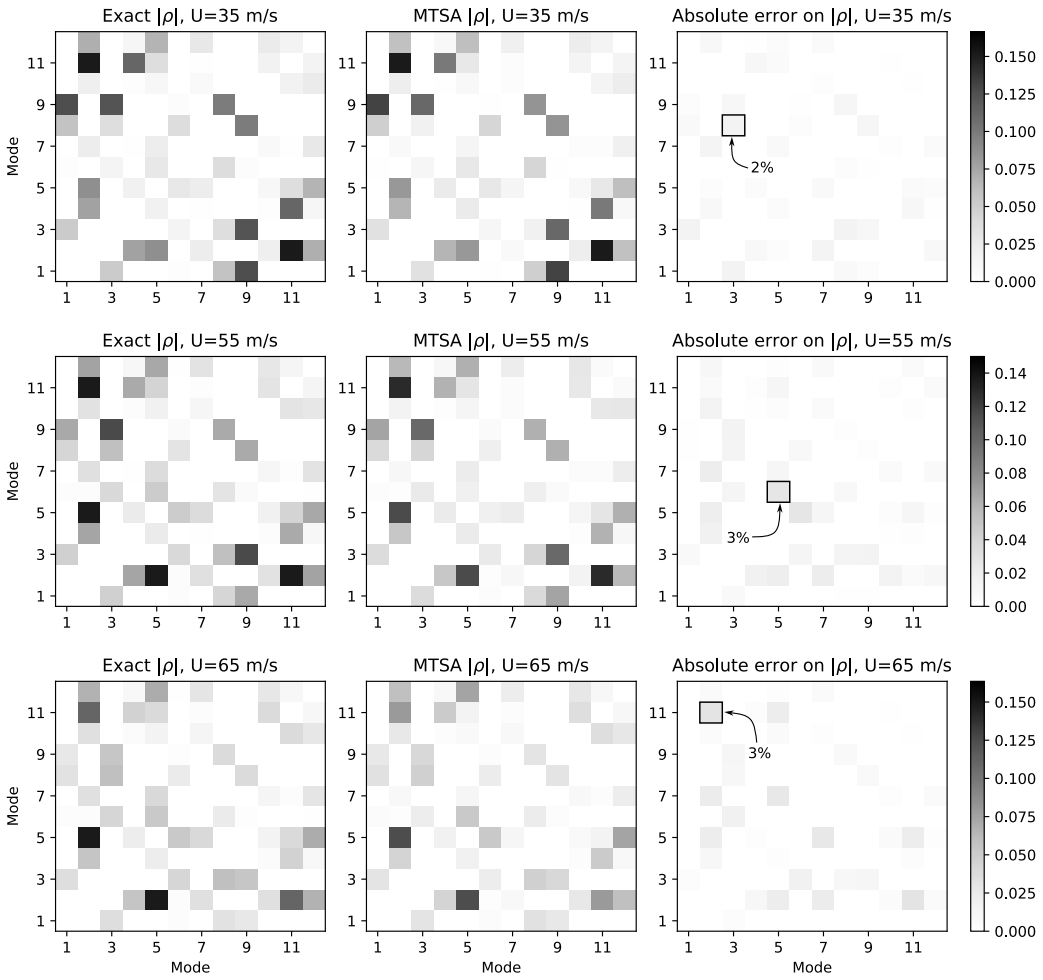

Figure 4.20: Exact and approximated correlation coefficients, and absolute error on the correlation coefficients evaluated at different wind speeds using a wind-on modal basis and a linear flexibility.

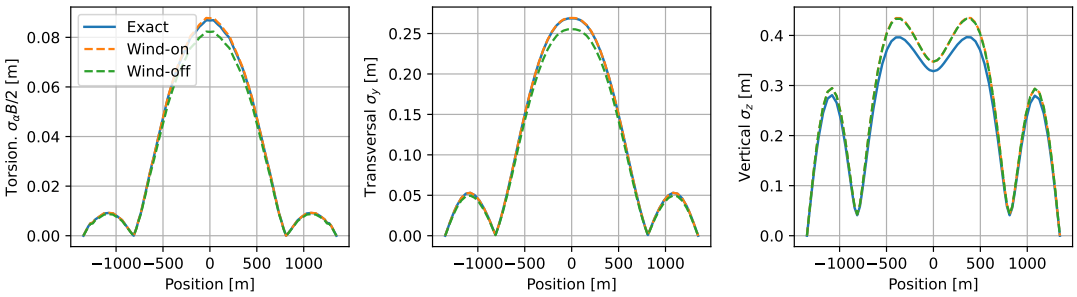

(a) $U = 35$ m/s

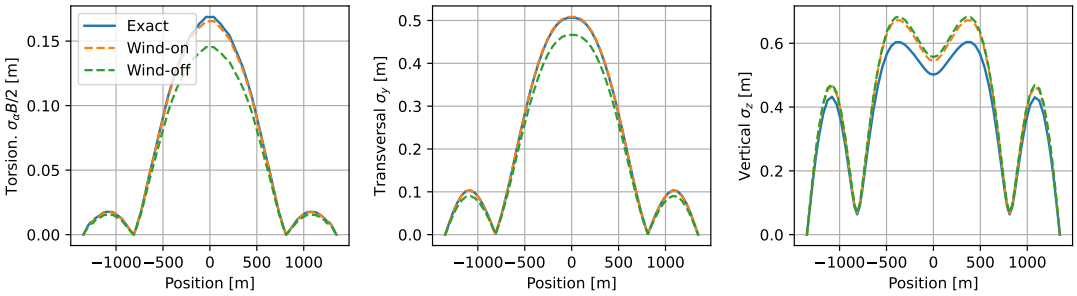

(b) $U = 45$ m/s

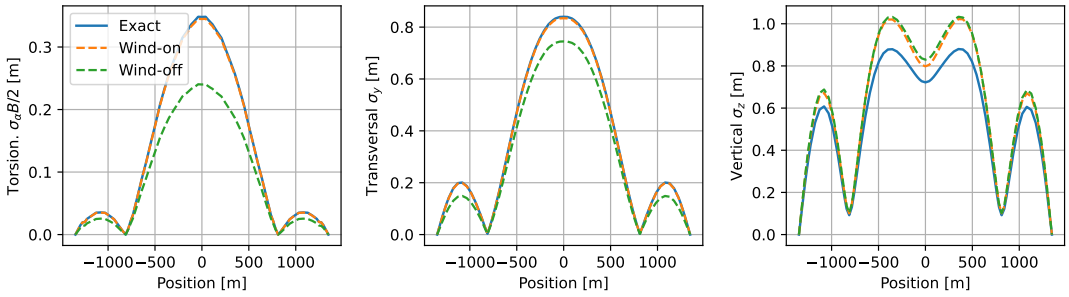

(c) $U = 55$ m/s

Figure 4.21: Profiles of the standard deviation of displacement and rotation, along the bridge deck, for the exact and MTSA approaches (wind-off or wind-on modal basis).

In contrast, the MTSA wind-off method is significantly less accurate, providing an acceptable estimation at $U = 35$ and 45 m/s, with relative errors of approximately 5% and 10%, respectively. At $U = 55$ m/s, the error associated with the wind-off method increases to around 30%.

Similar trends are observed for the vertical motion: the wind-on method yields highly accurate results, while the wind-off method exhibits increasing errors as the wind speed rises due to the growing diagonality index. For transverse displacement, the error is somewhat larger, but in this case, both methods show comparable accuracy, with neither significantly outperforming the other.

For the remainder of this section, the discussion will focus on the response at mid-span, as this section appears to provide a representative measure of the error across the entire deck.

4.6.3 A Promise on computational efficiency

While the core of this work focuses on the development and validation of the MTSA methodology, one of its primary motivations remains the reduction of computational burden typically associated with frequency-domain flutter analysis. A rigorous comparative benchmark could unfortunately not be carried out in the present work due to time constraints. However, the structure of both the exact and approximate methods allows a first quantitative assessment of their respective

computational loads, giving a preliminary taste of the efficiency gains.

The classical method used as a reference requires evaluating the power spectral density (PSD) of the structural response from its exact formulation:

$$\mathbf{S}_q(\omega) = \mathbf{H}(\omega)\,\mathbf{S}_{F_{\text{bu}}}(\omega)\,\mathbf{H}^*(\omega)$$

This operation must be repeated over a fine frequency grid to capture the resonant peaks accurately. In typical cases, about 2,000 integration points are required to ensure an accurate evaluation of the integral, no matter the smallness of the damping ratio, and the frequency drifting. For each of these frequencies, the following operations must be carried out:

1. **Evaluation of the dynamic flexibility $\mathbf{J}(\omega)$**, which includes assembling the nodal aeroelastic matrices (which are established only in nodal form), followed by their projection onto the modal basis.
2. **Inversion of the dynamic flexibility matrix**, to obtain $\mathbf{H}(\omega) = \left[-\omega^2\mathbf{M} + \mathrm{i}\omega\mathbf{C} + \mathbf{K}\right]^{-1}$.
3. **Evaluation and projection of the nodal PSD matrix $\mathbf{S}_{F_{\text{bu}}}(\omega)$** onto the modal basis.
4. **Evaluation of the response PSD**, involving matrix multiplications with the flexibility matrix and the projected forcing matrix.

Both the projection of the nodal aeroelastic matrices and that of the buffeting load matrix are known to be computationally expensive. This projection step must be repeated 2 `npoints` times per wind speed.

By contrast, the MTSA method splits the response PSD into background and resonant components, each treated with tailored approximations. For the background component, the frequency integration must still be performed numerically, but with far fewer points—typically on the order of 10 to 100. When the aeroelastic stiffness is approximately constant in the background frequency range, this component can even be computed from the variance of the buffeting forces alone, requiring a single evaluation and projection of the buffeting load PSD.

For the resonant component, an analytical integration is performed using the Cauchy residue theorem. At each wind speed, this step involves:

- Approximately 4 $\texttt{nmodes}^2$ evaluations and projections of the nodal aeroelastic matrices (for both the matrices and their gradients) corresponding to all particular frequencies ω_{ij}.
- Around $\texttt{nmodes}^2$ evaluations and projections of the nodal buffeting PSD matrix.

These operations yield a total of $100 + 5$ $\texttt{nmodes}^2$ projections per wind speed for the MTSA method, compared to 2 `npoints` for the exact method.

As an illustrative example, consider `npoints` $= 2000$ and `nmodes` $= 12$. The exact method requires about 4000 projections per wind speed, while the MTSA method requires approximately $200 + 5 \cdot 144 = 920$ projections.

This corresponds to a reduction by a factor of more than 4 in the number of modal projections. If the aeroelastic stiffness matrix is treated as constant in the background regime, this factor increases to nearly 6. Given that the modal projection is the dominant cost in large finite element models, this suggests substantial savings in computational time—especially for large parametric studies or iterative design processes. The scalability of the MTSA method is also particularly profitable: the gain in computational cost observed at one wind speed can be directly extrapolated to the entire buffeting analysis over a full wind speed envelope.

It should be noted, however, that the numbers presented above do not take into account the cost of the pre-flutter analysis required to determine the wind-dependent modal properties prior to instability, which are essential inputs to the MTSA method. Nonetheless, such an analysis must also be performed when using classical flutter methods to assess stability. Therefore,

Denomination	Damped/Undamped mode shapes	Wind-on/off	$\mathbf{\Phi}_L$ vs $\mathbf{\Phi}_R$
B1	undamped	Wind-off	$\Phi_L = \Phi_R$
B2	damped	Wind-on	$\Phi_L = \Phi_R$
B3	damped	Wind-on	$\Phi_L \neq \Phi_R$

Table 4.5: Denomination and description of the modal bases considered in this application.

including this cost when comparing the two approaches would not be appropriate, as it does not represent a specific burden of the MTSA method.

While these numbers are promising, they should be confirmed by a dedicated benchmark, ideally comparing both methods implemented within the same programming environment and using the same numerical libraries. Only under these conditions can a fair and accurate comparison of real computational time be established.

4.6.4 Influence of the modal basis

The results presented in the previous sections have highlighted significant differences in accuracy between the wind-off and wind-on modal bases. This section provides a more detailed comparison of these modal bases.

As briefly discussed in Chapter 3, the choice of the modal basis is not unique, and several alternative formulations could have been considered. The use of left and right eigenvectors as the modal basis was introduced based on mathematical intuition, but has not been explicitly justified. To address this, a third modal basis, in which left and right eigenvectors are set equal, is introduced in this section. In total, three modal bases are examined, and their characteristics are summarized in Table 4.5.

The interest in considering alternative modal bases stems from the objective of better diagonalizing the flexibility matrix. The degree of diagonalization is quantified by the diagonality index, shown in Figure 4.22 for $U = 45$ m/s and $U = 65$ m/s for the three considered modal bases. While the overall curve matters, the maximum value typically dictates the magnitude of the error on the integrated results (variances and covariances). The wind-on modal basis with left and right eigenvectors (B3), represented by the green curve, exhibits a significantly lower diagonality index than the wind-off modal basis (B1), reaching values below or close to the reference value $\varepsilon^2 = \mathcal{O}(1\%)$, which corresponds to an error of approximately 1% on the exact PSD according to equation (4.2). The wind-on modal basis without left eigenvectors (B2) results in a nearly constant but with very high diagonality index, demonstrating the importance of including left eigenvectors for effectively diagonalizing the flexibility matrix.

The standard deviation of the displacements at midspan for the different modal bases is shown in Figure 4.23. As expected from the analysis of the diagonality index, the error increases with speeds, following the trend of the diagonality index. The lower the diagonality index, the lower the relative error.

The torsional response is a characteristic example of the wind-off modal basis (B1) failing to capture the system's due to coupling. This aspect was already anticipated from the significant underestimation of the modal PSD of mode 9 in Figure 4.14(a), whereas the wind-on modal basis (B3) provided a much more accurate representation of the exact PSD, as shown in Figure 4.14(b). This tendency is confirmed on the nodal variances.

For the vertical displacement, the three modal bases yield similar results at low wind speeds but start diverging from $U = 45$ m/s, where coupling between modes 2, 3, and 9 becomes significant. Above 45 m/s, the wind-off method, fails at capturing the coupling, overestimating the contributions of mode 2 and 3, and disregarding that of mode 9. This may be observed in Figure 4.24 where the PSD of the vertical displacement at midspan is shown for the wind-off

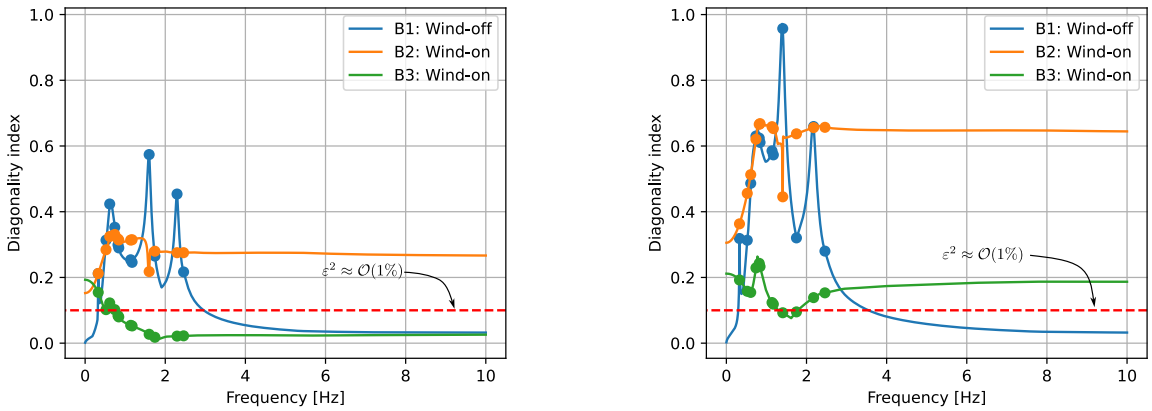

(a) $U = 45$ m/s (b) $U = 65$ m/s

Figure 4.22: Diagonality index $\rho\,[\mathbf{J}(\omega)]$ [-] for the considered wind-off and wind-on modal bases.

(B1) and wind-on (B3) modal bases. The black dashed curve, which represents the response PSD evaluated from (4.2) without further assumptions also fails to capture this coupling. This indicates that the inaccuracy is a direct consequence of the non-diagonality of the flexibility matrix.

Surprisingly, at low speeds, the relative error on the exact vertical displacement is similar for all methods. This unexpected behaviour is due to the poor separation of the background and resonant components, already observed in the modal PSD in Figure 4.17. Consequently, this error affects the MTSA methods regardless of the chosen modal basis. As wind speed increases, this issue becomes even more pronounced: the centroid of the background component shifts toward higher frequencies, further deteriorating the background/resonant separation (see Figure 4.17(a) and (b)), and the estimation of the nodal variance.

Overall, for all degrees-of-freedom, the error associated with the wind-off modal basis (B1) remains below or around 10% for wind speeds up to 50 m/s, corresponding to about 70% of the critical velocity. However, as coupling effects intensify, the method becomes increasingly less accurate, with errors exceeding 25% near the critical limit. The use of a wind-off modal basis (B1) should therefore be limited to structures with low aeroelastic effect.

By contrast, the relative error is reduced to a few percent when using the wind-on modal basis with left and right eigenvectors (B3), provided that other fundamental assumptions —such as timescale separation— are met, as is the case for vertical displacements. The wind-on modal basis without left eigenvectors exhibits inconsistent performance, sometimes outperforming the wind-off basis and sometimes underperforming, making its accuracy difficult to predict.

4.6.5 Influence of the formulation

Throughout this thesis, different formulations have been proposed for approximating the components of the impedance matrix $J_{d,i}(\omega)$ and $J_{o,ij}(\omega)$. These formulations are summarized in Table 4.1. This section compares the results obtained with these methods in terms of nodal variances. Three formulations have been selected for comparison: the gradient-free formulation (F0), the linear large damping formulation (F1B), and the quadratic large damping formulation (F2B).

The nodal standard deviations using either a wind-off or wind-on modal basis are shown in Figure 4.25 and Figure 4.26, respectively. A key observation is that the gradient-free formulation yields significantly worse results than the other two, regardless of the modal basis used. This formulation leads to relative errors of 30% or more. The consideration of aeroelastic gradients is therefore essential for accurately capturing aeroelastic behaviour.

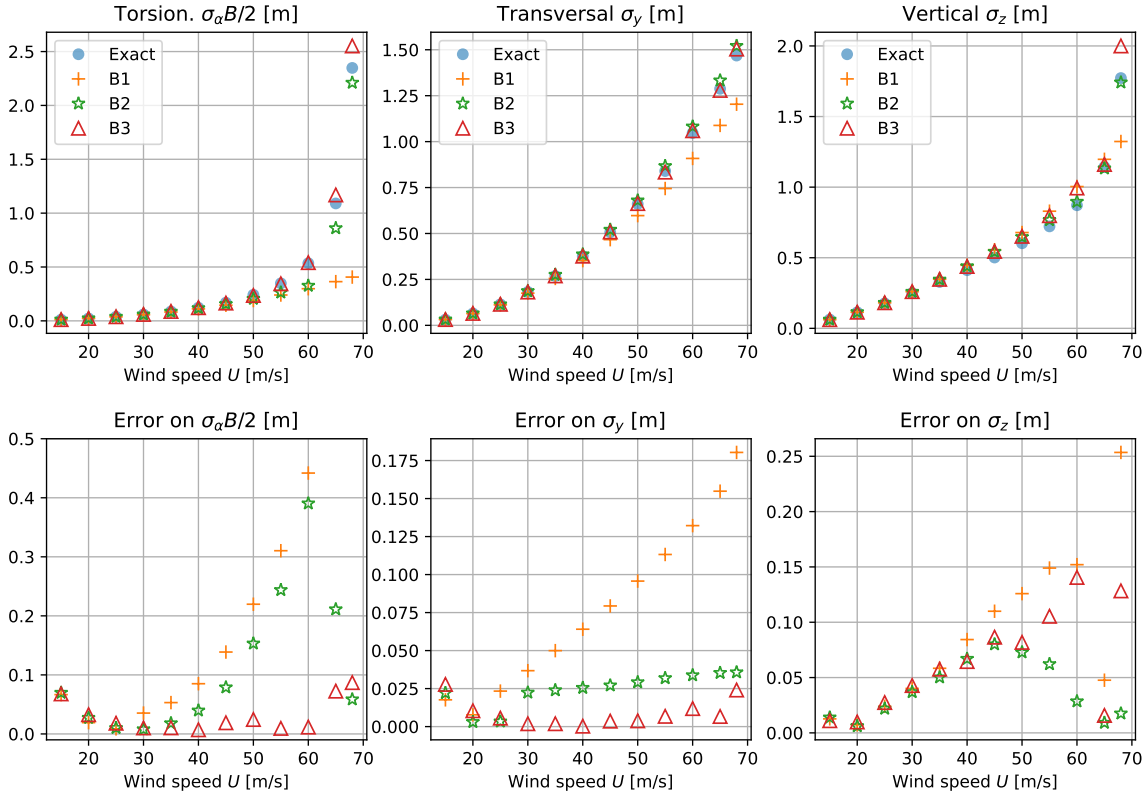

Figure 4.23: Evolution of the standard deviation of the torsional, transversal and vertical displacement at midspan for the three modal bases, and the exact method.

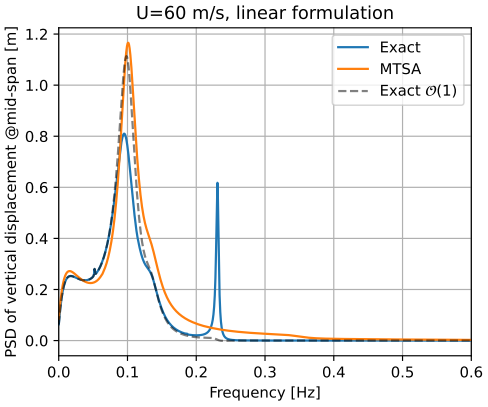

(a) Wind-off modal basis (B1) with over-reached diagonal index fails to capture coupling.

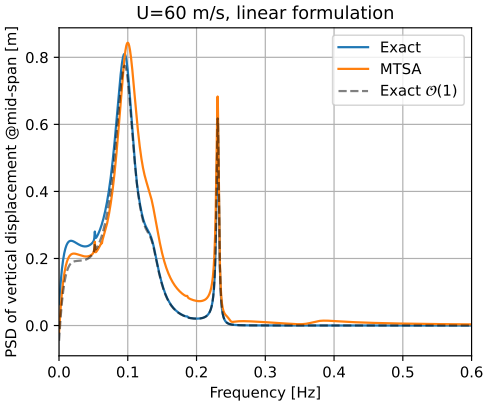

(b) Wind-on modal basis (B3) captures accurately the coupling

Figure 4.24: Comparison of the power spectral densities of the vertical displacement at mid-span at 60 m/s obtained using a wind-off and a wind-on modal basis. The exact $\mathcal{O}(1)$ method is obtained using equation (4.2) with exact formulations for $H_{d,\cdot}(\omega)$, $J_{o,ij}(\omega)$, and the exact PSD of the modal forces $S_{p,ij}(\omega)$

U [m/s]	b^*/a^* [%]	d^*/a^* [%]	$S^{\mathrm{I},-}_{q,99}/S^{\mathrm{I},+}_{q,99}$ [-]	$\Sigma^{\mathrm{I},-}_{q,99}/\Sigma^{\mathrm{I},+}_{q,99}$ [-]
55	-9.5	20	0.546	0.74
60	-12.7	25	0.2546	0.5
65	-17	31	28.8	0.19
65 (wind-off basis)	8e-5	1.6e-4	0.9999	0.9998

Table 4.6: Illustration of the asymmetry of the approximation of $S^{\mathrm{I}}_{q,99}(\omega)$ with quadratic formulation of the dynamic flexibility $J_{d,i}(\omega)$ with the complex wind-on modal basis with left and right eigenvectors (B3).

A second observation is that the linear (F1B) and quadratic (F2B) formulations produce very similar results. In fact, they are identical except in two specific cases. For the wind-off modal basis (B1), the quadratic formulation is slightly more accurate than the linear formulation. However, this gain in accuracy is marginal when compared to the overall accuracy of the MTSA method (e.g., a 2% improvement at $U = 60$ m/s when the error already exceeds 10%). The second difference between the linear and quadratic formulations is observed in Figure 4.26, specifically in the torsional displacement obtained with the wind-on modal basis (B3). Here, the difference is significant, but contrarily to expectations, the quadratic method does not yield more accurate results. Instead, it performs worse.

This discrepancy arises from the asymmetry in the representation of the PSD. When $J_{d,i}(\omega)$ is approximated as a linear function, the linear formulation exhibits a single root ω_i over all frequencies $\omega \in \mathbb{R}$. Consequently, $H_{d,i}(\omega) = J^{-1}_{d,i}(\omega)$ forms a function with a single resonance peak at ω_i in the positive frequency range. This linearization is used to integrate the frequency content of the PSD in the positive frequency range, while a separate linearization of $J_{d,i}(\omega)$ at $-\omega_i$ is used for the negative frequency range, ensuring a balanced treatment of both sides.

By contrast, when a quadratic approximation is used for $J_{d,i}(\omega)$, energy in both the positive and negative frequency ranges is handled simultaneously. For instance, if $J_{d,i}(\omega) = a_i\omega^2 + b_i\omega + c_i$, the first component of the PSD is therefore given by,

$$S^{\mathrm{I}}_{q,ij}(\omega) = H_{d,i}S_{p,ij}(\omega)\bar{H}_{d,j}(\omega) = a^*\omega^4 + b^*\omega^3 + c^*\omega^2 + d^*\omega + e^*, \tag{4.50}$$

where the coefficients a^*, b^*, c^*, d^*, and e^* are given by:

$$a^* = a_i\bar{a}_j, \quad b^* = a_i\bar{b}_j + \bar{a}_j b_i, \quad c^* = b_i\bar{b}_j + \bar{a}_j c_i + a_i\bar{c}_j, \quad d^* = \bar{b}_j c_i + b_i\bar{c}_j, \quad e^* = c_i\bar{c}_j.$$

However, nothing ensures that this function is symmetric. Symmetry is preserved if $b^* = d^* = 0$, but this is not necessarily the case in practice. In the wind-off modal basis (B1), b^* and d^* are observed to be close to zero, ensuring symmetry in the PSD approximation and thus an even treatment of the positive and negative spectral components. However, in the wind-on modal basis, these coefficients can become significant, leading to an asymmetric representation of the PSD. This asymmetry is particularly evident in mode 9, as shown in Figure 4.27, where the quadratic formulation significantly underestimates the negative frequency peak by a factor of four compared to the actual amplitude, which should be equal to the positive peak. Therefore, quadratic formulations of the dynamic flexibility should be applied cautiously in configurations where aeroelastic effects are significant. Ideally, one should verify in advance that the ratios b^*/a^* and d^*/a^* remain small for the relevant modes i and j, ensuring a symmetric approximation of the diagonal transfer function.

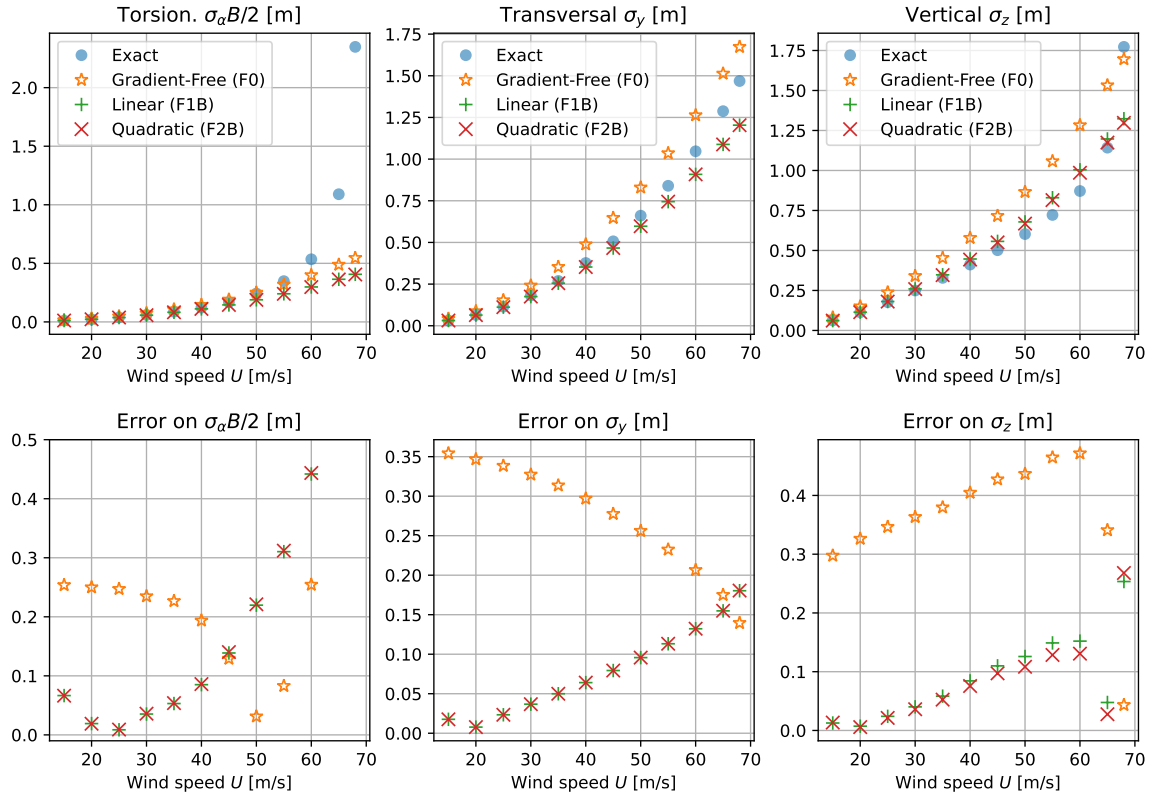

Figure 4.25: Evolution of the standard deviation of the torsional, transversal and vertical displacements at midspan (wind-off modal basis).

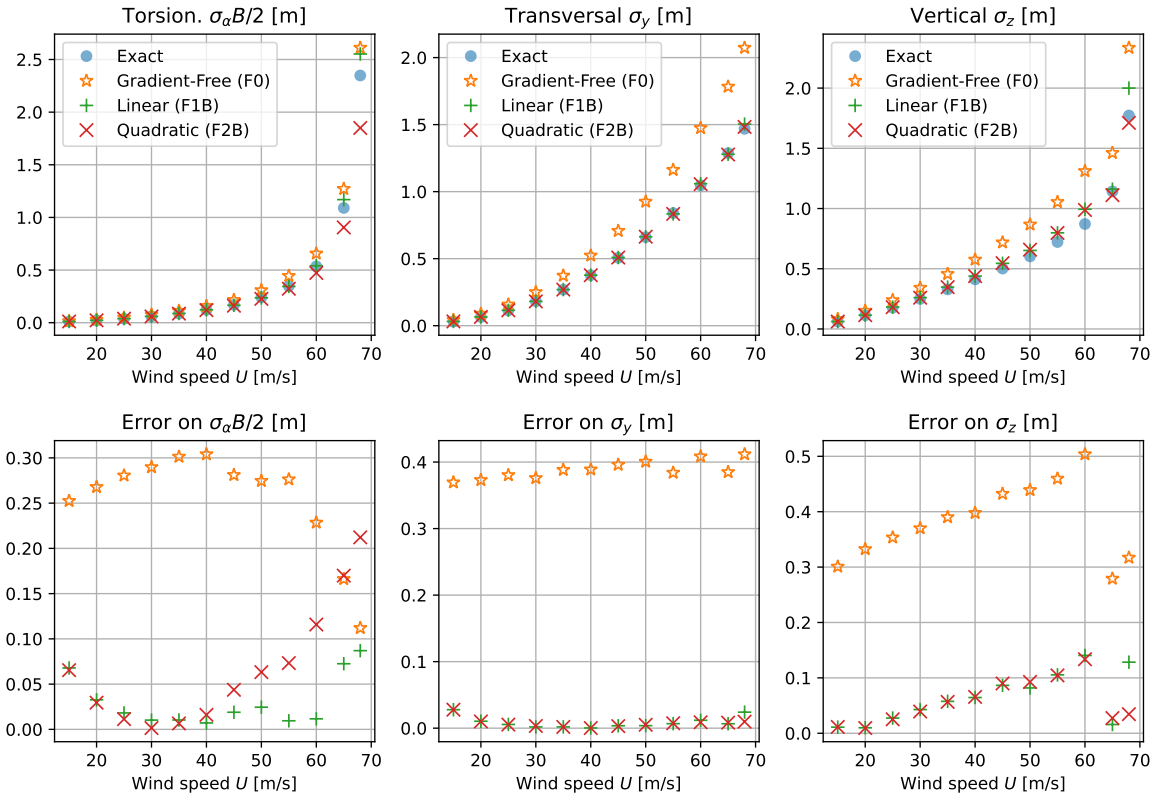

Figure 4.26: Evolution of the standard deviation of the torsional, transversal and vertical displacements at midspan (wind-on modal basis).

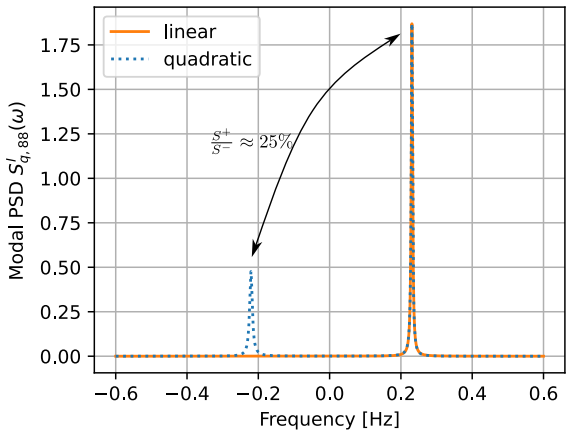

Figure 4.27: Illustration of the symmetry of $S^{\mathrm{I}}_{q,88}(\omega)$ with linear and quadratic expansions of the the diagonal flexibility $J_{d,i}(\omega)$ using the wind-on eigenmodes with left and right eigenvectors (B3). The quadratic expansion brings nonsymmetric content in negative frequencies.

4.7 Conclusion

This chapter has examined the application of the MTSA method to MDOF aeroelastic systems, with a particular focus on the choice of modal basis and the formulation of the impedance matrix. The results have demonstrated the significant impact of these choices on the accuracy of the predicted nodal variances.

A key development introduced in this work was the reformulation of the PSD components to accommodate complex modal forces, a necessary step when using a complex wind-on modal basis. The use of a wind-on modal basis with both left and right eigenvectors proved to be a significant advantage, systematically improving the diagonality of the flexibility matrix. This led to better decoupling of modal contributions and a more accurate representation of the system's response. The consideration of left and right eigenvectors is fundamental for achieving an ideal diagonal form of the dynamic flexibility, providing a favourable framework for the application of the MTSA method. By contrast, the wind-off modal basis introduces larger errors, particularly as aeroelastic coupling increases with wind speed. While acceptable for lightly loaded structures, where errors remain around 10%, it becomes sometimes unreliable near instability.

The wind-on modal basis with left and right eigenvectors demonstrated excellent performance, with errors limited to a few percent, provided that the separation between background and resonant components was sufficient. However, when this condition was not met —as observed for several modes of the benchmark— all MTSA methods exhibited inaccuracies.

Regarding the formulation of the dynamic flexibility matrix, the inclusion of aeroelastic gradients was shown to be essential. Gradient-free formulations resulted in errors exceeding 30%, making them unsuitable regardless of the chosen modal basis. Among gradient-based approaches, linear and quadratic formulations generally produced similar results, with minor differences depending on the modal basis. However, when using a wind-on basis, the quadratic formulation introduced asymmetries in the PSD approximation, leading to underestimation of resonant contributions in certain cases. Additionally, the gain in accuracy offered by the quadratic formulation over the linear formulation was minimal, especially when compared to the overall accuracy of the MTSA method.

The initial motivation for introducing a quadratic formulation of the dynamic flexibility was to achieve a faster decay in the far field (away from resonant peaks), thereby limiting the accumulation of parasitic errors. While the quadratic formulation did improve the representation of individual contributions to $\mathbf{S}_q^{\mathrm{II}}$, practical results showed that cross-contributions (for $i \neq k \neq j$) were negligible in the overall dynamics. Consequently, the advantages of quadratic formulations remained highly limited in terms of accuracy on the modal variance.

Overall, this study confirms that an accurate representation of MDOF aeroelastic systems behaviour using the MTSA method requires careful selection of both the modal basis and the flexibility formulation. The wind-on modal basis with left and right eigenvectors, combined with a well-balanced linear flexibility formulation, offers the best compromise between accuracy and robustness. If the aeroelastic effects on the system are low, the coupling is probably limited, and a wind-off modal basis can be considered.

The computational efficiency of the MTSA method was briefly assessed in Section 4.6.3, where a comparative estimate was conducted against the exact frequency-domain method. While a fully rigorous benchmark could not be carried out, the analysis provided a first quantitative insight into the expected computational savings. In particular, the number of modal projections—one of the most resource-intensive operations in large-scale finite element models—was shown to be reduced by a factor of 4 to 6 depending on the assumptions made on the aeroelastic stiffness matrix. These savings scale proportionally with the number of wind speeds considered in a full buffeting analysis, making the method particularly appealing for large parametric studies. This promising result reinforces the central motivation of this work: enabling rapid and reliable aeroelastic assessments at early design stages without compromising critical physical insight.

Part II

Pre-processing Numerical Tools

Chapter 5

The pre-flutter analysis

The models developed in Chapters 2 (1DOF), 3 (2DOF), and 4 (MDOF) have raised the need for an essential requirement for the application of the background/resonant decomposition: the determination of the modal properties of the structure. In an aeroelastic problem, these modal properties —such as eigenfrequencies, damping ratios, and eigenmodes— depend on the wind speed. The determination of the complex eigenvalues and eigenmodes, solutions to the damped eigenvalue problem, is therefore essential for applying the proposed methodology. This problem was already addressed in Section 2.1.4, where a first simple methodology for determining the aeroelastic eigenfrequency was presented. Additionally, solving for the corresponding complex mode shapes is advantageous for constructing a wind-on modal basis, which has been shown to better diagonalize the equations of motion than a wind-off modal basis, thereby broadening the applicability of the method.

The computations of complex eigenvalues and eigenmodes are not independent derivations; both can, in fact, be determined simultaneously. This was one of the main motivations for considering the mode shapes of the damped eigenvalue problem in the modal basis, as they can be obtained alongside the eigenvalues.

Moreover, modal properties must be computed as the wind speed U increases from 0 to U_{cr}. To mitigate the computational cost of the preliminary operations to the flutter analysis, it is beneficial to use the known solution at a given wind speed U_i as an initial guess for the next wind speed U_{i+1}. However, conventional eigenvalue solvers do not allow for the specification of an initial guess, necessitating a custom approach to take full advantage of this continuity in the solution. This advantage may be provided by continuation methods, which are very popular in nonlinear structural analysis.

In parallel, the characterization of aeroelastic modal damping and natural frequencies is fundamental for assessing the structure's aeroelastic response and monitoring its behaviour before flutter onset. Beyond providing insights into the structure's sensitivity to unsteady aerodynamic effects, analysing the solution of the eigenvalue problem (translated into damping and natural frequencies) offers crucial information about flutter failure modes —for instance alerting designers to whether the structure is prone to stall or soft flutter. For these reasons, designers are not only concerned with identifying the critical flutter state but also with understanding all preceding subcritical states. Each of these states is solution of the nonlinear eigenvalue problem at a given U and is referred to as a *pre-flutter state*. By extension, a *pre-flutter analysis* refers to the modal analysis of the aeroelastic system for various wind velocities; it consists therefore in computing the eigenvalues and eigenmodes of the fluid-elastic system.

Several well-established methodologies have been proposed in aeronautics for determining aeroelastic modal properties. While their application is straightforward for simple models such as the pitch-plunge system, the complexity increases when dealing with more sophisticated models as required by some modern applications, in which several dozens of modes may be involved [97, 111, 117, 118]. In these cases, an apparent difficulty arises from mode tracking when solving

the eigenvalue problem with frequency-dependent matrices. Indeed, when multiple modes are considered, this frequency-dependence may lead to mode swapping, one important inconvenience for existing solution techniques. A brief review of solution methods is presented in Section 5.2.

In this chapter an alternative approach is considered by investigating an explicit solution for the nonlinear generalized complex eigenvalue problem. The solution is carried out mode-by-mode and hinders therefore any mode swapping to occur. The algorithm is designed to carry out pre-flutter analysis, addressing the three key needs in parallel: (i) to identify pre-flutter states to assess the structure's behaviour before instability, (ii) to provide the required input for the approximation methods developed in the previous chapters, and (iii) to construct a wind-on modal basis. A globally convergent algorithm is then constructed using arc-length continuation methods offering hence a systematic and quickly converging tool for determining the pre-flutter states in the manner of those used in structural nonlinear push-over analyses [119, 120]. This approach was recently published in [121].

The specificity of arc-length methods relies in a continuation equation that is added to a set of algebraic equations that depends on a loading parameter (the wind velocity in this case). Since we focus on a homogeneous critical problem, the nonlinear eigenvalue problem is first transformed into a set of algebraic equations by adding an eigenvector normalization equation. Then only, a continuation equation is added so that the determination of the pre-flutter states, eigenvalues and damping ratios, can be established with the same approach as those used in nonlinear structural analysis.

After formalizing the problem and the proposed solution, this chapter presents in detail the continuation process, and constructs accordingly the system of equations to be solved in the case of an aeroelastic problem. The method is then illustrated on three selected examples. The performances of the method in terms of convergence and computational cost are then compared to standard methods.

The content of this chapter is broadly applicable, and can be specialized to aeronautical applications as well as civil engineering applications, even if of course, the orders of magnitude of some characteristic quantities are intrinsically linked to each specific field. The developments presented in this chapter are perfectly general, and may be applied to any flutter application, be it a wing or a bridge deck. For this reason, a general terminology is used in the following so that the free stream airspeed will be sometimes referred to as *wind speed*, while *bridge deck width* may also be called to *airfoil chord*.

5.1 Formalization

In full generality, we model the forcing-free aeroelastic response by a homogeneous second order differential equation with speed and frequency-dependent coefficients by introducing $\mathbf{f}_{\text{bu}} = \mathbf{0}$ and $\mathbf{f}_{\text{se}}$ as (1.40) into (1.12)

$$\mathbf{M}_s\ddot{\mathbf{x}}(t) + \mathbf{C}_s\dot{\mathbf{x}}(t) + \mathbf{K}_s\mathbf{x}(t) = \mathbf{p}(\mathbf{x}(t), \dot{\mathbf{x}}(t), \ddot{\mathbf{x}}(t)). \tag{5.1}$$

To reduce the size of the problem, the nodal displacement $\mathbf{x}$ is expressed using a modal basis $\mathbf{x}(t) = \mathbf{\Psi}\mathbf{y}(t)$, where $\mathbf{\Psi}$ gathers the column ordered mode shapes $\boldsymbol{\psi}_i$, and $\mathbf{y}(t)$ is a column vector collecting the modal coordinates $y_i(t)$. The choice of the modal basis is not discussed here as the proposed methodology is not specific to any modal basis. For instance, it can be the normal modes of vibration obtained with a detailed finite element model [122] of an aircraft, or the modes of a bridge deck under a reference aeroelastic loading, or $\mathbf{\Psi}$ may even be chosen equal to the identity matrix, in which case the "modal" basis is the same as the nodal basis. The following methodology applies regardless of the basis in which the problem is established. Projection of (5.1) in the modal basis leads to

$$\mathbf{M}_s^*\ddot{\mathbf{y}}(t) + \mathbf{C}_s^*\dot{\mathbf{y}}(t) + \mathbf{K}_s^*\mathbf{y}(t) = \mathbf{p}^*(\mathbf{y}(t), \dot{\mathbf{y}}(t), \ddot{\mathbf{y}}(t)). \tag{5.2}$$

where the modal matrices $\mathbf{M}_s^* = \mathbf{\Psi}^\mathsf{T}\mathbf{M}_s\mathbf{\Psi}$, $\mathbf{C}_s^* = \mathbf{\Psi}^\mathsf{T}\mathbf{C}_s\mathbf{\Psi}$ and $\mathbf{K}_s^* = \mathbf{\Psi}^\mathsf{T}\mathbf{K}_s\mathbf{\Psi}$ and the generalized modal force $\mathbf{\Psi}^\mathsf{T}\mathbf{p}(\mathbf{y}(t), \dot{\mathbf{y}}(t))$ are introduced. The aerodynamic load vector $\mathbf{p}^*$ may be expressed in the frequency domain according to (1.41), using the complex modal aerodynamic force matrix $\mathbf{Q}(k)$

$$\mathbf{p}^* = \frac{1}{2}\rho U^2 \mathbf{Q}\,(k)\,\mathbf{Y}(\omega). \tag{5.3}$$

with $k = \dfrac{\omega U}{b}$. In the frequency domain, Equation (5.2) reads

$$\left(-\mathbf{M}_s^*\omega^2 + \mathrm{i}\omega\mathbf{C}_s^* + \mathbf{K}_s^* - \frac{1}{2}\rho U^2 \mathbf{Q}\,(k)\right)\mathbf{Y}(\omega) = \mathbf{0}. \tag{5.4}$$

The goal of this chapter is to construct an efficient algorithm to solve this equation for the system's eigenvalues ω_i and eigenmodes $\mathbf{y}_i$ at different wind speeds of the design envelope. For the sake of conciseness, the superscript $*$ denoting the modal quantities will be dropped in the sequel, as one implicitly assume the use of the initial basis to formulate the original problem.

5.2 Existing solutions

The eigensolutions of (5.2) are usually obtained by defining a Laplace variable

$$p = \frac{\mathrm{d}}{\mathrm{d}t} \tag{5.5}$$

and substituting into (5.2) to obtain

$$\left(\mathbf{M}_s p^2 + \mathbf{C}_s p + \mathbf{K}_s - \frac{1}{2}\rho U^2 \mathbf{Q}(k)\right)\mathbf{Y} = \mathbf{0}. \tag{5.6}$$

This definition of p is equivalent to guessing a solution of the form

$$\mathbf{y} = \boldsymbol{\phi}\mathrm{e}^{pt} \tag{5.7}$$

where $\boldsymbol{\phi}$ is an eigenvector of the aeroelastic system and p the associated eigenvalue, and then substituting into (5.4). Consequently, p can be seen as both a Laplace variable or a system eigenvalue with the form $p = r + \mathrm{i}\omega$, such that its imaginary part is the frequency of oscillation

$$\omega = \frac{kU}{b}. \tag{5.8}$$

The airspeed U is treated here as an input parameter. There are two typical approaches for calculating p. The first one is called *determinant iteration* and determines r and ω such that

$$\left|\mathbf{M}_s p^2 + \mathbf{C}_s p + \mathbf{K}_s - \frac{1}{2}\rho U^2 \mathbf{Q}(k)\right| = 0. \tag{5.9}$$

As the determinant is complex, Equation (5.9) constitutes a set of two equations with two unknowns that can be solved using a nonlinear solver at all airspeeds of interest. The solution is started at $U = 0$ where r and ω are obtained from the eigensolutions of the wind-off structural system. A set of determinant iterations is carried out for each system state until the critical airspeed.

The second method is called *frequency matching* (or frequency lining-up) where the eigenvalues of an augmented state space matrix $\mathbf{A}$ are evaluated

$$\mathbf{A} = \begin{pmatrix} -\mathbf{M}_s^{-1}\mathbf{C}_s & -\mathbf{M}_s^{-1}\left(\mathbf{K}_s - \frac{1}{2}\rho U^2 \mathbf{Q}(k)\right) \\ \mathbf{I} & \mathbf{0} \end{pmatrix} \tag{5.10}$$

such that $\Im(p) = kU/b$. Several algorithms have already been formulated to solve this problem when $\mathbf{A}$ is a constant matrix, such as the QZ-algorithm [123] or Cholesky decomposition based solution [124]. The solution is started near $U = 0$ (but not at $U = 0$ because k is infinite) with initial guesses for p and k the solutions of the wind-off system. After each eigenvalue calculation, k is updated from $k = \Im(p)b/U$ until the old and new values of k are nearly identical. Again, one set of frequency matching iterations is carried out for each mode.

The matrix $\mathbf{Q}(k)$ is obtained numerically at a set of predefined discrete reduced frequency values k_i; it is calculated at intermediate values of k by interpolation. The problem that arises is the fact that $\mathbf{Q}(k)$ contains aerodynamic mass, stiffness and damping information but, due to their numerical nature, it is impossible to separate these contributions. Consequently, several flutter analysis methods have been developed, such as the k method [125], the p method [126], the p-k method [127], modified versions of the p-k method [128, 129] and the g method [130]. For instance, in the modified p-k method, the matrix $\mathbf{Q}(k)$ is separated into its real and imaginary parts. Then, equation (5.6) becomes

$$\left(\mathbf{M}_s p^2 + \left(\mathbf{C}_s - \frac{1}{2k}\rho b U \Im(\mathbf{Q}(k))\right) p + \mathbf{K}_s - \frac{1}{2}\rho U^2 \Re(\mathbf{Q}(k))\right) \mathbf{Y}(\omega) = \mathbf{0}, \tag{5.11}$$

such that $\Im(\mathbf{Q}(k))$ represents aerodynamic damping and $\Re(\mathbf{Q}(k))$ aerodynamic stiffness. Then, the p-k solution is obtained by calculating the eigenvalues of matrix

$$\mathbf{A} = \begin{pmatrix} -\mathbf{M}_s^{-1}\left(\mathbf{C}_s - \frac{1}{2k}\rho b U \Im(\mathbf{Q}(k))\right) & -\mathbf{M}_s^{-1}\left(\mathbf{K}_s - \frac{1}{2}\rho U^2 \Re(\mathbf{Q}(k))\right) \\ \mathbf{I} & \mathbf{0} \end{pmatrix}. \tag{5.12}$$

In civil engineering where the unsteady forces are more likely prescribed using the Scanlan derivatives such as in (1.49), the real and imaginary contributions to $\mathbf{Q}(k)$ are already separate and the issue of separating them out of a combined aerodynamic load matrix does not exist. There is thus no need to apply the modified p-k or g methods. Determinant iteration is carried out by solving

$$\left| \left[\mathbf{M}_s - \mathbf{M}_{\text{ae}}(k, U)\right] p^2 + \left(\mathbf{C}_s - \mathbf{C}_{\text{ae}}(k, U)\right) p + \left[\mathbf{K}_s - \mathbf{K}_{\text{ae}}(k, U)\right] \right| = 0 \tag{5.13}$$

while frequency matching is achieved by calculating the eigenvalues of matrix

$$\mathbf{A} = \begin{pmatrix} -\mathbf{M}^{-1}\left[\mathbf{C}_s - \mathbf{C}_{\text{ae}}(k, U)\right] & -\mathbf{M}^{-1}\left[\mathbf{K}_s - \mathbf{K}_{\text{ae}}(k, U)\right] \\ \mathbf{I} & \mathbf{0} \end{pmatrix} \tag{5.14}$$

where $\mathbf{M} = (\mathbf{M}_s - \mathbf{M}_{\text{ae}}(k, U))$.

Another method, which does not belong to either of the two previously discussed categories, was proposed by [115]. This approach relies on a perturbation-based series expansion of the solution of the complex eigenvalue problem to estimate variations in the complex eigenvalues due to small changes in system parameters. By reformulating the aeroelastic damped eigenvalue problem, this method provides then an approximation of the complex eigenvalues.

A major limitation of these methods is that they determine only the complex eigenvalues, without computing the corresponding eigenmodes, which only partially addresses our needs. Another common issue arises from mode swapping that can sometimes happen as the airspeed varies. For example, if the imaginary part of the eigenvalue of mode 1 is lower than that of mode 2 at a higher airspeed, the solution procedure will follow the lowest imaginary part and produce an eigenvalue branch that is a mix of the eigenvalues of modes 1 and 2. This situation can render the resulting stability plots difficult to interpret, especially when several modes are getting involved. It is also likely to cause troubles when evaluating the modal responses of the system. Some methods based on scalar products of mode shapes or the Modal Assurance Criterion (MAC) [131, 132] have been proposed to alleviate the mode swapping issue and to

reorder the output of the p-k method. As shown next, these methods are not unfailing and sometimes offer disappointing performance. Manual sorting turns out to be the last resort, but becomes rapidly cumbersome for larger systems.

Furthermore, the problem statement as formulated by the frequency matching method results in a waste of resources as, at every single iteration, all eigenvalues of (5.10) are calculated while only one of them is of interest. The unnecessary computational burden increases with the size of the model, and becomes significant when large models are employed. Alternative algorithms may be more efficient by specifying *a priori* the mode number being tracked, but must anyway at least evaluate several eigenvalues at a time if these are close to one another. The determinant iteration approach does not suffer from this inconvenience.

This section has thus far reviewed two categories of methods. However, the approach adopted in the following does not belong to any of them. It relies on an explicit solution of the generalized complex eigenvalue problem to solve the flutter equations. It may therefore be described as an hybridization between the two approaches. By assuming a solution of the form of (5.7), the proposed method solves for both p and $\boldsymbol{\phi}$, such that there is no possibility for mode swapping to occur, since the eigenvectors $\boldsymbol{\phi}$ are sufficiently orthogonal to each other at the same airspeed U. The process is initiated in wind-off conditions, as usual, and progresses towards the critical speed by implementing an arc-length continuation process rather than following a user predefined mesh.

5.3 Description of the method

5.3.1 Transformation of the eigenvalue problem into a nonhomogeneous algebraic problem

Since (5.2) is a linear problem, its solution is

$$\mathbf{y}(t) = \sum_{i=1}^{m} \boldsymbol{\phi}_i \mathrm{e}^{\lambda_i t}, \tag{5.15}$$

where m is the number of aeroelastic modes considered in the analysis, $\boldsymbol{\phi}_i$ is the i-th mode of the aeroelastic system and λ_i is used instead of p_i to emphasize that this is an eigensolution. This eigenvalue is such that $\lambda_i = -\xi_i \omega_{0,i} + \mathrm{i}\omega_i$ where $\omega_{0,i} = |\lambda_i|$ and ξ_i take the meaning of an undamped circular frequency and a damping ratio. Substituting (5.15) into (5.2) leads to

$$\lambda_i^2 \mathbf{M}(\omega_i, U)\boldsymbol{\phi}_i + \lambda_i \mathbf{C}(\omega_i, U)\boldsymbol{\phi}_i + \mathbf{K}(\omega_i, U)\boldsymbol{\phi}_i = \mathbf{0} \tag{5.16}$$

where $\mathbf{M}(\omega, U) = \mathbf{M}_s - \mathbf{M}_{\mathrm{ae}}(\omega, U)$, $\mathbf{C}(\omega, U) = \mathbf{C}_s - \mathbf{C}_{\mathrm{ae}}(\omega, U)$ and $\mathbf{K}(\omega, U) = \mathbf{K}_s - \mathbf{K}_{\mathrm{ae}}(\omega, U)$. This procedure is fully compatible with aircraft flutter; for instance, if the modified p-k approach is used,

$$\mathbf{M}_{\mathrm{ae}}(\omega, U) = \mathbf{0},\ \mathbf{C}_{\mathrm{ae}}(\omega, U) = \frac{1}{2k}\rho b U \Im(\mathbf{Q}(k)),\ \mathbf{K}_{\mathrm{ae}}(\omega, U) = \frac{1}{2}\rho U^2 \Re(\mathbf{Q}(k)). \tag{5.17}$$

If n refers to the initial number of coordinates to formulate the problem —nodal or wind-off modal—, equation (5.16) defines a set of $2n$ nonlinear real equations, and stages $2(n+1)$ real unknowns for a given airspeed U; two for the real and imaginary parts of λ_i, and $2n$ for the real and imaginary parts of the complex eigenvectors $\boldsymbol{\phi}_i$. This is typical of eigenvalue problems where the underdetermination is associated with the freedom to normalize the eigenvectors in any desired way. Consequently, a non-homogeneous and nonlinear algebraic problem can be obtained by supplementing two additional equations to normalize the eigenvectors. The normalization conditions chosen here are

$$\Re\{\boldsymbol{\phi}_i\} \cdot \Re\{\boldsymbol{\phi}_i\} = 1 \quad \text{and} \quad \Im\{\boldsymbol{\phi}_i\} \cdot \Im\{\boldsymbol{\phi}_i\} = 1. \tag{5.18}$$

For a given airspeed, Eqs. (5.16) and (5.18) form a closed set of $2(n+1)$ nonlinear algebraic equations with $2(n+1)$ unknowns. Introducing the objective function $\mathbf{f}(\mathbf{x}, U)$, the problem may be expressed in the general form

$$\mathbf{f}(\mathbf{x}_i, U) = \mathbf{0}, \quad \text{with} \quad \mathbf{x}_i = \left[\Re(\lambda_i),\ \Im(\lambda_i),\ \Re(\boldsymbol{\phi}_i)^\mathsf{T},\ \Im(\boldsymbol{\phi}_i)^\mathsf{T}\right]^\mathsf{T}, \tag{5.19}$$

and solved numerically for each mode and all U of interest using classical nonlinear solvers, such as the Newton–Raphson [133], Krylov [134] or Broyden [135] methods. The convergence of such algorithms may be quite sensitive to the initial guess and divergence may occur for some chosen U without apparent reason, especially when the aeroelastic system experiences rapid changes. The solution of (5.19) for $(\lambda_i, \boldsymbol{\phi}_i^R, \boldsymbol{\phi}_i^L)$ for all $i = 1, \ldots, M$ defines one pre-flutter state, corresponding to one given wind speed.

Note also that since (5.19) corresponds to a mode-by-mode approach, its solution for each mode can be carried out separately, possibly in parallel.

5.3.2 The continuation process

The continuation process is based on introducing a continuation equation to system (5.19). In parallel, the wind speed is now considered as a variable rather than a parameter. Introducing $\mathcal{D}$, the $2n+3$ dimensional space defined by the real unknowns of the problem —namely wind speed U, eigenvalues λ_i and eigenvectors $\boldsymbol{\phi}_i$— and starting from a known point $\mathbf{p}_0 \in \mathcal{D}$ that is a solution of $\mathbf{f}(\mathbf{x}, U) = \mathbf{0}$, the chosen arc-length method consists in finding the intersection of the objective function $\mathbf{f}(\mathbf{x}, U)$ with the hypersphere of radius r, defined in $\mathcal{D}$ and centred on $\mathbf{p}_0 = (\mathbf{x}_0, U_0)$. The situation is illustrated in two dimensions in Figure 5.1, which depicts two eigensolution branches —denoted by Mode 1 and Mode 2. Mode 1 is being tracked. Point $(\mathbf{x}_0, U_0)$ lies on Mode 1; the two intersections of this branch with the hypersphere centred at $(\mathbf{x}_0, U_0)$ are determined and the process is repeated by placing the new centre at the rightmost root. The equation of the hypersphere is

$$\begin{aligned} r^2 \;=\; & \left(\frac{U - U_0}{U_{\text{ref}}}\right)^2 + \left(\frac{\Re(\lambda) - \Re(\lambda_0)}{\Re(\lambda_{\text{ref}})}\right)^2 + \left(\frac{\Im(\lambda) - \Im(\lambda_0)}{\Im(\lambda_{\text{ref}})}\right)^2 \\ & + \sum_{k=1}^{n} \left(\frac{\Re(\phi_k) - \Re(\phi_{0,k})}{\Re(\phi_{\text{ref},k})}\right)^2 + \left(\frac{\Im(\phi_k) - \Im(\phi_{0,k})}{\Im(\phi_{\text{ref},k})}\right)^2 \end{aligned} \tag{5.20}$$

where the quantities with subscript $_{\text{ref}}$ are scaling parameters chosen to make sure that $((U - U_0)/U_{\text{ref}})^2$ and each term of the dot product in (5.20) have the same order of magnitude, so that they all bring a similar contribution to the sphere radius. In total for each mode, there are $2n+3$ unknowns and as many equations. The physical interpretation of the augmented system is important: in the current iteration, the solution of (5.19) is searched in space $\mathcal{D}$ so that the solution lies precisely at a distance r from the last converged point $\mathbf{p}_0$. The introduction of rescaling parameters relative to any direction of $\mathcal{D}$ and therefore the choice of an hyperellipsoid for (5.20) makes this equation dimensionally consistent; each term in the sum is dimensionless, as is the radius of the hypersphere. As well as being very general, this form allows the user to deform the hypersphere in any direction, potentially adjusting the weight relative to any direction. The freedom in choosing the rescaling parameter is a feature discussed and illustrated later in Section 5.4.2. Introducing the rescaling matrix, $\mathbf{S}^{-1} = \text{diag}\left[\Re(\lambda_{\text{ref}}),\ \ \Im(\lambda_{\text{ref}}),\ \ \Re(\phi_{\text{ref},1}), \ldots,\ \ \Im(\phi_{\text{ref},N})\right]$, the hypersphere equation can be written as

$$r^2 = \left(\frac{U - U_0}{U_{\text{ref}}}\right)^2 + (\mathbf{x} - \mathbf{x}_0)^\mathsf{T} \mathbf{S}^\mathsf{T} \mathbf{S} (\mathbf{x} - \mathbf{x}_0). \tag{5.21}$$

The system defined by (5.19) and (5.21) may then be solved to determine a new point on the branch. The identification of one single point, or one pre-flutter state, is referred to as one *step* within the algorithm and requires several *iterations* to be reached.

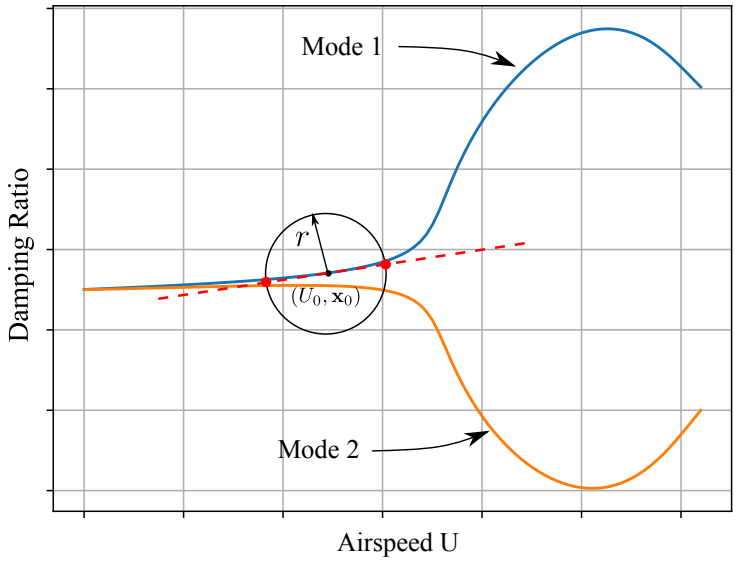

Figure 5.1: Illustration of the arc-length procedure in 2D space. The first iteration of the current step is investigated.

In practice, the process is initiated in wind-off conditions and progresses in the increasing wind speed direction. Starting from $U_0 = 0$, where the initial state $\mathbf{x}_0$ is easily obtained from the wind-off solution, a nearby point on the branch is found by solving (5.19) and (5.21). For small sphere radius, there are two solutions, one at a higher wind speed and one at a lower wind speed. The intersection at the highest of the two wind speeds is retained. This new point on the branch is then considered as the next starting point $(\mathbf{x}_0, U_0)$ and the process is repeated until flutter conditions are reached. The step length between two consecutive points in $\mathcal{D}$ is equal to r. However, in a subspace $\mathcal{E} \subset \mathcal{D}$, the step length depends on the gradient of $\mathbf{f}$ in $\mathcal{D}$. For example, if the steps of length r separating three consecutive points of a branch are $(\Delta U_j, \Delta \mathbf{x}_j)$ and $(\Delta U_k, \Delta \mathbf{x}_k)$, the steps in the U-direction ΔU_j and ΔU_k may not be equal and, likewise, the step $||\Delta \mathbf{x}_j||$ may not be equal to $||\Delta \mathbf{x}_k||$. This is one of the advantages of arc-length methods with respect to the systematic solution of (5.19) for a constant wind speed step ΔU, as the latter is smaller only where required.

The arc-length algorithm presented here is adapted from [119], whose approach consists in solving (5.19) and (5.21) using numerical nonlinear solvers; it will be referred to in the present work as Riks method. Furthermore, it is possible to take advantage of the fact that the problem is quadratic in U to improve this method. Linearizing $\mathbf{f}(\mathbf{x}, U)$ in (5.19) around the i-th point on the branch, $(\mathbf{x}_i, U_i)$, and solving for $\mathbf{x}$ gives

$$\mathbf{x} = \mathbf{x}_i - \mathbf{J}_\mathbf{x}^{-1}(\mathbf{x}_i, U_i)\left[\mathbf{f}(\mathbf{x}_i, U_i) + \mathbf{J}_U(\mathbf{x}_i, U_i)(U - U_i)\right] \tag{5.22}$$

with $\mathbf{J}_\mathbf{x}(\mathbf{x}, U) = \dfrac{\partial \mathbf{f}}{\partial \mathbf{x}}(\mathbf{x}, U)$ and $\mathbf{J}_U(\mathbf{x}, U) = \dfrac{\partial \mathbf{f}}{\partial U}(\mathbf{x}, U)$. Substituting (5.22) in (5.21) results in a quadratic equation in the sole unknown U

$$(1 + \mathbf{b}^\mathsf{T}\mathbf{S}^\mathsf{T}\mathbf{S}\mathbf{b})U^2 - 2(U_0 - \mathbf{a}^\mathsf{T}\mathbf{S}^\mathsf{T}\mathbf{S}\mathbf{b})U + U_0^2 - (r\ U_{\text{ref}})^2 + \mathbf{a}^\mathsf{T}\mathbf{S}^\mathsf{T}\mathbf{S}\mathbf{a} = 0 \tag{5.23}$$

with

$$\begin{aligned} \mathbf{a} &= \mathbf{x}_i - \mathbf{x}_0 - \mathbf{J}_x^{-1}(\mathbf{x}_i, U_i)\left[\mathbf{f}(\mathbf{x}_i, U_i) - \mathbf{J}_U(\mathbf{x}_i, U_i)U_i\right] \\ \mathbf{b} &= -\mathbf{J}_\mathbf{x}^{-1}(\mathbf{x}_i, U_i)\mathbf{J}_u(\mathbf{x}_i, U_i). \end{aligned}$$

This quadratic equation in U is easily solved analytically to obtain the two intersections with the hypersphere of radius r. As mentioned earlier, the rightmost solution is retained. Rejecting

systematically the lowest root prevents any unwanted changes in the continuation direction. The new wind speed U is now used to evaluate a new $\mathbf{x}$ by solving (5.19) using a Newton–Raphson or Broyden method. The idea of exploiting the quadratic nature of the continuation equation (5.21) was first raised by [136]. In the present work, this approach will be referred to as Crisfield method.

It must be highlighted that both Crisfield and Riks methods are tracking strategies. All continuation methods augment the nonlinear system by adding one additional tracking equation. This larger system must be solved with a nonlinear solver. Therefore, a continuation algorithm combines a tracking procedure and a nonlinear solver.

Note that, in regions where the curvature of the eigensolution branch is very high, the linearization used to obtain (5.22) may result in a wind speed prediction that lies too far from the branch for the Newton–Raphson calculation to converge. In such situations, the value of r may need to be reduced, by means of an arc-length step adaptation procedure. Note also that, as long as the solver converges, using a coarse radius r only affects the resolution of the branch, not the accuracy, as the latter is ensured by the convergence criterion.

As a summary of this development section, a flowchart describing the workflow of the continuation methods is proposed in Figure 5.2. This workflow is illustrated for a full multi-modal *pre-flutter analysis*, including the three loops on the modes, on the wind speed U and the iterative loop of the nonlinear solver.

5.3.3 Hypersphere radius adaptive refinement strategies

The choice of the radius r depends on the mesh density required by the user. It must be chosen based on the scaling parameters U_{ref}, λ_{ref}, ... that are calibrated on the expected orders of magnitude desired for each component $j = 1, \dots, N$ of the step $x_j - x_{0,j}$ and $U - U_0$. The procedure for the selection of these scaling parameters is discussed in Section 5.4.2. The initial radius is typically chosen of order 1, but is highly correlated to the scaling parameters chosen by the user. After one or several iterations, the radius r may be updated to improve the behaviour of the solution: decreasing r produces a better guess for the subsequent iterations, while increasing it will decrease the computational cost. Different strategies for adapting the radius to the gradient of the objective function have been proposed. One such strategy is to define an upper and a lower threshold for the number of iterations to convergence of the previous step above or below which the current radius is multiplied or divided by a chosen factor $m \in \mathbb{R}_0$ —for instance $m = 2$. One problem with this approach is that, depending on m, either the radius becomes rapidly very small (or very large), or it may take a long time for the radius to stabilize to the appropriate value when m is close to unity.

Another strategy depends on the number of iterations required for the Newton–Raphson system to converge at two consecutive points on the branch. If point $i-1$ is obtained after m_{i-1} iterations and point i after m_i, a convergence ratio can be defined as

$$\beta_i = \frac{m_{i-1}}{m_i}. \tag{5.24}$$

Then, the value of the radius used to predict point $i+1$ is given by

$$r_{i+1} = \beta_i r_i \tag{5.25}$$

such that β_i becomes an amplification or reduction factor. In practice, it is recommended to limit the number of iterations to around 20. If convergence has not been achieved after this number of iterations, it is possible to return to point i, or even $i-1$, and reduce r by a bigger factor, *e.g.* $r_{i+1} = r_i/2$.

While the first strategy allows the radius to take theoretically any value in a discrete set $\{r_0 \cdot m^p\}$ with $p \in \mathbb{Z}$, the second strategy is more flexible and allows r to take any value in $\mathbb{R}_0$. It is also more reactive as it accommodates brutal changes in gradients, and adapts in consequence the radius rapidly, while the first method would likely require many more updates of the radius before stabilizing. The second method is used in the following examples.

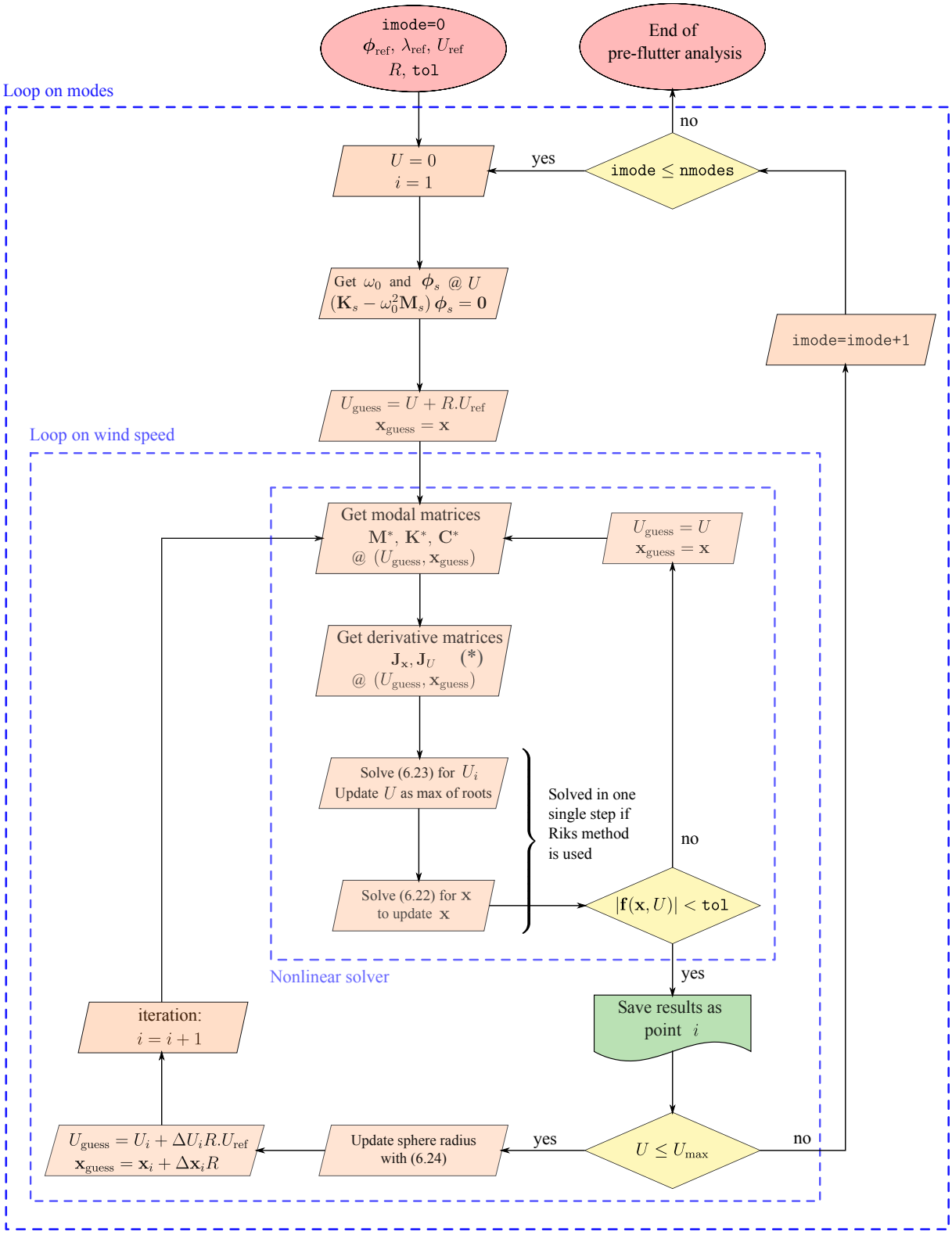

Figure 5.2: Flowchart of a complete pre-flutter analysis. (*) If a Broyden method is used, the derivative matrices $\mathbf{J}_{\mathbf{x}}$ and $\mathbf{J}_U$ are estimated using the current and previous value of $\mathbf{f}(\mathbf{x}, U)$.

Parameters	App. 1	App. 2	Units
Mass moment of Inertia I_α	2.46×10^6	0.0703	[kg.m^2/m]
Mass moment of inertia I_α	2.46×10^6	0.0703	[kg m^2/m]
Foil/Deck mass m_s	22 470	13.5	[kg/m]
Natural frequency $f_{s,h}$	0.1	5	[Hz]
Natural frequency $f_{s,\alpha}$	0.278	6.5	[Hz]
Damping ratios $\xi_{s,\theta}$ and $\xi_{s,h}$	0.3 / 0.3	0 / 0	[%]
Foil/Deck width c or B	31	0.25	[m]
Pitch axis x_f	$B/2$	$0.46 \cdot c$	[m]
Air density ρ	1.22	1.22	[kg/m^3]
Aeroelastic model	Theodorsen	Theodorsen+Jones	–

Table 5.1: Parameters for the first two proposed case studies. All the parameters are measured in wind-off conditions ($U = 0$ m/s). Variables $\xi_{s,\alpha}$ and $\xi_{s,h}$ respectively refer to the structural damping in pitch and plunge motion.

5.4 Illustrations

In this section, the behaviour of the algorithm will be illustrated on three selected examples. The first two illustrations are both 2-mode applications; a bridge deck, and a theoretical airfoil. The last application consists in a generic 7-mode aircraft model. The robustness of the continuation methods introduced previously will be discussed, and their performance in terms of computational burden and accuracy will be compared investigating two criteria: the number of iterations and the number of function evaluations.

It is important to note that the number of iterations may not be appropriated to compare the computational efficiency of two different methods, as the load associated with an iteration is not necessarily the same for each method. The three continuation methods have similar workloads in a given iteration, but these workloads are different from that of the p-k method. Therefore computational efficiency can be discussed based on the number of iterations to compare the continuation methods between themselves, but not to compare the continuation and p-k methods. The same applies to the second criterion, the number of function calls.

It must also be kept in mind that a fair comparison of the cumulated number of iterations is not possible when two computed curves have different numbers of points; more points require inevitably more iterations. To allow for a fair comparison, the continuation methods are set to use the same refinement strategy and the same sphere initial parameters —see Table 5.2. Concerning the p-k method, the number of points was chosen to match, approximately, that of the other three methods.

5.4.1 Streamlined bridge deck modeled with Scanlan's derivatives

The first test case is a pitch/plunge model of an idealized flat plate, namely the simplest model encapsulating the essential aerodynamic phenomena from which the unsteady aerodynamics of coupled aeroelastic systems may be investigated. The simplicity of this model makes it an ideal benchmark for validating computational tools and simulations.

In this case study, a bridge deck is modelled as a pitch/plunge model of a flat plate, as proposed in the benchmark published by [46]. The situation is schematically illustrated in Figure 1.13, while Table 5.1 summarizes all the parameter values used in this example. Adopting Scanlan's nomenclature for the aeroelastic loads, the frequency domain representations of the

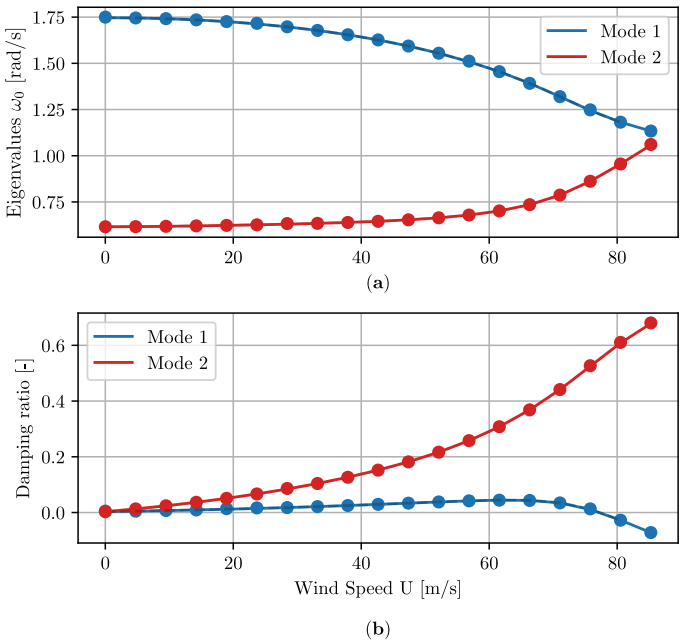

Figure 5.3: Application 1.Variation of natural frequencies and damping ratios with wind speed, calculated using the p-k method. The circle markers ● denote the pre-selected wind speeds at which the analysis was carried out.

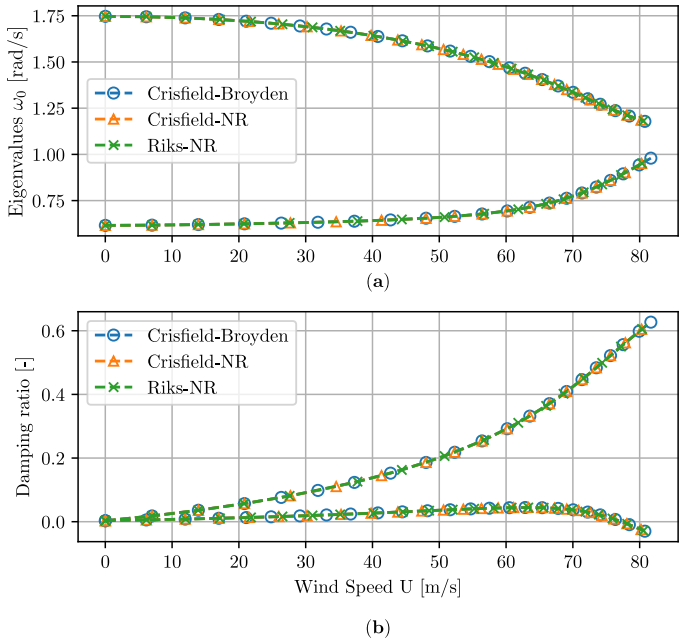

Figure 5.4: Application 1. Variation of natural frequencies and damping ratios with wind speed, calculated using the three continuation methods.

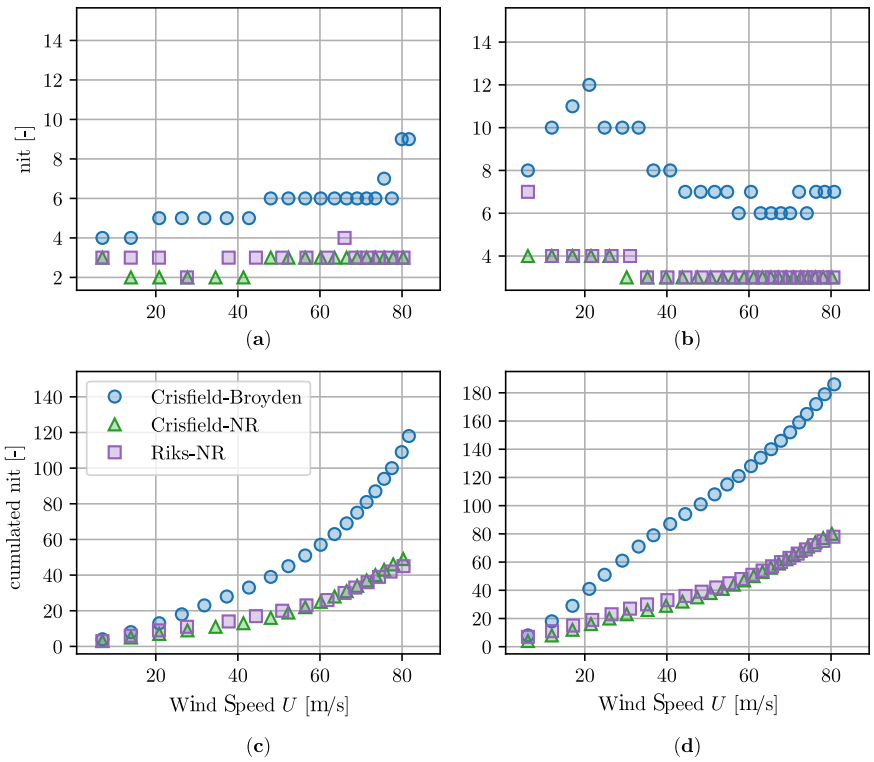

Figure 5.5: Application 1. Number of iterations (nit) and cumulated number of iterations for Mode 1 in (a,c) and Mode 2 in (b,d). The conclusion regarding the computational loads of the continuation methods should be made with care, as the workload per iteration for each method is not exactly the same.

lift l and moment m are described by the aeroelastic matrices $\mathbf{M}_{\text{ae}} = \mathbf{0}$, $\mathbf{C}_{\text{ae}}$ and $\mathbf{K}_{\text{ae}}$, obtained from equations (1.50) and (1.51),

$$\begin{aligned}\mathbf{C}_{\text{ae}}(\omega, U) &= \frac{1}{2}\rho UBK \begin{bmatrix} H_1^*(K) & BH_2^*(K) \\ BA_1^*(K) & B^2A_2^*(K) \end{bmatrix} \\ \mathbf{K}_{\text{ae}}(\omega, U) &= \frac{1}{2}\rho U^2BK^2 \begin{bmatrix} H_4^*(K)/B & H_3^*(K) \\ A_4^*(K) & BA_3^*(K) \end{bmatrix}.\end{aligned}$$

These functions are analytically derived from [57], neglecting the added mass effects that are usually low in wind engineering applications. This leads to the following equations as established by [39] for the case where the rotation axis is located at the center of the plate ($x_f = c/2$)

$$\begin{aligned} H_1^* &= -V^*F, & A_1^* &= -\tfrac{V^*}{4}F \\ H_2^* &= \tfrac{V^*}{4}\left(1 + F + V^*G\right) & A_2^* &= -\tfrac{V^*}{16}\left(1 - F - \tfrac{2}{\pi}V^*G\right) \\ H_3^* &= \tfrac{V^*}{2\pi}\left(FV^* - \tfrac{\pi}{2}G\right) & A_3^* &= \tfrac{V^*}{8\pi}\left(FV^* - \tfrac{\pi}{2}G\right) \\ H_4^* &= \tfrac{\pi}{2}\left(1 + \tfrac{2}{\pi}V^*G\right) & A_4^* &= \tfrac{V^*}{4}G, \end{aligned} \tag{5.26}$$

where $V^* = 2\pi/K$, F and G are respectively the real and complex parts of Theodorsen's function (1.45).

Once the aeroelastic loads are prescribed, the pre-flutter analysis can be carried out using the four methods presented in the previous section. The first method is the p-k method, and the others are three continuation methods: the Riks-Newton–Raphson (Riks-NR) couples the Riks method with a Newton–Raphson solver, while the Crisfield–Newton–Raphson (Crisfield–NR) and the Crisfield–Broyden techniques, respectively implement the Crisfield method together with a Newton–Raphson and Broyden solver, see for instance [133].

The results obtained with the p-k method are shown in Figure 5.3. In this figure, the circle markers denote the pre-selected wind speeds at which the system was solved. It can be seen that the natural frequencies of the two modes vary with wind speed, approaching each other as the wind speed increases. Both damping ratios initially increase with wind speed but, for $U > 63$ m/s, the damping of mode 1 starts to decrease while the other increases faster. This phenomenon is the typical binary flutter mechanism, whereby one of the modes transfers all of its energy to the other, such that the latter becomes undamped at $U = 75.8$ m/s and negatively damped at higher wind speeds.

The flutter solutions obtained using the three continuation methods are shown in Figure 5.4. Every single point of every curve is converged, as it satisfies the condition of maximum required tolerance on the residual defined as the euclidean norm of the objective function $\mathbf{f}(\mathbf{x}, U)$,

$$\text{Res} = \sqrt{\sum_{i=1}^{N} f_i^2(\mathbf{x}, U)} \leq \texttt{abstol} = 10^{-4}, \tag{5.27}$$

so that all results are the same and all curves are overlaid within the user defined tolerance.

Contrary to the p-k method, for which a uniform mesh in wind velocity U was imposed, each of the other three methods uses different custom nonuniform meshes. This is because of the adaptive refinement strategy of the sphere radius r, that increases or decreases the step between two consecutive points based on the number of iterations required by the method to converge, but also because of the gradient in $\mathcal{D}$. Each analysis is however initiated with the same algorithm parameters (see Table 5.2), and these are automatically adapted depending on the method's progress. The second refinement strategy presented in Section 5.3.3 was used for all examples presented in this chapter.

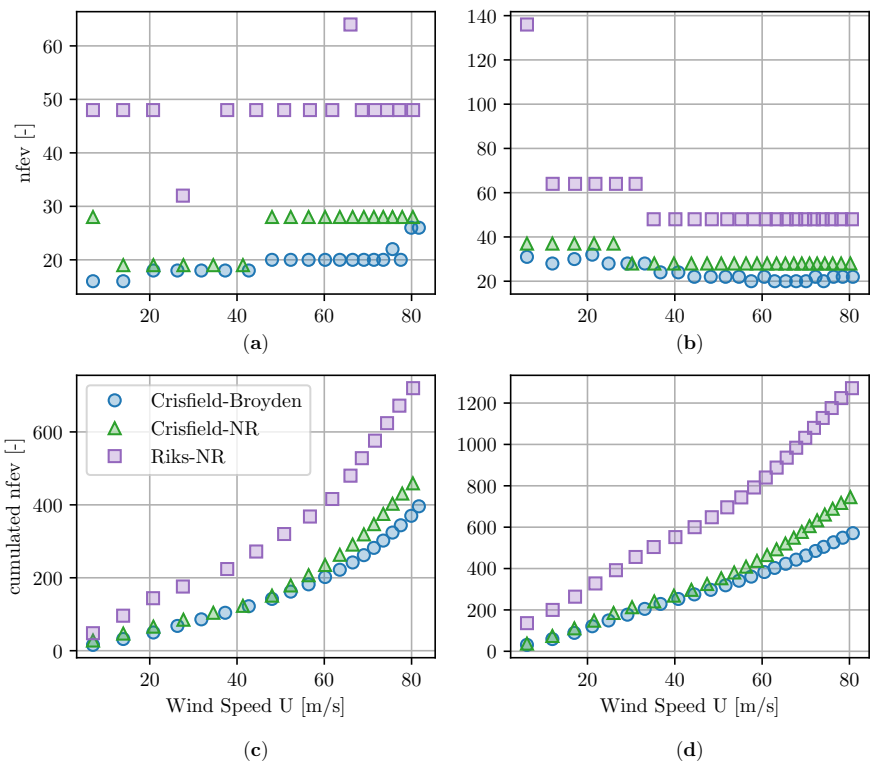

Figure 5.6: Application 1. Number of function evaluations (nfev) and cumulated number of calls to target function $\mathbf{f}(\mathbf{x}, U)$ for mode 1 in (a,c) and mode 2 in (b,d).

The convergence speed of the methods may be discussed by comparing the number of iterations required for each point to converge, depending on the chosen method. Figure 5.5 shows in (a) and (b) the number of iterations required by the four methods to obtain every point of the pre-flutter curve. It is seen that the Crisfield–Broyden method is always more iteration demanding. This is because this method has an inexact or even no knowledge of the Jacobian matrix. As a consequence it progresses in a sub-optimal manner to find the solution of the system. The other two methods have equivalent performance concerning the number of iterations. Figures (c) and (d) show the cumulated number of iterations and depict the clear separation between the two groups of methods.

The number n_{fev} of evaluations of the target function $\mathbf{f}(\mathbf{x}, U)$ for the continuation methods is presented in Figure 5.6(a) and (b), and its cumulate is shown in (c) and (d). Clearly, Riks method requires significantly more function calls than the others with roughly 50 calls per point on average, as opposed to the two Crisfield methods that require approximately half of that. The Broyden technique is slightly less expensive than the Newton–Raphson method, since it estimates the Jacobian based on the current and previous evaluations of $f(\mathbf{x}, U)$. For this flutter analysis, the Crisfield–Broyden method saves approximately 30% of the total number of calls with respect to the Crisfield–Newton–Raphson approach, and more than 130% with respect to the Riks method.

5.4.2 Pitch-Plunge model of an idealized flat airfoil

The second application is also a flat plate, but the lift and moment are expressed as as (1.43) and (1.44) particularized with the Jones' approximation to represent the Theodorsen function and with a possible eccentricity e between the quarter chord and the rotation axis. In these

conditions, the aerodynamic force matrix then reads,

$$\frac{1}{2}\rho U^2\mathbf{Q}(k) = \begin{pmatrix} -\omega^2 m + \pi\rho U c C^\dagger(k)\mathrm{i}\omega & \rho\pi b^2 U\mathrm{i}\omega + \rho\pi b^2\left(x_f - \frac{c}{2}\right)\omega^2 \\ -\omega^2\rho\pi b^2 & +\pi\rho U c C^\dagger(k)\left(U + \left(\frac{3}{4}c - x_f\right)\mathrm{i}w\right) \\ -\pi\rho U e c^2 C^\dagger(k)\mathrm{i}\omega & \left(\frac{3}{4}c - x_f\right)\rho\pi b^2 U\mathrm{i}\omega \\ + \left(x_f - \frac{c}{2}\right)\rho\pi b^2\omega^2 & -\pi\rho U e c^2 C^\dagger(k)\left(U + \left(\frac{3}{4}c - x_f\right)\mathrm{i}\omega\right) \\ & -\left(x_f - \frac{c}{2}\right)\rho\pi b^2\omega^2 - \frac{\rho\pi b^4}{8}\omega^2 \end{pmatrix}. \tag{5.28}$$

This aeroelastic model is similar to that used in Section 5.4.1, except that Jones' approximation [63] is used, and that the equations presented here accommodate the possibility that the rotation axis is not located at the foil centre $x_f \neq c/2$. The structural matrices are built according to Figure 1.13. Introducing the plate mass m_s per unit length,

$$\mathbf{K}_s = \begin{bmatrix} K_h & 0 \\ 0 & K_\alpha \end{bmatrix}, \quad \mathbf{C}_s = \mathbf{0}, \quad \mathbf{M} = \begin{bmatrix} m_s & S \\ S & I_\alpha \end{bmatrix} \tag{5.29}$$

where $I_a = \frac{m_s}{3}\left[c^2 - 3(x - c_f)x_f\right]$ is the mass moment of inertia of the plate per unit length, with respect to the rotation axis and $S = m\left(\frac{c}{2} - x_f\right)$ the static imbalance. The stiffnesses K_h and K_α are evaluated from the wind-off natural frequencies f_h and f_α.

The pre-flutter modal analysis is first carried out using the p-k method to give the results shown in Figure 5.7. There is one mode swapping around 30 m/s. This is in this case the lesser evil knowing that those points are by far supercritical —the critical velocity is slightly lower than 25 m/s— but illustrates well the possible shortcomings of the method. An attempt at automating data post-processing is presented in Appendix F to discard this problem of mode swapping by restoring mode shapes continuity by means of the scalar product of computed mode shapes and mode shapes obtained at the previous step. A detailed code snippet of the developed algorithm is proposed in Figure F.1. The processed output corresponding to the data shown is detailed in Figure 5.15 is represented in Figure F.2, illustrating a failure of the algorithm to prevent mode swapping, despite the sorting correction.

Concerning mode swapping, the continuation methods behave much better: there is simply no mode swapping because the analysis is conducted separately for each mode. In the post-critical regime, where the p-k method requires more iterations for convergence, the continuation methods converge without any trouble. However, the adaptive meshing feature of the continuation methods reduces automatically the radius r in this regime, as seen by the larger mesh density around 25 m/s in Figure 5.8. When the algorithm converges less rapidly, smaller radii are chosen as discussed in Section 5.3.3, and, on the contrary, a larger radius is selected when the solver converges faster. To illustrate the behaviour of the algorithm, the variation of the radius with respect to U is shown in Figure 5.9. For small wind speeds, the radius is constant; it decreases significantly at around 25 m/s, only to increase again at higher airspeeds. Methods that converge faster are more likely to use a less dense mesh. For instance, the Crisfield–NR method seems to use globally larger radii than the other methods. The second reason for this local refinement is a consequence of the variation in gradients $\mathbf{J}_\mathbf{x}$ and $\mathbf{J}_U$. Indeed, the radius r^2 given in equation (5.21) is expressed as a weighted sum of $\Delta U^2 = (U - U_0)^2$ and the squared norm of the step vector $\mathbf{dx} = \mathbf{x} - \mathbf{x}_0$ derived from equation (5.22)

$$\mathbf{x} - \mathbf{x}_0 = -\mathbf{J}_\mathbf{x}^{-1}(\mathbf{x}_0, U_0)\left[\mathbf{f}(\mathbf{x}_0, U_0) + \mathbf{J}_U(\mathbf{x}_0, U_0)(U - U_0)\right]. \tag{5.30}$$

Therefore, if the component related to the norm of $\mathbf{dx}$ is negligible with respect to r, the distance between two consecutive points will mostly be driven by $U - U_0$.

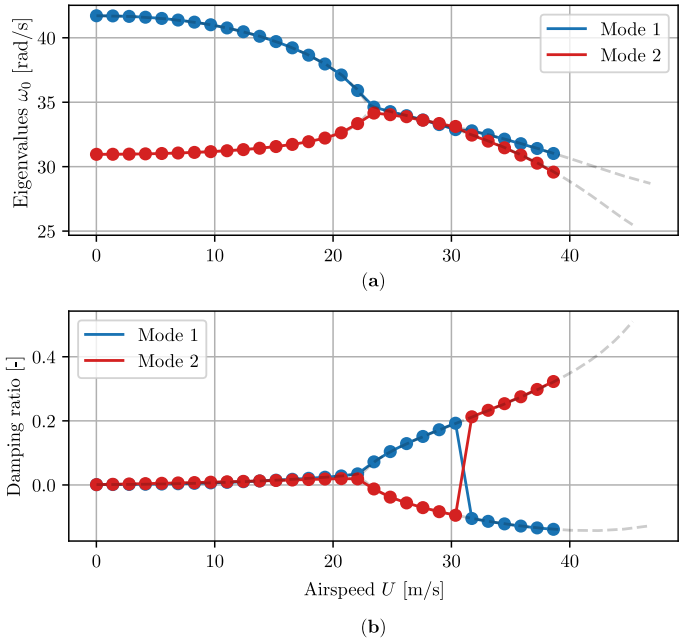

Figure 5.7: Application 2. Variation of natural frequencies and damping ratios with airspeed, calculated using the p-k method. Mode swapping occurs around $U = 30$ m/s.

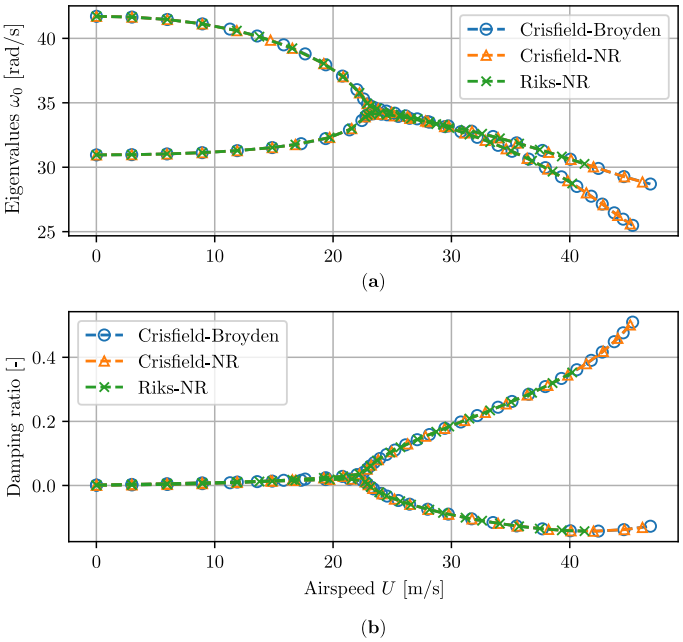

Figure 5.8: Illustration 2. Results of the pre-flutter analysis (a) Undamped eigenvalues and (b) Damping ratios for the first and second modes derived with the three continuation methods.

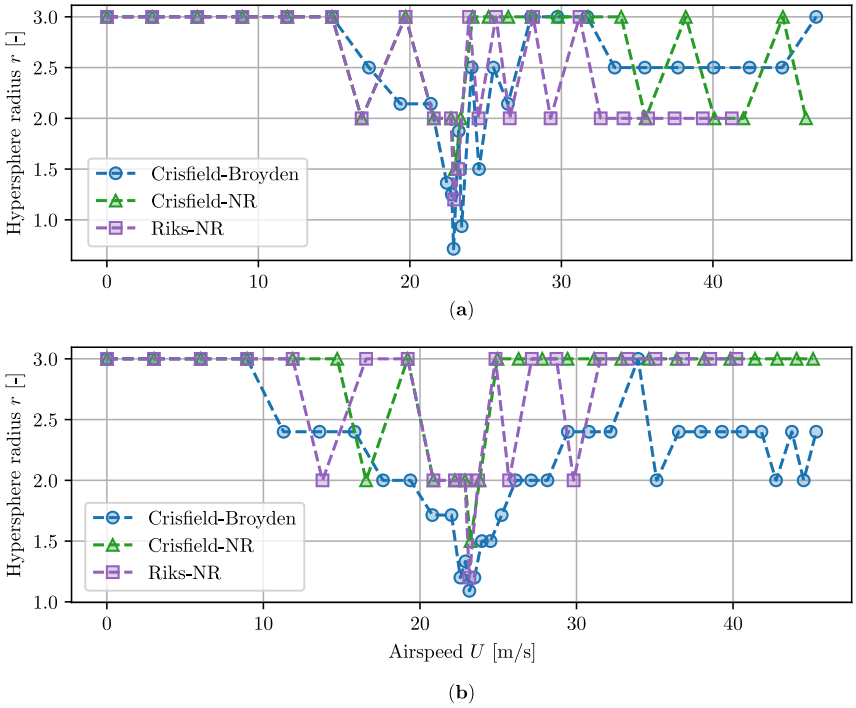

Figure 5.9: Application 2. Evolution of the sphere radius with respect to the wind speed U for the 3 continuation methods.

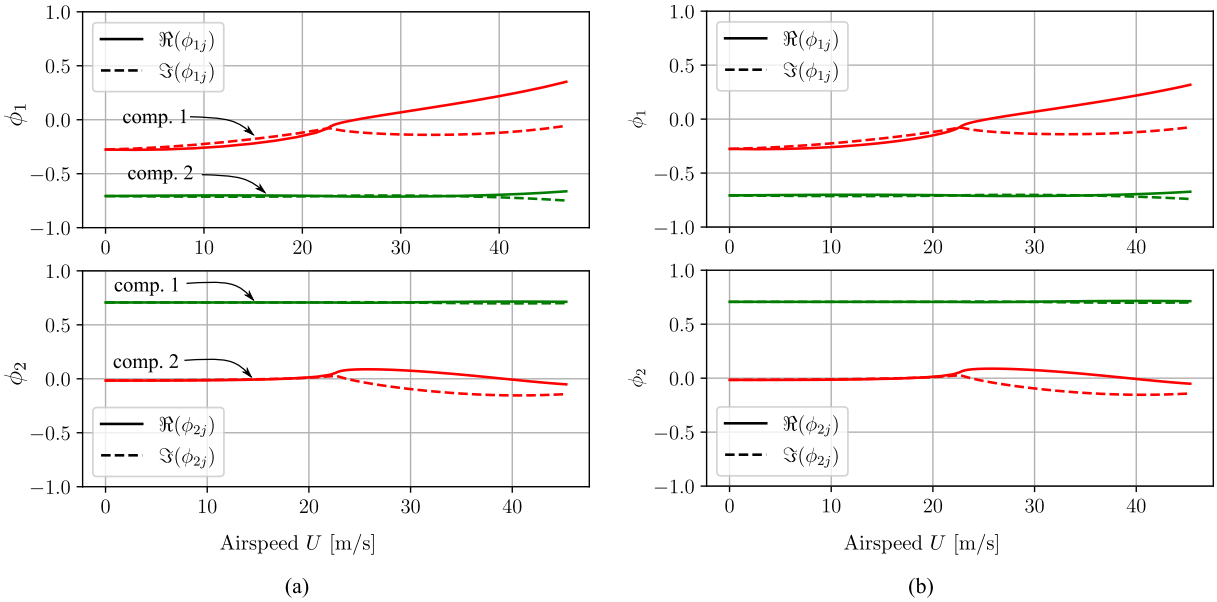

Figure 5.10: Application 2. Effect of the scaling parameters related to the mode shapes $\boldsymbol{\phi}_1$ and $\boldsymbol{\phi}_2$. (a) Cylindrical arc-length: $x_{\text{ref},j} = 100$, and (b) spherical arc-length $x_{\text{ref},j} = 0.01$.

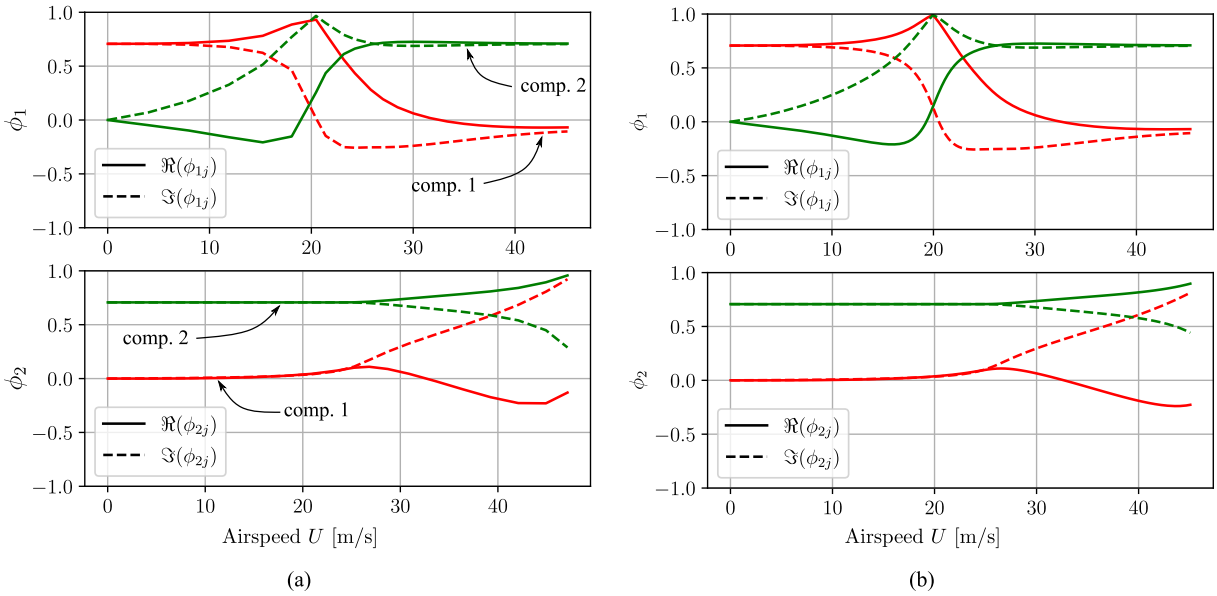

Figure 5.11: Application 2, with $x_f/c = 0.5$ instead of 0.46. Effect of the scaling parameters related to the mode shapes $\boldsymbol{\phi}_1$ and $\boldsymbol{\phi}_2$. (a) Cylindrical arc-length: $x_{\text{ref},j} = 100$, and (b) spherical arc-length $x_{\text{ref},j} = 0.01$. All other parameters are identical to those given in Table 5.2.

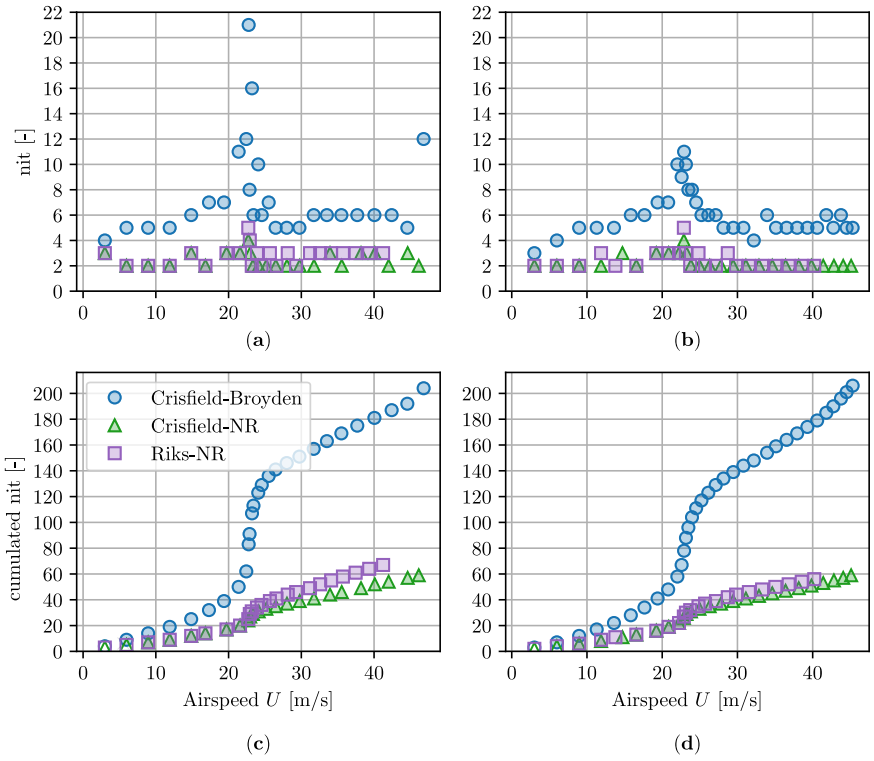

Figure 5.12: Application 2. Number of iterations (nit) and cumulated number of iterations for mode 1 in (a,c) and mode 2 in (b,d). The conclusion regarding the computational loads of the continuation methods should be made with care, as the workload per iteration for each method is not exactly the same.

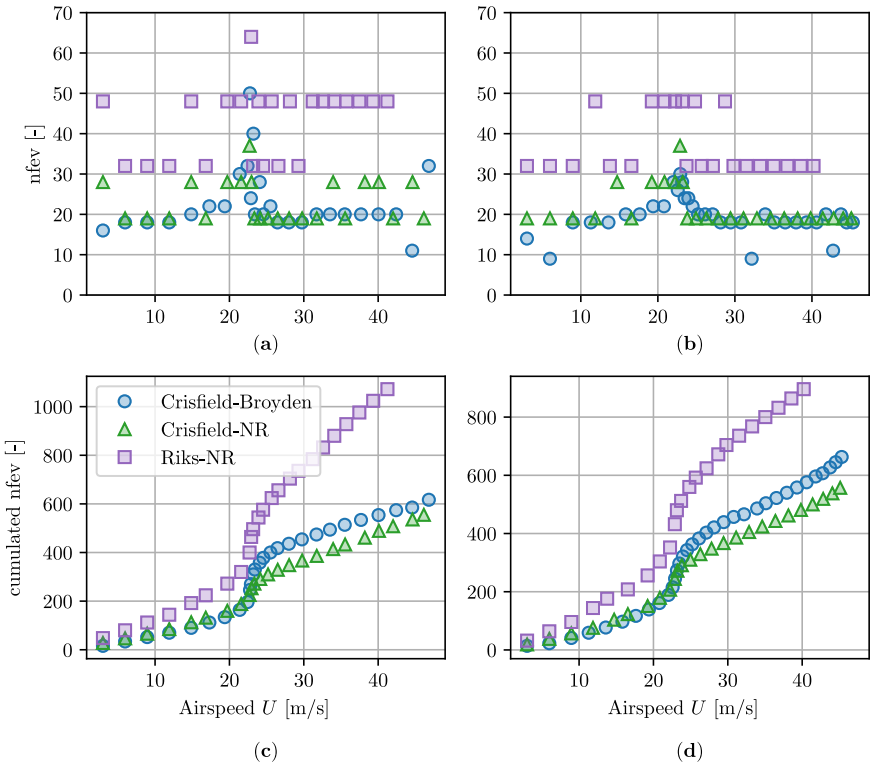

Figure 5.13: Application 2. Number of function evaluations (nfev) and cumulated number of calls to target function $\mathbf{f}(\mathbf{x}, U)$ for mode 1 in (a,c) and mode 2 in (b,d).

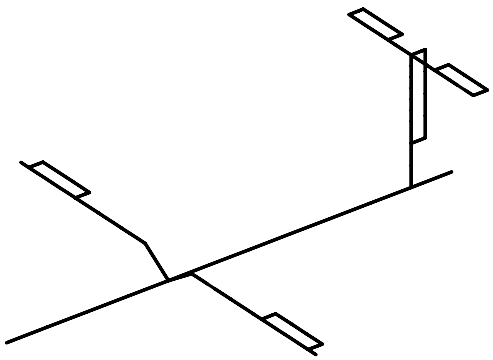

Figure 5.14: Schematic of the structural model of the GTA. Adapted from [137].

The behaviour of the adaptive refinement is also sensitive to the scaling parameters provided by the user. The parameter U_{ref} is probably the easiest to fix. For a radius $r \approx 1$, it can be chosen so that, in a given step where all variations $dx_j = \frac{x_j - x_{0,j}}{x_{\text{ref},j}}$ are zero for all j, the distance between two consecutive points $U_i - U_{0,i}$ is equal to rU_{ref}. The same principle is used to select $x_{\text{ref,j}}$, which must be chosen such that the largest expected step in the j direction $dx_j = \frac{x_j - x_{0,j}}{x_{\text{ref},j}}$ is at most equal to r. Hence, if all variations dU and dx_i are negligible, with $i \neq j$, the largest allowed step $x_j - x_{0,j}$ is $rx_{\text{ref},j}$.

The choice of the scaling parameter is also a tool for the improvement of the convergence of the method. For instance, if the user is able to identify directions in $\mathcal{D}$ along which no or almost no variation of the modal properties is observed, these can be discarded to drive the algorithm towards preferential directions where large gradients are observed, reducing hence the number of variables effectively contributing to the hypersphere radius. Such an approach may be referred to as a *cylindrical arc-length method* (see [138]), by reference to the shape of the continuity equation, initially spherical, that degenerates into a cylinder due to large x_{ref}. The use of a cylindrical continuation scheme is useful in large systems, where local contributions to the hypersphere radius of some directions in $\mathcal{D}$ are annihilated by a much larger fraction of other directions along which no gradient is observed.

In the present case, the mode shapes exhibit a linear variation with airspeed U, and this tendency is already well captured with a few points, as seen in Figure 5.10(a). Adding more points by decreasing $\Re[\phi_{\text{ref}}]$ and $\Im[\phi_{\text{ref}}]$ will not improve the representation of $\boldsymbol{\phi}_i$, as illustrated in Figure 5.10, where a comparison between the mode shapes obtained with $\Re[\boldsymbol{\phi}_{\text{ref}}] = \Im[\boldsymbol{\phi}_{\text{ref}}] = 100$ in (a) and $\Re[\boldsymbol{\phi}_{\text{ref}}] = \Im[\boldsymbol{\phi}_{\text{ref}}] = 0.01$ in (b) is illustrated, but where no apparent difference is observed due to the low variations of the gradients $\frac{\partial \boldsymbol{\phi}}{\partial U}$. To illustrate the differences between cylindrical and spherical arc-length, the same comparison as that made in Figure 5.10 is carried out in Figure 5.11, where the pitch axis x_f of the considered structure is set to $0.5c$ instead of $0.46c$ to observe larger gradient variations in the modes shapes. This figure shows that the mode shapes obtained in (b) are significantly smoother than those in (a), but a reasonably good description was already achieved in (a). It is important to recall that each point in the curve is calculated with the same absolute tolerance and that the density of the mesh does not affect this accuracy. However, interpolation errors may sometimes be induced, for instance if the modes shapes in Figure 5.11 (a) are used instead of those in (b). Therefore, the resolution of the resulting data must be verified to limit interpolation errors when interpolating between two consecutive points, as is required in order to pinpoint exactly the flutter airspeed [105, 139].

To analyse the performance of the methods, the number of iterations is compared in Figure 5.12 and contrasts well with the behaviour of the Riks and Crisfield methods. The latter reduce by a factor of 2 or even 3 the number of iterations with respect to Riks method. It must be noted that around 23 m/s, the Crisfield–Broyden method failed to converge after 15 iterations — i.e. the maximum allowed number of iterations. The reason for this is that this point is close to the critical velocity, and important variations in the gradients of $\mathbf{f}(\mathbf{x}, U)$ are expected there, affecting the performance of Broyden's method, which estimates the Jacobian from previous and current values of $\mathbf{f}$. This particular point requires 21 iterations in total instead of the 15 allowed. Except for this detail, the Crisfield–Broyden and Crisfield–NR techniques perform equally well, as confirmed by Figure 5.13, reducing the number of function calls per iteration by a factor of 2 or 3, and dividing by 2 the total cumulated number of calls required for a full flutter analysis. The Crisfield–NR method slightly outperforms the Crisfield–Broyden approach as shown in Figure 5.13(c) and (d) in terms of function calls, but Newton–Raphson requires the evaluation of the Jacobian matrix which is estimated by Broyden's method. Hence, because the evaluation of $\mathbf{f}$ potentially represents two different computational loads, a time-based benchmarking seems to be the only way to arbitrate which method is the most time-efficient between Broyden and Newton–Raphson, if computational time is the governing concern.

Parameters	App. 1	App. 2	App. 3	Units
Initial radius r_0	0.7	3	4	[–]
Min. Radius $r_{\min}$	0.05	0.5	0.5	[–]
Min. Radius $r_{\max}$	2.	7	5	[–]
Ref. Speed U_{ref}	10	1	10	[m/s]
Ref. $\Re\{\lambda_i\}$	1000	0.2 / 0.3	1	[rad/s]
Ref. $\Im\{\lambda_i\}$	0.3	1	5	[rad/s]
Ref. coordinate $\phi_{ij,\text{ref}}$	1	100	1	[–]

Table 5.2: Algorithm parameters used for the 3 proposed case studies.

5.4.3 Benchmark of the Generic Transport Aircraft (GTA)

The last illustration is a multi-mode model of a generic transport aircraft. The investigated prototype is taken from the ZAERO manual [61], and was used in the past by several authors [137, 140]. The model was generated using MCS-NASTRAN software and incorporates structural information from a simplified finite element model of the aircraft, whose mesh is schematically illustrated in Figure 5.14, and aerodynamic loads obtained using the doublet lattice method.

Using Roger's approximation [48], the aerodynamic forces $\mathbf{Q}(k)$ are written in the form

$$\mathbf{Q}(k) = \mathbf{A}_0 + \mathbf{A}_1 k + \mathbf{A}_2 k^2 + \sum_{j=1}^{n_l} \mathbf{A}_{2+j} \frac{k}{k+\gamma_j} \tag{5.31}$$

where $\mathbf{A}_j$ are $n_m \times n_m$ real matrices, n_m is the number of modes considered in the analysis and γ_j are aerodynamic lag coefficients given by

$$\gamma_j = -1.7 k_{\max} \frac{j}{(n_l+1)^2} \tag{5.32}$$

with $k_{\max}$ referring to the maximum reduced frequency at which the aerodynamic matrix $\mathbf{Q}(k)$ is evaluated by NASTRAN, and with $n_l = 4$. The number of retained modes is chosen equal to 7.

The variation of the natural frequencies and damping ratios with airspeed is displayed in Figure 5.15, revealing that the flutter mechanism is binary, while the other five modes are only slightly affected by aerodynamic effects, except their damping ratios which vary linearly with U. Figure 5.16 presents a less overloaded view of the eigenvalues, determined using the Crisfield–Broyden method in (a) and p-k method in (b). Once again, mode swapping can be observed at an airspeed of around 180 m/s in the predictions of the p-k method.

As this flutter analysis is conducted on a mode-by-mode basis, the inclusion of 7 modes in the system is not more difficult than the previous case studies involving only 2 modes. Naturally, this expansion entails an anticipated increase in computational workload: the single-mode analysis is now repeated 7 times instead of twice.

In addition, Figure 5.15 emphasizes one of the primary advantages of the arc-length method, which is its ability to fine-tune the mesh at specific wind speeds where refinement is necessary. In this example, modes 1 and 3 require a local refinement around 220 m/s, but a coarse mesh may be used elsewhere. This local refinement is well captured by continuation methods, in Figure 5.15(b), where the mesh density for modes 1 and 3 at 220 m/s is much higher than for

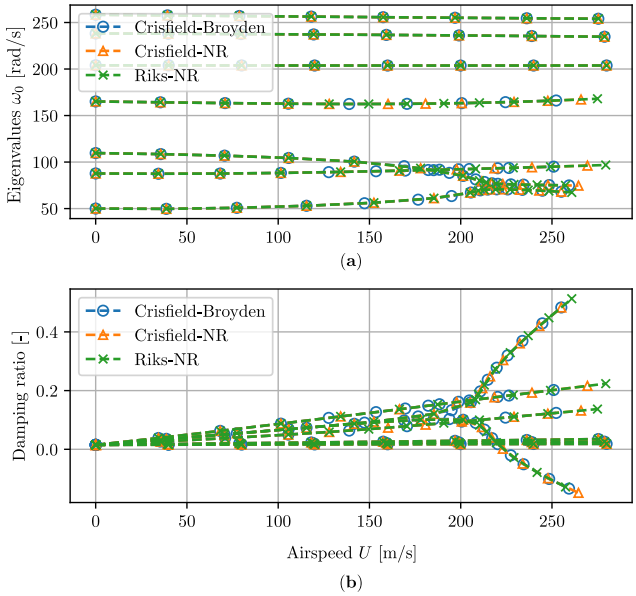

Figure 5.15: Illustration 3 (GTA Benchmark). Results of the *pre-flutter analysis* (a) Undamped eigenvalues and (b) Damping ratios derived with the 3 considered continuation methods.

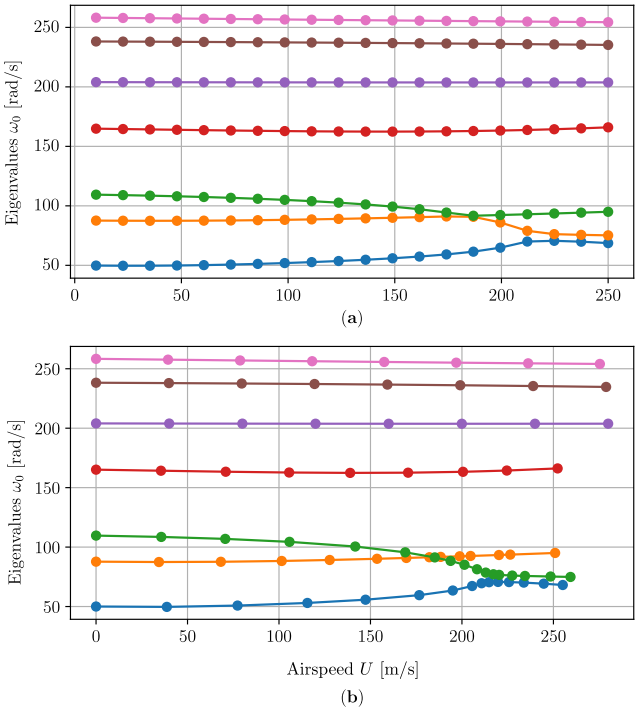

Figure 5.16: Illustration 3. Results of the *pre-flutter analysis* with (a) p-k method and with (b) Crisfield–Broyden. Mode swapping may be seen in (a) around 180 m/s.

speeds lower than 100 m/s. Furthermore, the mode-by-mode analysis allows a coarser mesh to be used for all other modes whose properties remain constant throughout the flight envelope. In this example, among the 7 modes in total, 5 of them remain mostly constant so that the local refinement required by modes 1 and 3 must not be transposed to other modes. Here, for 7 modes in total, the absolute workload saving is not substantial. But when many modes are involved, mesh refinement allows for an appreciable potential reduction in the global computation load with respect to methods that use a uniform and likely fine mesh identical for all modes of the system.

The number of function evaluations is presented in Figure 5.17 for modes 1 and 3. It once again depicts the same tendency as observed in the first two illustrations: the two Crisfield methods converge more rapidly. For a full flutter analysis, the number of function evaluations is reduced by a factor of 3 approximately for modes 1 and 3.

Modes 2, 4, 5, 6 and 7 are also good candidates to illustrate the sensitivity of the algorithm to badly chosen scaling parameters U_{ref} and $\mathbf{x}_{\text{ref}}$. Taking a closer look, for instance at the 5th mode, it is evident that it does not affected significantly by the aerodynamic loads, at least within the specified airspeed range. This mode exhibits constant properties, including eigenvalue, damping ratio and mode shape; it is insensitive to U. As a consequence, the only variation expected in the space $\mathcal{D}$ will be exclusively in a direction parallel to U. In such a case, performing cylindrical steps by discarding the U direction from the line search direction —*i.e.* choosing $U_{\text{ref}} \to \infty$— results in a divergence of the algorithm. To illustrate this issue, if the analysis is conducted for the 5th mode with $U_{\text{ref}} = 100$ m/s instead of $U_{\text{ref}} = 10$ m/s as presented before, the algorithm diverges. Then, if the scaling parameters are of major importance on the quality of the local refinement performed by the algorithm, they could also potentially govern the stability of the solution when badly chosen. Therefore, their selection should sometimes be approached with careful consideration, especially in cases where gradients are unidirectional or almost unidirectional— *i.e.* nearly all columns of $\mathbf{J}_{\mathbf{x}}$ are empty (except in one direction). In these particular cases, the use of cylindrical arc-length methods is the most appropriate choice to ensure stability. One of the key principles to ensure the robustness of the method can be summarized as including in the continuation equation at least one direction of $\mathcal{D}$ that affects $\mathbf{f}(\mathbf{x}, U)$, and noting that reducing the dimensionality of the hypersphere does not necessarily accelerate convergence.

5.5 Conclusion

This chapter presented an arc-length continuation process as an alternative to the classical p-k method for flutter analysis of aeroelastic systems. The primary objective was to develop a systematic and globally convergent tool for tracking the evolution of the system's modal properties with increasing wind speed. The proposed algorithm simultaneously addresses three key tasks: (i) identifying pre-flutter states to assess the structure's behaviour, (ii) providing these pre-flutter states as input for the background/resonant decomposition method, and (iii) constructing the wind-on modal basis, composed of the complex mode shapes from the damped eigenvalue problem. By integrating these tasks into a single framework, the proposed algorithm executes all the preliminary calculations necessary to carry out a full flutter analysis of buffeting excited structures using the methodology developed in Chapter 2, 3 and 4.

The principle hinges on solving the nonlinear generalized eigenvalue problem for a chosen wind speed U to determine one *pre-flutter state*. The critical problem is first reformulated and transformed into a nonhomogeneous system of equations by incorporating the normalization condition. One continuity equation is then added to offer a smart tracking process. The process is initiated at wind-off conditions and progresses incrementally toward aeroelastic instability, with step sizes controlled by a hypersphere radius.

A key feature of the proposed algorithm is its mode-by-mode approach, where each mode

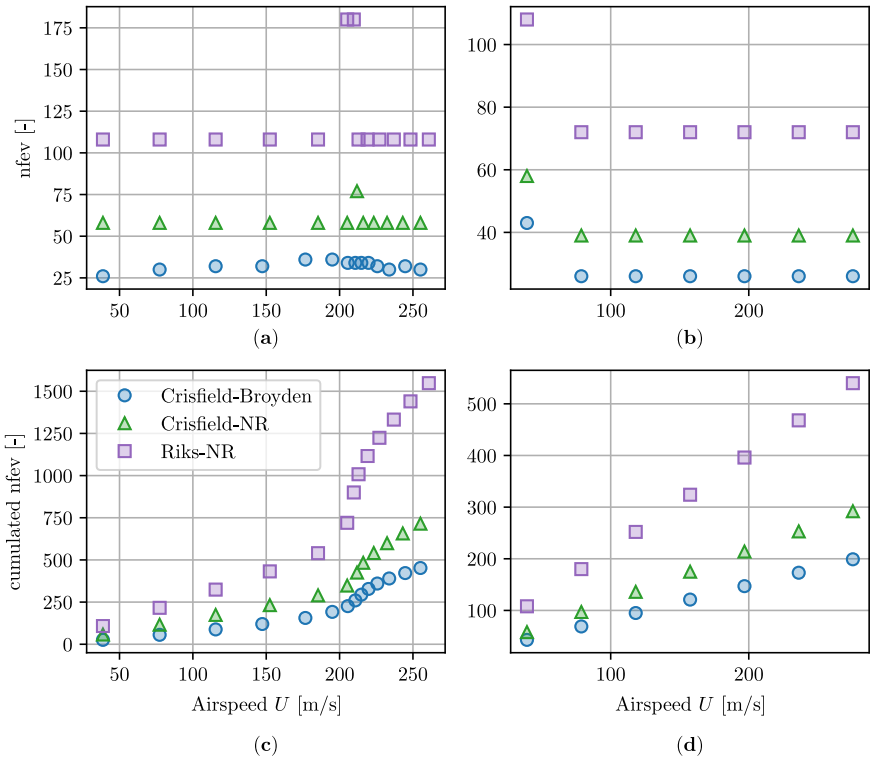

Figure 5.17: Application 3. Number of function evaluations (nfev) and cumulated number of calls to target function $\mathbf{f}(\mathbf{x}, U)$ for mode 1 in (a,c) and mode 3 in (b,d).

is treated independently. In that way, any undesired mode swapping phenomenon is prevented. Whenever modes behave independently from others, the algorithm automatically adapts, allowing them to be tracked with their own velocity mesh, optimizing computational efficiency.

Two classes of continuation methods have been described: Riks' and Crisfield's approaches. The first consists in solving systematically the system of equations formed by the transformed critical problem and the continuity equation. The second method takes advantage of the knowledge of the analytical form of the continuity equation to solve it analytically. The second approach was seen to be significantly faster than the first.

The continuation processes proposed here have proven to be appropriate to determine the flutter behaviour of a system, thanks to their ability to focus on regions where high local variations in modal properties are observed. By selecting suitable scaling parameter and sphere radius values, the user can guarantee that the algorithm will detect local variations that a uniformly distributed mesh —as those used with the traditional p-k method— could inadvertently miss. Additionally, the mode-by-mode approach provides a major advantage in computational efficiency. Since each mode is tracked independently, a custom mesh is assigned to each, allowing a coarser resolution for modes with nearly constant properties. This results in an overall optimization of computational resources, particularly in large multi-mode systems.

The performance of the methods was assessed on three selected examples evaluating in total four techniques : the p-k method, Riks-Newton–Raphson, Crisfield–Newton–Raphson and Crisfield–Broyden. Among the three continuation methods, the Riks-Newton–Raphson was seen to be the most computationally expensive, requiring in total approximately 3 times more function evaluations than the Crisfield-based methods. The Crisfield–Broyden method emerged as the most efficient in terms of objective function evaluations.

A direct comparison of computational efficiency between the p-k method and continuation methods could not be established. However, all continuation methods demonstrated excellent

stability, successfully solving the flutter problem without mode swapping or convergence issues. This robustness persisted even near critical points and in the post-critical regime, where the classical p-k method encountered mode swapping in two out of the three test cases.

Chapter 6

Solution to Critical Stability Problem

Determining the smallest critical velocity is a fundamental aspect of analysing aeroelastic systems. It is often the first consideration in the analysis of an actual bridge, as it offers insight into the significance of flutter in the design. Additionally, it may provide clues about how the buffeting response could be influenced by unsteady effects as the system approaches the flutter velocity. Despite it comes at early stages in a project, we have pushed in this thesis this task to the last Chapter, as it was not the main focus of this work.

Over the course of this research, we contributed to the development of a global numerical solution for determining the critical state by examining the two loci of couples (ω, U) where the real and respectively imaginary parts of the determinant of the aeroelastic impedance function vanish.

The concept of a locus originates from the works of Descartes in the 17th century, who used it to describe sets of points satisfying algebraic equations, thereby laying the groundwork for analytic geometry. In aeroelasticity, this concept was first incorporated by [141], who proposed a graphical method for evaluating the critical velocity. This method involves identifying the intersections of two branches, which represent the loci where either the real or imaginary part of the determinant of the dynamic flexibility matrix equals zero. These branches, known as critical loci, are defined by the condition that the determinant's real or imaginary part vanishes.

This method is very convenient for small systems, but its application to more complex systems becomes more difficult as the size of the problem increases. This chapter proposes an improved version of this method, based on a reformulation of the problem that is able to accommodate possibly large systems.

6.1 Formalization

Aeroelastic systems are governed by Equation (1.73), in the absence of external loading, which takes the form of a differential equation with frequency dependent coefficients. Being a linear homogenous problem, the only non trivial solutions of that problem evolve as exponential functions of time, $\boldsymbol{\phi}_i \mathrm{e}^{\lambda_i t}$ where λ_i and $\boldsymbol{\phi}_i$ form a pair of eigenvalue and eigenmode. They satisfy

$$\left(\lambda_i^2 \left[\mathbf{M} - \mathbf{M}_{\mathrm{ae}}(k, U)\right] + \lambda_i \left[\mathbf{C} - \mathbf{C}_{\mathrm{ae}}(k, U)\right] + \left[\mathbf{K} - \mathbf{K}_{\mathrm{ae}}(k, U)\right]\right)\boldsymbol{\phi}_i = 0. \tag{6.1}$$

where $k = \frac{\Im\{\lambda_i\} b}{U}$. Following the linear nature of the problem, the general solution of the homogenous problem is obtained as a linear combination of these elementary solutions,

$$\mathbf{q}(t) = \sum_i \boldsymbol{\phi}_i \mathrm{e}^{\lambda_i t} \tag{6.2}$$

where the summation extends over all roots of the characteristic polynomial.

The theory of linear stability of dynamical systems indicates that the system is stable if and only if $\Re\{\lambda_i\} < 0\ (\forall i)$, i.e. the real parts of all eigenvalues are negative. It is neutrally (critically) stable if there is one eigenvalue with a zero real part, $\exists i$ such that $\Re\{\lambda_i\} = 0$, while the real parts of all others are negative. The system is unstable if there is at least one eigenvalue whose real part is positive.

Another standard approach to the dynamic stability of linear systems, written in the form

$$\mathbf{J}(\lambda_i, U)\,\boldsymbol{\phi}_i = \mathbf{0}$$

where U is a problem parameter, consists in observing that non trivial solutions can only develop in critical conditions where matrix $\mathbf{J}(\lambda_i, U)$ is singular. In other words, in the homogenous problem, $\boldsymbol{\phi}_i = 0$ in both stable and unstable dynamic equilibrium configurations, while $\boldsymbol{\phi}_i$ can take a non trivial value, with undetermined amplitude, in some critical conditions. These critical conditions correspond to specific values $U_{\mathrm{cr},k}$ of the parameter U which are such that the determinant of $\mathbf{J}(\lambda_i, U)$ vanishes. There might be several values, but only the smallest one, $U_{\mathrm{cr},min} = \mathrm{argmin}_k\left[U_{\mathrm{cr},k}\right]$, is of interest. Indeed, the theory of linear stability of dynamical systems demonstrates that all trivial solutions corresponding to $0 \leq U < U_{\mathrm{cr},min}$ are stable, while all trivial solutions corresponding to $U > U_{\mathrm{cr},min}$ are unstable. This fundamental value $U_{\mathrm{cr},min}$ of the problem parameter is so important that it is designated as U_{cr} in the following. It is commonly coined "the" critical state.

This theory can be applied to the determination of the critical wind velocity by noticing that the modal dynamic flexibility reads

$$\mathbf{J}(\omega, U) = -\omega^2\mathbf{M}(\omega, U) + \mathrm{i}\omega\mathbf{C}(\omega, U) + \mathbf{K}(\omega, U). \tag{6.3}$$

It is also highlighted that a modal basis is chosen here but the following derivations are also applicable to a nodal basis, therefore to much larger matrices.

The critical velocity U_{cr} is obtained by imposing that

$$\det\left[\mathbf{J}(\omega_{\mathrm{cr}}, U_{\mathrm{cr}})\right] = \det\left[-\omega_{\mathrm{cr}}^2\mathbf{M}(\omega_{\mathrm{cr}}, U_{\mathrm{cr}}) + \mathrm{i}\omega_{\mathrm{cr}}\mathbf{C}(\omega_{\mathrm{cr}}, U_{\mathrm{cr}}) + \mathbf{K}(\omega_{\mathrm{cr}}, U_{\mathrm{cr}})\right] = 0. \tag{6.4}$$

This equation is complex, and may be formulated as a set of two real equations

$$\begin{cases} \Re\{\det(\mathbf{J}(\omega, U))\} = 0 & \text{(6.5a)} \\ \Im\{\det(\mathbf{J}(\omega, U))\} = 0 & \text{(6.5b)} \end{cases}$$

This set of two equations comes with the two unknowns ω_{cr} and U_{cr}, i.e. the frequency of the aeroelastic system in the critical state and the value of the critical wind velocity.

This formulation was proposed by [141], about 75 years ago, who studied pitch plunge models of aircraft wings. It provides a practical framework where the solutions of equations (6.5a) and (6.5b) are carried out analytically, and the contours of the two equations in the (ω, U) plane define two loci for the flat plate, whose intersection defines the critical state. In general, there are at least as many loci as the number of modes considered in the model. Some additional isolated solutions could exist though [142]. There are therefore several intersections, possibly, but the one corresponding to the lowest wind velocity only is of interest, and corresponds to U_{cr}.

A direct implementation of this approach is feasible when the size of the considered problem is not too large. It will be referred to as the *direct determinant method*, as it consists in tracking the singular nature of the system's dynamic flexibility $\mathbf{J}$ by explicitly evaluating the determinant. The intersection of the two loci characterized by Equations (6.5a) and (6.5b) may typically be determined geometrically, or numerically.

This model is quite convenient for small systems, but in practice, the use of the determinant as a quantitative measure of the singularity of a matrix is not robust as soon as the size of the

matrix grows. One of the reasons is that the order of magnitude of the determinant increases with the size of the matrix. Hence, characterizing the singularity of the system by demonstrating a small value of the determinant, which vanishes in theory, may be quite subjective as its potential smallness depends on the problem size. An effective measure of the singularity of a matrix is provided by the condition number, which establishes a dimensionless measure of the singularity

$$\hat{\rho}\left[\mathbf{J}(\omega, U)\right] = ||\mathbf{J}(\omega, U)||_q \cdot ||\mathbf{J}(\omega, U)||_q^{-1} \tag{6.6}$$

with q denoting the order of the matrix norm, commonly chosen as 1 or ∞ —in which case the evaluation of the diagonality index requires the calculation of a matrix inverse—, or $q = 2$ —in which case the condition number may be evaluated as the ratio of the largest and smallest eigenvalues. However, due to the highly localized nature of the singularities in the (ω, U) plane, identifying a precise point where $\hat{\rho} \to \infty$ is numerically delicate. In particular, attempting to isolate such a singularity by solving a single scalar condition —i.e., searching for one specific point in a two-dimensional space— can be challenging and inefficient, as the solution lies within a narrow region with large gradients variation. In contrast, reformulating the problem as the intersection of two well-behaved curves (the loci) offers a more robust approach. By tracking these curves independently and locating their crossing points, the critical velocity can be determined while avoiding numerical conditioning issues. An alternative method based on this observation is therefore proposed in the following.

A different form of the system (6.5) is first formulated. In a very general manner, the determinant of a matrix may be expressed as the product of its eigenvalues. This yields

$$\det\left[\mathbf{J}(\omega, U)\right] = \prod_{j=1}^{M} \mu_j(\omega, U) \tag{6.7}$$

where μ_j refers to the complex eigenvalues of the dynamic flexibility matrix. Because $\mathbf{J}(\omega, U)$ is complex and non-Hermitian, these eigenvalues are complex, and may be expanded under the form of an exponential complex notation, $\mu_j = r_j \exp(\mathrm{i}\psi_j)$. Equation (6.7) thus becomes

$$\det\left[\mathbf{J}(\omega, U)\right] = \prod_{j=1}^{M} r_j \exp(\mathrm{i}\psi_j). \tag{6.8}$$

where $r_j = |\mu_j|$ and $\psi_j = \arctan\left[\frac{\Im(\mu_j)}{\Re(\mu_j)}\right]$ refer to the amplitude and phase of μ_j. Because of the associativity of the product, one may write

$$\det\left[\mathbf{J}(\omega, U)\right] = \prod_{j=1}^{M} r_j \left(\prod_{j=1}^{M} \exp\left(\mathrm{i}\psi_j\right)\right) \tag{6.9}$$

or, equivalently

$$\det\left[\mathbf{J}(\omega, U)\right] = \prod_{j=1}^{M} r_j \exp\left(\mathrm{i}\sum_{j=1}^{M} \psi_j\right). \tag{6.10}$$

Using the Euler formula, the exponential is expressed as a sum of a sine and a cosine

$$\det\left[\mathbf{J}(\omega, U)\right] = \prod_{j=1}^{M} r_j \left[\cos\left(\sum_{j=1}^{M} \psi_j\right) + \mathrm{i}\sin\left(\sum_{j=1}^{M} \psi_j\right)\right]. \tag{6.11}$$

This equation expresses the determinant as a product of real amplitudes $\prod_{j=1}^{M} r_j$, and the complex sign expressed as $\prod_{j=1}^{M} \cos\left(\sum_{j=1}^{M} \psi_j\right) + \mathrm{i}\sin\left(\sum_{j=1}^{M} \psi_j\right)$. The first factor is the module and is

the product of all the eigenvalues of $\mathbf{J}(\omega, U)$ in absolute value. The complex sign differs from the usual "sign" function, which takes discrete values among $-1, 0, 1$ and is typically used to indicate the sign of a real number. In the present context however, the "sign" refers to a complex number of unit modulus that encodes the phase of the determinant (see for instance the "sign" output of the `slogdet` numpy function). In the sequel, any reference to the "sign" function should be understood in this latter sense and not as the conventional real-valued sign function.

The system of equations (6.5) may then be reformed as

$$\begin{cases} \displaystyle\prod_{j=1}^{M} r_j \cos\left(\sum_{j=1}^{M} \psi_j\right) = 0 & \text{(6.12a)} \\ \displaystyle\prod_{j=1}^{M} r_j \sin\left(\sum_{j=1}^{M} \psi_j\right) = 0. & \text{(6.12b)} \end{cases}$$

It is clear that it suffices that $r_j = 0$ for any $j \in [1, \dots, M]$ to get a solution of this system of equations. The phase related factor cannot be zero, as a complex number. Indeed, $\cos(\psi_{\text{tot}}) = 0$ for $\psi_{\text{tot}} = \frac{\pi}{2}(1 + 2k\pi)$ while $\sin(\psi_{\text{tot}}) = 0$ for $\psi_{\text{tot}} = k\pi$ so that there is no common solution for both the sine and the cosine. The only factor to root is thus the module product of the eigenvalues. Consequently, the critical condition degenerates in a single equation

$$\prod_{j=1}^{M} r_j = 0, \tag{6.13}$$

which formalizes the property that a matrix is singular if one of its eigenvalues at least vanishes. The critical solution is thus found by identifying the zero module eigenvalues of $\mathbf{J}(\omega, U)$ in the plane (ω, U). This system is in fact very similar to the method consisting in searching the point(s) of the plane (ω, U) where the condition number ρ is infinite with $q = 2$. The associated problem remains: equation (6.13) admits one —or maybe several— solutions in (ω, U) but localizing one of them in a plane where large gradients of the objective functions are observed is quite complicated numerically. Then, even though a more simple form of (6.12) may be obtained, it was investigated but with little success.

The new idea that is followed here is based on the observation that the solution of (6.12) is ill-conditioned. This is mostly due to the fact that the functions to cancel are very large in the (ω, U) plane, almost everywhere, except along the loci where the functions effectively cancel. The alternative consists therefore in avoiding the solution of that problem and replace it by the determination of all points (ω_k, U_k) of each loci, *i.e.* the independent solutions of (6.12a) and (6.12b). The separate treatment of the two equations makes it easier to alleviate the conditioning issue. When the loci associated with the real and imaginary parts are obtained, the final step of the analysis will consist in finding their intersections. Two options alleviating the conditioning issue are detailed next.

6.1.1 The log-method

Instead of solving (6.12) directly, an equivalent more robust form can be formulated using the Levenberg-Marquardt method [143]

$$\begin{cases} \displaystyle\prod_{j=1}^{M} r_j^2 \cos^2\left(\sum_{j=1}^{M} \psi_j\right) \leq \texttt{abstol} & \text{(6.14a)} \\ \displaystyle\prod_{j=1}^{M} r_j^2 \sin^2\left(\sum_{j=1}^{M} \psi_j\right) \leq \texttt{abstol} & \text{(6.14b)} \end{cases}$$

with `abstol` being the absolute tolerance on the objective functions to be solved. In this option, a different form of (6.5) was formulated, but the issue regarding the more-than-proportional growth of the determinant of $\mathbf{J}(\omega, U)$ with the problem size was still not addressed. A straightforward solution to mitigate this problem is to consider the logarithm of this equation. In this case, the two loci are obtained by solving

$$\begin{cases} f_r = 2\sum_{j=1}^{M} \ln(r_j) + \ln\left[\cos^2\left(\sum_{j=1}^{M}\psi_j\right)\right] \leq \ln(\texttt{abstol}) & \text{(6.15a)} \\ f_i = 2\sum_{j=1}^{M} \ln(r_j) + \ln\left[\sin^2\left(\sum_{j=1}^{M}\psi_j\right)\right] \leq \ln(\texttt{abstol}). & \text{(6.15b)} \end{cases}$$

The key advantage of this formulation is that the determinant is never explicitly computed, preventing overflow issues when evaluating the objective function for large matrices. Instead, a singular value decomposition is employed to evaluate the first and second terms of equations (6.15a) and (6.15b), ensuring that all terms of the objective function remain within a reasonable order of magnitude. When the smallest eigenvalues (r_j) or $\cos(\psi_{\text{tot}})$ is close to zero —or when both are close to zero—, the objective function f_r suddenly drops to lower values localizing the roots of (6.12a) at the anti-peak abscissa. The same applies to r_j, whose roots can be identified as the position of the anti-peaks occurring when either r_j or $\sin(\psi_{\text{tot}})$ are close to zero.

However, even tough the problem is mathematically well conditioned, the method's greatest strength also introduces its main limitation: due to their formulation involving an optimization problem, equations (6.15a) and (6.15b) must be solved using gradient-based nonlinear solvers. As illustrated in the example section, the (ω, U) plane still exhibits steep gradient in $\frac{\partial f_r}{\partial \omega}$ and $\frac{\partial f_r}{\partial U}$, despite the logarithm, making it difficult for these solvers to efficiently track a single solution branch at a time.

6.1.2 The sign method

The critical states $(\omega_{\text{cr}}, U_{\text{cr}})$ correspond to the intersections of the two loci (6.12a) and (6.12b). Among them, the intersection with the lowest wind velocity is of interest. For $U = U_{\text{cr}}$, and $\omega = \omega_{\text{cr}}$, one eigenvalue (at least) vanishes. For $U < U_{\text{cr}}$, all eigenvalues are non-zero, i.e. $r_j \neq 0 \ \forall j$. In the region of interest, $\prod r_i \neq 0$, and the two loci equations therefore reduce to

$$\begin{cases} \cos\left(\sum_{j=1}^{M}\psi_j\right) = 0 & \text{(6.16a)} \\ \sin\left(\sum_{j=1}^{M}\psi_j\right) = 0. & \text{(6.16b)} \end{cases}$$

With these considerations, the question of the order of magnitude, of the eigenvalues has disappeared. The set of points (ω_k, U_k) representing the loci are therefore obtained by only tracking the sum of the phases of the eigenvalues.

6.1.3 Numerical tracking of the loci

The equations of (6.15) and (6.16) can be solved numerically using any nonlinear solver. However, due to the large magnitude of the derivatives of the objective function, most gradient-based solvers should be avoided, as they may struggle to converge efficiently. A more suitable alternative is gradient-free methods such as the dichotomy method (bisection), where the function is iteratively bracketed within an interval and refined by evaluating midpoints. This approach

Parameters	Plunge	Pitch
Modal mass	22740 kg	2.47 $\times 10^6$ kg.m^2/m
Natural frequency	0.1 Hz	0.278 Hz
Structural Damping Ratios ξ_s	0.3 %	0.3 %

Table 6.1: Parameters for the first case study "Application 1".

ensures robustness, particularly in cases where the function exhibits steep variations, such as in the neighbourhood of the solution branches. Other derivative-free methods, such as the secant method or Brent's algorithm, could also be considered for improved convergence efficiency while maintaining numerical stability.

Brent's method offers a compromise between the dichotomy and the Newton-Raphson method, combining the robustness of bracketing techniques with the faster convergence of interpolation-based approaches. It efficiently progresses when the function behaves smoothly and switches to the reliability of the dichotomy method when rapid variations or discontinuities in the derivative are encountered. These methods have been implemented and have proved success in several test cases. The details of their implementation will be given in the next sections.

Also, as it will be shown later, the presence of damping smooths the sign change in the objective function, which tends to be abrupt, otherwise, in lightly damped systems as encountered in practice. The dichotomy method is best suited to handle such abrupt transitions, ensuring reliable root-finding. Conversely, for smoother objective functions, Brent's method can be used to accelerate convergence while retaining numerical stability.

6.2 Illustrations

6.2.1 Pitch-Plunge model

The test case considered is the original benchmark proposed by Polimi [46]. The aeroelastic model is the same as the one used in Section 3.6.1, but the original structural parameters detailed in Table 6.1 are used.

The critical loci are shown in Figure 6.1, where the intersection of the real and imaginary loci defines the critical velocity, occurring at 78 m/s. This result is fully consistent with the benchmark results [46]. The loci have been obtained using different methods. The first method used is a graphical solution of the direct determinant formulation, which involves sampling the (ω, U) plane into a chosen window and evaluating $\det(\mathbf{J}(\omega, U))$ over this grid. The critical loci are then extracted using a `contour` algorithm, such as those provided by `matplotlib` [144] or `Matlab` [145]. These algorithms allow for specifying a particular level —in this case, zero for both the real and imaginary critical loci. If the grid resolution is sufficiently high, these methods can accurately capture the critical curves. The result of the intermediate mapping used by the contour algorithm is illustrated in a log-scale in Figure 6.2, where important variations of the determinant (spanning 10 orders of magnitude!) are observed. The output of the first geometrical approach is shown in black in Figure 6.1 and is almost hidden behind the red curves.

The three investigated methods (1) the direct method, (2) the log method, and (3) the sign method provided virtually identical results shown by the red curves. For each approach, typical examples of target functions are shown in Figure 6.3 for the real part and in Figure 6.4 for the imaginary part. The upper and lower branches of the real critical locus is determined by numerically finding all the roots of curves like those in Figure 6.3 for all wind speeds. Similarly, each point of the imaginary critical locus is obtained by identifying the roots or minima of the functions shown in Figure 6.4. All approaches are theoretically equivalent.

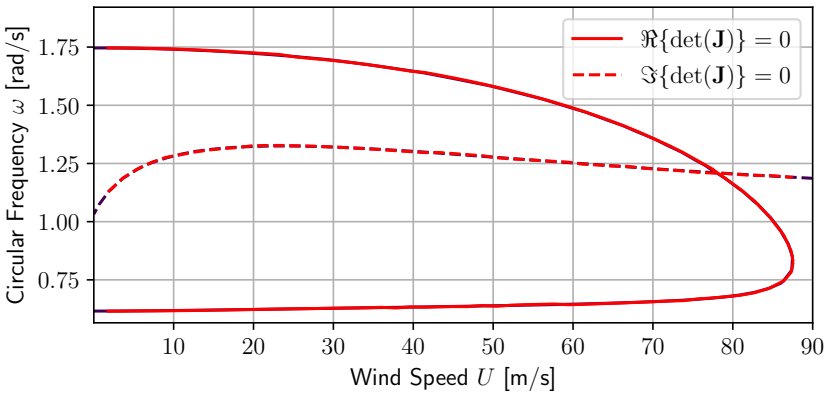

Figure 6.1: Application 1. Critical loci obtained for the first application using the sign method and graphical method. The critical state at 78 m/s is localized at the intersection of the solid and dashed loci.

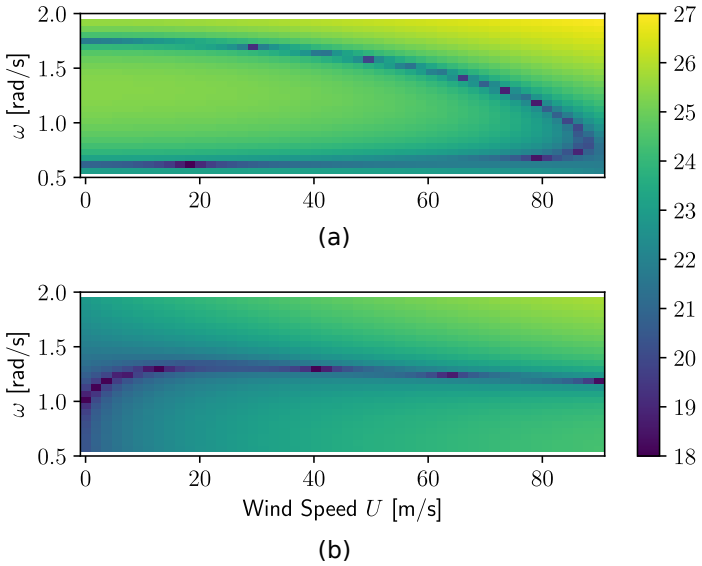

Figure 6.2: Illustration of the determinant in log scale. (a) Real part and (b) Imaginary part.

Figures 6.3 and 6.4 summarize the characteristics of the three formulations of the critical problem $\det(\mathbf{J}(\omega, U)) = 0$. The direct determinant target function, illustrated in (a), involves large numerical values, yet its roots are easily captured. The target function of the sign method, shown in (c), behaves similarly but remains bounded within $\mathcal{O}(1)$. This advantage was already pointed out, as it eliminates the risk of overflow when explicitly evaluating the determinant. As depicted in (b), the log method also maintains values with reasonable order of magnitude but requires locating a minimum instead of a root. In this example, all three methods yield identical results on Figure 6.1, indicating that none of them really suffers from numerical conditioning.

In the case of the sign formulation (6.16), it is important to highlight the sensitivity of the determinant's sign to damping. For undamped structures, the sum of the phase $\sum_{i=1}^{M} \phi_i = 0$, then one equation is systematically zero. For normally damped structures, Figures 6.3(c) and 6.4(c) show a smooth evolution of the complex sign of the determinant. However, Figure 6.3(d) and 6.4(d) —representing the same case study but with a very slight structural damping of $\xi_s = 0.003\%$— exhibit abrupt sign changes, which can be challenging to capture accurately, particularly for the imaginary critical locus. This issue is evident in the nearly horizontal blue curve of Figure 6.4(d), where the sign variation becomes difficult to track numerically. The

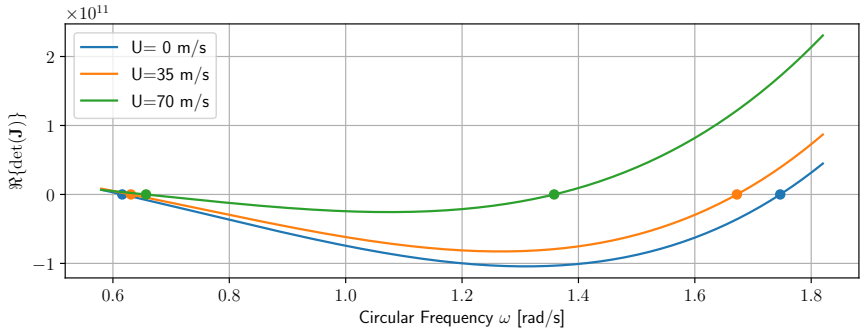

(a) Roots of the determinant based on the determinant of $\mathbf{J}(\omega)$. Large number are involved.

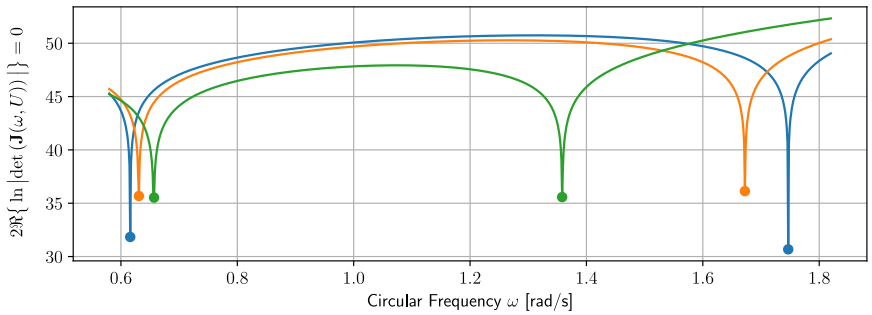

(b) Log method: Logarithm of the determinant of $\mathbf{J}(\omega)$ versus circular frequency ω for 3 different average wind speeds U.

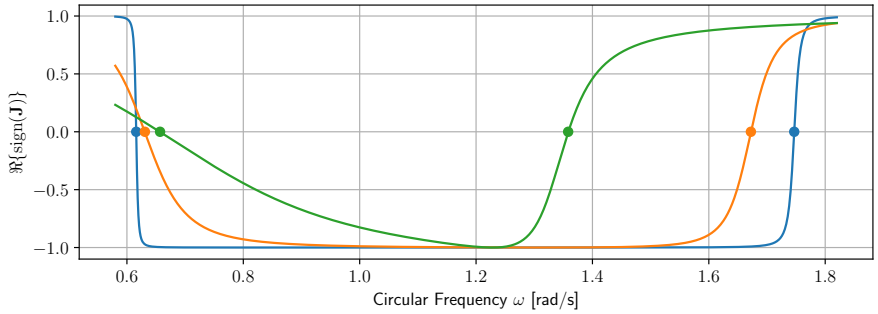

(c) Sign method: Sign of the determinant of $\mathbf{J}(\omega)$ versus circular frequency ω for 3 different average wind speeds U.

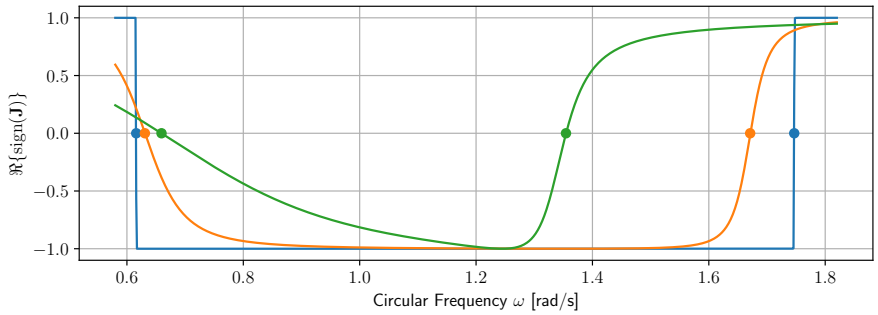

(d) Sign method: Illustration of the sensitivity of the continuity of the sign of the determinant to damping.

Figure 6.3: Illustration of the objective functions to be rooted or minimized as a function of the circular frequency ω for 3 different average wind speeds U. Each of the two roots obtained for a given wind speed defines one point of each of the two critical branches of the locus characterized by $\Re\{\det(\mathbf{J})\} = 0$.

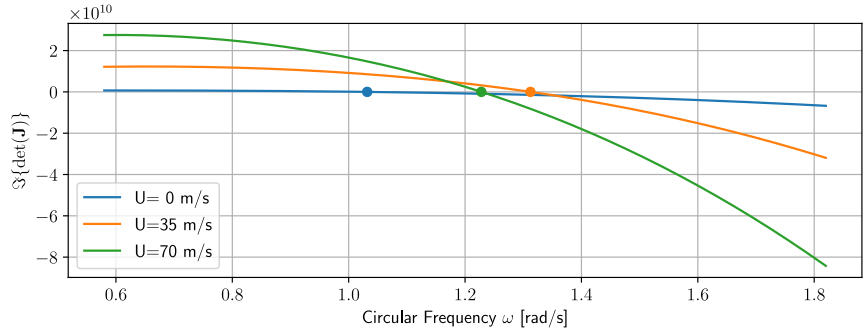

(a) Roots of the determinant using the direct determinant of $\mathbf{J}(\omega)$. Large number are involved.

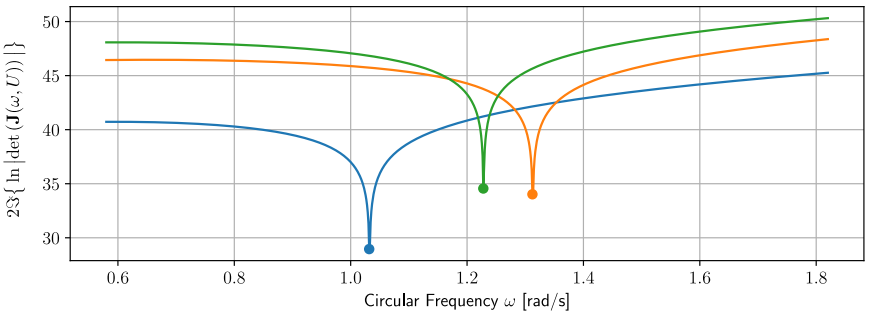

(b) Log method: Roots of the determinant using the logarithm of the determinant of $\mathbf{J}(\omega)$ versus circular frequency ω for 3 different average wind speeds U.

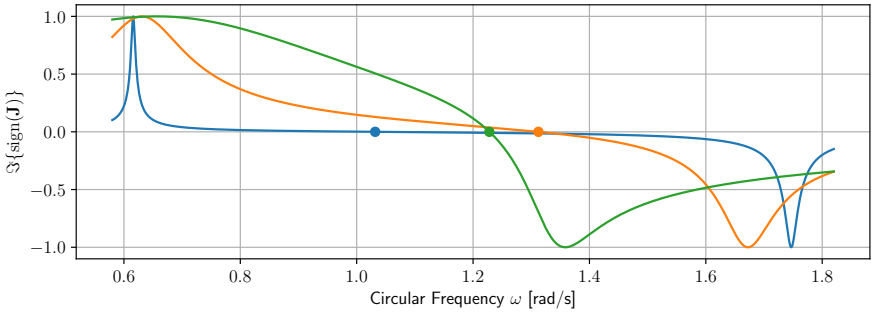

(c) Sign method: Roots of the determinant using the sign of the determinant of $\mathbf{J}(\omega)$.

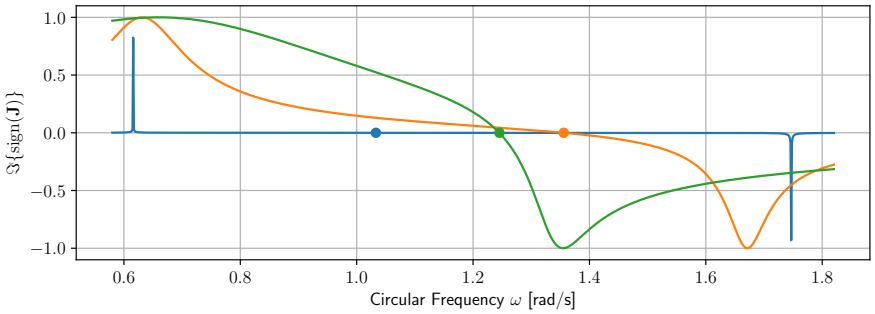

(d) Sign method: Illustration of the effect of damping on the continuity of the sign of the determinant.

Figure 6.4: Illustration of the objective functions to be rooted/minimized as a function of the circular frequency ω for 3 different average wind speeds U. The root obtained for a given wind speed defines one point of the critical locus characterized by $\Im\{\det(\mathbf{J})\} = 0$.

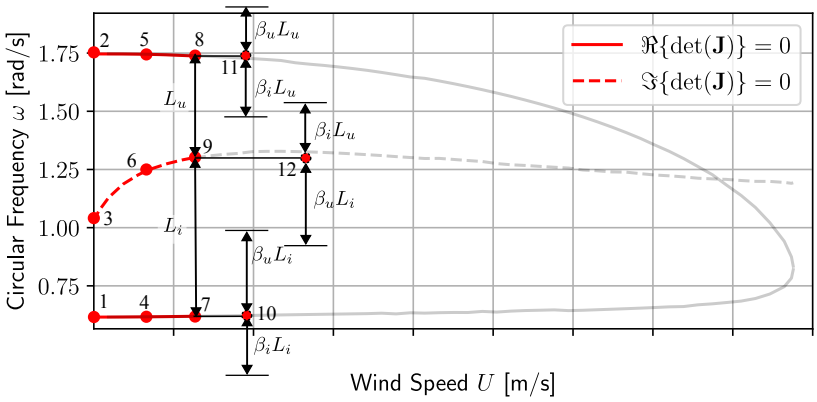

Figure 6.5: Application 1. Illustration of the dichotomic approach for determining the critical loci (without extrapolation). Definition of the intervals for determining points 10, 11 and 12.

situation improves at higher wind speeds, as the increased aeroelastic damping enhances the total net damping, smoothing out these transitions. It is then recommended to take care of possible frequency drifting of the imaginary critical loci of structures experiencing very low damping.

In the previous section, we highlighted that the bisection solver is particularly well suited for determining the critical loci. Unlike other classical root-finding algorithms, it requires the explicit definition of an interval to bracket the root, ensuring numerical robustness. While we have discussed alternative methods, the primary focus remains on demonstrating how the proposed algorithm, based on a bisection solver, systematically constructs the critical loci in a reliable and efficient manner. The methodology is illustrated for the first 12 points of the critical loci in Figure 6.5.

The process starts at wind-off, where the first two points (points 1 and 2) of each branch of $\Re\{\det(\mathbf{J}(\omega))\} = 0$ are identified as the eigenfrequencies of the damped system, given by $\omega_{d,i} = \omega_{s,i}\sqrt{1-\xi_i^2}$, neglecting any aeroelastic effects. These two points serve as bounds for the dichotomic solver, which is then used to evaluate the first point of the imaginary critical locus (point 3), systematically located between the two real branches. Assuming the objective function to be continuous and changing sign at the root, the dichotomic solver iteratively refines the interval while ensuring that the function retains opposite signs at its boundaries. This process continues until the interval width falls below a predefined threshold, ensuring convergence to the root.

Once point 3 has been obtained, the process advances to the next wind speed (points 4, 5, and 6). The second point of the lower branch (point 4) is found within an interval defined around point 1. The lower and upper bounds of this interval are defined using L_u and L_i, which represent the frequency differences between the imaginary branch and the upper and lower branches, measured at the previously determined wind speed. This interval definition is illustrated in Figure 6.5 for the determination of points 10, 11, and 12 —the wind speed corresponding to point 12 was slightly adjusted to avoid overloading the diagram. The scaling parameters β_i and β_u are used to refine the interval width and accelerate convergence, typically taking values of 1 or less. For the external branches, they may be chosen higher than 1, which seems to increase the stability of the algorithm even though slightly increasing the computational load.

From the third point of each curve (point 7) onward, an extrapolation strategy can be employed to define the search interval around a predicted point obtained via linear interpolation:

$$\omega_{(i)} = \omega_{(i-1)} + \left[\frac{\omega_{(i-1)} - \omega_{(i-2)}}{U_{(i-1)} - U_{(i-2)}}\right](U_{(i)} - U_{(i-1)}). \tag{6.17}$$

Similarly, updated intervals can be defined based on extrapolated values rather than those from the previous wind speed. For instance, when determining point 10, L_i can be taken as the difference between the extrapolated guess frequency for point 10 and the geometric mean of the extrapolated frequencies of points 10 and 11. The bounds of the imaginary branch remain unchanged, as the solutions relative to the real branches at a given wind speed are already known when solving for the imaginary branch.

This solving process is repeated step by step for increasing wind speeds until the real and imaginary critical loci have an intersection defining one critical state, or until all desired wind velocities have been covered.

The perfect superposition of the black and red curves show that both contouring and numerical approaches are in excellent agreement. The dichotomic process was tested on the direct determinant method —system (6.5)— and on the sign method —system (6.16)—, providing exactly the same results. Even though the direct use of the determinant is not recommended, it still provides convenient results as the size of the problem is reduced and no overflow issue must be feared. These two methods perform thus equally well in this application.

A possible improvement of the computational load is provided by the consideration of Brent's method, which is a nonlinear solver incorporating interval constraints. It is a hybrid algorithm that combines the robustness of the bisection method with the efficiency of the secant method and inverse quadratic interpolation [146]. By default, it attempts to maximize convergence speed using the secant method or inverse quadratic interpolation but reverts to the bisection method when necessary to ensure stability. This approach provides superior convergence performance, as illustrated in Figure 6.6, which compares the number of target function evaluations required to determine all critical loci at a given wind speed for Brent's method and the bisection method. The left bars, representing Brent's method, are on average lower by 20% than the right bars, representing the bisection method, confirming its higher efficiency. Additionally, the orange and red bars, corresponding to the determination of the real critical loci, are systematically higher than the blue and green bars, which represent the imaginary critical loci, since the number of real branches is twice that of imaginary branches. For comparison, the contour method used 25 uniformly distributed frequencies for each given wind speed to achieve similar performance. However, since the convergence criterion differs from those used in numerical methods, this comparison should be regarded as indicative rather than absolute.

It is important to note that if the presented algorithm was successfully applied to the direct formulation and the sign determinant formulation, the log formulation (6.15) is inherently incompatible with the dichotomic or Brent's solvers, as the target functions in (6.15a) and (6.15b) remain strictly positive, except perhaps very locally where they exhibit anti-peaks at the roots, see Figure 6.4(b) and 6.4(b). Consequently, solutions to (6.15a) and (6.15b) cannot be found using dichotomic solvers, since the fundamental requirement of opposite signs at the interval boundaries is not satisfied. Other solvers may still be employed, such as nonlinear root-finding methods like the secant or Newton-Raphson methods [71], or optimization-based approaches such as the Levenberg-Marquardt algorithm [143]. However, a key drawback of these methods is their reliance on gradient-based updates. In cases where steep gradients are present, they can easily escape the basin of convergence of the tracked branch and instead converge to another solution. For instance, when solving for point 8 in Figure 6.5, an overly large step size could lead the solver to converge to point 7, inadvertently switching from tracking the second mode to the first. To mitigate this risk, it is crucial to limit the iteration step size or, even better, enforce constraints on the search interval to ensure the solver remains within the desired solution branch.

6.2.2 MDOF model

The second application is the MDOF Polimi benchmark [42], introduced in Chapter 4. For this case study, only the sign and log formulations have been considered, in combination with the

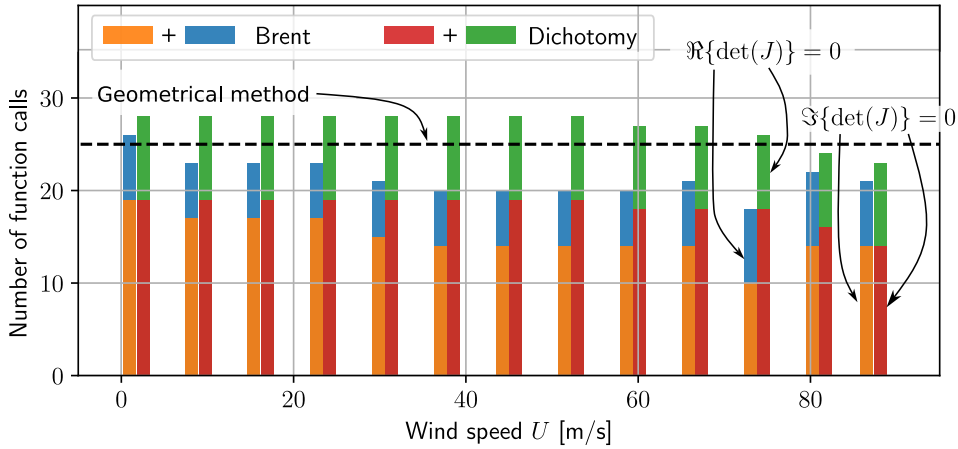

Figure 6.6: Application 1. Comparison of the number of function calls needed to get for all solutions of (6.16a) and (6.16b) for selected wind speeds from 0 to 90 m/s for 2 different methods: Brent method (left bars), and dichotomy (right bars). Lower bars: $\Re\{\text{sign}[\det(\mathbf{J}(\omega))]\} = 0$, Upper bars: $\Im\{\text{sign}[\det(\mathbf{J}(\omega))]\} = 0$. Dashed line: geometrical method

contour and dichotomic methods. The direct determinant formulation, which involves determinants with very different orders of magnitude reaching a factor of up to 10^{100}, is impractical for this example and has therefore not been considered in this analysis.

The critical maps obtained using the `contour` method and the dichotomic algorithm are presented in Figure 6.7(a) and (b). The results are quite similar excepted in two spots, where discrepancies are observed in the contour method, inducing 4 additional unreal critical states —highlighted by the blue circle in Figure 6.7(a). The performance of the contour algorithm is indeed restricted by the resolution of the initial mapping provided as input. This problem vanishes as a more dense mesh is used, but at the price of an increase in computational load. In the presented example, 50 points were used for the wind speeds, and 100 for the frequencies.

The main advantage of the dichotomic method over the `contour` method is that false positives are unlikely to occur, as an upper bound on the absolute error on each root is known at every iteration. Consequently, two curves cannot be mistaken for intersecting if their minimum distance exceeds the solver's tolerance. By appropriately setting this tolerance, one ensures that numerical artifacts do not lead to spurious intersections such as in Figure 6.7(a), thereby improving the robustness and reliability of the root-finding process.

The critical velocities are evaluated at 68.9 m/s for the dichotomic method against 69.4 m/s for the contour method, which are quite concordant. The actual critical speed is evaluated at 69.8 m/s by [42] as the average between ten values of different contributors to the benchmark.

At the critical state, the real and imaginary loci of mode 8 intersect, while the real branches of modes 8 and 9 merge. If one wishes to determine the post-critical behaviour, the dichotomic process can continue under the assumption that the disappeared mode never existed. However, if this mode later reappears at higher post-critical wind speeds, the dichotomic approach would be unable to capture it, as it has lost its trace. The same issue arises if a branch emerges at a given wind speed without being trackable from wind-off. This limitation of the dichotomic algorithm contrasts with the `contour` method, which is particularly well suited for such scenarios.

Figure 6.8 illustrates examples of target functions to be rooted or minimized to derive the critical loci presented in Figure 6.7. This case study illustrates well the reality of MDOF large-span bridge applications where a dozen of eigenfrequencies is typically distributed over a frequency range of about 0.5 Hz or less. Some eigenfrequencies are very close, such as those of modes 5 and 6 (with wind-off eigenfrequencies of 0.13317 Hz and 0.1345 Hz respectively), and modes 7 and 8 (0.1827 Hz and 0.1866 Hz respectively).

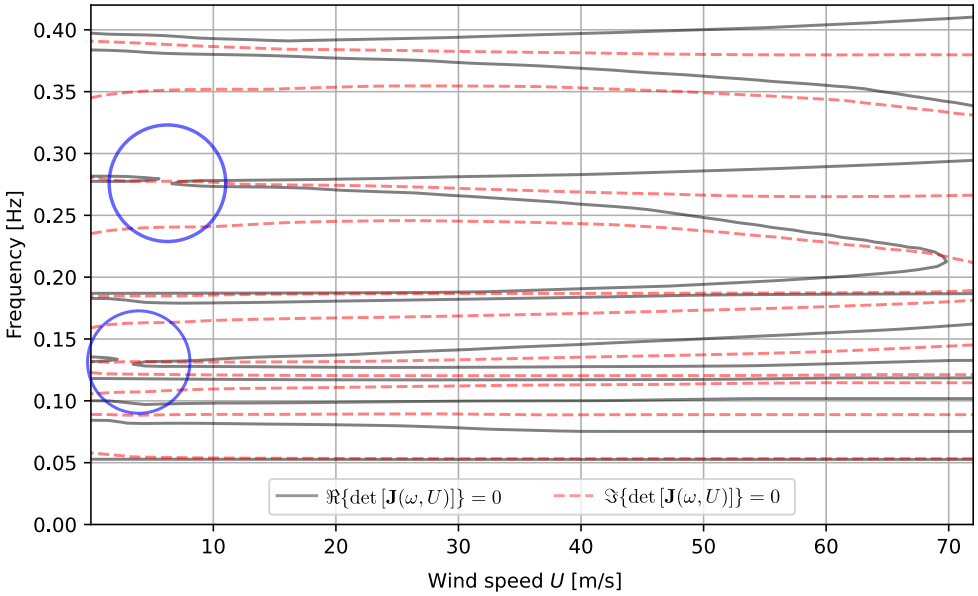

(a) `Contour` method with sign formulation (6.15)

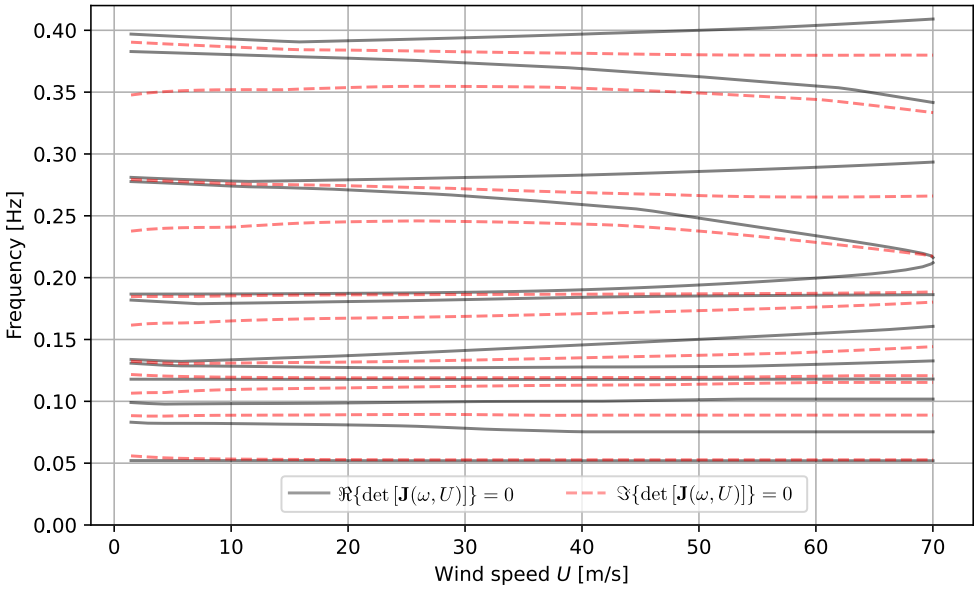

(b) Dichotomic method with sign formulation (6.15)

Figure 6.7: Application 1. Critical loci obtained for the first application using the sign method. The obtained critical velocity obtained is 69.4 m/s in (a) and 68.8 m/s in (b).

6.3 Discussion

The advantage of constructing a robust numerical scheme based on the bisection method for identifying all roots of a function, as illustrated in Figure 6.8(b), becomes particularly evident when considering the very short distances separating neighbouring roots—sometimes hundredths of a Hz. In such cases, relying on a gradient-based method to locate all local minima in Figure 6.8(c) and (d) presents a significant risk: if the iteration step is too large, the solver may inadvertently jump from one peak to another, effectively switching from one mode to another. While no apparent difficulty has been noted in the first application, this issue is particularly critical when dealing with closely spaced modes, where a poorly controlled step size can lead to incorrect mode tracking.

Additionally, the prominence of peaks is strongly influenced by damping, further complicating mode identification. While highly damped modes result in smaller gradients in the sign of the determinant—making root detection easier in the sign formulation—they in turn introduce flat peaks in the objective function of the log method, reducing the sharpness of the anti-peaks in the log-based objective function, and making it even harder to prevent unintended transitions between modes when using gradient-based optimizers. In such methods, a large iteration step can cause the algorithm to overshoot a peak and converge to an unintended root, effectively switching from one mode to another. This issue is particularly critical when peaks are closely spaced, as even a small misstep can lead to incorrect tracking. These challenges have motivated the development of a robust interval-based approach, which systematically isolates and refines each root, ensuring reliable mode tracking and preventing erroneous transitions.

Of course, the robustness of the algorithm relies entirely on the quality of the interval provided as input at each new wind speed. This fundamental task is complicated by the phenomenon of frequency drifting, typical of torsional modes, which is clearly visible when comparing the abscissae of several roots at different wind speeds (see, for instance, the root associated with the 11-th mode in Figure 6.8(b)). The only way to ensure high-quality intervals is to update them frequently enough to guarantee that each interval properly encloses a single root. Losing track of one mode is not just a loss of information: it also disrupts neighbouring intervals, which may then enclose two modes instead of one. This situation leads to two possible failure modes: at best, the algorithm simply fails when the opposite sign condition is no longer satisfied; at worst, it continues to track a neighbouring branch incorrectly, leading to a misidentification of the solution and potentially compromising the entire root-finding process.

The efficiency of the presented method is discussed in Figure 6.9, which compares the number of objective function calls for the bisection and Brent's methods applied to the sign formulation. The observations made in the previous application are transferable to this second case study. Brent's method achieves a computational saving of approximately 30%, and this reduction appears to be largely independent of wind speed. The total number of function calls is around 150 —roughly six times the average value observed in the previous application. This increase is explained by the fact that 12 branches were tracked for the real critical locus and 11 for the imaginary locus, compared to only 2 and 1, respectively, in the previous case. The factor of six is consistent with the increase in problem size, which now considers 12 modes instead of 2. This suggests that the computational cost scales proportionally with the number of modes being tracked.

The `contour` method required approximately 150 function evaluations per wind speed to achieve a similar level of accuracy as the dichotomic method, though this comparison was performed visually rather than quantitatively. While this estimate is not exact, it suggests that both the contour and dichotomic methods entail comparable computational loads.

Based on the observed performances, and good scaling up performance of the proposed algorithm, future studies should consider its deployment to complete Finite Element models (without a priori model reduction).

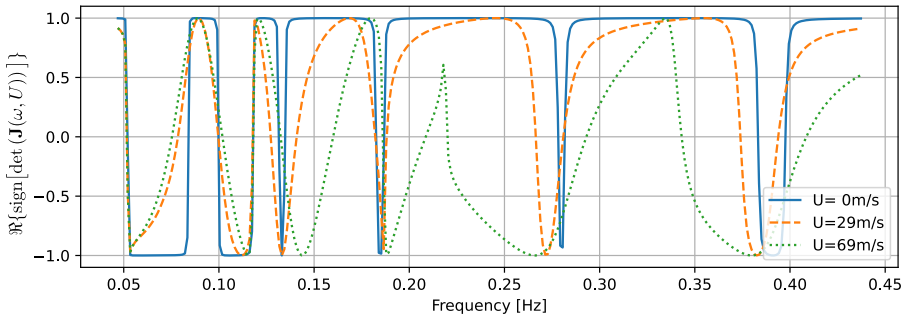

(a) Sign method: Real part of the sign of the determinant of $\mathbf{J}(\omega)$ versus frequency f for 3 different average wind speeds U.

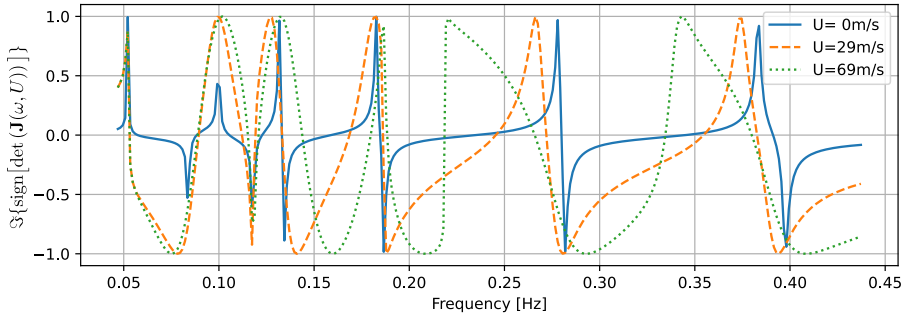

(b) Sign method: Complex part of the sign of the determinant of $\mathbf{J}(\omega)$ versus frequency f for 3 different average wind speeds U.

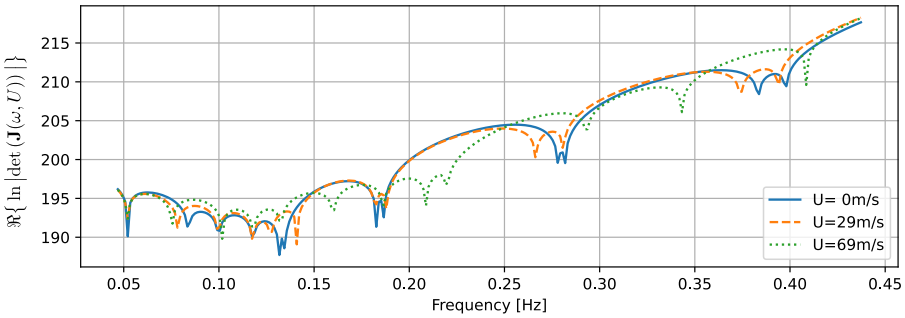

(c) Log method: Logarithm of the real part of the determinant of $\mathbf{J}(\omega)$ versus frequency f for 3 different average wind speeds U.

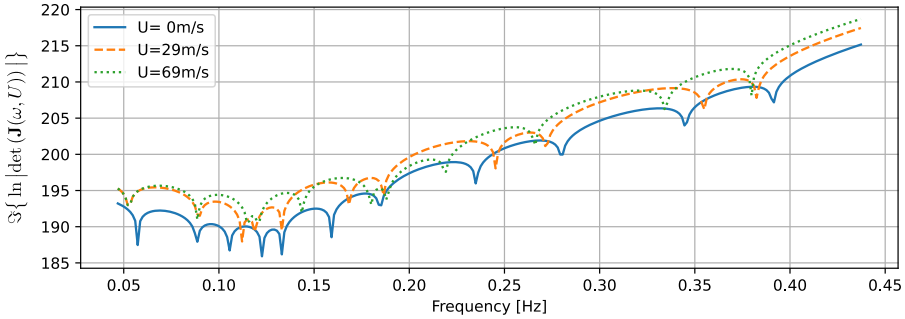

(d) Log method: Logarithm of the complex part of the determinant of $\mathbf{J}(\omega)$ versus frequency f for 3 different average wind speeds U.

Figure 6.8: Application 2. Illustration of the objective functions to be rooted or minimized as a function of the frequency f for 3 different average wind speeds U. Each of the roots obtained for a given wind speed defines one point corresponding to one point of the real or imaginary critical locus. These graphs were generated with an axis of 300 uniformly distributed points.

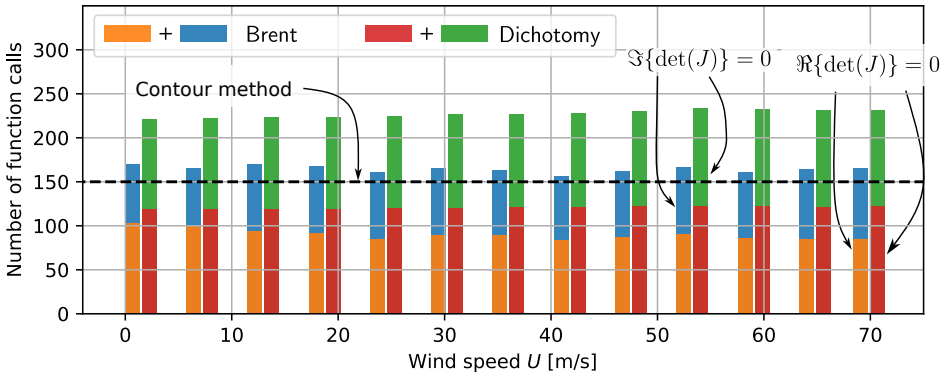

Figure 6.9: Application 2. Comparison of the number of function calls needed to get for all solutions of (6.16a) and (6.16b) for selected wind speeds from 0 to 70 m/s for 2 different methods: Brent's method (left bars), and dichotomy (right bars). Lower bars: $\Re\{\text{sign}[\det(\mathbf{J}(\omega))]\} = 0$, Upper bars: $\Im\{\text{sign}[\det(\mathbf{J}(\omega))]\} = 0$. Dashed line: geometrical method

6.4 Conclusion

The critical problem was reformulated into two distinct equations corresponding to the real and imaginary parts of the critical equation. This reformulation facilitates numerical resolution by allowing each equation to be solved separately before determining their intersection, which defines the critical state. Solving these two equations independently increases the basin of convergence, improving numerical robustness.

The direct determinant method, which relies on explicitly computing $\det(\mathbf{J}(\omega, U)) = 0$ was introduced as a straightforward approach but was found to be inconvenient due to potential numerical overflows in large matrices. To address this, alternative formulations were explored: the log formulation, which reformulates the problem as an optimization task, and the sign formulation, which transforms the determinant equation into a system of two equations with well-bounded numerical values. The latter was found to be the most convenient, particularly when combined with interval-based solvers.

This chapter proposed a systematic approach for determining critical loci, emphasizing the advantages of the bisection method. Unlike gradient-based solvers, which are prone to tracking errors when iteration steps are too large, the interval-based approach ensures consistent mode identification and prevents unintended transitions between branches. Comparisons with Brent's method demonstrated that, while it offers a computational speed-up of about 30%, the overall scaling of the method remains proportional to the number of tracked modes. The different approaches were tested on two case studies and compared with the `contour` method, which provides a viable alternative with a comparable computational cost. These findings reinforce the effectiveness of the proposed numerical strategy for accurately and efficiently mapping critical loci in aeroelastic systems.

Eventually, the algorithms presented in this chapter provide estimates of the critical wind velocity, and this quantity only. While this can be seen as a cheaper information, compared to the results of the pre-flutter analysis discussed in Chapter 5, it is always interesting to have access to an independent approach to the same problem. This offers indeed comparison and verification options.

Because of the good scaling-up performances observed for the proposed interval-based approach, its deployment to finite element software should seriously be considered.

Chapter 7

Conclusions

7.1 Purpose of the Thesis

The primary objective of this Thesis was to develop a computationally efficient method for analysing the aeroelastic response of large multi-degree-of-freedom (MDOF) structures subjected to turbulent wind excitation. Traditional buffeting analysis methods, while highly accurate, are often computationally expensive, making them impractical for early-stage design and parametric studies where frequent and iterative modifications of structural properties and aerodynamic loads occur. In the context of long-span bridge design, each design iteration requires a reassessment of the aeroelastic response, which, when performed using full-order numerical approaches, can result in excessive computation times.

Given the iterative nature of the design process, where multiple load cases, construction stages, and section configurations must be evaluated, a fast approximation method is crucial. In this context, the Eurocode provides a very simple pre-design method, based on a flat plate model corrected by empirical factors, but it is restricted to simple case studies. It does not account for the actual geometry of the deck, multi-mode interaction, or the use of custom aerodynamic data (skewed wind, custom aerodynamic section, ...). As such, its applicability is limited when dealing with modern bridge designs involving complex sections or possibly unconventional modal interactions. This thesis bridges that gap by offering a more general, yet computationally efficient, methodology that retains compatibility with early-stage design constraints while offering broader modelling capabilities. This method promises important reductions in computation time with respect to the classical design method while still capturing the essential aeroelastic effects. This efficiency allows engineers to conduct extensive parametric studies, optimizing the structure before committing to full-scale, high-fidelity simulations for final validation.

In civil engineering, aeroelastic design against flutter involves two key tasks. The first is determining the critical wind speed at which instability occurs, ensuring it remains sufficiently high relative to the design wind speed. The second is verifying that the structure meets resistance and serviceability criteria under the combined action of aeroelastic and buffeting loads. Unlike in aeronautics, where flutter is typically studied in exclusive presence of aeroelastic loads, civil engineering applications require an approach considering the combined effects of turbulence and self-excited forces introducing the buffeting excitation inherent to the turbulence of the atmospheric boundary layer on one side, and the unsteady forces resulting from the structure/fluid interaction on the other side. The presented method addresses this challenge by efficiently evaluating structural response variances across all wind speeds, providing a valuable tool for the preliminary assessment against flutter.

The full-stack methodology presented in this thesis also provides valuable estimates of key physical quantities that facilitate the interpretation, understanding and improvement of the dynamic behaviour of the studied structure. These include the separation and quantification of background and resonant response components, the evaluation of modal damping ratios, and the

estimation of intermodal correlations. Monitoring these parameters is a crucial task for engineers responsible for the iterative design and optimization of structural properties.

A particularly significant advantage of the full-chain methodology lies in its capability to perform full-order flutter analysis, thereby eliminating the need for expert-driven mode selection commonly required in reduced-order models. By addressing the full-order system from the outset, the method inherently captures all potentially relevant modal interactions. This enhances the robustness of the approach, reduces reliance on specialized expertise, and makes it more accessible to engineers without specific expertise in aeroelastic modal analysis.

7.2 The Background/Resonant decomposition

The methodology developed in this Thesis is a frequency domain approach designed to evaluate the aeroelastic response of structures across the entire wind speed range of the design envelope. It basically consists in the integration of the response Power Spectral Density (PSD) to compute the variance of the system, providing a direct estimation of the structural modal displacements. The approach is based on the Multiple Timescale Spectral Analysis (MTSA), a particularly suitable framework for analysing the response of lightly damped dynamic systems. The developed methodology can be seen as the extension of the classical background/resonant decomposition of Davenport, dedicated to buffeting excited structures. This method retains its computational efficiency in exploiting the particularities of dynamic response to carry out the analytical integrations of approximations of the response power spectral densities.

Assuming a complete separation of the dynamic timescales often observed in aeroelastic buffeting responses, the proposed methodology provides an analytical approximation of the response power spectral densities tailored to the low frequency regime (background component) and to the resonant regime (resonant component). Consisting in simple analytical expressions, each of these components is analytically integrated using the Cauchy's residue theorem to derive the response variances of the system. This analysis is repeated for each wind speed U, to derive the full aeroelastic response curve which will later be used in the structural design.

The SDOF model

Initial developments focused on single-degree-of-freedom (SDOF) systems, where the method was validated against reference solutions, demonstrating error levels below 1% in most cases. The results highlighted the method's ability to capture essential aeroelastic phenomena, such as torsional galloping and divergence instabilities, within the range of validity of the underlying assumptions. Furthermore, the computational efficiency of the MTSA approach was quantified, showing an important reduction in the number of required integration points compared to standard numerical methods using either uniformly distributed or adaptive frequency mesh to carry out the response PSD integration. One of the reasons for the important reduction in computational burden is due to the low number of integration points required, meaning a low number of establishment of the nodal forces, and their projection into the modal basis, which are known as the most resource consuming operation in the buffeting analysis. This first model served as a proof-of-concept for continuing the investigations to more develop more sophisticated models.

The 2DOF model

Building upon the SDOF formulation, the method was extended to two-degree-of-freedom (2DOF) systems to incorporate intermodal coupling effects, which play a fundamental role in the aeroelastic behaviour of real-world structures. Still invoking the separation of the background and resonant timescales, the resulting methodology enables a systematic decomposition of response variances into background and resonant contributions, each comprising multiple terms arising from the asymptotic expansion of the transfer function matrix.

Aside from the timescale separation, a key assumption in this extension was the light coupling of the system, which allowed for a linearization of the inverse transfer function, thereby eliminating the need for explicit matrix inversion. Instead, a pseudo-inverse was computed through a sequence of uncoupled problems, each of which could be analysed using simple analytical expressions. This assumption significantly reduced computational complexity while preserving accuracy within the range of weakly coupled modal interactions. The importance of modal coupling was quantified using the diagonality index, a scalar indicator derived from the spectral radius of the exact dynamic flexibility matrix. This index measures the strength of modal coupling and can be interpreted as an indicator of the singularity of the impedance matrix —similar in spirit to the condition number used in linear algebra.

Due to the light coupling assumption, the proposed method is restricted to a modal analysis framework. This aspect is fundamental to formulating the equations of motion in a form that is as diagonal as possible. The inclusion of self-excited forces introduces several complications that hinder the diagonalization typically achieved in classical structural dynamics. These include the asymmetry of the aeroelastic matrices, their dependence on frequency and wind speed, and the non-proportional nature of the damping matrix. As a result, perfect diagonalization of the dynamic system is not possible, regardless of the modal basis considered.

To mitigate this and achieve an almost diagonal form, several modal bases were explored, categorized into wind-off and wind-on formulations. The wind-off basis uses eigenmodes computed in the absence of aeroelastic loads, while the wind-on basis incorporates aeroelastic effects by computing eigenmodes at a specified wind speed. Furthermore, a distinction was made between damped and undamped modal bases: undamped bases yield real-valued eigenmodes, while damped formulations produce complex-valued modes, solution of the damped eigenvalue problem. Although the developments were initially restricted to real-valued modes, the generalization to complex modal bases was deferred to the MDOF chapter.

The methodology was validated using a pitch-plunge model of the Storebælt Bridge. The results demonstrated a high level of accuracy in estimating response covariances and correlation coefficients, with errors on the nodal about 1% or 2% when the diagonality index was sufficiently low. Moreover, the method effectively reconstructed physical displacements at critical deck locations using both Complete Quadratic Combination (CQC) and Square Root of the Sum of Squares (SRSS) techniques. In reason of the small computational burden associated with the evaluation of the full modal covariance matrix, the CQC nodal recombination could be carried out instead of a SRSS recombination, offering a much better representation of the nodal variance for importantly coupled responses, as long as a small diagonality index was observed.

Beyond accuracy, the study also highlighted the influence of modal basis selection on method performance. The results indicated that when the diagonality index exceeded 25%, significant deviations from the exact solution occurred. Additionally, wind-on modal bases were shown to reduce the diagonality index by a factor of three near singularities, significantly improving approximation quality.

7.2.1 The MDOF model

The final stage of this Thesis addressed the application of the MTSA methodology to large MDOF aeroelastic systems, where the dimensionality of the problem and the presence of modal coupling significantly complicate the aeroelastic response analysis.

A first advancement introduced was the generalization of the MTSA method to accommodate complex modal forces, enabling the use of wind-on modal bases, made up of complex mode shapes. Also left and right eigenvectors have been considered instead of right eigenvectors exclusively. These choices were shown to systematically improve the diagonality of the dynamic flexibility matrix, which we know to be a prerequisite for the presented methodology. The resulting gains in accuracy, often reducing errors to a few percent, were particularly significant near instability regions, where the aeroelastic coupling becomes dominant. In contrast, the wind-off modal basis,

although simpler and computationally lighter, led to substantial errors in the vicinity of critical wind speeds and should only be considered for structures subjected to unsteady loads having limited influence. At the immediate proximity of the singularity, none of the modal bases is able to keep the diagonality index sufficiently low to apply the MTSA method.

Beyond the modal basis selection, the flexibility matrix formulation was also shown to be a decisive factor in the accuracy of the response predictions. Several formulations have been proposed. A gradient-free formulation, although computationally appealing, resulted in large discrepancies and was found unsuitable in all tested configurations. The inclusion of aeroelastic gradients in the impedance matrix was essential to achieve a faithful representation of the resonant contributions. Between the linear and quadratic formulations, the former was generally preferred for its robustness and numerical stability. Although the quadratic formulation was initially motivated by a theoretical improvement in the asymptotic decay of the PSD components, the observed benefits remained marginal in terms of variance estimation, particularly due to the negligible role of cross-contributions between non-identical modes. On the contrary, in the case of complex modal basis, the quadratic formulation sometimes led to asymmetric representation of the response PSD, possibly resulting in significantly underestimating the contributions of the negative frequency energy peaks. Its use along with complex wind-on modal matrices is therefore not recommended.

These findings confirm the relevance and applicability of the MTSA method for large aeroelastic systems, provided that care is taken to (i) pre-computing the diagonality index and (ii) verifying the separation of the timescales. When these aspects are appropriately treated, the MTSA approach provides a reliable and efficient alternative to full-order buffeting analysis, allowing for rapid evaluations of aeroelastic response variances across the wind speed envelope. This capability is particularly valuable for early-stage design iterations and parametric studies, where computational efficiency and modelling flexibility are essential.

A preliminary evaluation of the computational benefits provided by the MTSA method was proposed in the MDOF Chapter. While a detailed benchmark remains to be conducted, the initial estimates demonstrated a substantial reduction in computational demand—particularly in the number of costly modal projections—by a factor ranging from 4 to 6 compared to classical frequency-domain integration. These gains are scalable with respect to the number of wind speeds considered, and therefore extend naturally to the complete aeroelastic response curve. Although the MTSA method requires a pre-flutter analysis to track modal properties with wind speed, this step is equally necessary in conventional flutter analysis and should not be considered an additional cost. These results confirm that the MTSA framework delivers on its promise of enabling fast yet accurate aeroelastic design tools for large MDOF systems, particularly suited for early-stage iterations and parametric exploration.

7.3 The global solution for flutter analysis

The overarching goal of this project was to develop a full-stack methodology for the aeroelastic design of bridges at the early stages of development. While the core of this solution is the MTSA method, presented in Part 1 of the Thesis, it has been integrated into a broader toolchain designed to support preliminary computations. To this end, two complementary tools have been developed.

The critical problem solver

The first tool is dedicated to determining the critical velocities. Although the buffeting response, which includes both self-excited and turbulent aerodynamic forces, already provides a comprehensive view of the aeroelastic instability, identifying the position of the instability remains a valuable addition. For this purpose, Chapter 6 introduced an algorithm specifically designed

to compute critical wind speeds only. Although not strictly necessary for applying the MTSA method, this tool provides useful insight into the stability margins of the structure and supports early-stage design verification. The method is based on a reformulation of the flutter condition into two scalar equations corresponding to the real and imaginary parts of the determinant of the system's impedance matrix. This decomposition not only offers a clearer geometric interpretation of the critical state, but also facilitates numerical resolution by improving robustness and convergence.

Several formulations were examined in this context. The direct determinant method, which consists in solving $\det(\mathbf{J}(\omega, U)) = 0$ explicitly, was found to be straightforward but prone to numerical difficulties, especially in large-scale systems. To overcome this, alternative strategies were explored. Among them, the sign-based formulation offered the best compromise between robustness and efficiency, particularly when embedded in an interval-based framework. By working with well-scaled quantities, this approach avoids the numerical overflow issues associated with large determinants and ensures consistent mode tracking across the solution domain.

A systematic bisection approach was proposed for solving the resulting equations, ensuring high reliability even in scenarios involving complex root trajectories and closely spaced modes. Compared to classical gradient-based algorithms, the interval-based solver demonstrated improved robustness against tracking errors and unintended branch switching. Brent's method and the classical dichotomy were also considered, with Brent's method reducing the computational load by 20% to 30%. The `contour` method emerged as a viable alternative, offering comparable performance. Together, these developments form a solid and versatile framework for mapping critical loci across a range of wind speeds and system configurations, thereby complementing the buffeting analysis.

The pre-flutter analysis

The second tool in the proposed aeroelastic analysis framework is dedicated to the pre-computation of key inputs required by the MTSA method. Regardless of the chosen modal basis, a precise knowledge of the evolution of the system's eigenvalues with wind speed is essential for formulating the approximation of the response power spectral density (PSD). Furthermore, if a wind-on modal basis is used, the method also requires the determination of the subcritical modal properties— namely the left and right eigenvectors— across the range of interest. These elements are crucial for building an accurate dynamic flexibility matrix and ensuring the modal decoupling needed for efficient variance evaluation.

To this end, Chapter 5 introduced an arc-length continuation method, providing a systematic and globally convergent strategy to track the evolution of the system's modal characteristics with increasing wind speed. The continuation algorithm was designed to simultaneously fulfil three objectives: (i) identify pre-flutter states to assess the structure's stability, (ii) provide input data for the background/resonant decomposition method, and (iii) construct the wind-on modal basis by computing the complex mode shapes of the damped aeroelastic system. By unifying these tasks into a single framework, the algorithm performs all preliminary steps required for the complete application of the MTSA methodology introduced in Chapters 2, 3, and 4.

The principle is based on solving a nonlinear generalized eigenvalue problem at a given wind speed U, reformulated as a non-homogeneous system by incorporating a normalization condition. A continuity equation is added to guide the tracking process, allowing for robust and consistent progression from wind-off conditions toward instability. The process is governed by a hypersphere-based step size control, ensuring adaptive resolution in regions of high sensitivity.

A key advantage of the proposed algorithm lies in its mode-by-mode formulation, which allows each mode to be tracked independently. This eliminates the risk of undesired mode swapping and enables the use of a custom wind speed mesh for each mode, thereby optimizing computational resources. Preventing mode swapping was one of the initial motivations for exploring this solution: in the context of the MTSA method, inverting two modes would lead to erroneous

estimations of the modal covariances, potentially compromising the accuracy of the response prediction.

This continuation strategy was shown to be suitable for flutter analysis, particularly in capturing localized variations in modal properties that might be overlooked by uniformly spaced wind speed meshes as used in classical p-k method. By adjusting the sphere radius and scaling parameters, the user can ensure reliable tracking even near bifurcations or rapid property changes. This algorithm handled the flutter problem reliably, even in challenging regimes near instability and beyond, where the p-k method occasionally failed due to mode swapping. These qualities make the continuation approach a powerful and reliable tool for pre-computing modal data in complex MDOF aeroelastic systems, as a preprocessor of the MTSA method.

7.4 A complete toolchain solution for flutter pre-design

7.5 Perspectives

Several avenues remain open for further refinement and assessment of the MTSA methodology. First, in order to definitively assess the relevance of higher-order representations, the implementation of a real quadratic formulation that includes second-order derivatives of the aeroelastic matrices with respect to frequency should be considered. While preliminary results have shown limited gains from such approaches, a rigorous implementation of a real quadratic formulation of the flexibility could be envisaged before this direction can be conclusively closed.

Second, the comparison of the computational efficiency between the MTSA method and classical buffeting analysis was, in the present work, limited to a comparison of the number of integration points and modal projection required. For a truly fair comparison in terms of time consumption, both methods should be implemented using the same programming language and numerical libraries. Moreover, the implementations should be optimized, stripped of any unnecessary intermediate steps or overhead, so that the execution time reflects only the essential operations required by each methodology. Due to time constraints, the implementation in a unified framework could not be carried out in this study but would be a valuable addition for better circumscribe the computational capabilities of the MTSA method.

Finally, any performance comparison should also account for the computational cost of preprocessing steps, particularly the determination of modal properties. In the case of the MTSA method, this cost is non-negligible and largely depends on the chosen approach (to be noted though, that this result is a fundamental deliverable that the designer must provide anyway). To this end, a dedicated benchmark comparing the runtime of the proposed continuation method with the classical p-k algorithm would provide useful insights. Since p-k methods are typically implemented in low-level compiled languages, a comparable implementation of the continuation algorithm would be required to ensure a meaningful and unbiased comparison.

Bibliography

[1] J. Heremans, A. Mayou, and V. Denoël, "Perspectives on the acceleration of the numerical assessment of flutter and buffeting response of bridge decks," pp. 5201–5213, 01 2021.

[2] J. C. Kaimal and J. J. Finnigan, *Atmospheric Boundary Layer Flows: Their Structure and Measurement*. Oxford University Press, 03 1994.

[3] N. Isyumov, "Alan G. Davenport's mark on wind engineering," *Journal of Wind Engineering and Industrial Aerodynamics*, vol. 104-106, pp. 12–24, 2012. 13th International Conference on Wind Engineering.

[4] M. Shinozuka and G. Deodatis, "Simulation of stochastic processes by spectral representation," *Applied Mechanics Reviews*, vol. 44, pp. 191–204, 04 1991.

[5] A. G. Davenport, "Wind effects on buildings and structures," in *Proceedings of the Conference "Wind Effects on Buildings and Structures"*, pp. 54–111, HMSO, 1965.

[6] *EN 1992-1-4 Eurocode 1: Actions on structures - Part 1-4: General actions - Wind actions*, (Bruxelles), CEN, 2005.

[7] A. G. Davenport, "The spectrum of horizontal gustiness near the ground in high winds," *Quarterly Journal of the Royal Meteorological Society*, vol. 87, no. 372, pp. 194–211, 1961.

[8] J. C. Kaimal, J. C. Wyngaard, Y. Izumi, and O. R. Coté, "Spectral characteristics of surface-layer turbulence," *Quarterly Journal of the Royal Meteorological Society*, vol. 98, no. 417, pp. 563–589, 1972.

[9] J. L. Lumley and H. A. Panofsky, *The structure of Atmospheric Turbulence*. John Wiley and Sons, 1964.

[10] H. A. Panofsky and J. A. Dutton, *Atmospheric turbulence. Models and methods for engineering applications*. 1984.

[11] L. Caracoglia and N. P. Jones, "Time domain vs. frequency domain characterisation of aeroelastic forces for bridge sections," *Journal of Wind Engineering and Industrial Aerodynamics*, 2002.

[12] F. W. Diederich and J. A. Drischler, *Effect of spanwise variations in gust intensity on the lift due to atmospheric turbulence*. 1957.

[13] W. Heisenberg, "On the theory of statistical and isotropic turbulence," *Proceedings of the Royal Society of London. Series A, Mathematical and Physical Sciences*, vol. 195, no. 1042, pp. 402–406, 1948.

[14] A. N. Kolmogorov, V. Levin, J. C. R. Hunt, O. M. Phillips, and D. Williams, "The local structure of turbulence in incompressible viscous fluid for very large reynolds numbers," *Proceedings of the Royal Society of London. Series A: Mathematical and Physical Sciences*, vol. 434, no. 1890, pp. 9–13, 1991.

[15] G. Solari and G. Piccardo, "Probabilistic 3-d turbulence modeling for gust buffeting of structures," *Probabilistic Engineering Mechanics*, vol. 16, no. 1, pp. 73–86, 2001.

[16] F. Farquharson, *Aerodynamic Stability of Suspension Bridges with Special Reference to the Tacoma Narrows Bridge: Investigations prior to oct. 1941.* No. vol. 1 in Bulletin, University of Washington Engineering Experiment Station, 1950.

[17] *Wind Storms and Cable-Supported Bridges*, ch. 1, pp. 1–23. John Wiley & Sons, Ltd, 2013.

[18] B. of Engineers Appointed to Report on the Failure of the Tacoma Narrows Bridge, O. Ammann, and U. S. F. W. Agency, *The Failure of the Tacoma Narrows Bridge: A Report to the Honorable John M. Carmody, Administrator, Federal Works Agency, Washington, D.C. Board of Engineers: Othmar H. Ammann, Theodore Von Kármán [and] Glenn B. Woodruff.* 1941.

[19] G. K. Batchelor, *An Introduction to Fluid Dynamics.* Cambridge Mathematical Library, Cambridge University Press, 2000.

[20] F. M. White, *Fluid mechanics.* Mcgraw-Hill series in mechanical engineering, New York, NY: McGraw-Hill, 6th ed ed., 2009.

[21] F. Ricciardelli, E. T. de Grenet, and H. Hangan, "Pressure distribution, aerodynamic forces and dynamic response of box bridge sections," *Journal of Wind Engineering and Industrial Aerodynamics*, vol. 90, no. 10, pp. 1135–1150, 2002. 3rd European-African Conference on Wind Engineering.

[22] K. Kwok, X. Qin, C. Fok, and P. Hitchcock, "Wind-induced pressures around a sectional twin-deck bridge model: Effects of gap-width on the aerodynamic forces and vortex shedding mechanisms," *Journal of Wind Engineering and Industrial Aerodynamics*, vol. 110, pp. 50–61, 2012.

[23] M. Belloli, F. Fossati, S. Giappino, and S. Muggiasca, "Vortex induced vibrations of a bridge deck: Dynamic response and surface pressure distribution," *Journal of Wind Engineering and Industrial Aerodynamics*, vol. 133, pp. 160–168, 2014.

[24] J. H. Ferziger and M. Perić, *Computational Methods for Fluid Dynamics.* Berlin, Germany: Springer, 2002.

[25] J. Katz and A. Plotkin, "Low-speed aerodynamics: From wing theory to panel methods," *Cambridge Aerospace Series*, vol. 13, pp. 263–278, 2001. Focuses on discrete vortex methods for aerodynamic coefficients.

[26] D. Rocchi, T. Argentini, and M. Sbrosi, "Pressure distribution and global forces on a bridge deck section: Experimental and cfd analysis of static aerodynamic forces," *Journal of Bridge Engineering*, vol. 20, no. 9, p. 04014097, 2015.

[27] H. Schlichting and K. Gersten, *Boundary-Layer Theory.* 01 2017.

[28] *Bluff Body Aerodynamics*, ch. 4, pp. 73–104. John Wiley & Sons, Ltd, 2019.

[29] W. R. Sears, "Some aspects of non-stationary airfoil theory and its practical application," *Journal of the Aeronautical Sciences*, vol. 8, no. 3, pp. 104–108, 1941.

[30] H. W. Liepmann, "On the application of statistical concepts to the buffeting problem," *Journal of the Aeronautical Sciences*, vol. 19, no. 12, pp. 793–800, 1952.

[31] P. W. Bearman, "Vortex shedding from oscillating bluff bodies," *Annual Review of Fluid Mechanics*, vol. 16, pp. 195–222, 1984.

[32] M. Mastumoto, "Vortex shedding of bluff bodies: A review," *Journal of Fluids and Structures*, vol. 13, no. 7, pp. 791–811, 1999.

[33] S. Komatsu and H. Kobayashi, "Vortex-induced oscillation of bluff cylinders," *Journal of Wind Engineering and Industrial Aerodynamics*, vol. 6, no. 3, pp. 335–362, 1980.

[34] T. Abbas, I. Kavrakov, and G. Morgenthal, "Methods for flutter stability analysis of long-span bridges: A review," *Proceedings of the Institution of Civil Engineers: Bridge Engineering*, vol. 170, no. 4, pp. 271–310, 2017. Cited by: 30; All Open Access, Bronze Open Access.

[35] C. Cremona and F. Jean-Claude, *Comportement au vent des ponts*. 01 2002.

[36] R. H. Scanlan, "Bridge flutter derivatives at vortex lock-in," *Journal of Structural Engineering*, vol. 124, no. 4, pp. 450–458, 1998.

[37] R. H. Scanlan, "Amplitude and turbulence effects on bridge flutter derivatives," *Journal of Structural Engineering*, vol. 123, no. 2, pp. 232–236, 1997.

[38] A. Jain, N. P. Jones, and R. H. Scanlan, "Coupled flutter and buffeting analysis of long-span bridges," *Journal of Structural Engineering*, vol. 122, no. 7, pp. 716–725, 1996.

[39] R. H. Scanlan, "Problematics in formulation of wind-force models for bridge decks," *Journal of Engineering Mechanics*, vol. 119, no. 7, pp. 1353–1375, 1993.

[40] S. Cammelli, A. Bagnara, and J. G. Navarro, "Viv-galloping interaction of the deck of a footbridge with solid parapets," *Procedia Engineering*, vol. 199, pp. 1290–1295, 2017. X International Conference on Structural Dynamics, EURODYN 2017.

[41] R. H. Scanlan, "Bridge flutter derivatives at vortex lock-in," *Journal of Structural Engineering*, vol. 124, no. 4, pp. 450–458, 1998.

[42] G. Diana, S. Stoyanoff, A. Allsop, L. Amerio, M. S. Andersen, T. Argentini, F. Calamelli, M. C. Montoya, V. de Ville de Goyet, S. Hernandez, J. A. Jurado, I. Kavrakov, G. Larose, A. Larsen, G. Morgenthal, D. Rocchi, M. N. Svendsen, and T. Wu, "Iabse task group 3.1 benchmark results. numerical full bridge stability and buffeting simulations," *Structural Engineering International*, vol. 33, no. 4, pp. 623–634, 2023.

[43] V. Denoël, "Polynomial approximation of aerodynamic coefficients based on the statistical description of the wind incidence," *Probabilistic Engineering Mechanics*, vol. 24, no. 2, pp. 179–189, 2009.

[44] M. Esposito Marzino and V. Denoël, "Non-gaussian buffeting analysis of large structures by means of a proper orthogonal decomposition," *Journal of Wind Engineering and Industrial Aerodynamics*, vol. 242, November 2023.

[45] V. Denoël and H. Degée, "Influence of the non-linearity of the aerodynamic coefficients on the skewness of the buffeting drag force," *Wind and Structures*, vol. 9, no. 6, 2006.

[46] G. Diana, S. Stoyanoff, K. Aas-Jakobsen, A. Allsop, M. Andersen, T. Argentini, M. C. Montoya, S. Hernandez, J. A. Jurado, H. Katsuchi, I. Kavrakov, H.-K. Kim, G. Larose, Allan, G. Morgenthal, O. Øiseth, S. Omarini, D. Rocchi, M. Svendsen, and T. Wu, "Iabse task group 3.1 benchmark results. part 1: Numerical analysis of a two-degree-of-freedom bridge deck section based on analytical aerodynamics," *Structural Engineering International*, vol. 0, no. 0, pp. 1–10, 2019.

[47] H. Wagner, "Über die entstehung des dynamischen auftriebes von tragflügeln," *ZAMM - Journal of Applied Mathematics and Mechanics / Zeitschrift für Angewandte Mathematik und Mechanik*, vol. 5, no. 1, pp. 17–35, 1925.

[48] K. L. Roger, "Airplane math modeling methods for active control design," 1977.

[49] M. Karpel, "Design for active flutter suppression and gust alleviation using state-space aeroelastic modeling," *Journal of Aircraft*, vol. 19, no. 3, pp. 221–227, 1982.

[50] R. H. Scanlan, J.-G. Béliveau, and K. S. Budlong, "Indicial aerodynamic functions for bridge decks," *Journal of the Engineering Mechanics Division*, vol. 100, no. 4, pp. 657–672, 1974.

[51] L. Caracoglia and N. Jones, "Time domain vs. frequency domain characterization of aeroelastic forces for bridge deck sections," *Journal of Wind Engineering and Industrial Aerodynamics*, vol. 91, no. 3, pp. 371–402, 2003.

[52] L. Caracoglia and N. Jones, "A methodology for the experimental extraction of indicial functions for streamlined and bluff deck sections," *Journal of Wind Engineering and Industrial Aerodynamics*, vol. 91, no. 5, pp. 609–636, 2003.

[53] A. G. Chowdhury and P. P. Sarkar, "Experimental identification of rational function coefficients for time-domain flutter analysis," *Engineering Structures*, vol. 27, no. 9, pp. 1349–1364, 2005.

[54] E. Jonsson, C. Riso, C. A. Lupp, C. E. S. Cesnik, J. R. R. A. Martins, and B. I. Epureanu, "Flutter and post-flutter constraints in aircraft design optimization," *Progress in Aerospace Sciences*, vol. 109, p. 100537, 2019.

[55] G. Dimitriadis, *Introduction to Nonlinear Aeroelasticity*. Wiley, 2017.

[56] G. Dimitriadis, *Unsteady Aerodynamics: Potential and Vortex Methods*. John Wiley & Sons, Ltd.

[57] T. Theodorsen, "General theory of aerodynamic instability and the mecanism of flutter.," *NACA Report*, vol. 496, 1935.

[58] Y. Tamura and A. Kareem, *Advanced Structural Wind Engineering*. 01 2013.

[59] R. H. Scanlan and J. J. Tomko, "Airfoil and bridge deck flutter derivatives," *Journal of the Engineering Mechanics Division*, vol. 97, no. 6, pp. 1717–1737, 1971.

[60] E. Albano and W. P. Rodden, "A doublet-lattice method for calculating lift distributions on oscillating surfaces in subsonic flows," *AIAA Journal*, vol. 7, no. 2, pp. 279–285, 1969.

[61] Z. Technology, *ZAERO Ver. 7.2: Theoretical Manual*. AZ, Scottsdale, 2004.

[62] I. E. Garrick, "On some reciprocal relations in the theory of nonstationary flows," 1938.

[63] R. T. Jones, "Operational treatment of the nonuniform-lift theory in airplane dynamics," tech. rep., NASA Langley Research Center Hampton (United States), 1938.

[64] T. Miyata and H. Yamada, "Coupled flutter estimate of a suspension bridge," *Journal of Wind Engineering and Industrial Aerodynamics*, vol. 33, no. 1-2, pp. 341–348, 1990.

[65] *EN 1990:2002 Eurocode 0: Basis of structural design*, (Bruxelles), CEN, 2002.

[66] N. M. Newmark, "A method of computation for structural dynamics," *Journal of the Engineering Mechanics Division*, vol. 85, no. 3, pp. 67–94, 1959.

[67] J. Butcher, "A history of runge-kutta methods," *Applied Numerical Mathematics*, vol. 20, no. 3, pp. 247–260, 1996.

[68] J.-G. Beliveau, R. Vaicaitis, and M. Shinozuka, "Motion of suspension bridge subject to wind loads," *Journal of the Structural Division*, vol. 103, no. 6, pp. 1189–1205, 1977.

[69] Z. Zhang, Z. Chen, Y. Cai, and Y. Ge, "Indicial functions for bridge aeroelastic forces and time-domain flutter analysis," *Journal of Bridge Engineering*, vol. 16, no. 4, pp. 546–557, 2011.

[70] A. Papoulis, *Probability and statistics*. USA: Prentice-Hall, Inc., 1990.

[71] W. H. Press, S. A. Teukolsky, W. T. Vetterling, and B. P. Flannery, *Numerical Recipes in C*. Cambridge, USA: Cambridge University Press, second ed., 1992.

[72] V. Denoël, "Quantifying complexity in the envelope reconstruction problem: Review, comparison and a detailed illustration," *Journal of Wind Engineering and Industrial Aerodynamics*, vol. 254, p. 105879, 2024.

[73] G. Warburton, "Dynamics of structures, by ray w. clough and joseph penzien, mcgraw-hill, new york, 1993. no. of pages: 738. isbn 0-07-011394-7," 1995.

[74] S. S. Rao, *Mechanical vibrations*. Wokingham, Don Mills, Ont: Addison-Wesley, 1995.

[75] M. Géradin and D. J. Rixen, *Mechanical vibrations: theory and application to structural dynamics*. John Wiley & Sons, 2015.

[76] H. Katsuchi, N. Jones, R. Scanlan, and H. Akiyama, "Multi-mode flutter and buffeting analysis of the Akashi-Kaikyo bridge," *Journal of Wind Engineering and Industrial Aerodynamics*, vol. 77-78, pp. 431–441, 1998.

[77] X. Hua and Z. Chen, "Full-order and multimode flutter analysis using ansys," *Finite Elements in Analysis and Design*, vol. 44, no. 9, pp. 537–551, 2008.

[78] Q. Ding, A. Chen, and H. Xiang, "Coupled flutter analysis of long-span bridges by multimode and full-order approaches," *Journal of Wind Engineering and Industrial Aerodynamics*, vol. 90, no. 12, pp. 1981–1993, 2002. Fifth Asia-Pacific Conference on Wind Engineering.

[79] V. Denoël and H. Degée, "Asymptotic expansion of slightly coupled modal dynamic transfer functions," *Journal of Sound and Vibration - J SOUND VIB*, vol. 328, pp. 1–8, 11 2009.

[80] B. M. da Costa, J. Wang, J. B. Jakobsen, O. A. Øiseth, and J. Þ. Snæbjörnsson, "Bridge buffeting by skew winds: A revised theory," *Journal of Wind Engineering and Industrial Aerodynamics*, vol. 220, p. 104806, 2022.

[81] A. G., "Gust loading factors," *Journal of the Structural Division*, vol. 93, no. 3, pp. 11–34, 1967.

[82] V. Denoël, "Multiple timescale spectral analysis," *Probabilistic Engineering Mechanics*, vol. 39, pp. 69–86, 2015.

[83] V. Denoël, "On the background and biresonant components of the random response of single degree-of-freedom systems under non-gaussian random loading," *Engineering Structures*, vol. 33, no. 8, pp. 2271–2283, 2011.

[84] V. Denoël and L. Carassale, "Response of an oscillator to a random quadratic velocity-feedback loading," *Journal of Wind Engineering and Industrial Aerodynamics*, vol. 147, pp. 330–344, 2015.

[85] M. Geuzaine, A. Fenerci, O. Øiseth, and V. Denoël, "Multiple timescale spectral analysis of floating structures subjected to hydrodynamic loads," *Journal of Engineering Mechanics*, vol. 149, no. 3, p. 04023006, 2023.

[86] M. Gu and X. yi Zhou, "An approximation method for resonant response with coupling modes of structures under wind action," *Journal of Wind Engineering and Industrial Aerodynamics*, vol. 97, no. 11, pp. 573–580, 2009.

[87] E. J. Hinch, *Perturbation Methods*. Cambridge Texts in Applied Mathematics, Cambridge University Press, 1991.

[88] A. G. Davenport, "The response of slender, line-like structures to a gusty wind.," *Proceedings of the Institution of Civil Engineers*, vol. 23, no. 3, pp. 389–408, 1962.

[89] T. Canor, L. Caracoglia, and V. Denoël, "Application of random eigenvalue analysis to assess bridge flutter probability," *Journal of Wind Engineering and Industrial Aerodynamics*, vol. 140, pp. 79–86, 2015.

[90] A. Larsen, "Aerodynamics of the tacoma narrows bridge - 60 years later," *Structural Engineering International*, vol. 10, no. 4, pp. 243–248, 2000.

[91] A. Larsen, "Advances in aeroelastic analyses of suspension and cable-stayed bridges," *Journal of Wind Engineering and Industrial Aerodynamics*, vol. 74-76, pp. 73–90, 1998.

[92] R. Jones, "The unsteady lift on a wing of finite aspect ratio," *NACA Technical Report 681*, 1940.

[93] T. Andrianne and V. de Ville de Goyet, "Mitigation of the torsional flutter phenomenon of bridge deck section during a lifting phase," in *8th International Colloquium on Bluff Body Aerodynamics and Application*, 2016.

[94] S. Pindado, J. Meseguer, and S. Franchini, "The influence of the section shape of box-girder decks on the steady aerodynamic yawing moment of double cantilever bridges under construction," *Journal of wind engineering and industrial aerodynamics*, vol. 93, no. 7, pp. 547–555, 2005.

[95] X. Chen, M. Matsumoto, and A. Kareem, "Aerodynamic coupling effects on flutter and buffeting of bridges," *Journal of Engineering Mechanics*, vol. 126, no. 1, pp. 17–26, 2000.

[96] V. Denoël, "Estimation of modal correlation coefficients from background and resonant responses," *Structural Engineering and Mechanics: an International Journal*, vol. 32, no. 6, 2009.

[97] H. Katsuchi, N. P. Jones, and R. H. Scanlan, "Multimode coupled flutter and buffeting analysis of the Akashi-Kaikyo bridge," *Journal of Structural Engineering*, vol. 125, no. 1, pp. 60–70, 1999.

[98] W. H. Press, S. A. Teukolsky, W. T. Vetterling, and B. P. Flannery, *Numerical Recipes in C*. Cambridge, USA: Cambridge University Press, second ed., 1992.

[99] L. Meirovitch, *Elements of vibration analysis*. New York, NY: McGraw-Hill, second ed., 1986.

[100] F. Tisseur and K. Meerbergen, "The quadratic eigenvalue problem," *SIAM Review*, vol. 43, no. 2, pp. 235–286, 2001.

[101] N. N. Minh, H. Yamada, T. Miyata, and H. Katsuchi, "Aeroelastic complex mode analysis for coupled gust response of the Akashi Kaikyo bridge model," *Journal of Wind Engineering and Industrial Aerodynamics*, vol. 88, no. 2, pp. 307–324, 2000. International Conference on wind Engineering.

[102] T. Canor, N. Blaise, and V. Denoël, "Efficient uncoupled stochastic analysis with non-proportional damping," 2012.

[103] J. Heremans, A. Mayou, and V. Denoël, "Perspectives on the acceleration of the numerical assessment of flutter and buffeting response of bridge decks," in *8th International Conference on Computational Methods in Structural Dynamics and Earthquake Engineering Methods in Structural Dynamics and Earthquake Engineering*, Institute of Structural Analysis and Antiseismic Research National Technical University of Athens, 2021.

[104] L. Rouleau, J.-F. cois Deü, and A. Legay, "A comparison of model reduction techniques based on modal projection for structures with frequency-dependent damping," *Mechanical Systems and Signal Processing*, vol. 90, pp. 110–125, 2017.

[105] J. Heremans, A. Mayou, and V. Denoël, "Background/resonant decomposition of the stochastic torsional flutter response of an aeroelastic oscillator under buffeting loads," *Journal of Wind Engineering and Industrial Aerodynamics*, vol. 208, p. 104423, 11 2020.

[106] R. H. Scanlan and J. J. Tomko, "Airfoil and bridge deck flutter derivatives," *Journal of the Engineering Mechanics Division*, vol. 97, no. 6, pp. 1717–1737, 1971.

[107] A. K. Chopra, "Modal combination rules in response spectrum analysis: Early history," *Earthquake Engineering & Structural Dynamics*, vol. 50, no. 2, pp. 260–269, 2021.

[108] N. Barni, O. A. Øiseth, and C. Mannini, "Buffeting response of a suspension bridge based on the 2d rational function approximation model for self-excited forces," *Engineering Structures*, vol. 261, p. 114267, 2022.

[109] A. Fenerci, K. A. K. le, X. Xiang, and O. Øiseth, "Hydrodynamic interaction of floating bridge pontoons and its effect on the bridge dynamic responses," *Marine Structures*, vol. 83, p. 103174, 2022.

[110] C. Mannini, N. Barni, and S. G. Morano, "Multimodal flutter of a long-span suspension bridge in service and during construction," *Structural Engineering International*, vol. 0, no. 0, pp. 1–12, 2022.

[111] X. Chen, A. Kareem, and M. Matsumoto, "Multimode coupled flutter and buffeting analysis of long span bridges," *Journal of Wind Engineering and Industrial Aerodynamics*, vol. 89, no. 7, pp. 649–664, 2001. 10th International Conference on Wind Engineering.

[112] Y. Ge and H. Tanaka, "Aerodynamic flutter analysis of cable-supported bridges by multi-mode and full-mode approaches," *Journal of Wind Engineering and Industrial Aerodynamics*, vol. 86, no. 2, pp. 123–153, 2000.

[113] N. B. Claudio Mannini and S. G. Morano, "Multimodal flutter of a long-span suspension bridge in service and during construction," *Structural Engineering International*, vol. 33, no. 4, pp. 611–622, 2023.

[114] R. H. Scanlan, "Interpreting aeroelastic models of cable-stayed bridges," *Journal of Engineering Mechanics*, vol. 113, no. 4, pp. 555–575, 1987.

[115] X. Chen and A. Kareem, "Curve veering of eigenvalue loci of bridges with aeroelastic effects," *Journal of Engineering Mechanics*, vol. 129, no. 2, pp. 146–159, 2003.

[116] T. von Kármán, "Progress in the statistical theory of turbulence*," *Proceedings of the National Academy of Sciences*, vol. 34, no. 11, pp. 530–539, 1948.

[117] X. Chen and A. Kareem, "Advanced analysis of coupled buffeting response of bridges: a complex modal decomposition approach," *Probabilistic Engineering Mechanics*, vol. 17, no. 2, pp. 201–213, 2002.

[118] Q. Ding, A. Chen, and H. Xiang, "Coupled flutter analysis of long-span bridges by multimode and full-order approaches," *Journal of Wind Engineering and Industrial Aerodynamics*, vol. 90, no. 12, pp. 1981–1993, 2002. Fifth Asia-Pacific Conference on Wind Engineering.

[119] E. Riks, "An incremental approach to the solution of snapping and buckling problems," *International Journal of Solids and Structures*, vol. 15, no. 7, pp. 529–551, 1979.

[120] E. Riks, "Some computational aspects of the stability analysis of nonlinear structures," *Computer Methods in Applied Mechanics and Engineering*, vol. 47, no. 3, pp. 219–259, 1984.

[121] J. Heremans, G. Dimitriadis, and V. Denoël, "A continuation method for determining the speed dependent modal properties of large mdof aeroelastic systems," *Journal of Wind Engineering and Industrial Aerodynamics*, vol. 252, p. 105804, 2024.

[122] O. C. Zienkiewicz, R. L. Taylor, and J. Z. Zhu, *The finite element method: its basis and fundamentals*. Elsevier, 2005.

[123] C. B. Moler and G. W. Stewart, "An algorithm for generalized matrix eigenvalue problems," *SIAM Journal on Numerical Analysis*, vol. 10, no. 2, pp. 241–256, 1973.

[124] G. Lindfield and J. Penny, "Chapter 2 - linear equations and eigensystems," in *Numerical Methods (Fourth Edition)* (G. Lindfield and J. Penny, eds.), pp. 73–156, Academic Press, fourth edition ed., 2019.

[125] R. L. Bisplinghoff, H. Ashley, and R. L. Halfman, *Aeroelasticity*. New York:: Dover Publications, 1996.

[126] H. Hassig, "An approximate true damping solution of the flutter equations by determinant iteration," *Journal of Aircraft*, vol. 8, no. 11, pp. 885–889, 1971.

[127] W. P. Rodden and E. Dean Bellinger, "Aerodynamic lag functions, divergence, and the British flutter method," *Journal of Aircraft*, vol. 19, no. 7, pp. 596–598, 1982.

[128] W. P. Rodden, *Handbook for Aeroelastic Analysis*, vol. 1. MSC/NASTRAN Ver. 65, 1987.

[129] Y. Gu and Z. Yang, "Modified p-k method for flutter solution with damping iteration," *AIAA Journal*, vol. 50, no. 2, pp. 507–509, 2012.

[130] P. C. Chen, "Damping perturbation method for flutter solution: The g-method," *AIAA Journal*, vol. 38, no. 9, pp. 1519–1524, 2000.

[131] R. Allemang, "The modal assurance criterion - twenty years of use and abuse," *Sound & vibration*, vol. 37, pp. 14–23, 08 2003.

[132] M. Pastor, M. Binda, and T. Harčarik, "Modal assurance criterion," *Procedia Engineering*, vol. 48, pp. 543–548, 2012. Modelling of Mechanical and Mechatronics Systems.

[133] W. H. Press, S. A. Teukolsky, W. T. Vetterling, and B. P. Flannery, *Numerical Recipes in C*. Cambridge, USA: Cambridge University Press, second ed., 1992.

[134] D. Knoll and D. Keyes, "Jacobian-free newton-krylov methods: A survey of approaches and applications," *Journal of Computational Physics*, vol. 193, pp. 357–397, 01 2004.

[135] C. G. Broyden, "A class of methods for solving nonlinear simultaneous equations," *Mathematics of Computation*, vol. 19, pp. 577–593, 1965.

[136] M. Crisfield, "A fast incremental/iterative solution procedure that handles snap-through," *Computers & Structures*, vol. 13, no. 1, pp. 55–62, 1981.

[137] G. Dimitriadis, "Bifurcation analysis of aircraft with structural nonlinearity and freeplay using numerical continuation," *Journal of Aircraft*, vol. 45, no. 3, pp. 893–905, 2008.

[138] M. Ritto-Corrêa and D. Camotim, "On the arc-length and other quadratic control methods: Established, less known and new implementation procedures," *Computers & Structures*, vol. 86, no. 11, pp. 1353–1368, 2008.

[139] J. Heremans, M. Geuzaine, and V. Denoël, "A background/resonant decomposition based method to predict the behavior of 2-dof aeroelastic oscillators," *Journal of Wind Engineering and Industrial Aerodynamics*, vol. 233, p. 105290, 2023.

[140] M. Karpel, B. Moulin, and P. C. Chen, "Dynamic response of aeroservoelastic systems to gust excitation," *Journal of Aircraft*, vol. 42, no. 5, pp. 1264–1272, 2005.

[141] H. L. Runyan and C. E. Watkins, "Flutter of a uniform wing with an arbitrarily placed mass according to a differential-equation analysis and a comparison with experiment," 1949.

[142] D. V. Swinney, "A fractional calculus model of aeroelasticity," 1989.

[143] D. W. Marquardt, "An algorithm for least-squares estimation of nonlinear parameters," *Journal of the Society for Industrial and Applied Mathematics*, vol. 11, no. 2, pp. 431–441, 1963.

[144] J. D. Hunter, "Matplotlib: A 2d graphics environment," *Computing in Science & Engineering*, vol. 9, no. 3, pp. 90–95, 2007.

[145] T. M. Inc., ""contour" contour plot of matrix," 2022.

[146] R. P. Brent, *Algorithms for Minimization without Derivatives*. Englewood Cliffs, New Jersey: Prentice-Hall, 1st ed., 1973.

[147] V. Denoël and R. Maquoi, "The concept of numerical admittance," *Archive of Applied Mechanics*, vol. 82, pp. 1–18, 10 2012.

Appendix A

SDOF aeroelastic oscillator with large damping gradient

In the single degree-of-freedom model presented in Chapter 2, the derivation of the first order approximation for $H(\omega)$ was obtained in (2.20) truncating (2.19) at leading order. If it is clear that that $\overline{\omega}/\omega$ and $\mathcal{C}(\omega) = 1 - c_{ae}(\omega)/c_s$ are of order $\mathcal{O}(1)$ at most, the magnitude of $\partial_\omega C(\overline{\omega})$ is less easily predicted, and some applications could theoretically embed a large damping gradient, especially if they are subjected to galloping instabilities, where the damping is expected to vary rapidly close to critical velocity. This section details this uncovered particular case of a large $\partial_\omega \mathcal{C}(\overline{\omega})$. Restarting from (2.19) and remembering the definition (2.14) of $\overline{\omega}$

$$\begin{aligned} H\left[\omega(\eta)\right] =& \frac{1}{k_\mathrm{s}}\Bigg[\left(-2\eta\frac{\overline{\omega}^2}{\omega_\mathrm{s}^2} + 2\mathrm{i}\frac{\overline{\omega}}{\omega_s}\mathcal{C}\left(\overline{\omega}\right) + \overline{\omega}\partial_\omega\mathcal{K}(\overline{\omega})\,\eta\right)\xi_\mathrm{s} + \\ &+ \left(-\eta^2\frac{\overline{\omega}^2}{\omega_\mathrm{s}^2} + 2\mathrm{i}\frac{\overline{\omega}}{\omega_s}\left(\mathcal{C}\left(\overline{\omega}\right) + \overline{\omega}\partial_\omega\mathcal{C}(\overline{\omega})\right)\eta\right)\xi_\mathrm{s}^2 + \mathcal{O}(\xi_\mathrm{s}^3)\Bigg]^{-1}. \end{aligned}$$

Assuming now that $\partial_\omega C(\overline{\omega})$ is of order $\mathcal{O}\left(\frac{1}{\xi_s}\right)$, and truncating at leading order, the transfer matrix is approached by

$$\tilde{H}\left(\omega(\eta)\right) = \frac{1}{2\xi_\mathrm{s}k_\mathrm{s}}\left[\left(-\frac{\overline{\omega}^2}{\omega_\mathrm{s}^2} + \frac{1}{2}\overline{\omega}\partial_\omega\mathcal{K}(\overline{\omega})\right)\eta + \mathrm{i}\frac{\overline{\omega}}{\omega_s}\eta\,\overline{\omega}\partial_\omega\mathcal{C}(\overline{\omega})\xi_\mathrm{s}\right]^{-1}. \tag{A.1}$$

This expression generalizes (2.20) to large damping gradient. Since $H(0)$ is still asymptotic to $1/k_\mathrm{s}\mathcal{K}\left(\omega\right)$, the background component remains unchanged, and the resonant component only deserves further study.

This equation can be plugged in that of the residual $\hat{S}_{q_1}$ to get the equivalent of the approximation (2.21)

$$\tilde{S}_{q,1}\left(\omega\left(\eta\right)\right) = \frac{1}{\left(2k_\mathrm{s}\xi_\mathrm{s}\right)^2}\frac{1}{\alpha\eta^2 + \beta\eta + \gamma}S_{f,\mathrm{bu}}\left(\omega\left(\eta\right)\right) \tag{A.2}$$

with $\alpha = \left(\frac{\overline{\omega}^2}{\omega_\mathrm{s}^2} - \frac{1}{2}\overline{\omega}\partial_\omega\mathcal{K}(\overline{\omega})\right)^2 + \xi_\mathrm{s}^2\left(\frac{\overline{\omega}}{\omega_s}\right)^2\left(\overline{\omega}\partial_\omega\mathcal{C}(\overline{\omega})\right)^2$, $\beta = 2\xi_\mathrm{s}\left(\frac{\overline{\omega}}{\omega_s}\right)^2\mathcal{C}\left(\overline{\omega}\right)\overline{\omega}\partial_\omega\mathcal{C}(\overline{\omega})$ and $\gamma = \left(\frac{\overline{\omega}}{\omega_s}\mathcal{C}\left(\overline{\omega}\right)\right)^2$.

Again, we assume that the power spectral density of the buffeting loading does not vary too fast in the neighborhood of the resonance peak such that $S_{f,\mathrm{bu}}\left(\omega\left(\eta\right)\right) = S_{f,\mathrm{bu}}\left(\overline{\omega}\right) + \mathcal{O}(\xi_\mathrm{s})$. In this case, this term is seen as a constant with respect to integration along ω. The resonance component associated with the resonance peak in the positive range of frequencies therefore reads

$$\sigma_{q,\mathrm{R}}^2 = \frac{\overline{\omega}\,S_{f,\mathrm{bu}}(\overline{\omega})}{2\xi_\mathrm{s}k_s^2}\int_{-\infty}^{+\infty}\frac{d\eta}{\alpha\eta^2 + \beta\eta + \gamma} = \frac{\overline{\omega}\,S_{f,\mathrm{bu}}(\overline{\omega})}{2\xi_\mathrm{s}k_s^2}\left(\frac{2\pi}{\sqrt{4\alpha\gamma - \beta^2}}\right) \tag{A.3}$$

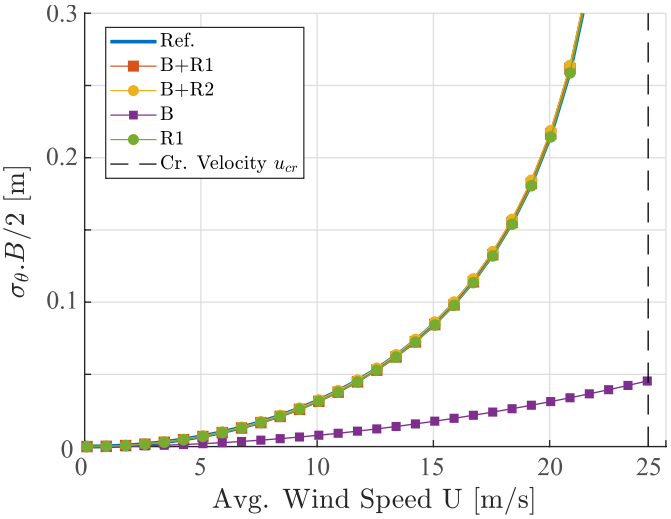

Figure A.1: Scaled standard deviations obtained from background component (B), resonant components (R), and the sum of them (B)+(R).

which constitutes the extension of the resonant component to high damping gradient structures. Accordingly, the superposition of the background and resonant components gives an estimate of the variance of the response

$$\sigma_q^2 = \left(\frac{\sigma_{f,\mathrm{bu}}}{k_\mathrm{s}}\right)^2 + \frac{\overline{\omega}\, S_{f,\mathrm{bu}}(\overline{\omega})}{2\xi_\mathrm{s} k_s^2}\left(\frac{2\pi}{\sqrt{4\alpha\gamma - \beta^2}}\right). \tag{A.4}$$

To illustrate the gain in accuracy brought with this additional term, the results of the first (B)+(R1) and the second (B)+(R2) methods are compared for the Golden Gate application in Figure A.1. It is seen that the scaled damping gradient remains very low, indicating that the gain in accuracy is very limited. This is confirmed observing the error committed on the displacement standard deviation.

Appendix B

Proposed Implementation of an Adaptive Integration Scheme

The results obtained and presented in section 2.4 are partly obtained with a simple in-house adaptive integration scheme. The algorithm works as follows. First, the domain of integration is divided into segments separated by the integration points. On each segment, the contribution to the integral is computed by means of the trapezoidal rule. These segments are then iteratively refined, if required, until a desired accuracy is reached.

The refinement procedure consists in adding an integration point in the middle of the interval, creating therefore two sub-segments instead of the initial one. The sum of the contribution on the two sub-segments is compared to the contribution along the domain before subdivision. If the relative difference between both is lower than a user-defined threshold, then this domain is not subdivided anymore. This process is continued until no segments require being divided anymore.

This algorithm performs better when the original distribution of points includes the inflexion points in the function to integrate. This is due to the fact that the break-down condition originates from a concept built on a curvature with a constant sign along the domain. The termination criteria may incorrectly indicate convergence in case of a domain with an inflexion point in the middle.

```
doloop = 1;iter=1;
while doloop
  ir = find(r==1);
  nz = length(ir);
  jr=1;
  while jr<=nz
    iz = ir(jr);
    xn = (x(iz)+x(iz+1))/2;
    fn = fct(xn);
    I1 = trapz( [x(iz) x(iz+1)], [f(iz) f(iz+1)] );
    I2 = trapz( [x(iz) xn], [f(iz) fn] ) + trapz( [xn x(iz+1)], [fn f(iz+1)] );
    err = abs(I2-I1) / (Itot / (x(end)-x(1))*(x(iz+1)-x(iz)) );
    x = [x(1:iz) xn x(iz+1:end)];
    f = [f(1:iz) fn f(iz+1:end)];
    if err < tol
      r = [r(1:iz-1) 0 0 r(iz+1:end)];
    else
      r = [r(1:iz-1) 1 1 r(iz+1:end)];
    end ir = ir+1; jr = jr+1;
    Itot = trapz( x,f );
  end
  if sum(r) == 0; doloop=0; end
  iter=iter+1;
end
Itot = trapz( x,f );
```

Appendix C

Asymptotic expansions of the 2DOF system

C.1 Expansion of the transfer function

The transfer function is obtained by inversion of the flexibility matrix $\mathbf{J}(\omega)$. This matrix can be split into a diagonal matrix $\mathbf{J}_d(\omega)$ and a out-of-diagonal matrix $\mathbf{J}_o(\omega)$

$$\mathbf{H}(\omega) = [\mathbf{J}_d(\omega) + \mathbf{J}_o(\omega)]^{-1} \tag{C.1}$$

Factorizing for $\mathbf{J}_d(\omega)$

$$\mathbf{H}(\omega) = \left[\mathbb{I} + \mathbf{J}_d^{-1}\mathbf{J}_o\right]^{-1} \mathbf{J}_d^{-1} = \left[\mathbb{I} + \mathbf{J}_d^{-1}\mathbf{J}_o\right]^{-1} \mathbf{H}_d. \tag{C.2}$$

f The first factor of the right hand side acts as a correcting factor applied to $\mathbf{H}_d$ to recover the exact transfer matrix $\mathbf{H}(\omega)$. Considering the series proposed by [79]

$$\mathbf{Y}(\omega) = \mathbb{I} + \sum_{k=1}^{+\infty} (-1)^k (\mathbf{J}_d^{-1}\mathbf{J}_o)^k \tag{C.3}$$

an proving that

$$\begin{aligned}
\mathbf{Y}(\omega)(\mathbb{I} + \mathbf{J}_d^{-1}\mathbf{J}_o) &= \left(\mathbb{I} + \sum_{k=1}^{+\infty} (-1)^k (\mathbf{J}_d^{-1}\mathbf{J}_o)^k\right) (\mathbb{I} + \mathbf{J}_\mathbf{d}^{-\mathbf{1}}\mathbf{J}_o) \\
&= \mathbb{I} + \mathbf{J}_d^{-1}\mathbf{J}_o + \sum_{k=1}^{+\infty} (-1)^k (\mathbf{J}_d^{-1}\mathbf{J}_o)^k + \sum_{k=1}^{+\infty} (-1)^k (\mathbf{J}_d^{-1}\mathbf{J}_o)^{k+1} \\
&= \mathbb{I} + \mathbf{J}_d^{-1}\mathbf{J}_o + \sum_{k=1}^{+\infty} (-1)^k (\mathbf{J}_d^{-1}\mathbf{J}_o)^k - \sum_{k=0}^{+\infty} (-1)^k (\mathbf{J}_d^{-1}\mathbf{J}_o)^k \\
&= \mathbb{I}
\end{aligned}$$

shows that the correcting factor is exactly $\mathbf{Y}(\omega)$. The derivation of an approximation for $\mathbf{H}(\omega)$ can be made by substituting in (C.2) an asymptotic expansion for $\mathbf{Y}(\omega)$. This correcting factor $\mathbf{Y}(\omega)$ constitutes therefore our first subject of interest.

It is first proven that the series (C.3) is convergent. Introducing $\boldsymbol{\Psi}$ and $\boldsymbol{\mu}$ respectively the matrices containing the eigenvectors and eigenvalues of $\mathbf{J}_d^{-1}\mathbf{J}_o$, the diagonalisation of the full matrix $\mathbf{J}_d^{-1}\mathbf{J}_o$ reads

$$\mathbf{J}_d^{-1}\mathbf{J}_o = \boldsymbol{\Psi}\boldsymbol{\mu}\boldsymbol{\Psi}^{-1}. \tag{C.4}$$

Assuming that the eigenvalues of $\mathbf{J}_d^{-1}\mathbf{J}_o$ are small, the eigenvalues matrix $\boldsymbol{\mu}$ can be expressed as the product of a small number ϵ and a matrix $\boldsymbol{\nu}$ of order $\mathcal{O}(1)$

$$\boldsymbol{\mu} = \epsilon\boldsymbol{\nu} \qquad 0 < \epsilon \ll 1. \tag{C.5}$$

Note that this ϵ has nothing to do with the parameter ε introduced previously even if it is used for the same purpose. The smallness of the eigenvalues of $\mathbf{J}_d^{-1}\mathbf{J}_o$ is asserted by evaluating the diagonality index ρ of the flexiblity matrix $\mathbf{J}(\omega)$ defined as the spectral radius of $\mathbf{J}_d^{-1}\mathbf{J}_o$, which by definition establishes its highest eigenvalue in module,

$$\rho(\mathbf{J}) = \max_i \left[\left|\mathrm{eig}\left(\mathbf{J}_d^{-1}\mathbf{J}_o\right)\right|\right]. \tag{C.6}$$

Its main benefit is to provide a scalar characterization of the smallness of the off-diagonal elements $\mathbf{J}_o$ with respect to the diagonal ones $\mathbf{J}_d$ and hence, provides an excellent indicator of the coupling rate of the flexibility matrix. Since $\mathbf{J}$ is a function of ω and the wind speed U, it is also a function of ω. The diagonalisation of $\mathbf{J}_d^{-1}\mathbf{J}_o$ reads now

$$\mathbf{J}_d^{-1}\mathbf{J}_o = \epsilon\boldsymbol{\Psi}\boldsymbol{\nu}\boldsymbol{\Psi}^{-1}. \tag{C.7}$$

Substituting (C.7) in (C.3) gives

$$\mathbf{Y}(\omega) = \mathbb{I} + \sum_{k=1}^{+\infty}(-1)^k\epsilon^k\boldsymbol{\Psi}\boldsymbol{\nu}^k\boldsymbol{\Psi}^{-1} \tag{C.8}$$

which shows clearly that $\mathbf{Y}(\omega)$ is a convergent series of common ratio of order $\epsilon \ll 1$. It is proposed to truncate this series at first order so that the correcting factor involves two terms

$$\mathbf{Y}(\omega) \simeq \mathbb{I} - \mathbf{J}_d^{-1}\mathbf{J}_o \tag{C.9}$$

and a quite simple expression at first order is obtained for $\mathbf{H}(\omega)$

$$\mathbf{H}(\omega) \simeq \left(\mathbb{I} - \mathbf{J}_d^{-1}\mathbf{J}_o\right)\mathbf{H}_d \tag{C.10}$$

C.1.1 Expansion of the power spectral density of the response

Introduction of (3.33) in (3.27) leads to (3.37) that can be expressed on the following equivalent form

$$\mathbf{S}_q(\omega) = \mathbf{S}_q^{\mathrm{I}} - \mathbf{H}_d(\omega)\mathbf{J}_o(\omega)\mathbf{S}_q^{\mathrm{I}} - \mathbf{S}_q^{\mathrm{I}}\left[\mathbf{H}_d(\omega)\mathbf{J}_o(\omega)\right]^* + \mathbf{H}_d(\omega)\mathbf{J}_o(\omega)\mathbf{S}_q^{\mathrm{I}}\left[\mathbf{H}_d(\omega)\mathbf{J}_o(\omega)\right]^*. \tag{C.11}$$

where the diagonal form $\mathbf{J}_d^{-1}\mathbf{J}_o$ of (C.7) can be substituted to give

$$\mathbf{S}_q(\omega) = \mathbf{S}_q^{\mathrm{I}} - \epsilon\boldsymbol{\Psi}\boldsymbol{\nu}\boldsymbol{\Psi}^{-1}\mathbf{S}_q^{\mathrm{I}} - \epsilon\mathbf{S}_q^{\mathrm{I}}\left[\boldsymbol{\Psi}\boldsymbol{\nu}\boldsymbol{\Psi}^{-1}\right]^* + \epsilon^2\boldsymbol{\Psi}\boldsymbol{\nu}\boldsymbol{\Psi}^{-1}\mathbf{S}_q^{\mathrm{I}}\left[\boldsymbol{\Psi}\boldsymbol{\nu}\boldsymbol{\Psi}^{-1}\right]^*. \tag{C.12}$$

Because ϵ is of order of the diagonality index $\rho(\mathbf{J}) \ll 1$, it is proposed to truncate this series at first order, in which case the output power spectral density admits a quite simple form

$$\mathbf{S}_q(\omega) = \mathbf{H}_d\mathbf{S}_f\mathbf{H}_d^* - \mathbf{H}_d(\omega)\mathbf{J}_o(\omega)\mathbf{S}_q^{\mathrm{I}} - \mathbf{S}_{\mathbf{q}}^{\mathrm{I}\,*}\mathbf{J}_o^*(\omega)\mathbf{H}_d^*(\omega). \tag{C.13}$$

C.2 Properties of the modal basis

Starting from the equation of motion in frequency domain and in nodal basis

$$\left[-\omega^2\mathbf{M}(\omega) + \mathrm{i}\omega\mathbf{C}(\omega) + \mathbf{K}(\omega)\right]\mathbf{Q}(\omega) = \mathbf{F}_{bu}(\omega) \tag{C.14}$$

the generalized eigenvalues problem reads

$$\left[-\omega_i^2\mathbf{M}(\omega_i) + \mathrm{i}\omega_i\mathbf{C}(\omega_i) + \mathbf{K}(\omega_i)\right]\boldsymbol{\phi}_i^R = \mathbf{0}. \tag{C.15}$$

Premultiplying by $\boldsymbol{\phi}_i^{L,\mathsf{T}}$ leads to

$$\boldsymbol{\phi}_i^{L,\mathsf{T}}\left[-\omega_i^2\mathbf{M}(\omega_i) + \mathrm{i}\omega_i\mathbf{C}(\omega_i) + \mathbf{K}(\omega_i)\right]\boldsymbol{\phi}_i^R = 0 \tag{C.16}$$

in which the diagonal elements of the modal matrices of mass $M_{ii}^*(\omega) = \boldsymbol{\phi}_i^{L,\mathsf{T}}\mathbf{M}(\omega)\boldsymbol{\phi}_i^R$, damping $C_{ii}^*(\omega) = \boldsymbol{\phi}_i^{L,\mathsf{T}}\mathbf{C}(\omega)\boldsymbol{\phi}_i^R$ and stiffness $K_{ii}^*(\omega) = \boldsymbol{\phi}_i^{L,\mathsf{T}}\mathbf{K}(\omega)\boldsymbol{\phi}_i^R$ are readily identified to give

$$\left[-\omega_i^2 M_{ii}^*(\omega_i) + \mathrm{i}\omega_i C_{ii}^*(\omega_i) + K_{ii}^*(\omega_i)\right] = 0 \tag{C.17}$$

Splitting the matrix of mass into one diagonal and ones out-of-diagonal matrices, and performing the same operation for the matrix of stiffness gives

$$-\omega_i^2\left[M_{d,ii}(\omega_i) + M_{o,ii}(\omega_i)\right] + \mathrm{i}\omega_i\left[C_{d,ii}^*(\omega_i) + C_{o,ii}^*(\omega_i)\right] + K_{d,ii}(\omega_i) + K_{o,ii}(\omega_i) = 0. \tag{C.18}$$

where it is evident from their definition that $K_{o,ii}(\omega) = C_{o,ii}^*(\omega_i) = M_{o,ii}(\omega) = 0$. Finally, it is held the following property, valid independently from the choice of the modal basis

$$-\omega_i^2 M_{d,ii}(\omega_i) + \mathrm{i}\omega_i C_{d,ii}(\omega_i) K_{d,ii}(\omega_i) = 0. \tag{C.19}$$

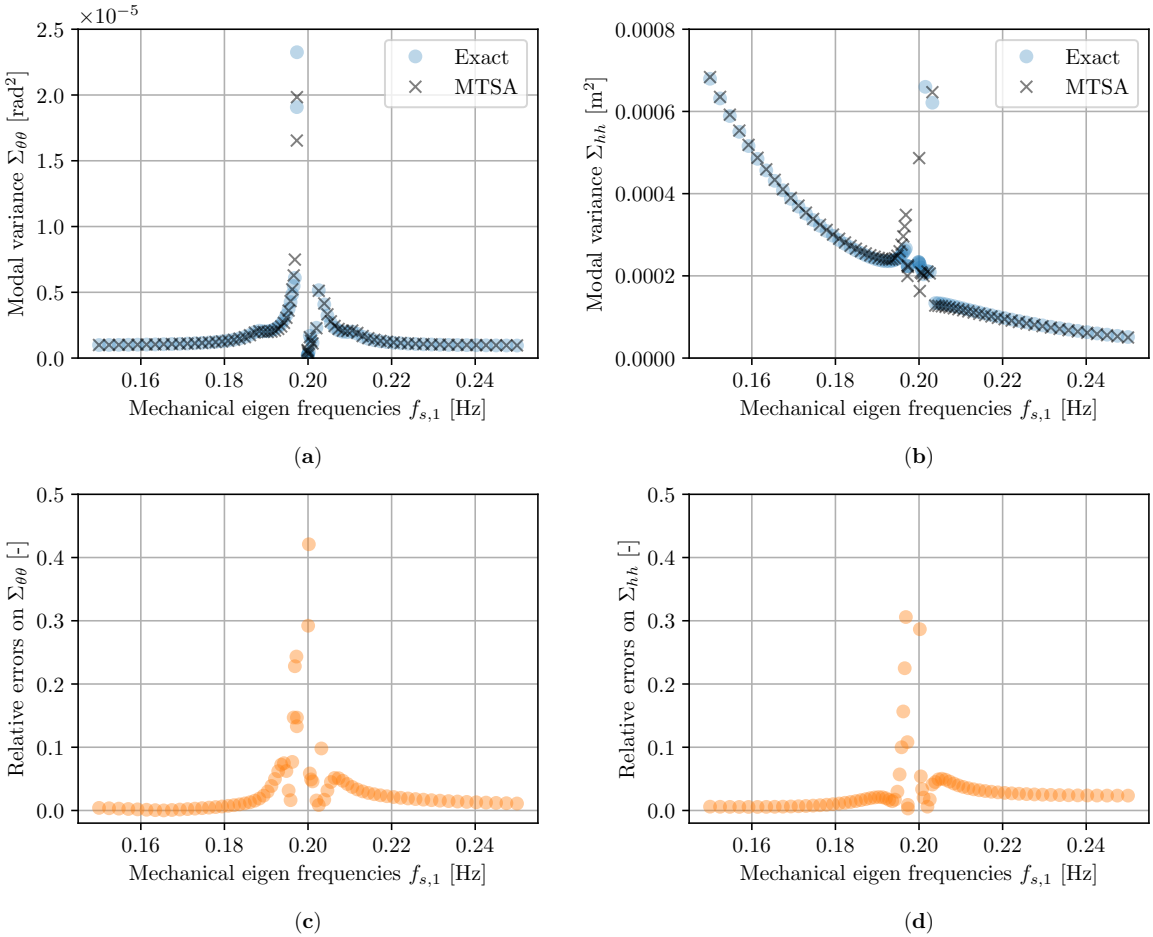

Figure C.1: Evolution of the modal variances for pitch (a) and plunge (b), and associated relative errors with respect to the exact solution (c) and (d). Results obtained for $\beta = 1$, at $U = 20$ m/s and considering $\mathbf{S}_q^{\mathrm{III}}(\omega)$.

C.3 Effect of the enriched asymptotic expansion of the modal PSD matrix.

This section presents the results obtained for the second example of Chapter 3 when the third term $\mathbf{S}_q^{\mathrm{III}}(\omega)$ of (3.37) is considered. The variance Σ^{III} corresponding to the integral $\mathbf{S}_q^{\mathrm{III}}(\omega)$ was evaluated numerically, as no analytical formulation could be found for the integral of $\mathbf{S}_q^{R,\mathrm{III}}(\omega)$. Results are presented in Figures C.1, C.2 and C.3.

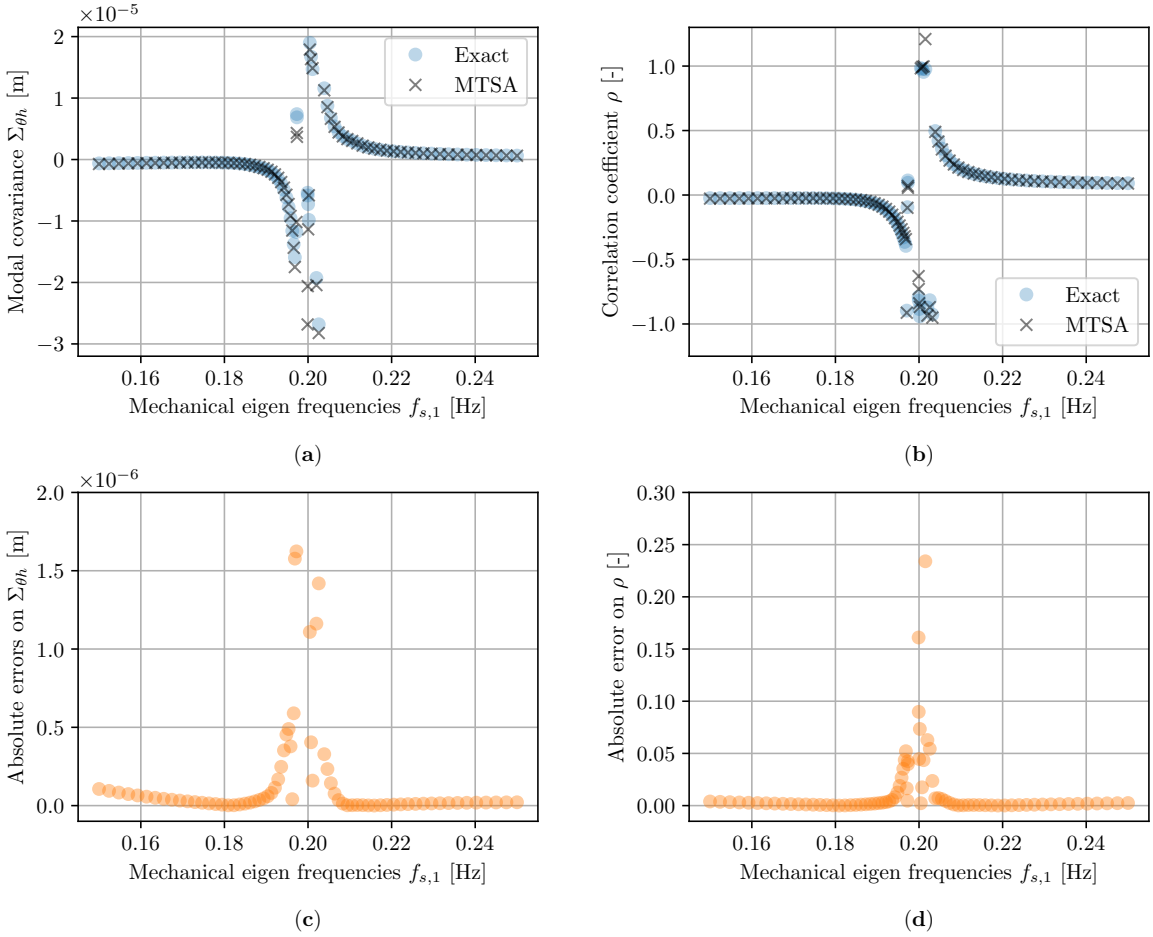

Figure C.2: (a) Evolution of the modal covariance for the exact solution, and the MTSA approximation with respect to the wind-off pitch eigenfrequency $f_{s,1}$. (b) Correlation coefficients for the exact solution, and MTSA approximation with respect to the wind-off plunge eigenfrequency $f_{s,1}$. (c) Evolution with the $f_{s,1}$ of the absolute errors on modal covariances evaluated with the MTSA method on exact covariances. (d) Error committed on the exact correlation coefficients when using the MTSA method. Results obtained for $\beta = 1$, at $U = 20$ m/s and considering $\mathbf{S}_q^{\mathrm{III}}(\omega)$.

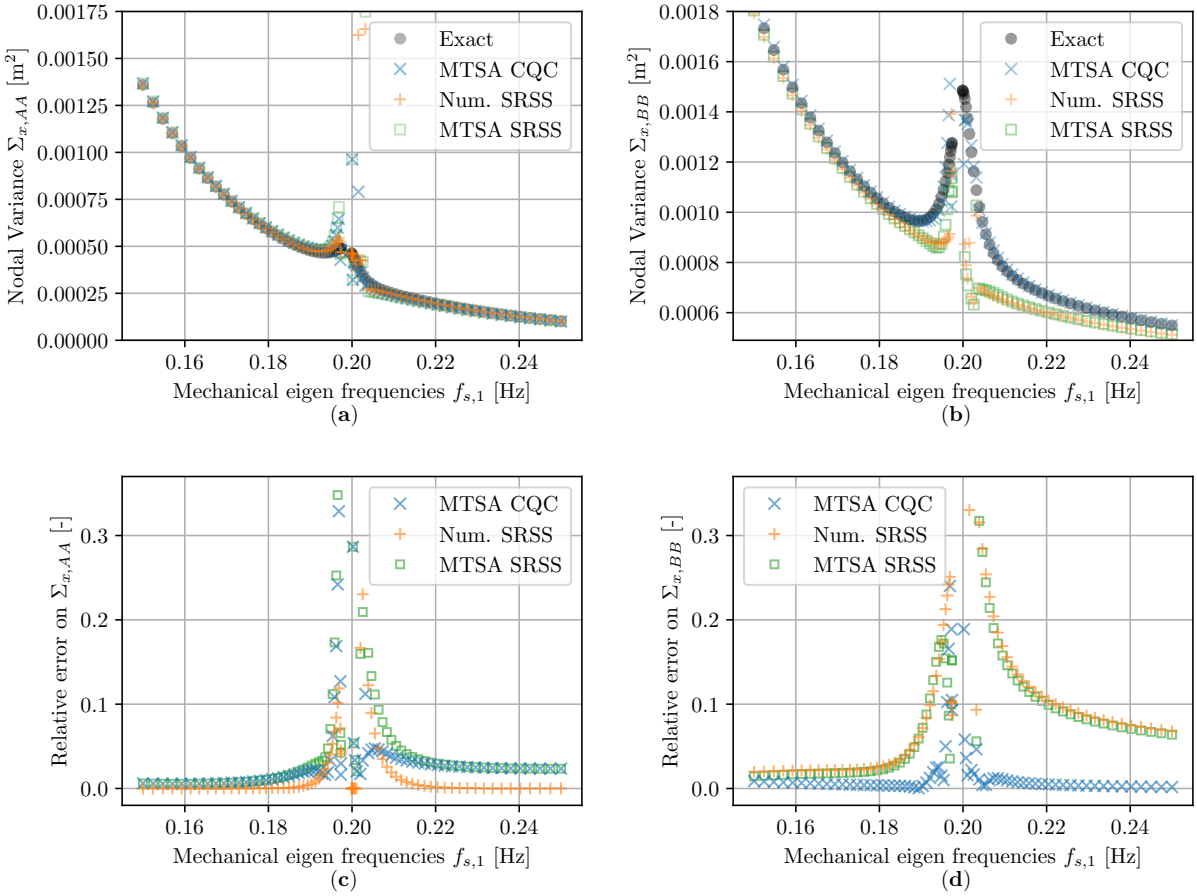

Figure C.3: Nodal variances obtained from integration of the exact solution, from a CQC or SRSS recombination process with the exact solution or MTSA approximation: (a) vertical displacement in A (b) vertical displacement in B. Error committed on the exact nodal variance using an SRSS recombination with the exact solution, or using a SRSS or CQC with the MTSA approximation: (c) vertical displacement in A, (d) vertical displacement in B. Results obtained for $\beta = 1$, at $U = 20$ m/s and considering $\mathbf{S}_q^{\mathrm{III}}(\omega)$.

Appendix D

Finite Element Formulation of Buffeting and Aeroelastic Effects

D.1 The FEM method

Unlike low-dimensional models, where individual modal characteristics can be extracted with straightforward techniques such as shown in chapters 2, and 3, high-order models can offer a systematic discretization of the structure to capture its geometry and dynamic behaviour accurately. The necessity of a systematic framework becomes evident when dealing with large systems, often with hundreds or thousands of DOFs. The Finite Element Method (FEM) provides a framework to achieve this by dividing the structure into finite elements, each contributing to the global system matrices.

The use of FEM in aeroelastic applications allows for a detailed representation of the mode shapes and wind-on natural frequencies of complex structures, which is crucial for evaluating their stability under aerodynamic loads. As the number of DOFs increases, solving the eigenvalue problem and tracking stability trends becomes significantly more challenging, making FEM an essential tool for practical aeroelastic analysis.

In this appendix, the FEM framework is introduced for constructing MDOF aeroelastic models, deriving the structural and aeroelastic matrices of mass, damping, and stiffness, as well as the associated nodal load vector. The model developed is a three-dimensional representation that considers five degrees-of-freedom per node: the horizontal and vertical displacements, h and p and their spatial derivatives (slope) $\frac{\partial h}{\partial x}$, and $\frac{\partial p}{\partial x}$ and the torsional angle α. The first four variables govern the bending behaviour of the structure, while the latter captures its torsional dynamics. For the structural matrices, the y- and y-bending matrices and the torsional matrices are established independently.

This framework is also used to formulate the buffeting forces. The nodal load vector is first derived, and the associated power spectral density matrices required for the frequency-domain analysis are accordingly formulated. Additionally, specific aspects related to modal analysis are discussed.

The goal of this appendix chapter is to establish a formal framework for the methodologies regarding the self-excited and buffeting forces that is applied in the 4, which focuses on the extension of the 2DOF background/resonant decomposition to MDOF systems. A key novelty compared to established literature is the ability of the proposed formulation to incorporate skewed average wind profiles acting on bridge decks. Some aspects related to the computational efficiency of the proposed implementation are also discussed.

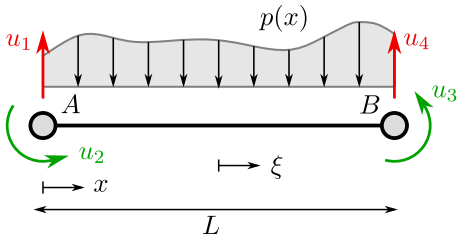

Figure D.1: Schematic representation of an isolated finite element of type "beam".

D.2 Formulation of the structural matrices

The following developments are structured into separate sections addressing vertical and horizontal bending, followed by torsion. Each component is examined independently to provide a clear understanding of its influence on the overall system behaviour. Once these individual solutions are established, they will be integrated into a comprehensive framework that accounts for the global effects of bending and torsion, ultimately leading to a complete modelling of the structural and aeroelastic effects.

D.2.1 The bending behaviour

This section considers the case of a beam of rigidity EI and linear density μ subjected to a variable transversal load $p(x)$. The finite element method is used to derive the expressions of the mass and stiffness matrices. It consists in discretizing the beam into multiple elements, each defined by nodal displacements at its extremities and interpolated within the element using shape functions. The displacement field inside each element is constructed based on these nodal displacements and the associated shape functions, which ensure continuity and compatibility between adjacent elements. The selection of appropriate shape functions is crucial for accurately capturing the deformation behaviour.

D.2.1.A The shape functions

A schematic representation of an isolated element of type "beam" is shown in Figure D.1. The displacement $v(x)$ inside an element is expressed as a linear combination $\tilde{v}(x)$ of these shape functions and the corresponding nodal displacements:

$$v(x) \approx \tilde{v}(x) = \mathbf{N}(x)\mathbf{a} = \mathbf{a}^{\mathsf{T}}\mathbf{N}^{\mathsf{T}}(x) \tag{D.1}$$

where $\mathbf{N}(x) = \begin{bmatrix} h_1(x) & h_2(x) & h_3(x) & h_4(x) \end{bmatrix}$ is the row vector of shape functions, and $\mathbf{a}$ is a column vector gathering the nodal displacements. Referring to Figure D.1, the vector of nodal unknown is given by

$$\mathbf{a} = \begin{bmatrix} u_1 & u_2 & u_3 & u_4 \end{bmatrix}^{\mathsf{T}}. \tag{D.2}$$

The shape functions $h_i(x)$ are chosen as Hermite polynomials, ensuring continuity of both displacement and slope across element boundaries. They are typically defined in both physical

and normalized coordinate systems. They are expressed in the form $\xi = \dfrac{2x}{L} - 1$

$$h_1(x) = 2\frac{x^3}{L^3} - 3\frac{x^2}{L^2} + 1 \qquad \longleftrightarrow \qquad h_1(\xi) = \frac{1}{4}(2 - 3\xi + \xi^3) \tag{D.3}$$

$$h_2(x) = 3\frac{x^2}{L^2} - 2\frac{x^3}{L^3} \qquad \longleftrightarrow \qquad h_2(\xi) = \frac{L}{8}\left(1 - \xi - \xi^2 + \xi^3\right) \tag{D.4}$$

$$h_3(x) = x - 2\frac{x^2}{L} + \frac{x^3}{L^2} \qquad \longleftrightarrow \qquad h_3(\xi) = \frac{1}{4}\left(2 + 3\xi - \xi^3\right) \tag{D.5}$$

$$h_4(x) = \frac{x^3}{L^2} - \frac{x^2}{L} \qquad \longleftrightarrow \qquad h_4(\xi) = \frac{1}{8}L\left(-1 - \xi + \xi^2 + \xi^3\right) \tag{D.6}$$

The normalized coordinate ξ varies from -1 to 1 along the element length L. Each shape function $h_i(x)$ is associated with a specific nodal degree-of-freedom (displacement or slope) and is constructed to satisfy interpolation conditions at the corresponding node. Specifically, these functions are such that

$$\begin{aligned}
\mathbf{N}(\xi = -1) &= \begin{bmatrix} 1 & 0 & 0 & 0 \end{bmatrix} \\
\frac{\partial \mathbf{N}}{\partial \xi}(\xi = -1) &= \begin{bmatrix} 0 & 1 & 0 & 0 \end{bmatrix} \\
\mathbf{N}(\xi = 1) &= \begin{bmatrix} 0 & 0 & 1 & 0 \end{bmatrix} \\
\frac{\partial \mathbf{N}}{\partial \xi}(\xi = 1) &= \begin{bmatrix} 0 & 0 & 0 & 1 \end{bmatrix}.
\end{aligned}$$

The Hermite shape functions also ensure $\mathbb{C}_1$ continuity across elements. They allow for an accurate representation of beam bending by incorporating both displacement and slope continuity at the nodes.

D.2.1.B The weak form

The in-plane elastic bending of a beam of linear density μ and rigidity EI subjected to a transverse load $p(x)$ is governed by the following differential equation,

$$\mu\frac{\partial^2 v}{\partial t^2} + EI\frac{\partial^4 v}{\partial x^4} = p(x). \tag{D.7}$$

The weighted residual method [122] consists in forming the residual of (D.7)

$$R(x) = \mu\frac{\partial^2 v}{\partial t^2} + EI\frac{\partial^4 v}{\partial x^4} - p(x) = 0 \tag{D.8}$$

and weighting it by an arbitrary virtual displacement $\delta v(x)$, leading to the weighted residual

$$\delta v(x) \cdot R(x) = \delta v(x)\left[\mu\frac{\partial^2 v}{\partial t^2} + EI\frac{\partial^4 v}{\partial x^4} - p(x)\right] = 0. \tag{D.9}$$

Integrating over the length of the beam,

$$\int_0^L \delta v(x)\left[\mu\frac{\partial^2 v}{\partial t^2} + EI\frac{\partial^4 v}{\partial x^4} - p(x)\right] \mathrm{d}x = 0. \tag{D.10}$$

To reduce the order of differentiation, the second term is integrated by parts twice:

$$-EI\left[\frac{\partial^2 v}{\partial x^2}\delta v'(x)\right]_0^L + \left[\frac{\partial^3 v}{\partial x^3}\delta v(x) EI\right]_0^L - \int_0^L \mu\frac{\partial^2 v}{\partial t^2} + v''(x)\delta v''(x)\,\mathrm{d}x - \int_0^L p(x)\,\mathrm{d}x \tag{D.11}$$

The first two terms vanish under appropriate essential boundary conditions, leaving the weak form of the elastic bending problem with inertial effects:

$$\int_0^L \left[\mu \frac{\partial^2 v}{\partial t^2}\delta v(x) + EIv''(x)\delta v''(x)\right] \mathrm{d}x = \int_0^L p(x)\delta v(x), \mathrm{d}x. \tag{D.12}$$

This weak form provides an integral formulation of the governing differential equation, transforming it into a more flexible framework for numerical approximation. By reducing the continuity requirements on the solution, it allows for piecewise-defined shape functions, which are essential in the finite element method. Additionally, the integration by parts lowers the order of differentiation, facilitating computational implementation while naturally incorporating boundary conditions.

D.2.1.C Determination of the Structural matrices

The nodal displacement (D.1) can be substituted in the weak form (D.12) to get

$$EI \int_0^L \delta \mathbf{a}^\mathsf{T} \frac{\partial^2 \mathbf{N}^\mathsf{T}}{\partial x^2} \frac{\partial^2 \mathbf{N}}{\partial x^2} \mathbf{a}\, \mathrm{d}x + \mu \int_0^L \delta \mathbf{a}^\mathsf{T} \mathbf{N}^\mathsf{T} \frac{\partial^2}{\partial t^2}(\mathbf{N}\mathbf{a})\, \mathrm{d}x - \int_0^L p(x)\delta \mathbf{a}^\mathsf{T} \mathbf{N}^\mathsf{T}\, \mathrm{d}x = 0. \tag{D.13}$$

Or, equivalently

$$\delta \mathbf{a}^\mathsf{T} \left[EI \int_0^L \frac{\partial^2 \mathbf{N}^\mathsf{T}}{\partial x^2} \frac{\partial^2 \mathbf{N}}{\partial x^2}\, \mathrm{d}x\, \mathbf{a} + \mu \int_0^L \mathbf{N}^\mathsf{T}\mathbf{N}\, \mathrm{d}x\, \ddot{\mathbf{a}} - \int_0^L p(x)\mathbf{N}^\mathsf{T}\, \mathrm{d}x\right] = 0. \tag{D.14}$$

Because the displacement $\delta\mathbf{a}$ is arbitrary, this equation is only satisfied if

$$EI \int_0^L \frac{\partial^2 \mathbf{N}^\mathsf{T}}{\partial x^2} \frac{\partial^2 \mathbf{N}}{\partial x^2}\, \mathrm{d}x\, \mathbf{a} + \mu \int_0^L \mathbf{N}^\mathsf{T}\mathbf{N}\, \mathrm{d}x\, \ddot{\mathbf{a}} - \int_0^L p(x)\mathbf{N}^\mathsf{T}\, \mathrm{d}x = \mathbf{0} \tag{D.15}$$

which is an equation of the form

$$\mathbf{M}\ddot{\mathbf{a}} + \mathbf{K}\mathbf{a} = \mathbf{g}. \tag{D.16}$$

where the structural stiffness matrix

$$\mathbf{K}_s = EI \int_0^L \frac{\partial^2 \mathbf{N}^\mathsf{T}}{\partial x^2} \frac{\partial^2 \mathbf{N}}{\partial x^2}\, \mathrm{d}x, \tag{D.17}$$

the mass matrix

$$\mathbf{M}_s = \mu \int_0^L \mathbf{N}^\mathsf{T}\mathbf{N}\, \mathrm{d}x, \tag{D.18}$$

and the nodal load vector

$$\mathbf{g}_s = \int_0^L p(x)\mathbf{N}^\mathsf{T}\, \mathrm{d}x = 0 \tag{D.19}$$

in the in-plane bending problem.

Assuming that the flexural rigidity EI, the linear density μ and the load $p(x)$ vary linearly

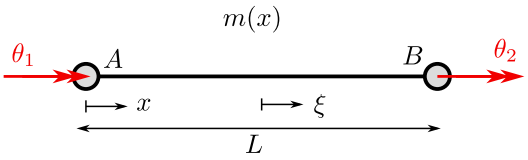

Figure D.2: Schematic representation of an isolated finite element of type "torsion".

along the element, the matrices are given by

$$\mathbf{K}_s = \begin{bmatrix} \frac{6\,(\mathrm{EI}_A+\mathrm{EI}_B)}{L^3} & \frac{2\,(2\,\mathrm{EI}_A+\mathrm{EI}_B)}{L^2} & -\frac{6\,(\mathrm{EI}_A+\mathrm{EI}_B)}{L^3} & \frac{2\,(\mathrm{EI}_A+2\,\mathrm{EI}_B)}{L^2} \\ \frac{2\,(2\,\mathrm{EI}_A+\mathrm{EI}_B)}{L^2} & \frac{3\,\mathrm{EI}_A+\mathrm{EI}_B}{L} & -\frac{2\,(2\,\mathrm{EI}_A+\mathrm{EI}_B)}{L^2} & \frac{\mathrm{EI}_A+\mathrm{EI}_B}{L} \\ -\frac{6\,(\mathrm{EI}_A+\mathrm{EI}_B)}{L^3} & -\frac{2\,(2\,\mathrm{EI}_A+\mathrm{EI}_B)}{L^2} & \frac{6\,(\mathrm{EI}_A+\mathrm{EI}_B)}{L^3} & -\frac{2\,(\mathrm{EI}_A+2\,\mathrm{EI}_B)}{L^2} \\ \frac{2\,(\mathrm{EI}_A+2\,\mathrm{EI}_B)}{L^2} & \frac{\mathrm{EI}_A+\mathrm{EI}_B}{L} & -\frac{2\,(\mathrm{EI}_A+2\,\mathrm{EI}_B)}{L^2} & \frac{\mathrm{EI}_A+3\,\mathrm{EI}_B}{L} \end{bmatrix}, \tag{D.20}$$

$$\mathbf{M}_s = \begin{bmatrix} \frac{L\,(10\,\mu_1+3\,\mu_2)}{35} & \frac{L^2\,(15\,\mu_1+7\,\mu_2)}{420} & \frac{9\,L\,(\mu_1+\mu_2)}{140} & -\frac{L^2\,(7\,\mu_1+6\,\mu_2)}{420} \\ \frac{L^2\,(15\,\mu_1+7\,\mu_2)}{420} & \frac{L^3\,(5\,\mu_1+3\,\mu_2)}{840} & \frac{L^2\,(6\,\mu_1+7\,\mu_2)}{420} & -\frac{L^3\,(\mu_1+\mu_2)}{280} \\ \frac{9\,L\,(\mu_1+\mu_2)}{140} & \frac{L^2\,(6\,\mu_1+7\,\mu_2)}{420} & \frac{L\,(3\,\mu_1+10\,\mu_2)}{35} & -\frac{L^2\,(7\,\mu_1+15\,\mu_2)}{420} \\ -\frac{L^2\,(7\,\mu_1+6\,\mu_2)}{420} & -\frac{L^3\,(\mu_1+\mu_2)}{280} & -\frac{L^2\,(7\,\mu_1+15\,\mu_2)}{420} & \frac{L^3\,(3\,\mu_1+5\,\mu_2)}{840} \end{bmatrix}, \tag{D.21}$$

$$\mathbf{g}_s = \begin{bmatrix} \frac{L\,(13\,p_a-3\,k_b)}{20} \\ \frac{L^2\,(7\,p_a-2\,k_b)}{60} \\ \frac{L\,(17\,p_a-7\,k_b)}{20} \\ -\frac{L^2\,(8\,p_a-3\,k_b)}{60} \end{bmatrix} \tag{D.22}$$

These matrices and nodal load vectors are local because they are defined at the element level, representing the contribution of a single finite element to the overall system. The stiffness and mass matrices characterize the structural properties of each element, while the nodal load vector accounts for external forces applied within the element. These local quantities will later be assembled into the global stiffness and mass matrices, which describe the entire discretized structure by enforcing continuity and equilibrium across all elements.

This formulation applies similarly to both the y- and z-direction bending problems. The derivation remains identical, with only the displacement variable $v(x)$ being replaced by either $p(x)$ or $h(x)$, corresponding to bending in the z or y plane, respectively. Consequently, the structural matrices and nodal load vector retain the same form, with the appropriate shape functions $\mathbf{N}_y(x)$ or $\mathbf{N}_z(x)$ and nodal displacement $\mathbf{a}_y$ or $\mathbf{a}_z$ used to describe the deformation in the respective plane.

D.2.2 The torsion behaviour

In this section, the torsional behaviour of a uniform rod of torsional rigidity GJ and of inertia J_p is studied under the action of a non-uniform torsional torque $m(x)$ acting along the rod. A similar process to that used in previous section is followed to derive the mass and stiffness matrices for the torsional problem.

D.2.2.A The shape functions

The kinematics of the torsion problem differs from the bending problem. In torsion, the governing differential equation is only second order compared to the 4th. order in the bending problem, meaning that a single degree-of-freedom per node is sufficient to model the torsional behaviour of the element. As a result, linear shape functions can be used for two-node torsion elements, as

illustrated in Figure D.2. These shape functions are given by

$$h_1(x) = \left(1 - \frac{x}{L}\right) \qquad \longleftrightarrow \qquad h_1(\xi) = \frac{1}{2}(1-\xi) \tag{D.23}$$

$$h_2(x) = \frac{x}{L} \qquad \longleftrightarrow \qquad h_1(\xi) = \frac{1}{2}(1+\xi)\,. \tag{D.24}$$

They are collected in the shape function vector $\mathbf{N}_\alpha(x) = \begin{bmatrix} h_1(x) & h_2(x) \end{bmatrix}$, and are such that

$$\mathbf{N}(x=0) = \begin{bmatrix} 1 & 0 \end{bmatrix}$$
$$\mathbf{N}(x=L) = \begin{bmatrix} 0 & 1 \end{bmatrix}.$$

These shape functions ensure $\mathbb{C}_0$ continuity, meaning that the torsional displacement $\alpha(x)$ is continuous across element boundaries, but its derivative may be discontinuous. Unlike the cubic Hermite polynomials used for bending, which enforce $\mathbb{C}_1$ continuity, the linear shape functions do not impose continuity on the torsional rotation gradient. This is sufficient for the torsion problem, as the governing differential equation is of second order, requiring only $\mathbb{C}_0$ continuity for a well-posed finite element formulation.

Using these shape functions, the torsional displacement inside the element is interpolated as

$$\alpha(x) \approx \tilde{\alpha}(x) = \mathbf{N}_\alpha(x)\mathbf{a}_\alpha = \mathbf{a}_\alpha^{\mathsf{T}}\mathbf{N}_\alpha^{\mathsf{T}}(x) \tag{D.25}$$

where, in this section, $\mathbf{a}_\alpha = \begin{bmatrix} \theta_1 & \theta_2 \end{bmatrix}$ is the nodal torsional displacement vector. This vector plays the same role as $\mathbf{a}$ in (D.1), but here the displacements are torsional. To avoid unnecessary heavy notation, $\mathbf{a}_\alpha$ will be designated by $\mathbf{a}$ in this section only.

D.2.2.B The weak form

The differential equation modelling the behaviour of an inertial rod of torsional rigidity GJ subjected to a non uniform torsion torque is

$$m(x) + \frac{\partial}{\partial x}\left[GJ\frac{\partial \alpha(x,t)}{\partial x}\right] = J_p\frac{\partial^2\alpha(x,t)}{\partial t^2}. \tag{D.26}$$

Forming the residual of (D.26) and integrating over the length of the rod,

$$\int_{\text{rod}} \delta\alpha(x,t)\, m(x) + \delta\alpha(x,t)\left[\frac{\partial}{\partial x}\left(GJ\frac{\partial\alpha(x,t)}{\partial x}\right)\right] \mathrm{d}x = \int_{\text{rod}} \delta\alpha(x,t)\, J_p\, \ddot{\alpha}(x,t)\, \mathrm{d}x \tag{D.27}$$

This integral can be calculated as the superposition of individual contributions at the finite element level, expressed as

$$\int_0^L \delta\alpha(x,t)\, m(x) + \delta\alpha(x,t)\left[\frac{\partial}{\partial x}\left(GJ\frac{\partial\alpha(x,t)}{\partial x}\right)\right] \mathrm{d}x = \int_0^L \delta\alpha(x,t)\, J_p\, \ddot{\alpha}(x,t)\, \mathrm{d}x. \tag{D.28}$$

Integrating by part

$$\Big[\delta\alpha\, m(x)\Big]_0^L + \int_0^L \delta\alpha(x,t)\, m(x)\, \mathrm{d}x = \int_0^L GJ\,\frac{\partial\delta\alpha}{\partial x}\frac{\partial\alpha(x,t)}{\partial x}\,\mathrm{d}x + \int_0^L \delta\alpha(x,t)\, J_p\, \ddot{\alpha}(x,t)\, \mathrm{d}x \tag{D.29}$$

Appropriate boundary conditions annihilate the first term, which is also zero even if the isolated finite element is not subjected to any boundary conditions, as the virtual torsion angle $\delta\alpha$ is arbitrary but finite, and the weak form must hold for all admissible variations, ensuring the continuity of the torsional moment $m(x)$ across element boundaries in the assembled global system. Thus

$$\int_0^L \delta\alpha\, m(x)\, \mathrm{d}x = \int_0^L GJ\,\frac{\partial\delta\alpha}{\partial x}\frac{\partial\alpha(x,t)}{\partial x}\,\mathrm{d}x + \int_0^L \delta\alpha(x,t)\, J_p\, \ddot{\alpha}(x,t)\, \mathrm{d}x. \tag{D.30}$$

D.2.2.C Determination of the structural matrices

Introducing the approximation of the displacement (D.25) in the weak form (D.30) yields

$$\int_0^L \mathbf{N}_\alpha\,\delta\mathbf{a}\,m(x) - \frac{\partial}{\partial x}(\mathbf{N}_\alpha\,\delta\mathbf{a})\,GJ\,\frac{\partial}{\partial x}(\mathbf{N}_\alpha\mathbf{a})\,\mathrm{d}x = \int_0^L \mathbf{N}_\alpha\delta\mathbf{a}\,J_p\,\mathbf{N}_\alpha\ddot{\mathbf{a}}\,\mathrm{d}x \tag{D.31}$$

Noting that $\mathbf{N}_\alpha\,\delta\mathbf{a}$ is scalar, and that $\mathbf{a}$ and $\delta\mathbf{a}$ are not functions of x, one gets

$$\delta\mathbf{a}^\mathsf{T}\left[\int_0^L J_p\,\mathbf{N}_\alpha^\mathsf{T}\mathbf{N}_\alpha + \frac{\partial\mathbf{N}_\alpha^\mathsf{T}}{\partial x}\frac{\partial\mathbf{N}_\alpha}{\partial x}\,GJ\,\mathrm{d}x\,\mathbf{a} - \int_0^L \mathbf{N}_\alpha^\mathsf{T}\,m(x)\,\mathrm{d}x\right] = 0. \tag{D.32}$$

And because $\delta\mathbf{a}^\mathsf{T}$ is arbitrary,

$$\left[\int_0^L J_p\,\mathbf{N}_\alpha^\mathsf{T}\mathbf{N}_\alpha + \frac{\partial\mathbf{N}_\alpha^\mathsf{T}}{\partial x}\frac{\partial\mathbf{N}_\alpha}{\partial x}\,GJ\,\mathrm{d}x\right]\mathbf{a} = \int_0^L \mathbf{N}_\alpha^\mathsf{T}\,m(x)\,\mathrm{d}x, \tag{D.33}$$

which results in

$$\mathbf{K}_s^\alpha\mathbf{a} + \mathbf{M}_S^\alpha\ddot{\mathbf{a}} = \mathbf{g}_s^\alpha \tag{D.34}$$

with $\mathbf{M}_s^\alpha$ referring to the mass matrix

$$\mathbf{M}_s^\alpha = \int_0^L \frac{\partial\mathbf{N}_\alpha^\mathsf{T}}{\partial x}\frac{\partial\mathbf{N}_\alpha}{\partial x}\,GJ\,\mathrm{d}x\,\mathbf{a} - \int_0^L \mathbf{N}_\alpha^\mathsf{T}\,m(x)\,\mathrm{d}x, \tag{D.35}$$

$\mathbf{K}_s^\alpha$ to the stiffness matrix

$$\mathbf{K}_s^\alpha = \int_0^L J_p\,\mathbf{N}_\alpha^\mathsf{T}\mathbf{N}_\alpha\,\mathrm{d}x, \tag{D.36}$$

and $\mathbf{g}_s$ to the nodal load vector

$$\mathbf{g}_s^\alpha = \int_0^L m(x)\,\mathbf{N}_\alpha^\mathsf{T}\,\mathrm{d}x. \tag{D.37}$$

Assuming that the torsional rigidity of the section varies linearly, the following local matrices and local vectors are obtained after analytical integration of (D.35), (D.36) and (D.37)

$$\mathbf{M}_s^\alpha = \frac{L}{12}\begin{bmatrix}3k_A + k_B & k_A + k_B\\ k_A + k_B & k_A + 3k_B\end{bmatrix},\quad \mathbf{K}_s^\alpha = \frac{k_A + k_B}{2L}\begin{bmatrix}1 & -1\\ -1 & 1\end{bmatrix},\quad \mathbf{g}_s^\alpha = \begin{bmatrix}T/2\\ T/2\end{bmatrix}$$

with $k_A = (GJ)_A$ and $k_B = (GJ)_B$ referring to the torsional rigidity GJ evaluated at nodes A and B, respectively.

D.2.3 The damping matrix

In the previous sections, only the effects of inertia and stiffness were considered in deriving the mass and stiffness matrices using the finite element method. However structural damping plays a important role in determining the system's dynamic response, particularly in stability analyses.

To incorporate the structural damping, the Rayleigh damping assumption is adopted. This approach assumes that the damping matrix $\mathbf{C}$ is a linear combination of the mass and stiffness matrices:

$$\mathbf{C} = \alpha\mathbf{M} + \beta\mathbf{K} \tag{D.38}$$

where α and β are the Rayleigh coefficients, which can be calibrated to match experimental or theoretical modal damping ratios for two specific modes of interest. Because the analysis is later carried out in modal basis, the structural nodal damping matrix is not necessarily evaluated. The modal damping matrix may directly be evaluated from (D.38).

As briefly introduced in Chapter 3, Rayleigh damping is widely used because it preserves the orthogonality of the system's wind-off eigenmodes with respect to both the damping and stiffness matrices. This property greatly simplifies the modal analysis, allowing for the uncoupled evaluation of modal damping ratios and facilitating efficient numerical computations.

In the following sections, we describe how the damping matrix is assembled under this assumption and discuss its implications for aeroelastic stability analysis.

D.2.4 Combining bending and torsion

In general, the structural behaviour of bridge decks may involve coupling between vertical bending (z), lateral bending (y), and torsional rotation (α). Such coupling can arise from geometric features of the cross-section or from non-uniform material properties, and can be incorporated into the finite element formulation through appropriate cross-stiffness and cross-mass terms. The finite element framework used in this chapter is fully compatible with such generalizations.

However, in the present work, no coupling between bending and torsion has been introduced in the structural stiffness or mass matrices. This simplification is justified by the fact that such coupling effects were not necessary for the examples and applications considered in this thesis. It also allows the formulation to remain focused on the essential ingredients required for the development of the background/resonant decomposition method.

In contrast, cross-coupling terms between degrees of freedom will be retained in the formulation of the aeroelastic matrices. While not essential for the method to function, their inclusion ensures the completeness of the formulation, especially since the derivation of the aeroelastic matrices is less well documented in the literature compared to that of structural matrices.

D.3 Formulation of the aeroelastic matrices

In the previous section, the structural mass and stiffness matrices, as well as the nodal force vector, were derived using the finite element method. In this section, we extend the formulation to include the aeroelastic contributions by deriving the aeroelastic damping and stiffness matrices.

So far, the bending and torsional problems have been treated independently, as we assumed no intrinsic coupling between them in the structural formulation. However, the introduction of aeroelastic forces fundamentally changes this, as they induce coupling between bending and torsion. A key example of this interaction is the aerodynamic torque generated by the eccentricity of the aerodynamic centre, where the aeroelastic lift is applied.

To properly account for this coupling, the complete three-dimensional bending-torsion finite element is considered. Each node of the element is associated with five degrees-of-freedom: the torsional displacement, as well as the displacement and slope for the bending motion in both the y and z planes. The degrees-of-freedom are defined and numbered as illustrated in Figure D.3. To account for all five degrees-of-freedom per node and ensure consistency with

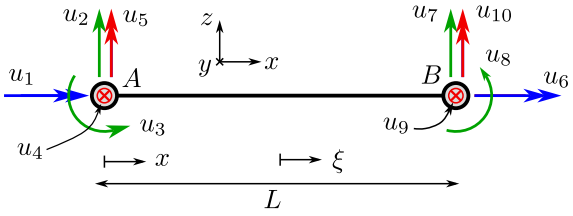

Figure D.3: Orientation and nomenclature of the degrees-of-freedom of the 3D torsion-bending element.

the numbering scheme shown in Figure D.3, the shape function vectors must be reordered and adapted accordingly.

$$\mathbf{N}_\alpha(x) = \begin{bmatrix} 1 - \frac{x}{L} & 0 & 0 & 0 & 0 & \frac{x}{L} & 0 & 0 & 0 & 0 \end{bmatrix}, \tag{D.39}$$

$$\mathbf{N}_y^{\mathsf{T}}(x) = \begin{bmatrix} 0 \\ 0 \\ 0 \\ \frac{3\,(L-2\,x)}{4\,L} - \frac{(L-2\,x)^3}{4\,L^3} + \frac{1}{2} \\ \frac{L}{8}\left(\frac{L-2\,x}{L} - \frac{(L-2\,x)^2}{L^2} - \frac{(L-2\,x)^3}{L^3} + 1\right) \\ 0 \\ 0 \\ 0 \\ \frac{(L-2\,x)^3}{4\,L^3} - \frac{3\,(L-2\,x)}{4\,L} + \frac{1}{2} \\ \frac{L}{8}\left(\frac{L-2\,x}{L} + \frac{(L-2\,x)^2}{L^2} - \frac{(L-2\,x)^3}{L^3} - 1\right) \end{bmatrix}, \qquad \mathbf{N}_z^{\mathsf{T}}(x) = \begin{bmatrix} 0 \\ \frac{3\,(L-2\,x)}{4\,L} - \frac{(L-2\,x)^3}{4\,L^3} + \frac{1}{2} \\ \frac{L}{8}\left(\frac{L-2\,x}{L} - \frac{(L-2\,x)^2}{L^2} - \frac{(L-2\,x)^3}{L^3} + 1\right) \\ 0 \\ 0 \\ 0 \\ \frac{(L-2\,x)^3}{4\,L^3} - \frac{3\,(L-2\,x)}{4\,L} + \frac{1}{2} \\ \frac{L}{8}\left(\frac{L-2\,x}{L} + \frac{(L-2\,x)^2}{L^2} - \frac{(L-2\,x)^3}{L^3} - 1\right) \\ 0 \\ 0 \end{bmatrix} \tag{D.40}$$

To clearly distinguish the contributions of the torsion and the y and z bending deformations, the shape functions vectors are used with the indexes α, y and z referring to the torsion and bending in y and z planes, respectively. At the element level, the interpolated displacement is expressed with the introduced shape function vectors $\mathbf{N}_\alpha$, $\mathbf{N}_y$ and $\mathbf{N}_z$, and a common nodal unknown vector $\mathbf{a}$ which varies in time.

$$\alpha(x,t) \approx \tilde{\alpha}(x,t) = \mathbf{N}_\alpha(x)\,\mathbf{a}(t) \tag{D.41a}$$
$$h(x,t) \approx \tilde{h}(x,t) = \mathbf{N}_y(x)\,\mathbf{a}(t) \tag{D.41b}$$
$$p(x,t) \approx \tilde{p}(x,t) = \mathbf{N}_z(x)\,\mathbf{a}(t) \tag{D.41c}$$

Starting from the expressions of the aeroelastic forces and moment (1.48)

$$m_{\text{ae}}(\omega) = \frac{1}{2}\rho U^2 B^2 \left(K A_1^* \frac{\dot{h}}{U} + K A_2^* \frac{B\dot{\alpha}}{U} + K^2 A_3^* \alpha + K^2 A_4^* \frac{h}{B} + K A_5^* \frac{\dot{p}}{U} + K^2 A_6^* \frac{p}{B}\right),$$
$$l_{\text{ae}}(\omega) = \frac{1}{2}\rho U^2 B \left(K H_1^* \frac{\dot{h}}{U} + K H_2^* \frac{B\dot{\alpha}}{U} + K^2 H_3^* \alpha + K^2 H_4^* \frac{h}{B} + K H_5^* \frac{\dot{p}}{U} + K^2 H_6^* \frac{p}{B}\right),$$
$$d_{\text{ae}}(\omega) = \frac{1}{2}\rho U^2 B \left(K P_1^* \frac{\dot{p}}{U} + K P_2^* \frac{B\dot{\alpha}}{U} + K^2 P_3^* \alpha + K^2 P_4^* \frac{p}{B} + K P_5^* \frac{\dot{h}}{U} + K^2 P_6^* \frac{h}{B}\right),$$

and substituting the approximated nodal displacements (D.41),

$$m_{\text{ae}}(\omega) = \frac{1}{2}\rho U^2 B^2 \left[\frac{K}{U}\left(A_1^* \mathbf{N}_y + B A_2^* \mathbf{N}_\alpha + A_5^* \mathbf{N}_z\right)\dot{\mathbf{a}} + \frac{K^2}{B}\left(B A_3^* \mathbf{N}_\alpha + A_4^* \mathbf{N}_y + A_6^* \mathbf{N}_z\right)\mathbf{a}\right], \tag{D.42a}$$
$$l_{\text{ae}}(\omega) = \frac{1}{2}\rho U^2 B \left[\frac{K}{U}\left(H_1^* \mathbf{N}_y + B H_2^* \mathbf{N}_\alpha + H_5^* \mathbf{N}_z\right)\dot{\mathbf{a}} + \frac{K^2}{B}\left(B H_3^* \mathbf{N}_\alpha + H_4^* \mathbf{N}_y + H_6^* \mathbf{N}_z\right)\mathbf{a}\right], \tag{D.42b}$$
$$d_{\text{ae}}(\omega) = \frac{1}{2}\rho U^2 B \left[\frac{K}{U}\left(P_1^* \mathbf{N}_z + B P_2^* \mathbf{N}_\alpha + P_5^* \mathbf{N}_z\right)\dot{\mathbf{a}} + \frac{K^2}{B}\left(B P_3^* \mathbf{N}_\alpha + P_4^* \mathbf{N}_z + P_6^* \mathbf{N}_y\right)\mathbf{a}\right]. \tag{D.42c}$$

The resulting nodal loads to apply are obtained by projecting the forces onto the shape functions basis such as shown in (D.19) and (D.37), with the only difference that the force coefficients are frequency-dependent. Starting with the aerodynamic moment,

$$\mathbf{g}_{\text{ae}}^{\alpha}(\omega) = \int_0^L \mathbf{N}_\alpha^{\mathsf{T}}(x)\, m_{\text{ae}}(\omega)\, \mathrm{d}x. \tag{D.43}$$

Developing $m_{\text{ae}}(\omega)$

$$\mathbf{g}_{\text{ae}}^{\alpha}(\omega) = \int_0^L \frac{1}{2}\rho U B^2 K\, \mathbf{N}_\alpha^{\mathsf{T}}\left(A_1^* \mathbf{N}_y + B A_2^* \mathbf{N}_\alpha + A_5^* \mathbf{N}_z\right)\mathrm{d}x\,\dot{\mathbf{a}} + \int_0^L \frac{1}{2}\rho U^2 B K^2 \mathbf{N}_\alpha^{\mathsf{T}}\left(B A_3^* \mathbf{N}_\alpha + A_4^* \mathbf{N}_y + A_6^* \mathbf{N}_z\right)\mathrm{d}x\,\mathbf{a} \tag{D.44}$$

This equation is of the form

$$\mathbf{g}_{\text{ae}}^{\alpha}(\omega) = \mathbf{C}_{\text{ae}}^{\alpha}\,\dot{\mathbf{a}} + \mathbf{K}_{\text{ae}}^{\alpha}\,\mathbf{a} \tag{D.45}$$

with $\mathbf{K}_{\text{ae}}^{\alpha}$ and $\mathbf{C}_{\text{ae}}^{\alpha}$ being stiffness and damping matrices representing the contribution of the aerodynamic moment to the damping matrix. They read

$$\mathbf{C}_{\text{ae}}^{\alpha} = \int_0^L \frac{1}{2}\rho U B^2 K \left(A_1^*\mathbf{N}_\alpha^\mathsf{T}\mathbf{N}_y + BA_2^*\mathbf{N}_\alpha^\mathsf{T}\mathbf{N}_\alpha + A_5^*\mathbf{N}_\alpha^\mathsf{T}\mathbf{N}_z\right)\mathrm{d}x \tag{D.46a}$$

$$\mathbf{K}_{\text{ae}}^{\alpha} = \int_0^L \frac{1}{2}\rho U^2 B K^2 \left(BA_3^*\mathbf{N}_\alpha^\mathsf{T}\mathbf{N}_\alpha + A_4^*\mathbf{N}_\alpha^\mathsf{T}\mathbf{N}_y + A_6^*\mathbf{N}_\alpha^\mathsf{T}\mathbf{N}_z\right)\mathrm{d}x. \tag{D.46b}$$

The same process is used to derive the lift and drag contributions to the stiffness and damping matrices, and finally obtain the lift contribution

$$\mathbf{C}_{\text{ae}}^{h} = \int_0^L \frac{1}{2}\rho U B K \left(H_1^*\mathbf{N}_y^\mathsf{T}\mathbf{N}_y + BH_2^*\mathbf{N}_y^\mathsf{T}\mathbf{N}_\alpha + H_5^*\mathbf{N}_y^\mathsf{T}\mathbf{N}_z\right)\mathrm{d}x \tag{D.47a}$$

$$\mathbf{K}_{\text{ae}}^{h} = \int_0^L \frac{1}{2}\rho U^2 K^2 \left(BH_3^*\mathbf{N}_y^\mathsf{T}\mathbf{N}_\alpha + H_4^*\mathbf{N}_y^\mathsf{T}\mathbf{N}_y + H_6^*\mathbf{N}_y^\mathsf{T}\mathbf{N}_z\right)\mathrm{d}x \tag{D.47b}$$

and the drag contribution

$$\mathbf{C}_{\text{ae}}^{p} = \int_0^L \frac{1}{2}\rho U B K \left(P_1^*\mathbf{N}_z^\mathsf{T}\mathbf{N}_y + BP_2^*\mathbf{N}_z^\mathsf{T}\mathbf{N}_\alpha + P_5^*\mathbf{N}_z^\mathsf{T}\mathbf{N}_z\right)\mathrm{d}x \tag{D.48a}$$

$$\mathbf{K}_{\text{ae}}^{p} = \int_0^L \frac{1}{2}\rho U^2 K^2 \left(BP_3^*\mathbf{N}_z^\mathsf{T}\mathbf{N}_\alpha + P_4^*\mathbf{N}_z^\mathsf{T}\mathbf{N}_y + P_6^*\mathbf{N}_z^\mathsf{T}\mathbf{N}_z\right)\mathrm{d}x. \tag{D.48b}$$

Finally, the aeroelastic damping and stiffness matrices are obtained by adding the three contributions

$$\mathbf{C}_{\text{ae}} = \mathbf{C}_{\text{ae}}^{\alpha} + \mathbf{C}_{\text{ae}}^{h} + \mathbf{C}_{\text{ae}}^{p} \tag{D.49a}$$

$$\mathbf{K}_{\text{ae}} = \mathbf{K}_{\text{ae}}^{\alpha} + \mathbf{K}_{\text{ae}}^{h} + \mathbf{K}_{\text{ae}}^{p}. \tag{D.49b}$$

Equations (D.46) to (D.48) all require the evaluation of integrals of the form

$$\mathbf{I}_{ij}(\omega) = \int_0^L f(\omega, x)\mathbf{N}_i^\mathsf{T}\mathbf{N}_j\,\mathrm{d}x \tag{D.50}$$

with i and j in $\{\alpha, y, z\}$. Given the relatively simple expressions of the shape functions, these integrals can be computed analytically when $f(\omega, x)$ has a sufficiently simple form. Assuming that $f(\omega, x)$ varies linearly along the element, it can be expressed

$$f(\omega, x) = \left[f_A(\omega) - f_B(\omega)\right]\frac{x}{L} + f_A(\omega) \tag{D.51}$$

where $f_A(\omega)$ and $f_B(\omega)$ denotes the values of $f(\omega, x)$ taken at the nodes A and B, respectively. Under this assumption, all the required integrals for i and j in $\{\alpha, y, z\}$ can be computed explicitly. The resulting expressions are provided in Appendix E.1. The formulation of a trapezoidal force $f_A \neq f_B$ allows for instance to consider skewed wind profiles, resulting from a non uniform distribution of the average wind speed along the deck due to particular topography.

In the case of a uniform wind profile and constant aeroelastic section properties, the flutter derivatives depend only on the frequency and remain constant over the element length. Consequently, f is purely frequency-dependent and can be factored out of the integrals in (D.46) to (D.48). This allows these integrals to be computed once for all frequencies, after which they are simply scaled by f and the flutter derivatives sampled at the considered frequency ω

$$\begin{aligned}\mathbf{C}_{\text{ae}}(\omega) = {} & \frac{1}{2}\rho B^3\omega\left[A_1^*\mathbf{I}_{\alpha y}^* + BA_2^*\mathbf{I}_{\alpha\alpha}^* + A_5^*\mathbf{I}_{\alpha z}^*\right] + \frac{1}{2}\rho B^2\omega\left[H_1^*\mathbf{I}_{yy}^* + BH_2^*\mathbf{I}_{y\alpha}^* + H_5^*\mathbf{I}_{\alpha z}^*\right] \\ & + \frac{1}{2}\rho B^2\omega\left[P_1^*\mathbf{I}_{zy}^* + BP_2^*\mathbf{I}_{z\alpha}^* + P_5^*\mathbf{I}_{zz}^*\right],\end{aligned} \tag{D.52}$$

$$\mathbf{K}_{\text{ae}}(\omega) = \frac{1}{2}\rho B^3\omega^2\left[A_3^*\mathbf{I}_{\alpha\alpha}^* + BA_4^*\mathbf{I}_{\alpha y}^* + A_6^*\mathbf{I}_{\alpha z}^*\right] + \frac{1}{2}\rho B^2\omega^2\left[H_3^*\mathbf{I}_{y\alpha}^* + BH_4^*\mathbf{I}_{yy}^* + H_6^*\mathbf{I}_{yz}^*\right] + \frac{1}{2}\rho B^2\omega^2\left[P_3^*\mathbf{I}_{z\alpha}^* + BP_4*\mathbf{I}_{zy}^* + P_6^*\mathbf{I}_{zz}^*\right], \quad \text{(D.53)}$$

where $\mathbf{I}_{ij}^*$ is defined as the integral

$$\mathbf{I}_{ij}^* = \int_0^L \mathbf{N}_i^\mathsf{T}\mathbf{N}_j\,\mathrm{d}x, \quad \text{(D.54)}$$

with i and j in $\{\alpha, y, z\}$ (see Appendix E.1 for analytical expressions). While the direct computational savings from this approach may seem marginal due to the small size of the local aeroelastic matrices in (D.46) to (D.48), the benefits become significant when the deck section and wind profile remain uniform across all finite elements. In that case, this method avoids the repeated assembly of local elementary matrices to the global system matrices.

The general idea to reduce the computational burden for such case is that all local aeroelastic integrals $\mathbf{I}_{ij}^*$ for i and j in $\{\alpha, y, z\}$ can be precomputed and stored in 18 reference global aeroelastic matrices. The final aeroelastic damping and stiffness matrices are then obtained by scaling these reference matrices according to (D.52) and (D.53) at the chosen frequency. If a modal analysis is performed, an additional efficiency gain can be achieved by first projecting these 18 reference matrices onto the modal basis before storage, ensuring that the modal aeroelastic matrices can be efficiently evaluated when needed.

D.4 Formulation of the buffeting forces

In the introduction, the aerodynamic forces—drag, lift, and moment—were presented in (1.26). These expressions were derived for a single cross-section of the deck, considering the local deck motions $\dot{p}$, $\dot{h}$, $\dot{\alpha}$ and the wind turbulence components u and w at the same location. This section extends the formulation to model the aerodynamic forces acting on the entire structure and the associated power spectral density matrix.

Starting from (1.26), and neglecting all the motion-induced terms already incorporated in the aeroelastic matrices derived in previous section, the lift, drag and moment simplify to

$$F_L = \frac{1}{2}\rho U^2 B\left[\bar{C}_L + 2\bar{C}_L\frac{u(t)}{U} + (\bar{C}_L' + \bar{C}_D)\frac{w(t)}{U}\right], \quad \text{(D.55a)}$$

$$F_D = \frac{1}{2}\rho U^2 B\left[\bar{C}_D + 2\bar{C}_D\frac{u(t)}{U} + (\bar{C}_D' - \bar{C}_L)\frac{w(t)}{U}\right], \quad \text{(D.55b)}$$

$$F_M = \frac{1}{2}\rho U^2 B^2\left[\bar{C}_M + 2\bar{C}_M\frac{u(t)}{U} + \bar{C}_M'\frac{w(t)}{U}\right]. \quad \text{(D.55c)}$$

The fields of fluctuating wind speeds $u(t)$ and $w(t)$ are determined from their power spectral density matrix, as introduced in Section 1.1, which provides wind speed values at the system's nodes. In the same way that a continuous displacement field was reconstructed at the element level in the previous section, a continuous wind profile can be inferred from the discrete wind field using shape functions.

Figure D.4 illustrates a finite element and the interpolated wind speed profile for $u(t)$ using linear shape functions. The wind velocities along the finite element are given by

$$u(x,t) = \mathbf{N}_e(x)\mathbf{u}(t) \qquad \text{and} \qquad w(x,t) = \mathbf{N}_e(x)\mathbf{w}(t) \quad \text{(D.56)}$$

where $\mathbf{u}(t) = \begin{bmatrix} u_A(t) & u_B(t)\end{bmatrix}$ and $\mathbf{w}(t) = \begin{bmatrix} w_A(t) & w_B(t)\end{bmatrix}$ are the local nodal wind velocities, and $\mathbf{N}_e(x)$ is the shape function matrix,

$$\mathbf{N}_e(x) = \begin{bmatrix} 1 - \dfrac{x}{L}, & \dfrac{x}{L}\end{bmatrix}. \quad \text{(D.57)}$$

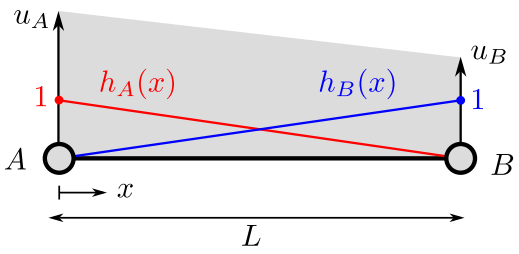

Figure D.4: Illustration of the interpolation of the wind velocity u field in a finite element.

Equation (D.56) assumes that $u(x,t)$ and $v(x,t)$ follow the same profile as the shape functions $\mathbf{N}(x)$, in space. This assumption is valid at low frequency (large eddies) but is conservative at high frequency. As for other interpolation schemes, an admittance correction can be applied to correct this [147]. The lift contribution to nodal load vector $\mathbf{f}^y$ is evaluated by projecting the lift force onto the shape functions vector $\mathbf{N}_y$ and integrating over the length of the element

$$\mathbf{f}^y = \int_0^L \mathbf{N}_y^\mathsf{T} F_L(x,t)\,\mathrm{d}x. \tag{D.58}$$

Substituting (D.55a) and (D.56),

$$\mathbf{f}^y = \frac{1}{2}\rho U^2 B \left[\bar{C}_L \int_0^L \mathbf{N}_y^\mathsf{T}(x)\,\mathrm{d}x + \frac{2}{U}\int_0^L \mathbf{N}_y^\mathsf{T}\mathbf{N}_e(x)\,\mathrm{d}x\,\left[\bar{C}_L\,\mathbf{u} + (\bar{C}'_L + \bar{C}_D)\,\mathbf{w}\right]\right]. \tag{D.59}$$

Introducing the force coefficient matrices $\mathbf{A}_u^y$ and $\mathbf{A}_w^y$ and the mean force vector $\mathbf{b}^y$, this expression becomes

$$\mathbf{f}^y = \mathbf{A}_u^y\mathbf{u} + \mathbf{A}_w^y\mathbf{w} + \mathbf{b}^y \tag{D.60}$$

with

$$\mathbf{A}_u^y = \rho U B \bar{C}_L \mathbf{I}_{ye}^* \tag{D.61}$$

$$\mathbf{A}_u^y = \frac{1}{2}\rho U B (\bar{C}'_L + \bar{C}_D)\mathbf{I}_{ye}^* \tag{D.62}$$

$$\mathbf{b}^y = \frac{1}{2}\rho U^2 B \bar{C}_L \mathbf{I}_{y1}^*. \tag{D.63}$$

where $\mathbf{I}_{ye}^*$ and $\mathbf{I}_{y1}^*$ are obtained from (D.54) with $i = y$ and $j = e$ or $\mathbf{N}_j = [1]$ when $j = 1$. Analytical expressions of these reference integrals are detailed in Appendix E.2.

The same process is used to get the drag and moment contributions to the nodal loads

$$\mathbf{g}^z = \mathbf{A}_u^z\mathbf{u} + \mathbf{A}_w^z\mathbf{w} + \mathbf{b}^z \qquad \text{and} \qquad \mathbf{g}^\alpha = \mathbf{A}_u^\alpha\mathbf{u} + \mathbf{A}_w^\alpha\mathbf{w} + \mathbf{b}^\alpha \tag{D.64}$$

with

$$\mathbf{A}_u^z = \frac{1}{2}\rho U B\, 2\bar{C}_D\, \mathbf{I}_{ze}^* \qquad \mathbf{A}_u^\alpha = \frac{1}{2}\rho U B\, 2\bar{C}_D\, \mathbf{I}_{\alpha e}^* \tag{D.65}$$

$$\mathbf{A}_u^z = \frac{1}{2}\rho U B\, (\bar{C}'_D + \bar{C}_L)\, \mathbf{I}_{ze}^* \qquad \mathbf{A}_u^\alpha = \frac{1}{2}\rho U B\, (\bar{C}'_D + \bar{C}_L)\, \mathbf{I}_{\alpha e}^* \tag{D.66}$$

$$\mathbf{b}^z = \frac{1}{2}\rho U^2 B\, \bar{C}_D\, \mathbf{I}_{z1}^* \qquad \mathbf{b}^\alpha = \frac{1}{2}\rho U^2 B\, \bar{C}_D\, \mathbf{I}_{\alpha 1}^*. \tag{D.67}$$

The resulting nodal load vector related to the buffeting forces $\mathbf{f}_{\mathrm{bu}}(t)$ is obtained from the superposition of the three contributions

$$\mathbf{f}_{\mathrm{bu}}(t) = \mathbf{g}^\alpha(t) + \mathbf{g}^y(t) + \mathbf{g}^z(t) = \mathbf{A}_u\,\mathbf{u}(t) + \mathbf{A}_w\,\mathbf{w}(t) + \mathbf{b} \tag{D.68}$$

with $\mathbf{A}_u$, $\mathbf{A}_w$ buffeting force coefficient matrices

$$\mathbf{A}_u = \mathbf{A}_u^{\alpha} + \mathbf{A}_u^{y} + \mathbf{A}_u^{z} \qquad \text{and} \qquad \mathbf{A}_w = \mathbf{A}_w^{\alpha} + \mathbf{A}_w^{y} + \mathbf{A}_w^{z} \tag{D.69}$$

and $\mathbf{b}$ the nodal static force vector

$$\mathbf{b} = \mathbf{b}^{\alpha} + \mathbf{b}^{y} + \mathbf{b}^{z}. \tag{D.70}$$

Considering the frequency representation $\mathbf{f}_{\text{bu}}(\omega)$ of the fluctuating part of the loading, the power spectral density of the nodal forces is calculated as follows

$$\mathbf{S}_{\mathbf{f}_{\text{bu}}}(\omega) = \lim_{T\to\infty} \frac{2\pi}{T} \mathbb{E}\big[\mathbf{f}_{\text{bu}}(\omega) \cdot \mathbf{f}_{\text{bu}}^{*}(\omega)\big] = \lim_{T\to\infty} \frac{2\pi}{T} \mathbb{E}\Big[\left(\mathbf{A}_u \mathbf{u} + \mathbf{A}_w \mathbf{w}\right) \left(\mathbf{u}^{*} \mathbf{A}_u^{\mathsf{T}} + \mathbf{w}^{*} \mathbf{A}_w^{\mathsf{T}}\right) \Big]. \tag{D.71}$$

Expanding the product, and identifying the definition of the power spectral density matrix of two vectors $\mathbf{x}$ and $\mathbf{y}$

$$\mathbf{S}_{\mathbf{xy}}(\omega) = \lim_{T\to\infty} \frac{2\pi}{T} \mathbb{E}\big[\mathbf{x}\mathbf{y}^{\mathsf{T}}\big] \tag{D.72}$$

conducts to

$$\mathbf{S}_{\mathbf{f}_{\text{bu}}}(\omega) = \mathbf{A}_u \mathbf{S}_{\mathbf{uu}}(\omega) \mathbf{A}_u^{\mathsf{T}} + \mathbf{A}_w \mathbf{S}_{\mathbf{ww}}(\omega) \mathbf{A}_w^{\mathsf{T}} + \mathbf{A}_u \mathbf{S}_{\mathbf{uw}}(\omega) \mathbf{A}_w^{\mathsf{T}} + \mathbf{A}_w \mathbf{S}_{\mathbf{wu}}(\omega) \mathbf{A}_u^{\mathsf{T}}. \tag{D.73}$$

The cross power spectral densities $\mathbf{S}_{\mathbf{uw}}(\omega)$ characterize the coherence between the turbulent wind fields $u(x, y, z, t)$ and $w(x, y, z, t)$. It has been reported that this coherence is negligible [15], in which case the last two terms are zero and the power spectral density matrix of the buffeting forces simplifies to

$$\mathbf{S}_{\mathbf{f}_{\text{bu}}}(\omega) = \mathbf{A}_u \mathbf{S}_{\mathbf{uu}}(\omega) \mathbf{A}_u^{\mathsf{T}} + \mathbf{A}_w \mathbf{S}_{\mathbf{ww}}(\omega) \mathbf{A}_w^{\mathsf{T}}. \tag{D.74}$$

This matrix is the local element matrix in nodal basis. The global matrix is assembled by adding all the elementary contributions. If a modal analysis is carried out, the power spectral density of the modal forces is obtained by

$$\mathbf{S}_{\mathbf{f}_{\text{bu}}^{*}}(\omega) = \mathbf{\Phi}^{\mathsf{T}} \mathbf{S}_{\mathbf{f}_{\text{bu}}^{*}}(\omega) \mathbf{\Phi} = \mathbf{\Phi}^{\mathsf{T}} \mathbf{A}_u \mathbf{S}_{\mathbf{uu}}(\omega) \mathbf{A}_u^{\mathsf{T}} \mathbf{\Phi} + \mathbf{\Phi}^{\mathsf{T}} \mathbf{A}_w \mathbf{S}_{\mathbf{ww}}(\omega) \mathbf{A}_w^{\mathsf{T}} \mathbf{\Phi}. \tag{D.75}$$

In the last expression, only the power spectral density matrices $\mathbf{S}_{\mathbf{uu}}$ and $\mathbf{S}_{\mathbf{ww}}$ are frequency-dependent. To minimize the computational load, it is interesting to first project the matrices $\mathbf{A}_u$ and $\mathbf{A}_w$ on the modes shapes $\mathbf{\Phi}^{\mathsf{T}}$ once, and store these intermediate results, which can be used to evaluate the modal PSD of the forces for all frequencies

$$\mathbf{S}_{\mathbf{f}_{\text{bu}}^{*}}(\omega) = \mathbf{A}_u^{\dagger} \mathbf{S}_{\mathbf{uu}}(\omega) \mathbf{A}^{\dagger}{}_u^{\mathsf{T}} + \mathbf{A}_w^{\dagger} \mathbf{S}_{\mathbf{ww}}(\omega) \mathbf{A}^{\dagger}{}_w^{\mathsf{T}} \tag{D.76}$$

with

$$\mathbf{A}_u^{\dagger} = \mathbf{\Phi}^{\mathsf{T}} \mathbf{A}_u \qquad \text{and} \qquad \mathbf{A}_w^{\dagger} = \mathbf{\Phi}^{\mathsf{T}} \mathbf{A}_w. \tag{D.77}$$

D.5 Conclusion

This appendix chapter provided an essential groundwork for the application of the MTSA methodology to MDOF aeroelastic systems, focusing on the mathematical establishment of the aerodynamic loads in large systems. The main objective was to formalize the derivation of the aeroelastic stiffness and damping matrices, as well as the buffeting force power spectral density matrix, using the finite element method.

The chosen finite elements account for the possibility of linearly varying static loads along the bridge span, enabling the representation of nonuniform wind profiles or varying section properties—conditions sometimes encountered in practical bridge design. The projection of nodal matrices into the modal basis was also briefly addressed, notably to mention the potential source of computational load savings.

This appendix chapter concentrated exclusively on local element matrices. The standard procedures required for assembling the global system matrices were intentionally omitted, as they are well-documented in finite element literature. The complete aeroelastic matrices developed here is used as input for the full MDOF buffeting analysis presented in chapter 4.

Appendix E

Shape function integrals for aeroelastic matrices of damping and stiffness, and PSD matrices

E.1 Trapezoidal aeroelastic force profile

Here are presented the analytical results of the integrals

$$\mathbf{I}^*_{ij} = \int_0^L \left[(b-a)\frac{x}{L} + a\right] \cdot \mathbf{N}_i^T \mathbf{N}_j \, \mathrm{d}x \tag{E.1}$$

with i and j in $\{\alpha, y, z\}$, and with a and b being complex numbers. The vectors $\mathbf{N}_\alpha$, $\mathbf{N}_i$ and $\mathbf{N}_j$ are the shape functions vectors, here expressed as

$$\mathbf{N}_\alpha(x) = \begin{bmatrix} 1 - \frac{x}{L} & 0 & 0 & 0 & 0 & \frac{x}{L} & 0 & 0 & 0 & 0 \end{bmatrix}, \tag{E.2}$$

$$\mathbf{N}_y^\intercal(x) = \begin{bmatrix} 0 \\ \frac{3\,(L-2\,x)}{4\,L} - \frac{(L-2\,x)^3}{4\,L^3} + \frac{1}{2} \\ \frac{L}{8}\left(\frac{L-2\,x}{L} - \frac{(L-2\,x)^2}{L^2} - \frac{(L-2\,x)^3}{L^3} + 1\right) \\ 0 \\ 0 \\ 0 \\ \frac{(L-2\,x)^3}{4\,L^3} - \frac{3\,(L-2\,x)}{4\,L} + \frac{1}{2} \\ \frac{L}{8}\left(\frac{L-2\,x}{L} + \frac{(L-2\,x)^2}{L^2} - \frac{(L-2\,x)^3}{L^3} - 1\right) \\ 0 \\ 0 \end{bmatrix}, \qquad \mathbf{N}_z^\intercal(x) = \begin{bmatrix} 0 \\ 0 \\ 0 \\ \frac{3\,(L-2\,x)}{4\,L} - \frac{(L-2\,x)^3}{4\,L^3} + \frac{1}{2} \\ \frac{L}{8}\left(\frac{L-2\,x}{L} - \frac{(L-2\,x)^2}{L^2} - \frac{(L-2\,x)^3}{L^3} + 1\right) \\ 0 \\ 0 \\ 0 \\ \frac{(L-2\,x)^3}{4\,L^3} - \frac{3\,(L-2\,x)}{4\,L} + \frac{1}{2} \\ \frac{L}{8}\left(\frac{L-2\,x}{L} + \frac{(L-2\,x)^2}{L^2} - \frac{(L-2\,x)^3}{L^3} - 1\right) \end{bmatrix} \tag{E.3}$$

$$\mathbf{I}^*_{\alpha\alpha} = \begin{pmatrix} \frac{L\,(5\,a-b)}{12} & 0 & 0 & 0 & 0 & \frac{L\,(3\,a-b)}{12} & 0 & 0 & 0 & 0 \\ 0 & 0 & 0 & 0 & 0 & 0 & 0 & 0 & 0 & 0 \\ 0 & 0 & 0 & 0 & 0 & 0 & 0 & 0 & 0 & 0 \\ 0 & 0 & 0 & 0 & 0 & 0 & 0 & 0 & 0 & 0 \\ 0 & 0 & 0 & 0 & 0 & 0 & 0 & 0 & 0 & 0 \\ \frac{L\,(3\,a-b)}{12} & 0 & 0 & 0 & 0 & \frac{L\,(7\,a-3\,b)}{12} & 0 & 0 & 0 & 0 \\ 0 & 0 & 0 & 0 & 0 & 0 & 0 & 0 & 0 & 0 \\ 0 & 0 & 0 & 0 & 0 & 0 & 0 & 0 & 0 & 0 \\ 0 & 0 & 0 & 0 & 0 & 0 & 0 & 0 & 0 & 0 \\ 0 & 0 & 0 & 0 & 0 & 0 & 0 & 0 & 0 & 0 \end{pmatrix} \tag{E.4}$$

$$\mathbf{I}^*_{\alpha y} = \begin{pmatrix} 0 & \frac{L\,(26\,a-5\,b)}{60} & \frac{L^2\,(4\,a-b)}{60} & 0 & 0 & 0 & \frac{L\,(14\,a-5\,b)}{60} & -\frac{L^2\,(3\,a-b)}{60} & 0 & 0 \\ 0 & 0 & 0 & 0 & 0 & 0 & 0 & 0 & 0 & 0 \\ 0 & 0 & 0 & 0 & 0 & 0 & 0 & 0 & 0 & 0 \\ 0 & 0 & 0 & 0 & 0 & 0 & 0 & 0 & 0 & 0 \\ 0 & 0 & 0 & 0 & 0 & 0 & 0 & 0 & 0 & 0 \\ 0 & \frac{L\,(13\,a-4\,b)}{60} & \frac{L^2\,(3\,a-b)}{60} & 0 & 0 & 0 & \frac{L\,(37\,a-16\,b)}{60} & -\frac{L^2\,(5\,a-2\,b)}{60} & 0 & 0 \\ 0 & 0 & 0 & 0 & 0 & 0 & 0 & 0 & 0 & 0 \\ 0 & 0 & 0 & 0 & 0 & 0 & 0 & 0 & 0 & 0 \\ 0 & 0 & 0 & 0 & 0 & 0 & 0 & 0 & 0 & 0 \\ 0 & 0 & 0 & 0 & 0 & 0 & 0 & 0 & 0 & 0 \end{pmatrix} \tag{E.5}$$

$$\mathbf{I}^*_{\alpha z} = \begin{pmatrix} 0 & 0 & 0 & \frac{L\,(26\,a-5\,b)}{60} & \frac{L^2\,(4\,a-b)}{60} & 0 & 0 & 0 & \frac{L\,(14\,a-5\,b)}{60} & -\frac{L^2\,(3\,a-b)}{60} \\ 0 & 0 & 0 & 0 & 0 & 0 & 0 & 0 & 0 & 0 \\ 0 & 0 & 0 & 0 & 0 & 0 & 0 & 0 & 0 & 0 \\ 0 & 0 & 0 & 0 & 0 & 0 & 0 & 0 & 0 & 0 \\ 0 & 0 & 0 & 0 & 0 & 0 & 0 & 0 & 0 & 0 \\ 0 & 0 & 0 & \frac{L\,(13\,a-4\,b)}{60} & \frac{L^2\,(3\,a-b)}{60} & 0 & 0 & 0 & \frac{L\,(37\,a-16\,b)}{60} & -\frac{L^2\,(5\,a-2\,b)}{60} \\ 0 & 0 & 0 & 0 & 0 & 0 & 0 & 0 & 0 & 0 \\ 0 & 0 & 0 & 0 & 0 & 0 & 0 & 0 & 0 & 0 \\ 0 & 0 & 0 & 0 & 0 & 0 & 0 & 0 & 0 & 0 \\ 0 & 0 & 0 & 0 & 0 & 0 & 0 & 0 & 0 & 0 \end{pmatrix} \tag{E.6}$$

$$\mathbf{I}^*_{y\alpha} = \begin{pmatrix} 0 & 0 & 0 & 0 & 0 & 0 & 0 & 0 & 0 & 0 \\ \frac{L\,(26\,a-5\,b)}{60} & 0 & 0 & 0 & 0 & \frac{L\,(13\,a-4\,b)}{60} & 0 & 0 & 0 & 0 \\ \frac{L^2\,(4\,a-b)}{60} & 0 & 0 & 0 & 0 & \frac{L^2\,(3\,a-b)}{60} & 0 & 0 & 0 & 0 \\ 0 & 0 & 0 & 0 & 0 & 0 & 0 & 0 & 0 & 0 \\ 0 & 0 & 0 & 0 & 0 & 0 & 0 & 0 & 0 & 0 \\ 0 & 0 & 0 & 0 & 0 & 0 & 0 & 0 & 0 & 0 \\ \frac{L\,(14\,a-5\,b)}{60} & 0 & 0 & 0 & 0 & \frac{L\,(37\,a-16\,b)}{60} & 0 & 0 & 0 & 0 \\ -\frac{L^2\,(3\,a-b)}{60} & 0 & 0 & 0 & 0 & -\frac{L^2\,(5\,a-2\,b)}{60} & 0 & 0 & 0 & 0 \\ 0 & 0 & 0 & 0 & 0 & 0 & 0 & 0 & 0 & 0 \\ 0 & 0 & 0 & 0 & 0 & 0 & 0 & 0 & 0 & 0 \end{pmatrix} \tag{E.7}$$

$$\mathbf{I}^*_{yy} = \begin{pmatrix} 0 & 0 & 0 & 0 & 0 & 0 & 0 & 0 & 0 & 0 \\ 0 & \frac{L\,(16\,a-3\,b)}{35} & \frac{L^2\,(29\,a-7\,b)}{420} & 0 & 0 & 0 & \frac{9\,L\,(3\,a-b)}{140} & -\frac{L^2\,(19\,a-6\,b)}{420} & 0 & 0 \\ 0 & \frac{L^2\,(29\,a-7\,b)}{420} & \frac{L^3\,(11\,a-3\,b)}{840} & 0 & 0 & 0 & \frac{L^2\,(20\,a-7\,b)}{420} & -\frac{L^3\,(3\,a-b)}{280} & 0 & 0 \\ 0 & 0 & 0 & 0 & 0 & 0 & 0 & 0 & 0 & 0 \\ 0 & 0 & 0 & 0 & 0 & 0 & 0 & 0 & 0 & 0 \\ 0 & 0 & 0 & 0 & 0 & 0 & 0 & 0 & 0 & 0 \\ 0 & \frac{9\,L\,(3\,a-b)}{140} & \frac{L^2\,(20\,a-7\,b)}{420} & 0 & 0 & 0 & \frac{L\,(23\,a-10\,b)}{35} & -\frac{L^2\,(37\,a-15\,b)}{420} & 0 & 0 \\ 0 & -\frac{L^2\,(19\,a-6\,b)}{420} & -\frac{L^3\,(3\,a-b)}{280} & 0 & 0 & 0 & -\frac{L^2\,(37\,a-15\,b)}{420} & \frac{L^3\,(13\,a-5\,b)}{840} & 0 & 0 \\ 0 & 0 & 0 & 0 & 0 & 0 & 0 & 0 & 0 & 0 \\ 0 & 0 & 0 & 0 & 0 & 0 & 0 & 0 & 0 & 0 \end{pmatrix} \tag{E.8}$$

$$\mathbf{I}^*_{yz} = \begin{pmatrix} 0 & 0 & 0 & 0 & 0 & 0 & 0 & 0 & 0 & 0 \\ 0 & 0 & 0 & \frac{L\,(16\,a-3\,b)}{35} & \frac{L^2\,(29\,a-7\,b)}{420} & 0 & 0 & 0 & \frac{9\,L\,(3\,a-b)}{140} & -\frac{L^2\,(19\,a-6\,b)}{420} \\ 0 & 0 & 0 & \frac{L^2\,(29\,a-7\,b)}{420} & \frac{L^3\,(11\,a-3\,b)}{840} & 0 & 0 & 0 & \frac{L^2\,(20\,a-7\,b)}{420} & -\frac{L^3\,(3\,a-b)}{280} \\ 0 & 0 & 0 & 0 & 0 & 0 & 0 & 0 & 0 & 0 \\ 0 & 0 & 0 & 0 & 0 & 0 & 0 & 0 & 0 & 0 \\ 0 & 0 & 0 & 0 & 0 & 0 & 0 & 0 & 0 & 0 \\ 0 & 0 & 0 & \frac{9\,L\,(3\,a-b)}{140} & \frac{L^2\,(20\,a-7\,b)}{420} & 0 & 0 & 0 & \frac{L\,(23\,a-10\,b)}{35} & -\frac{L^2\,(37\,a-15\,b)}{420} \\ 0 & 0 & 0 & -\frac{L^2\,(19\,a-6\,b)}{420} & -\frac{L^3\,(3\,a-b)}{280} & 0 & 0 & 0 & -\frac{L^2\,(37\,a-15\,b)}{420} & \frac{L^3\,(13\,a-5\,b)}{840} \\ 0 & 0 & 0 & 0 & 0 & 0 & 0 & 0 & 0 & 0 \\ 0 & 0 & 0 & 0 & 0 & 0 & 0 & 0 & 0 & 0 \end{pmatrix} \tag{E.9}$$

$$\mathbf{I}^*_{z\alpha} = \begin{pmatrix} 0 & 0 & 0 & 0 & 0 & 0 & 0 & 0 & 0 & 0 \\ 0 & 0 & 0 & 0 & 0 & 0 & 0 & 0 & 0 & 0 \\ 0 & 0 & 0 & 0 & 0 & 0 & 0 & 0 & 0 & 0 \\ \frac{L\,(26\,a-5\,b)}{60} & 0 & 0 & 0 & 0 & \frac{L\,(13\,a-4\,b)}{60} & 0 & 0 & 0 & 0 \\ \frac{L^2\,(4\,a-b)}{60} & 0 & 0 & 0 & 0 & \frac{L^2\,(3\,a-b)}{60} & 0 & 0 & 0 & 0 \\ 0 & 0 & 0 & 0 & 0 & 0 & 0 & 0 & 0 & 0 \\ 0 & 0 & 0 & 0 & 0 & 0 & 0 & 0 & 0 & 0 \\ 0 & 0 & 0 & 0 & 0 & 0 & 0 & 0 & 0 & 0 \\ \frac{L\,(14\,a-5\,b)}{60} & 0 & 0 & 0 & 0 & \frac{L\,(37\,a-16\,b)}{60} & 0 & 0 & 0 & 0 \\ -\frac{L^2\,(3\,a-b)}{60} & 0 & 0 & 0 & 0 & -\frac{L^2\,(5\,a-2\,b)}{60} & 0 & 0 & 0 & 0 \end{pmatrix} \tag{E.10}$$

$$\mathbf{I}^*_{zy} = \begin{pmatrix} 0 & 0 & 0 & 0 & 0 & 0 & 0 & 0 & 0 & 0 \\ 0 & 0 & 0 & 0 & 0 & 0 & 0 & 0 & 0 & 0 \\ 0 & 0 & 0 & 0 & 0 & 0 & 0 & 0 & 0 & 0 \\ 0 & \frac{L\,(16\,a-3\,b)}{35} & \frac{L^2\,(29\,a-7\,b)}{420} & 0 & 0 & 0 & \frac{9\,L\,(3\,a-b)}{140} & -\frac{L^2\,(19\,a-6\,b)}{420} & 0 & 0 \\ 0 & \frac{L^2\,(29\,a-7\,b)}{420} & \frac{L^3\,(11\,a-3\,b)}{840} & 0 & 0 & 0 & \frac{L^2\,(20\,a-7\,b)}{420} & -\frac{L^3\,(3\,a-b)}{280} & 0 & 0 \\ 0 & 0 & 0 & 0 & 0 & 0 & 0 & 0 & 0 & 0 \\ 0 & 0 & 0 & 0 & 0 & 0 & 0 & 0 & 0 & 0 \\ 0 & 0 & 0 & 0 & 0 & 0 & 0 & 0 & 0 & 0 \\ 0 & \frac{9\,L\,(3\,a-b)}{140} & \frac{L^2\,(20\,a-7\,b)}{420} & 0 & 0 & 0 & \frac{L\,(23\,a-10\,b)}{35} & -\frac{L^2\,(37\,a-15\,b)}{420} & 0 & 0 \\ 0 & -\frac{L^2\,(19\,a-6\,b)}{420} & -\frac{L^3\,(3\,a-b)}{280} & 0 & 0 & 0 & -\frac{L^2\,(37\,a-15\,b)}{420} & \frac{L^3\,(13\,a-5\,b)}{840} & 0 & 0 \end{pmatrix} \tag{E.11}$$

$$\mathbf{I}^*_{zz} = \begin{pmatrix} 0 & 0 & 0 & 0 & 0 & 0 & 0 & 0 & 0 & 0 \\ 0 & 0 & 0 & 0 & 0 & 0 & 0 & 0 & 0 & 0 \\ 0 & 0 & 0 & 0 & 0 & 0 & 0 & 0 & 0 & 0 \\ 0 & 0 & 0 & \frac{L\,(16\,a-3\,b)}{35} & \frac{L^2\,(29\,a-7\,b)}{420} & 0 & 0 & 0 & \frac{9\,L\,(3\,a-b)}{140} & -\frac{L^2\,(19\,a-6\,b)}{420} \\ 0 & 0 & 0 & \frac{L^2\,(29\,a-7\,b)}{420} & \frac{L^3\,(11\,a-3\,b)}{840} & 0 & 0 & 0 & \frac{L^2\,(20\,a-7\,b)}{420} & -\frac{L^3\,(3\,a-b)}{280} \\ 0 & 0 & 0 & 0 & 0 & 0 & 0 & 0 & 0 & 0 \\ 0 & 0 & 0 & 0 & 0 & 0 & 0 & 0 & 0 & 0 \\ 0 & 0 & 0 & 0 & 0 & 0 & 0 & 0 & 0 & 0 \\ 0 & 0 & 0 & \frac{9\,L\,(3\,a-b)}{140} & \frac{L^2\,(20\,a-7\,b)}{420} & 0 & 0 & 0 & \frac{L\,(23\,a-10\,b)}{35} & -\frac{L^2\,(37\,a-15\,b)}{420} \\ 0 & 0 & 0 & -\frac{L^2\,(19\,a-6\,b)}{420} & -\frac{L^3\,(3\,a-b)}{280} & 0 & 0 & 0 & -\frac{L^2\,(37\,a-15\,b)}{420} & \frac{L^3\,(13\,a-5\,b)}{840} \end{pmatrix} \tag{E.12}$$

E.2 Particular integral for the constituting of the nodal load vector

The following section presents the results of the following integral

$$\mathbf{I}^*_{ie} = \int_0^L \mathbf{N}_i(x)\mathbf{N}_e(x)\,\mathrm{d}x \tag{E.13}$$

$\mathbf{N}_i$ being the shape function vector associated with the degree-of-freedom in the $\{\alpha, y, z\}$ direction, and $\mathbf{N}_e$ the linear shape function vector associated with the left and right nodes of a two-node finite element $\mathbf{N}_e(x) = \left[1 - \frac{x}{L}, \quad \frac{x}{L}\right]$.

$$\mathbf{I}^*_{\alpha e} = \begin{pmatrix} \frac{L}{3} & \frac{L}{6} \\ 0 & 0 \\ 0 & 0 \\ 0 & 0 \\ 0 & 0 \\ \frac{L}{6} & \frac{L}{3} \\ 0 & 0 \\ 0 & 0 \\ 0 & 0 \\ 0 & 0 \end{pmatrix}, \qquad \mathbf{I}^*_{ye} = \begin{pmatrix} 0 & 0 \\ \frac{7\,L}{20} & \frac{3\,L}{20} \\ \frac{L^2}{20} & \frac{L^2}{30} \\ 0 & 0 \\ 0 & 0 \\ 0 & 0 \\ \frac{3\,L}{20} & \frac{7\,L}{20} \\ -\frac{L^2}{30} & -\frac{L^2}{20} \\ 0 & 0 \\ 0 & 0 \end{pmatrix}, \qquad \mathbf{I}^*_{ze} = \begin{pmatrix} 0 & 0 \\ 0 & 0 \\ 0 & 0 \\ \frac{7\,L}{20} & \frac{3\,L}{20} \\ \frac{L^2}{20} & \frac{L^2}{30} \\ 0 & 0 \\ 0 & 0 \\ 0 & 0 \\ \frac{3\,L}{20} & \frac{7\,L}{20} \\ -\frac{L^2}{30} & -\frac{L^2}{20} \end{pmatrix} \tag{E.14}$$

If $\mathbf{N}_e(x) = [1]$, the integral simplifies to

$$\mathbf{I}^*_{\alpha 1} = \begin{pmatrix} \frac{L}{2} \\ 0 \\ 0 \\ 0 \\ 0 \\ \frac{L}{2} \\ 0 \\ 0 \\ 0 \\ 0 \end{pmatrix}, \qquad \mathbf{I}^*_{y1} = \begin{pmatrix} 0 \\ \frac{L}{2} \\ \frac{L^2}{12} \\ 0 \\ 0 \\ 0 \\ \frac{L}{2} \\ -\frac{L^2}{12} \\ 0 \\ 0 \end{pmatrix}, \qquad \mathbf{I}^*_{z1} = \begin{pmatrix} 0 \\ 0 \\ 0 \\ \frac{L}{2} \\ \frac{L^2}{12} \\ 0 \\ 0 \\ 0 \\ \frac{L}{2} \\ -\frac{L^2}{12} \end{pmatrix} \tag{E.15}$$

Appendix F

Prevention of mode swapping for the p-k method using eigen mode orthogonality

The p-k method is sometimes used together with a post-treatment to discard the issue of mode swapping. Figure F.1 shows the code that is used in order to sort modes at a given step, after they have been computed using the `eig` function. The chosen mode is the one that maximizes the dot product between the modes considered in the current step, and that kept in the previous step.

The corresponding results for application 2 are shown in Figure F.2, where the algorithm is seen to fail around 33 m/s.

```
def process_pre_flutter( U, w0, xi, phi ):

    # U: wind speeds vector of size nU
    # w0: matrix (2 x nU) containing eigenvalues
    # xi: matrix (2 x nU) containing damping ratios
    # phi: matrix (2 x 2 x nU) containing the eigen vectors
    #       consistently normalized

    w0_ = np.zeros( (2,len(U)), dtype='float64')
    xi_ = np.zeros( (2,len(U)), dtype='float64')

    w0_[:,0] = w0[:,0]
    xi_[:,0] = xi[:,0]

    dprod = np.zeros( 2, dtype='complex128' )
    for iU in range( 1, len(U) ):
        dprod[0] = phi[0,:,iU-1].T @ phi[0,:,iU] \
             + phi[1,:,iU-1].T @ phi[0,:,iU]
        dprod[1] = phi[0,:,iU-1].T @ phi[1,:,iU] \
             + phi[1,:,iU-1].T @ phi[1,:,iU]
        idmax = np.argmax( np.abs( dprod ) )
        idcmp = int(idmax == 0) # complementary index

        w0_[0,iU] = w0[idmax,iU]
        w0_[1,iU] = w0[idcmp,iU]

        xi_[0,iU] = xi[idmax,iU]
        xi_[1,iU] = xi[idcmp,iU]

    return w0_, xi_
```

Figure F.1: Function used to post-process the data obtained with the p-k method to prevent the mode swapping. The eigen modes given as inputs must be consistently normalized (see for example (5.18)).

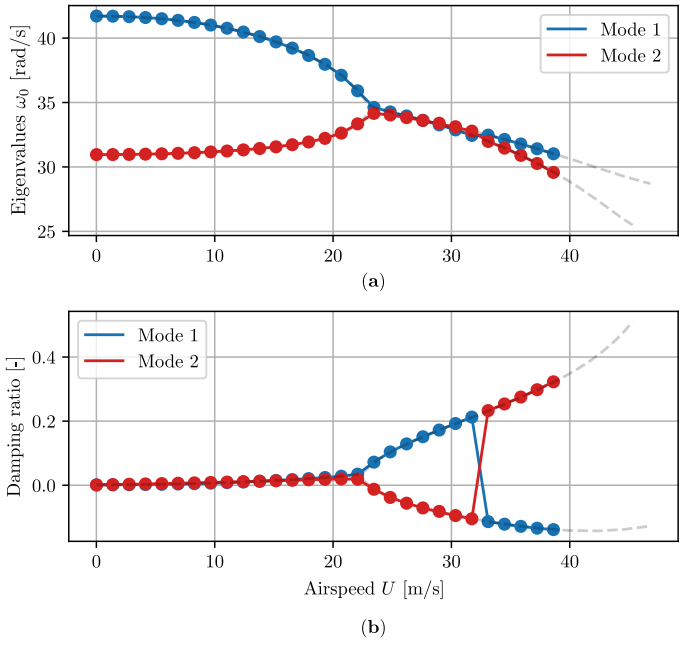

Figure F.2: Application 2 of Chapter 5 . Failure of the algorithm that aims at preventing mode swapping. There is one mode swapping around 32 m/s.